UNIVERSITÀ
DEGLI STUDI
DI PADOVA

Sede Amministrativa: Università degli Studi di Padova

Dipartimento di Geoscienze

CORSO DI DOTTORATO DI RICERCA IN: Scienze della Terra

CICLO: XXXII

MINERALOGICAL COMPOSITION AND GEOLOGICAL FEATURES OF C-TYPE ASTEROIDS INFERRED FROM METEORITES AND SPACE MISSIONS DATA

Coordinatore: Prof. Claudia Agnini

Supervisore: Prof. Matteo Massironi

Co-Supervisore: Prof. Luigi Folco

Co-Supervisore: Dr. Ernesto Palomba

Dottorando: Jacopo Nava

Table of Contents

Chapter 5
Outburst nature of hydrocarbons on icy bodies of the Solar System

Chapter 6
Hydrothermal experiments on the MCY14001 CM2 and FRO95002 CO3 chondrites with H_2O and ammoniated-H_2O - close affinities with Ceres-like asteroids

Chapter 7
An aqueously altered, thermally metasomatized CO chondritic micrometeorite – a new intermediate member within the CO-CM gap

Summary

In this PhD project we investigate the composition of primitive bodies of the Solar System (C-type asteroids and comets) providing insights with the combined petrographic and spectroscopic study of micrometeorites, carbonaceous chondrites (CCs) and laboratory experiments on CCs. The composition of C-type asteroids is similar, though not equal, to that of CCs. The IR reflectance spectra of C-type asteroids show as main features absorption bands at 2.7-2.8 μm, 3-3.1 μm, 3.3 μm and at 3.4-3.5 μm. The 2.7-2.8 μm band is indicative of Mg-OH bonds if centred at 2.7 μm and of Fe-OH bonds if at 2.8 μm. The 3 μm band is difficult to attribute to a specific compound. The 3 μm band is also used to distinguish 4 different C-type asteroid families, based on the band centre (BC): Sharp asteroids (BC at 3 μm), Ceres-like (BC at3.05 μm), Europa-like (BC at 3.15 μm) and rounded asteroids (rounded band at 3 μm). The 3.3 μm and the 3.4-3.5 μm bands are attributed respectively to aromatic and aliphatic hydrocarbons. The 3 μm band and organics are also common on comets. The main processes suggested to create these features and the associated minerals are low-T aqueous alteration and hydrothermalism, whereas sublimation and cryovolcanism, both characterised by outbursts, are distinctive processes of primitive icy bodies. To provide new insights on mineralogy and geological processing of primitive icy bodies we studied micrometeorites (MMs) (3 samples in particular: TAM5.29, TAM5.30, TAM18c.11 and TAM18c.13). We also made some laboratory experiments on CCs (FRO95002, FRO99040, FRO90006, MCY14001 and DaG521) to reproduce hydrothermal alteration and cryovolcanism.

Several different techniques were used for this project. Petrographic analyses have been done with Raman, Field emission SEM-EDS, SEM-EDS equipped with EBSD, XRD, μXRD and EMPA. Petrographic observations have been coupled with spectroscopy and gas chromatography analysis for organic matter investigations. For the cryovolcanism experiments we mixed some powders of CCs with deionized water and other with NH_4-water, froze them and heated up in vacuum from -195 to 100°C. For the hydrothermal experiments we mixed powders of FRO95002 with deionized water (water/rock= 0.1) and MCY14001 with NH_4-water (water/rock=1), put them in two autoclaves and heated at 240°C for nearly two months. The CCs powders were analysed both before and after the treatment.

TAM5.29 is dominated by a matrix of Fe-olivines and clasts of andradite surrounded by diopside-jarosite. We discovered that TAM5.29 records extensive hydrothermal alteration at T~250°C. A second episode of alteration at T<100°C occurred and resulted in the formation of iddingsite. CH and SH functional groups are ubiquitous. TAM5.29 mineralogy is unique among the micrometeorites and is also slightly different from the known CV chondrites. TAM5.29 mineralogy lies in between the CV_{oxA} and CV_{oxB}. This intermediate mineralogy may represent a newly described alteration environment on the CV parent body. TAM18c.11 have a high porosity that favoured high Antarctic alteration and widespread replacement with jarosite. Phyllosilicates are recognisable along with small metal alloys. A portion of TAM18c.11 matrix has been detected and is composed of olivine crystals (1-2 μm) immersed in a mesostasis plus tiny metal-alloys. Raman analyses revealed that in TAM18c.11 there is also the ubiquitous presence of CH and SH functional groups. Another peak at 3412 cm^{-1} and can be due to NH functional groups, likely in the jarosite.

TAM5.30 is a "*wet*" CO-like micrometeorite. TAM5-30 records a two-part processing history characterised by an initial episode of low-temperature CM-like aqueous alteration leading to the formation of Fe-phyllosilicate, Cr-spinel and Fe-oxides, which later transitioned into higher

temperature (~300°C) CV-like thermal metasomatic alteration, resulting in the formation of abundant fayalite, apatite, diffusion profiles in mafic silicates and partially heated organic matter.

FRO99040, FRO95002 and FRO90006 (CO3) are composed of olivine and pyroxene with compositions $Fa_{1\text{-}59}$ and $Fs_{1\text{-}7}$ respectively. Fe-Ni alloys and troilite are abundant (~5 vol%) and also CAIs (~10 vol%). MCY14001 (CM2) olivines have fayalite content of $Fa_{0.3\text{-}57}$ and low-Ca pyroxenes a ferrosilite content of $Fs_{0.6\text{-}5}$. Serpentine is widespread replacing chondrules mesostasis and in the matrix, minor calcite crystals often associated to troilite, FeNi alloys are generally rare. CAIs builds up ~7 vol% of the sample. DaG521 is a CV3 chondrite and is the only meteorite of our set with reddish colour, probably due to iron oxide generated by weathering in the Libyan desert.

After the hydrothermal experiments FRO95002 didn't show any substantial mineralogical change, whereas MCY14001 showed the presence of magnetite and sulfides-hydrated sulfides (e.g. pentlandite-tochilinite) plus other minerals that we described later.

The 3.15 µm band of TAM5.29 is found scattered around the matrix associated to the 2.8 µm band, thus related to Fe-rich hydrous phases. An isolated spot gave spectra characterised by a 3.04 µm band that always appears together with the 3.4 µm and 3.5 µm bands of the aliphatic organics, indicating a relation between the 3.04 µm band and the organic matter. In TAM18c.11 the 3 µm is also shifted towards shorter wavelength at 3.05-3.06 µm. The band is associated with the 2.8-2.9 µm band and a broad band at 3.8 µm, suggesting close relationship with ammonium-jarosite. The CCs studied have spectra with a hydration band at 2.7 µm, the rest of the spectra is almost featureless. FRO95002 powders processed during the hydrothermal experiment gave a noisy spectra, the main change is the disappearing of the hydration band at 2.7 µm. Spectra of MCY14001 after the experiment exhibit two bands at 2.9 and 3.05 µm, not present in the original spectra. The 3.05 µm band is due to ammoniation of serpentine, a task never achieved before. Original powders of MCY14001 also had Na-carbonates, which after the experiment were replaced by ammoniated analcime-natrolite. In addition Fe-enstatite and diopside are also formed during the hydrothermal alteration. Cryovolcanism experiments gave insights on the hydrocarbon formation. The ejected outgassed powders of FRO90006, FRO99040, FRO95002 and DaG521 always show absorption bands at 3.4 µm and 3.5 µm while in the original unprocessed powders and on the powders that remained in the sample holder this feature is not found. Gas-chromatography analyses show that these features are given by aliphatic hydrocarbons, in particular by C_{17}, C_{19} and C_{21}.

We found the first 3 µm bearing samples, found a new way for organics processing and ammoniation process on planetary bodies and we also give new perspectives into cryovolcanism and hydrothermalism. The 3.15 µm band in TAM 5.29 is given by Fe-OH bonds, proving that the Europa-like asteroids are most likely Fe-rich hydrous worlds involved by hydrothermal and low-T aqueous alteration. The 3.07 µm band in TAM18c.11 is related to organic matter, in particular CH and NH in aromatic or aliphatic hydrocarbons, in phyllosilicates structure, sulphates and salts.

Hydrothermal experiments on MCY14001 confirm that the 3.05 µm band is related to NH and indicates that C-type asteroids went through hydrothermalism. Ceres-like asteroids with the 3.05 ± 0.01 µm band are thus enriched in organic matter.

We experimentally show that aliphatic hydrocarbons are created through outbursting at T≤-40°C, which on planetary bodies is induced by cryovolcanism and sublimation. This is also evidence that

comet's organics are not only remnants of the Solar Nebula, but can be created by Cometary activity itself.

TAM5.29 and TAM5.30 give new perspectives in the hydrothermal alteration of CCs parent bodies. They are products of unique accretion windows, occurring on a more heterogeneous CVs parent body in the case of TAM5.29 and in a mixed environment in-between the CO and CM chondrites parent bodies in case of TAM5.30.

Riassunto

In questo progetto di dottorato abbiamo indagato la composizione dei corpi primitivi del Sistema Solare (asteroidi di tipo C e comete) fornendo approfondimenti combinando analisi petrografiche e spettrali di micrometeoriti, condriti carbonacee (CC) ed esperimenti di laboratorio su CCs. La composizione degli asteroidi di tipo C è simile, sebbene non uguale, a quella delle CCs. Le firme spettrali di riflettanza nell'infra rosso (IR) degli asteroidi di tipo C mostrano come caratteristiche principali bande di assorbimento a 2.7-2.8 µm, 3-3.1 µm, 3.3 µm e 3.4-3.5 µm. La banda da 2.7-2.8 µm è indicativa dei legami Mg-OH se centrata a 2.7 µm e dei legami Fe-OH se a 2.8 µm. La banda a 3 µm è difficile da attribuire a un composto specifico. La banda a 3 µm viene anche utilizzata per distinguere 4 diverse famiglie di asteroidi di tipo C in base al centro di banda (BC): asteroidi "sharp" (BC a 3 µm), simili a Cerere (BC a 3.05 µm), simili a Europa (BC a 3.15 µm) e asteroidi "rounded" (banda arrotondata a 3 µm). Le bande a 3.3 µm e 3.4-3.5 µm sono attribuite rispettivamente agli idrocarburi aromatici e alifatici. La banda a 3 µm e i composti organici sono comuni anche nelle comete. I principali processi che si pensa aver creato queste caratteristiche spettrali e i minerali associati sono l'alterazione acquosa a bassa temperatura e alterazione idrotermale, mentre la sublimazione e il criovulcanismo, entrambi caratterizzati da outburst (episodi violenti esplosivi), sono processi distintivi di corpi ghiacciati primitivi. Per fornire nuove informazioni sulla mineralogia e sui processi geologici di corpi ghiacciati primitivi, abbiamo studiato diverse micrometeoriti (MM) (3 campioni in particolare: TAM5.29, TAM5.30, TAM18c.11 e TAM18c.13). Abbiamo anche fatto alcuni esperimenti di laboratorio sui CCs (FRO95002, FRO99040, FRO90006, MCY14001 e DaG521) per riprodurre l'alterazione idrotermale e il criovulcanismo.

Diverse tecniche analitiche sono state utilizzate per la realizzazione di questo progetto. Sono state condotte analisi petrografiche con Raman, Field-Emission-SEM-EDS, SEM-EDS equipaggiato con EBSD, XRD, µXRD ed EMPA. Le osservazioni petrografiche sono state abbinate alle analisi di spettroscopia e alle analisi sulla materia organica condotte con il gascromatografo. Per gli esperimenti di criovolcanismo abbiamo mescolato alcune polveri di CCs con acqua deionizzata e altre con acqua ammoniata, le abbiamo congelate e riscaldate in vuoto da -195 a 100°C. Per gli esperimenti di alterazione idrotermale abbiamo miscelato polveri della meteorite FRO95002 con acqua deionizzata (acqua/roccia = 0,1) e MCY14001 con acqua ammoniata (acqua/roccia = 1), le abbiamo messe in due autoclavi e riscaldate a 240°C per quasi due mesi. Le polveri di CCs sono state analizzate sia prima che dopo il trattamento. L'interpretazione e la datazione di un'area rilevante della superficie di Cerere sono state eseguite su immagini acquisite dalla sonda Dawn utilizzando sistemi GIS.

TAM5.29 è dominata da una matrice di olivine ricche in Fe e da clasti di andradite circondati da diopside-jarosite. La composizione della TAM5.29 è il risultato di alterazione idrotermale a T ~ 250°C. In aggiunta alla fase idrotermale si è verificato un secondo episodio di alterazione a bassa temperatura (T<100°C) che ha portato alla formazione di iddingsite. Si trovano anche sparsi in tutta la micrometeorite composti CH e SH. La mineralogia della TAM5.29 è unica tra le micrometeoriti ed è anche in parte diversa dalle condriti CV note fino ad ora. La mineralogia della TAM5.29 si trova tra CV_{oxA} e CV_{oxB}. Questa mineralogia intermedia può rappresentare un nuovo ambiente di alterazione sul corpo genitore CV mai descritto prima. La micrometeorite TAM18c.11 invece ha un'elevata porosità che ha favorito l'alta alterazione antartica e la sostituzione diffusa con il jarosite. Si riconoscono fillosilicati insieme a piccole leghe metalliche. Parte della matrice della TAM18c.11 è ancora visibile ed è composta da cristalli di olivina (1-2 µm) immersi in una mesostasi nella quale si

trovano anche leghe metalliche di dimensioni sotto il micron. Le analisi di Raman hanno rivelato che anche in TAM18c.11 c'è anche la presenza di gruppi funzionali CH e SH. Un altro picco a 3412 cm^{-1} può invece essere dovuto a gruppi funzionali NH, probabilmente presenti nella jarosite.

TAM5.30 è una micrometeorite simile alle condriti CO. La mineralogia della TAM5.30 mostra una storia evolutiva divisa in due parti: un episodio iniziale di alterazione acquosa simile a quello delle condriti CM a bassa temperatura che porta alla formazione di fillosilicati ferrosi, spinelli di cromo e ossidi di ferro, che in seguito sono passati a temperature più elevate (~ 300°C) andando incontro ad un metasomatismo simile a quello descritto nelle condriti CV, con conseguente formazione di fayalite, apatite, profili di diffusione in silicati mafici e parziale riscaldamento della materia organica.

FRO99040, FRO95002 e FRO90006 (CO3) sono composte da olivina e pirosseno con composizione $Fa_{1\text{-}59}$ e $Fs_{1\text{-}7}$ rispettivamente. Le leghe Fe-Ni e la troilite sono abbondanti (~ 5% in volume) così come i CAI (~ 10% in volume). Le olivine nella MCY14001 (CM2) hanno un contenuto di fayalite più eterogeneo $Fa_{0.3\text{-}57}$ e pirosseni a basso contenuto di Ca mostrano un contenuto di ferrosilite di $Fs_{0.6\text{-}5}$. Minerali del serpentino sono diffusi nella matrice e sostituiscono la mesostasi delle condrule. Nella MCY14001 si trovano anche cristalli di calcite spesso associati alla troilite, le leghe FeNi sono generalmente rare. I CAI sono circa il 7% in volume del campione. DaG521 è una condrite di tipo CV3 ed è l'unica meteorite studiata di colore rossastro, probabilmente a causa dell'ossido di ferro generato dagli agenti atmosferici nel deserto libico.

A seguito degli esperimenti idrotermali, FRO95002 non ha mostrato alcun sostanziale cambiamento mineralogico, mentre MCY14001 ha mostrato la presenza di magnetite e solfuri solfuri idratati (ad es. pentlandite-tochilinite) ed altre modifiche descritte in seguito.

Nella micrometeorite TAM5.29 si trova la banda a 3.15 µm sparsa nella matrice associata alla banda a 2.8 µm, quindi correlata a fasi idrate ricche di Fe. Un punto isolato ha dato spettri caratterizzati da una banda a 3.04 µm che appare sempre insieme alle bande 3.4 µm e 3.5 µm degli idrocarburi alifatici, indicando una relazione tra la banda a 3.04 µm e la materia organica. Nella TAM18c.11 la banda a 3 µm è spostata verso una lunghezza d'onda più corta a 3.05-3.06 µm. La banda è associata agli assorbimenti a 2.8-2.9 µm e una banda larga a 3.8 µm, suggerendo una stretta relazione con l'ammonio-jarosite. Le CCs studiate hanno spettri con una banda di idratazione a 2.7 µm, il resto degli spettri è quasi privo di assorbimenti. Le polveri della FRO95002 alterate durante l'esperimento idrotermale hanno dato uno spettro rumoroso, il cambiamento principale è la scomparsa della banda di idratazione a 2.7 µm. Gli spettri della MCY14001 dopo l'esperimento presentano due bande a 2.9 e 3.05 µm, non presenti negli spettri originali. La banda da 3.05 µm è dovuta ai composti NH che entrano nella struttura del serpentino, un risultato mai raggiunto prima. Le polveri originali di MCY14001 contenevano anche carbonati di Na, che dopo l'esperimento vengono sostituiti da analcime-natrolite anch'essi con segni di ammoniatura. Inoltre, durante l'alterazione idrotermale si formano anche enstatite ferrosa e diopside. Gli esperimenti di criovulcanismo hanno fornito spunti sulla formazione di idrocarburi. Le polveri che hanno subito sublimazione e outburst delle condriti FRO90006, FRO99040, FRO95002 e DaG521 mostrano sempre bande di assorbimento a 3.4 µm e 3.5 µm mentre nelle polveri originali e sulle polveri rimaste nel porta campione queste bande non sono state trovate. L'analisi col gascromatografo mostrano che queste caratteristiche sono date dagli idrocarburi alifatici, in particolare da C_{17}, C_{19} e C_{21}. Le polveri espulse della MCY14001 invece non hanno chiari e netti assorbimenti a 3.4 µm e 3.5 µm.

In conclusione, abbiamo trovato i primi campioni tra le collezioni di meteoriti che mostrano bande a 3 µm, abbiamo scoperto un inaspettato meccanismo di formazione della materia organica e un possibile processo di ammoniatura sui corpi planetari dando anche nuove prospettive sul criovulcanismo e sull'idrotermalismo. La banda a 3.15 µm in TAM5.29 è data da legami Fe-OH, a dimostrazione del fatto che gli asteroidi simili a Europa sono probabilmente mondi idrati ricchi di ferro coinvolti in processi di alterazione acquosa idrotermale e a bassa temperatura. La banda a 3.07 µm in TAM18c.11 è correlata alla materia organica, in particolare alle molecole CH e NH in idrocarburi aromatici o alifatici, nella struttura di fillosilicati, solfati e sali.

Gli esperimenti idrotermali sulla MCY14001 confermano che la banda da 3.05 µm è correlata a legami NH e indica che gli asteroidi di tipo C hanno attraversato un periodo di alterazione idrotermale. Gli asteroidi simili a Cerere con la banda diagnostica a 3.05 ± 0.01 µm sono quindi arricchiti di materia organica.

Inoltre mostriamo sperimentalmente che gli idrocarburi alifatici vengono creati da sublimazione e outburst a T≤-40°C. Questa è anche la prova che i composti organici delle comete non sono solo resti della Nebulosa Solare, ma possono essere creati dall'attività cometaria stessa.

TAM5.29 e TAM5.30 offrono nuove prospettive sull'alterazione idrotermale dei corpi dei loro genitori (e quindi delle CCs). Sono prodotti che rispecchiano finestre di accrescimento uniche, che indicano un corpo genitore delle condriti CV più eterogeneo di quanto si pensava nel caso di TAM5.29 e in un ambiente con composizioni e caratteristiche miste tra i corpi progenitori delle condriti CO e CM nel caso della TAM5.30.

Chapter 1

Introduction

1. Importance of meteorites

Meteorites are pieces of asteroids, planets (e.g. Mars) and satellites (e.g. Moon) that fell on Earth (Brearley and Jones, 1998). These rocks are thus a natural laboratory to study composition and geological processes of planetary and small bodies. Meteorites on Earth fall homogeneously around the Globe (tens of thousands tons every year, Love and Brownlee, 1993; Bland, 2001), however the majority of them are recovered on cold and hot deserts (e.g. Antarctica, Sahara, Atacama desert). They are divided into undifferentiated, not affected by strong geologic processes such as metamorphism and melting (Scott and Krot, 2003; Krot et al., 2014), and differentiated, which on the contrary are meteorites that went throught substantial geological processes in particular magmatic differentiation (Brearley and Jones, 1998; Mittleflehdt, 2003; Krot et al., 2014). The undifferentiated meteorites are the chondrites, the differentiated meteorites are instead divided in 3 subgroups: achondrites, stony-iron meteorites and iron meteorites as show in figure 1 (Brearley and Jones, 1998; Mittleflehdt, 2003; Krot et al., 2014; Benedix et al., 2014). Chondrites are the oldest known materials of our Solar System and bring information mainly on the Solar Nebula composition and processes and on the first geologic activity that took place in the early Solar System (see paragraph 2 for more detailed description) (Brearley and Jones, 1998; Scott and Krot, 2003; Krot et al., 2014;). Achondrites on the contrary are more evolved rocks that are the result of magmatic processes occurred later in the Solar System evolution (Brearley and Jones, 1998; Mittlefehldt, 2003, Krot et al., 2014). Achondrites are almost entirely made of silicates (mainly olivine and pyroxene and minor plagioclase), while the stony-iron and iron meteorites are made respectively of silicates plus Fe-Ni alloys and Fe-Ni alloy only and probably represent the core of a disrupted differentiated asteroid (Brearley and Jones, 1998; Mittlefehldt, 2003; Krot et al., 2014; Benedix et al., 2014).

With the help of reflectance spectroscopy data acquired by spacraft and ground based observations, some of the meteorite families have been associated with a specific asteroid or asteroid families (Burbine, 2013). Asteroids are subdivided into C-type, S-type and X-type (Burbine, 2013). C-type asteroids are those with a carbonaceous chondrite-like spectra and composition, to this group belong asteroids such as 1 Ceres, 2 Pallas, 10 Hygiea, 96 Aegle (Burbine, 2013). The S-type are the stony asteroids, the most famous of these is the asteroid 4 Vesta (Burbine, 2003) to which HED (Howardite-Eucrite-Diogenite) achondrites are attributed (Burbine et al., 2001; McSween et al., 2013). X-type asteroids are mostly metallic M-type asteroids (the most famous is the asteroid 16 Psyche made of iron meteorite-like material), other sub groups are the "primitive" P-type (259 Aletheia and 190 Ismene) and E-type asteroids rich in enstatite (Burbine, 2013). It is thus of huge importance the spectroscopic study of meteorites and the comparison with space mission data in order to find possible parent bodies of the different meteorites groups and thus understand composition of small bodies.

In this project we focused on C-type asteroids and their closest analogues: the carbonaceous chondrites. Different processes such as aqueous alteration, mild heating, sublimation-cryovolcanism and space weathering have interested these meteorites. Many of these processes took place on the parent body (i.e. space weathering irradiation, sublimation-cryovolcanism), while some others (i.e.

thermal metamorphism and aqueous alteration) might have taken place in the Solar Nebula or within the parent body in the early Solar System history (Brearley, 2014). With this project we want to deepen our knowledge on these still unresolved processes and on the C-type asteroids composition and geologic features.

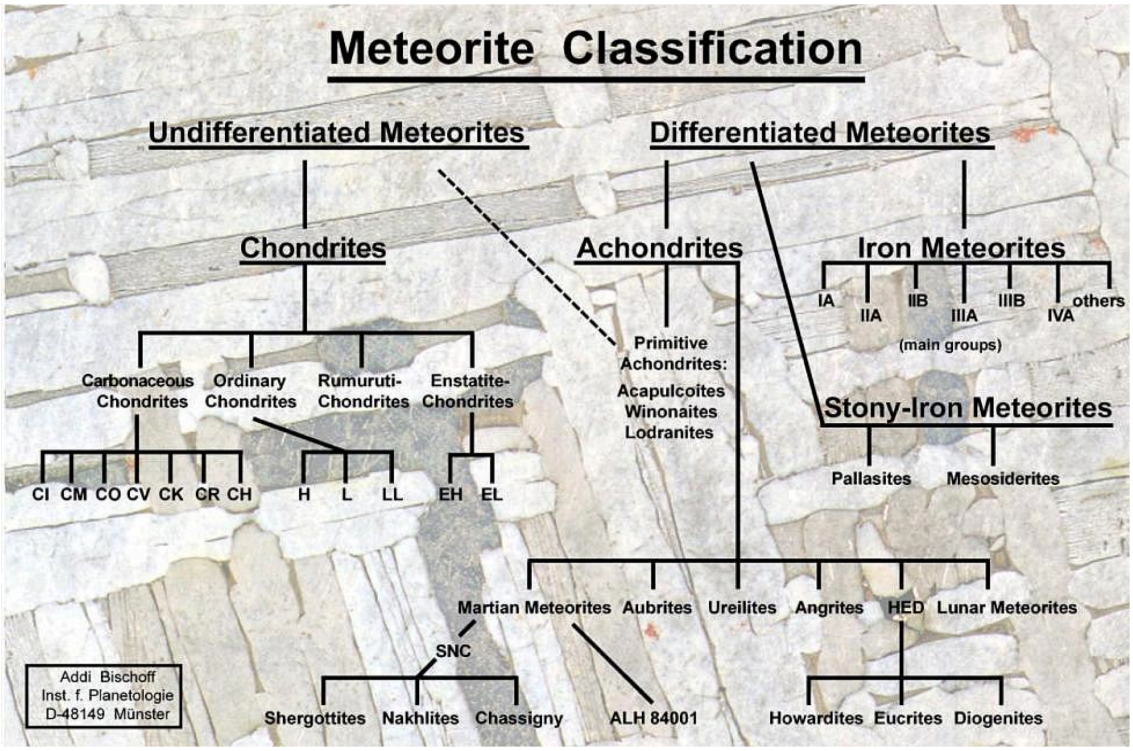

Fig. 1. Classification of all meteorite classes. Carbonaceous chondrites are divided in CI: Ivuna-like; CM: Mighei-like; CR: Renazzo-like; CO: Ornans-like; CV: Vigarano-like; CK: Karoonda-like; CH: ALH85085-like; CB: Bencubbin-like. Ordinary chondrites are divided in H: high total iron contents; L: low total iron contents; LL: low metallic iron and low total iron contents. Enstatite chondrite are divided in EH: high total iron; EL: low total iron. Iron meteorites are divided in groups from I to IV base on decreasing Ga and Ge concentrations. Furthermore IIAB, IID, IIIAB, VIA, IVB, IIIE and IIIF are iron meteorites free of silicates, while the IAB, IIE and IIICD have abundant silicates as well as graphite and carbides. (Brearley and Jones, 1998; Krot et al., 2014; Benedix et al., 2014).

2. Composition of C-type asteroids

In the recent years the interest in primitive C-type asteroids (Burbine, 2003) raised thanks to the successful space missions like the NASA-Dawn mission at 1 Ceres, Osiris-Rex on 101955 Bennu, Hayabusa 2 that is studying the 162173 Ryugu asteroid or also the Rosetta mission to the 67P/Churyumov-Gerasimenko comet. Indeed the composition of these primitive bodies of the Solar System is thought to be similar to that of the most pristine carbonaceous chondrites (CCs) (McCord and Gaffey, 1974).

CCs are the oldest (~4.5 Ga) and most pristine known materials of our Solar System (Brearley and Jones, 1998; Scott and Krot, 2003) and are divided in seven different groups based on mineralogy, textures and isotope composition. Such groups are: CI, CM, CR, CO, CV, CK and CH. CCs can be considered as conglomerates mainly made of chondrules, metal alloys, Calcium-Aluminium inclusions (CAIs) and other exotic materials like interstellar dust grains and presolar grains immersed

in a fine grained matrix (Brearley and Jones, 1998; Scoot and Krot, 2003). Chondrules are sub-millimetre igneous spheres made mainly of Mg and Fe silicates (i.e. olivine and low-Ca pyroxene) found in mesostasis with the composition of a feldspatic glass (Brearley and Jones, 1998; Scoot and Krot, 2003). The most accredited formation of chondrules is through transient heating events that melted dust grains in the Solar Nebula (Brearley and Jones, 1998; Scott and Krot, 2003). Chondrules show different textures such as barred-olivine, porphyritic, radial pyroxene and microcrystalline textures (Brearley and Jones, 1998; Scoot and Krot, 2003). Their abundances vary among the different CCs groups, where CIs and CMs are the most depleted in chondrules and are instead dominated by the matrix (Brearley and Jones, 1998). In the matrix Mg-Fe-phyllosilicates are also found together with Fe-Ni alloys and sulphides, oxides (e.g. spinel, magnetite, chromite), hydrous minerals like phyllosilicates, carbonates and organic matter as well as presolar grains and interstellar particles (Brearley and Jones, 1998; Scoot and Krot, 2003; MacPherson, 2003; Zinner, 2003). Secondary processing is observed in CCs, in particular aqueous alteration, thermal metamorphism and shock metamorphism (Brearley and Jones, 1998; Scoot and Krot, 2003). Thermal metamorphism or aqueous alteration degree on meteorites are defined by the petrologic type, which goes from 1 to 6. Petrologic type 1 indicates high aqueous alteration that decreases in the type 2. From petrologic type 3 to 6 instead increases the thermal metamorphic grade. Shock metamorphism on meteorites is based on a scale from S0 to S6, indicating respectively un-shocked samples and high shocked samples that underwent complete melting (Brearley and Jones, 1998; Scoot and Krot, 2003). CCs don't show high shock stages, the highest reported shock stage is S3 recorded especially in CV chondrites, which also show crystal-preferred orientation created by impact compaction (Scott et al., 1992). The highest thermal metamorphism recorded don't exceed 300°C (petrologic type 3) (with the exception of CK and CR chondrites that can reach petrologic type 6-7) (Brearley and Jones, 1998; Scott and Krot, 2003), in particular CV chondrite record high fluid assisted thermal metamorphism (Krot et al., 1995-1998). On the contrary, CCs suffered extensive aqueous alteration caused by melting of trapped ice that created phyllosilicates and carbonates (Brearley and Jones, 1998; Scoot and Krot, 2003). The highest grade of aqueous alteration is found in the CIs chondrites, followed by CMs chondrites (Brearley and Jones, 1998; Scoot and Krot, 2003). Another important and distinctive component of Ccs are the Calcium-Aluminium Inclusions (CAIs) (Brearley and Jones, 1998; Scoot and Krot, 2003; MacPherson, 2003). CAIs are enigmatic inclusions made of Ca-Al rich phases as well as Ti and Mg minerals (i.e. corundum, hibonite, grossite, perovskite, anorthite, spinel, fassaite and melilite) (Brearley and Jones, 1998; MacPherson, 2003). The constituent minerals of CAIs have high vaporization temperatures (above 1300 K) and are probably formed from direct condensation from the Solar Nebula (Brearley and Jones, 1998; MacPherson, 2003).

The composition of C-type asteroids and CCs is not completely equal. The surface composition of C-type asteroids is known thanks to reflectance spectra acquired by spacecrafts or by ground-based acquisitions. The average spectra of C-type asteroids display 4 main absorption regions in the NIR range (fig. 2): the 2.7 µm band, 3 µm band, 3.3-3.5 µm and 3.9-4 µm bands regions.
The 2.7 µm region has a band centre (BC) that varies between 2.7 and 2.8 µm. This shift is indicative of Mg-phyllosilicates in case of BC towards 2.7 µm and Fe-phyllosilicates when the BC is at longer 2.8 µm wavelengths (Takir et al., 2013).
The 3 µm band region has a BC that goes from 3 µm up to 3.15 µm (Takir and Emery, 2012). The origin of this band is controversial and still unresolved. Many mineral phases and compounds have been attributed to this band. Generally the 3 µm is interpreted as a hydration band attesting the

presence of hydrated phyllosilicates and water ice (Takir and Emery, 2012; Hargrove et al., 2012-2015). Other authors suggested that the 3 µm absorption is given by the water-iron bond in hydrated Fe-rich phyllosilicates (e.g. cronstedtite) or in goethite (Rivkin et al., 2006; Beck et al., 2011). Another possible carrier of the 3 µm band is a mixture of crystalline water ice and ion-irradiated organics, mainly asphaltite (Vernazza et al., 2005). King et al. (1992) proposed that on Ceres ammonium bearing minerals as the main minerals that can give the 3 µm band. This interpretation received more consensus after the NASA-Dawn space mission at Ceres since spectral fitting models suggest that the 3 micron absorption, revealed on Ceres by the VIR spectrometer is well matched by ammoniated phyllosilicates (De Sanctis et al., 2015; Ferrari et al., 2019). More recently a 2.99-3 µm band has been detected on Ceres spectra and is found coupled with the 3.4 µm band of aliphatic hydrocarbons (De Sanctis et al., 2019). This additional band is probably also linked to NH functional groups in the organic matter (De Sanctis et al., 2019). De Sanctis et al. (2015) considered also other minerals as possible carriers of the 3 µm band such as cronstedtite, brucite and tochilinite. However these minerals don't fit the Ceres spectrum very well, especially the 2.46 µm band of brucite is not found on Ceres (De Sanctis et al., 2015). The 3 micron band is a feature detected also on comets: it was found on the 17P/Holmes comet during a massive outburst (Yang et al. 2009) and on the 17P comet was attributed to the presence of water ice (Yang et al., 2009). Goto et al. (2003) reported the detection of the 3 µm band in the centre of the proto-planetary nebula IRAS 22272+5435, and is probably derived from acetylene C_2H_2 and hydrogen cyanide HCN. Finally is is worth to highlight here that, among the meteorite collections it has never been found a sample with a clear 3 µm band.

The 3.3-3.5 µm region is related to organic matter. Band centres at around 3.3 µm are indicative of aromatic hydrocarbons, while 3.4 and 3.5 µm bands are the ones of aliphatic hydrocarbons (Orthus-Daunay et al., 2013; De Sanctis et al., 2017). Organic Material (OM) has been found in different Solar System bodies: 67P/Churyumov-Gerasimenko, Ceres, 24 Themis, 65 Cybele, Phoebe, Iapetus and Enceladus (De Sanctis et al., 2017 and references therein). There are several theories on the origin of the OM. Modifications of OM in icy bodies is related to internal processes, such as hydrothermal activity or relative low-temperature aqueous alteration between 2-250°C (Schulte and Shock, 2004; Vinogradoff et al., 2017). The timing of the alteration is also controversial, both short-duration and long-duration heating have been invoked for the formation of organics (Orthus-Daunay et al., 2013). Low- temperature (20-50°C) short-duration minimal alteration with local melting of cometary ice was also proposed for the formation of UltraCarbonaceous Antarctic Micrometeorites (UCAMM) (Yabuta et al., 2017). Irradiation of ices or the polymerization of mixtures of ices at low temperatures is another processes that affects organics and was proposed for the 67P/Churyumov-Gerasimenko comet (De Bergh et al., 2008). Interestingly an anomalous enrichment in organic material in micrometeorites (MMs) compared to CCs is systematically found (Yabuta et al., 2017; Bonal et al., 2019; See also chapter 3 of this work). The reason for this enrichment is not clear, but the most plausible explanation so far is a different starting composition of the MMs parent body(-ies) compared to those of CCs (Bonal et al., 2019).

Finally the 3.9-4 µm band is related to carbonates. The highest concentration of carbonates is found on Ceres (De Sanctis et al., 2016; Tosi et al., 2017; Carrozzo et al., 2017). Indeed Ceres has few localized spots enriched in Na-carbonates (e.g. Occator bright spots, Haulani crater – De Sanctis et al., 2016; Tosi et al., 2018; Carrozzo et al., 2017), whereas its whole surface is dominated by Ca-Mg-carbonates (Carrozzo et al., 2017).

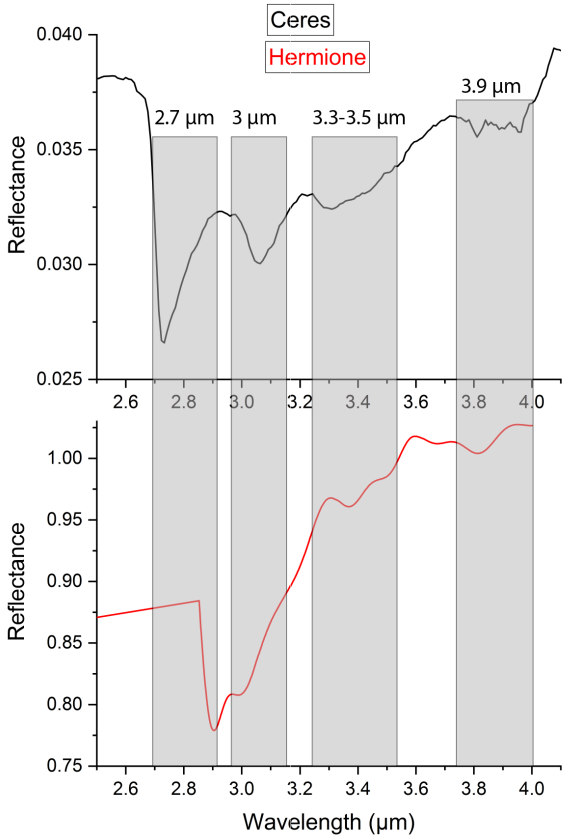

Fig. 2. IR reflectance spectra of C-asteroids Ceres and Hermione. Grey areas highlight the main important spectral regions distinctive of these bodies.

3. Hydrothermal and aqueous alteration on chondrites and their parent bodies

The main processes that shaped these C-type asteroids and changed their composition into the one we detect now in reflectance spectra are hydrothermal alteration (Neveu et al., 2015; Hendrix et al., 2016), low-temperature aqueous alteration and cryovolcanism, which is characterised by sublimation and outburst (Miles, 2016; Ruesch et al., 2016). Hydrothermal activity on CCs parent bodies is enhanced by impact and by decay of ^{26}Al and ^{40}K that heated a pristine homogeneous mixture of ice and rock (Grimm and McSween, 1989; Castillo-Rogez et al., 2008). The interior of CCs parent bodies were heated up to dehydration temperatures creating H_2 gas that migrated to the surface through cracks and fractures even with explosive processes that could even cause a break-up of the parent body (Grimm and McSween, 1989; Wilson et al., 1999). CCs parent bodies internal heating and hydrothermal convection were modelled by Wilson et al. (1999). In a body with endogenous radiogenic heating and a frozen outer shell can be recognized 4 different types of hydrothermal convections (Wilson et al., 1999). Wilson et al. (1999) considered a starting parent body (nominal case) with the following conditions: 20% porosity, 1 darcy uniform permeability (10^{-12} m^2), 3 x 10^{-8} weight fraction of ^{26}Al, density of 3000 kg m^{-3}, specific heat of 1000 J kg^{-1} K^{-1}, body radius of 50 km, solid rock thermal conductivity of 3 W m^{-1} K^{-1}, an exterior temperature of 170 K. In these conditions hydrothermal circulation is minimal (Wilson et al., 1999). Higher permeability and/or enhanced heating of the CCs parent body are necessary to trigger strong convections and plume-like structures, in particular permeability must increase to 10 darcys and the ^{26}Al fraction of 50% (Wilson et al., 1999).

Evidences of hydrothermal alteration are recognised also in meteorites, in particular in CV chondrites, with the formation of secondary mineral assemblages like fayalite-andradite/grossular-

diopside/hedenbergite-magnetite (Krot et al., 1998). The CV (Vigarano-like) carbonaceous chondrites (CCs) are a group of primitive meteorites sharing approximately equal ratios of chondrules and matrix, as well as the highest abundances of refractory phases (CAIs [Ca-Al-rich inclusions] and AOAs [ameboid olivine aggregate]) among any chondrite class (~10 vol%, McSween, 1977; Brearley and Jones, 1998; Weisberg et al., 2006). The CV class is divided into two subgroups: a reduced (CV_{red}) and an oxidized group (CV_{ox}) – dependent on their ratio of metal/magnetite and on the Ni content of sulfide phases (McSween, 1977). The oxidised CVs are further classified into Bali-like (CV_{oxB}) and Allende-like (CV_{oxA}) subtypes, with the Bali-like population containing high abundances of hydrated minerals (up to 4.2 vol%, Howard et al., 2010) (including Fe-phyllosilicate) and nearly pure fayalite (Fa_{90}) (e.g. Kaba: Fo_{100}=20.9 vol% and Fo_{90}=23 vol%; Mokoia: Fo_{100}=19.3 vol% and Fo_{90}=13.3 vol%; Howard et al., 2010), while the Allende-like population lack hydrated minerals and do not contain pure fayalite (Weisberg et al., 2006; MacPhearson & Krot 2014). Further differences are observed in the abundance and speciation of secondary minerals formed by metasomatic alteration (MacPhearson & Krot 2014). Fe-rich olivine and diopside-hedenbergite are found in all CVs. CV_{ox} and CV_{red} groups can be distinguished as CV_{ox} (especially the Allende-like members) contain nepheline, sodalite, andradite, magnetite and Fe-Ni-sulfides, whereas, these minerals are rare or absent in the CV_{red} group that instead contain kirschteinite (MacPhearson & Krot 2014).

These distinct mineralogies reflect different alteration histories of the CV parent body(-ies). It is known that the oxidised subgroup is enriched in alkali elements and Fe-rich silicates, attesting to Fe-alkali-halogen metasomatism (Krot et al., 1995; 1998). However, the formation of fayalite remains unresolved. Different processes have been invoked: alteration of low-Ca pyroxene into fayalitic olivine (Housley and Cirlin 1983), hydrothermal growth of fayalite (Krot et al., 2004) or the formation of fayalite through dehydration of phyllosilicates (Brearley 1999). At present, the most accredited mechanism of formation of fayalite is development during thermal metamorphism by growth from an amorphous precursor phase whilst in the presence of aqueous fluids (Abreu and Brearley 2011). Thermodynamic constraints on the formation of fayalite were delineated by Zolotov et al. (2006) who suggested that the presence of Ca-Fe-silicates (fayalite, nepheline, sodalite, diopside-hedenbergite, andradite, grossular, kirschteinite and phyllosilicates) are clear evidence of alteration from primary minerals held inside CAIs (i.e. melilite, anorthite, Al-Ti-diopside, hibonite, spinel and perovskite) (Krot et al 1995) with dissolution of anorthite and albite in chondrule mesostasis releasing CaO and SiO_2 for secondary mineral growth (Krot et al., 1995). The study of CV chondrites clearly shows that their parent body have a strong heterogeneity. However, it is unclear how much variability is possible within a single asteroid. As such the question of whether a carbonaceous chondrite group represents a single parent body or multiple parent bodies is a pertinent and unresolved question. This is not only the case of CV chondrites, it is also particularly true for the CO-CM chondrite clan which represents one of the largest and most studied carbonaceous chondrite groups and whose component meteorites exhibit a wide range of properties (Krot et al., 2000; Schrader and Davidson, 2017; Alexander et al., 2018).

Experiments on CCs were carried out by Nomura and Miyamoto (1998), Jones and Brearley (2006) and Palmer and Lauretta (2011) to investigate mineral changes during hydrothermal alteration. Nomura and Miyamoto (1998) made hydrothermal experiments on CAIs minerals such as gehlenite, spinel and diopside to reproduce secondary minerals found in CAIs. Most of the secondary minerals in CAIs are produced by the alteration of gehlenite, which releases Ca-Al-Si (Nomura and Miyamoto

1998). Ca reacts with CO_3 in the fluids to produce calcite and Na-Al-Si react to crystallize hydrated nepheline, sodalite, and analcime (Nomura and Miyamoto 1998). If CO_3 is absent also hydrogrossular can crystallize (Nomura and Miyamoto 1998). Jones and Brearly (2006) made hydrothermal experiments on the CV3 Allende at 100 to 200°C showing that Ca-Mg salts are the first phases affected by alteration. With increasing alteration Fe-olivines are replaced with interlayered serpentine-saponite and Fe-oxy-hydroxes assemblages (Jones and Brearley, 2006). The FeNi alloys, one of the main constituents of CCs, follow an alteration path in presence of fluids controlled by Si and S activity (Palmer and Lauretta, 2011). With high activity of S kamacite alters into tochilinite, P-sulfides, eskolaite and schreibersite (Palmer and Lauretta, 2011). With high Si activity alteration of kamacite turns into sulfide-bearing cronstedtite and with low S and Si activity altered kamacite crystallizes magnetite (Palmer and Lauretta, 2011).

Low-temperature alteration is a process that has been reported in meteorites and typically forms weathering films of the so-called iddingsite. Iddingsite is a common alteration feature that affects olivine in terrestrial rocks and is also found as a native minor component in chondritic meteorites. Iddingsite forms as a weathering film and represents a complex mixture of secondary hydrated silicates as well as carbonates, sulphates halides and oxides.
Lee et al. (2015) described iddingsite in the Lafayette meteorite as an alteration sequence affecting olivine and augite concurrent with the formation of hydrous Fe-Mg-phyllosilicates. These newly formed phyllosilicates are then partially replaced by siderite. During the growth of siderite Fe-oxides also begin to form (Abreu and Brearley 2011). The alteration sequence ends with saponite and other fibrous phyllosilicates replacing siderite. Tomeoka and Buseck (1985) described similar alteration features in the matrix of CM chondrites formed as an intergrowth of Fe-Ni-S-O phases and cronstedtite.

4. Cryovolcanism, sublimation and outbursting

Cryovolcanic activity is a process that characterised and is still active on minor bodies like Ceres (Ruesch et al., 2016), satellites like Europa (Quick et al., 2017), Enceladus (Postberg et al., 2009) and Charon (Desch and neveu, 2017). Cometary nuclei are also involved in cryovolcanic-like processes such as sublimation and outbursts (Miles, 2016; Vincent et al., 2016). Cryovolcanic processes and related products are still not well understood since the role of rock-ice interactions is still to be clarified. CCs, the closest match of the rocky and dusty fraction of the icy-bodies, are rich in soluble salts and unstable anhydrous minerals that can react with water even at low temperatures (Kargel, 1991). The Petrogenesis of the brines thought to take part cryovolcanism was described in the H_2O-Mg_SO_4-Na_2SO_4 system, where Mg_SO_4 and Na_2SO_4 are main solutes with minor sulphates of K, Ni, Mn and Ca (Kargel, 1991). Carbon-nitrogen-sulphur species and hydrogen are also very important since their exsolution lead to a gas-driven activity resulting in an explosive cryovolcanic event (Neveu et al., 2015). Surface expressions of cryovolcanism are multiple: conical mountains (Desch and Neveu, 2017), domes (Quick et al., 2017; Ruesch et al., 2016), sub-crustal water evaporation and comet-like sublimation (Küppers et al., 2014), salt rich water fountains (Ruesch et al., 2019), cryogenic flows (Krohn et al., 2016), ejecta curtain-like deposits (Belton and Melosh, 2009) as well as low–lying and low-albedo smooth surfaces (Fagents, 2003) and pits from sinkhole collapse (Vincent et al., 2015). Endogenic sources of energy necessary for outbursting are present on planetary bodies like endogenic heating derived from long-lived radioisotopes (Vincent et al., 2015; McCord et al., 2011), tidal stress (Neveu et al., 2015) or ascent of liquids and brines due to natural buoyancy (Desch and

Neveu, 2017). On cometary bodies mechanisms for sublimation-outbursting may slightly change from those active on asteroids. Outbursting on comets is driven by gas exsolution (Belton and Melosh, 2009), post impact heating (Krohn et al., 2016), rapid change of temperatures due to solar heating (Vincent et al., 2016), rapid release of pressure (e.g. cliff collapse) (Vincent et al., 2016) or by transition of amorphous ice to crystalline ice, a process that creates energy (Vincent et al., 2015). Volatiles exsolution is caused by thermal stress induced by solar illumination (De Sanctis et al., 2015), a process that is in common with some cometary-like sublimation seen on Ceres and Themis (Rivkin and Emery, 2010; Küppers et al., 2014), or by fluidization created by internal pressure of super-volatiles (Belton, 2010). Cometary outburst may be either a low-intensity widespread sublimation process related to sunlight or localized destructive episodes caused by supervolatiles release (Belton, 2010).

5. Open questions and aims of the project

As outlined above there are still many open questions regarding the composition of minor bodies of the Solar System and their geological processes. With this work we want to give new insights and answer to some of these unresolved questions.

In particular the main objectives of this project are:

- Attribute the different 3 µm band of C-type asteroid to mineral phases.
- Give new insights into hydrothermal alteration on minor bodies.
- Expand our knowledge on cryovolcanic processes and sublimation-outburst.
- Better understand formation and post-accretion processing of organic matter.

Considering that only one CV chondrite with 3 µm band have been found so far (Takir et al., 2019), we focused and searched among micrometeorites, never considered before for spectral analyses and comparison with C-type asteroids. The study of MMs as possible C-asteroids analogues was already accomplished by Vernazza et al. (2015) who searched among IDPs. Micrometeorites are dust grains with sub-millimetre dimensions (Genge et al., 2008) and are the main contributors of the incoming extraterrestrial material on Earth. In a year approximately 20000 - 60000 tons of micrometerites fall on Earth (Love and Brownlee, 1993; Zolensky et al., 2006). Micrometeorites sample minor bodies especially from the asteroid belt (Genge et al., 2008; van Ginneken et al., 2012; Carrillo-Sanchez et al., 2015) and cometary sources (Noguchi et al., 2015), the study of these particles can thus be a useful support to recent and upcoming space missions to C-type asteroids (e.g. NASA-Dawn mission at [1] Ceres, Hayabusa 2 at [162173] Ryugu, Osiris-Rex at [101955] Bennu) giving possible insights into the surface and subsurface composition and geological processes. Micrometeorites are liberated from their parent bodies in many different ways: impacts (Nesvorny et al., 2003; Flynn et al., 2009), spontaneous disruption (Nesvorny et al., 2010), sublimation (Schulz et al., 2004; Yang et al., 2009) and mantle shedding events (Schulz et al., 2015). According to oxygen isotopic composition and mineralogy, the majority of the micrometeorites (~75%) have an affinity to the carbonaceous chondrites (Suavet et al., 2010; van Ginneken et al., 2012; Taylor et al., 2012; Cordier et al., 2018). These micrometeorites are mainly porous and friable material named fine-grained unmelted micrometeorites (Fg-MM) (Genge et al., 2008). The Fg-MMs are divided in 3 groups, a division based on the hydration degree: C1 particles have extensively hydrated matrix, C2 less aqueously altered and C3 anhydrous (Genge et al., 2008). With this work we report the first

micrometeorites showing an unambiguous 3 µm band. The samples we studied are labelled TAM5.29, TAM18c.11 and TAM18c.13 and were collected on the Transantarctic Mountains by the Italian expedition (PNRA – Programma Nazionale delle Ricerche in Antartide). The study of these micrometeorites suggest that the 3 µm absorption is related to either Fe-rich hydrated minerals or organic matter or a combination of both. In addition, TAM5.29 turned out to be a unique particle with a CV-like composition resulted from hydrothermal alteration on the parent body. Thus, this discovery extend the range of known micrometeorites and brings additional insights into thermal metamorphism and hydrothermal history of the CV parent body-(ies).

In this study we also examine TAM5.30, a new and anomalous giant micrometeorite that shade light on the hydrothermal and aqueous alteration transition on CC parent bodies. Petrographic properties of TAM5.30 suggest a close affinity to the CO chondrites but with an otherwise anomalously high abundance of phyllosilicate and fayalite, and therefore a partially hydrated mineralogy, recording a significant episode of parent body aqueous alteration and subsequent thermal metasomatism, inconsistent with the known geological history of the CO or CM chondrite groups. This has implications for the number of parent bodies formed from a single source region of the solar nebula as well as for the general parent body processing pathways for chondritic samples.

To better understand cryovolcanic and hydrothermal processes we made experiments on CCs, the closest known meteorites to C-asteroids.

The cryovolcanism experiments show that organic matter (OM) forms during sublimation-outburst processes at low temperature (~ -40°C) in vacuum and reducing conditions. Formation of OM under these conditions has never been seen before and we experimentally show that during cryovolcanism and outbursting OM has a crucial role by being potentially synthesised. Thus, cryovolcanism and sublimation outbursting and OM post-accretion processing and formation are closely related. Implications of these findings are very interesting and add new important knowledge regarding C-asteroids, comets and other materials of the Solar System like micrometeorites.

Hydrothermal experiments have also been done. The results of the experiments show that during hydrothermal alteration there is an enrichment in Fe and Ca in the silicates as predicted by the CV chondrites metasomatic history and by the TAM5.29 micrometeorite we studied. Furthermore Na-phases (e.g. natron and nitrite) are leached during hydrothermal alteration and are replaced by analcime-natrolite.

During the hydrothermal alteration experiments we also used ammoniated water to recreated ammoniation, one of the main processes that occurred on Ceres (De Sanctis et al., 2015). Ammoniation experiments have already been done before under different conditions (room temperature and short duration experiments) (Ehlmann et al., 2018; Ferrari et al., 2019). These experiments failed to recreate ammoniation of serpentine, the main phyllosilicate in CCs. With our hydrothermal experiments we show for the first time that ammoniation of serpentine is possible in an environment where the temperature is higher (~250°C) and for longer alteration processes. We also show that phyllosilicates are not the only minerals that can carry NH compounds, also zeolites like analcime-natrolite can take ammonia in their structures. Ammoniation of both serpentine and analcime-natrolite give rise to the 3 µm band in the spectra of the weathered samples. Thus, hydrothermal experiments also bring additional knowledge on the nature of the 3 µm band of the C-type asteroids and on the geological processes that shaped the compositions of these bodies.

Finally, in the appendix we report a work that shows another possible application of carbonaceous chondrites. In this work powders of CCs were used for light scattering measurements to constrain the nature and behaviour of dust grains produced by comets and asteroids. The experimental curves have been obtained at the IAA Cosmic Dust Laboratory at a wavelength of 520 nm covering a phase angle range from 3° to 175° and direct observations and comparison on the 67P/Churyumov-Gerasimenko comet are reported. The polarization curves are qualitatively similar to ground-based observations of comets and asteroids and appears that the position of the inversion polarization angle is dependent on the composition of the grains. In addition, we found opposite dependence of P_{max} (maximum polarization at phase angles) for grain sizes in the Rayleigh-resonance and geometric optics domains, respectively. P_{max} decreases when the particle size increases, while in optical regime P_{max} increases with the particle size.

Chapter 2

Methods

In this project numerous different analytical techniques have been used. The multidisciplinary approach brought us to use mineralogical-petrographic techniques, remote sensing analyses comprehensive of compositional and morphological data as well as laboratory experiments.
We carried out the micro-morphological and preliminary chemical analysis of the samples using the Scanning Electron Microscope with Energy Dispersive X-ray spectrometry (SEM-EDS) and, for more detailsthe Field-Emission SEM (FE-SEM). For more precise chemical analyses we used the Electron Microprobe (EMPA). The mineralogical phases identification has been performed with micro-Raman, X-ray Powder Diffraction (XRD) and micro-XRD analyses. Electron BackScattered Diffraction (EBSD) was also used for minerals identification and for crystallographic orientations.
We took advantage of bidirectional reflectance spectroscopy for the comparison between meteorites and micrometeorites with asteroids. Macro-samples (meteorites and meteorites powders) were put in vacuum chambers and their reflectance spectra in the Near-IR (NIR) and Mid-IR (MIR) wavelength range (from 1 to 25 μm) have been acquired under asteroid-like conditions. Micrometeorites are instead small samples that need a microscope associated to the spectrometer in order to be analysed and for this reason they have been analysed under ambient conditions. In absence of vacuum some atmospheric phases (e.g. CO_2 between 4.15 and 4.35 μm or adsorbed water that might interfere with the 2.7 μm band) can be detected in the spectra and good care must be taken when analysing the results.
We compared both micrometeorites and meteorites spectra with space missions' data. For this comparison we focused on the 1.5 – 4 μm and in particular the 2.5-4 μm region which is the diagnostic range of C-type asteroids (detailes explained in paragraph 3). The data derived from spacecrafts (mainly from the Dawn mission) and all the spectra acquired in the laboratories have been processed with different software like ENVI and Origin, for compositional purposes, and ArcGis equipped with CraterTool for geological mapping and crater retention ages.

1. Sample collection and preparation

The micrometeorites studied were recovered from Frontier Mountain (72°59'S–160°20'E; at ~2800m above sea level and ~600m above the local icesheet surface), within Victoria Land, Antarctica. Micrometeorites were collected by the Italian Programma Nazionale delle Ricerche in Antartide (PNRA) during the 2003 expedition (Folco et al., 2008). Frontier Mountain consists of igneous rocks belonging the Granite Harbour Igneous Complex. The top of the mountain is characterised by flat-glacially eroded surfaces, created by an overriding icesheet in the past (Folco et al., 2008). On these flat surfaces numerous joints and weathering pits are found. These are filled with loose fine-grained bedrock detritus in which thousands of micrometeorites accumulated during the last ~1-2 million years along with a relatively small component of background terrestrial sediment (Folco et al., 2008). Particles TAM5.29, TAM18c.11 and TAM18c.13 were embedded in epoxy resin, sectioned and polished. The resulting thick section was used for whole-section petrographic analysis (FE-SEM-EDS, Raman, EMPA, EBSD, μXRD).

The Carbonaceous Chondrites (CCs) FRO95005, FRO99040, FRO90006 and MCY14001 were also collected by the Italian Programma Nazionale delle Ricerche in Antartide (PNRA) in the Frontier Mountain and Mount DeWitt blue ice fields. The other CCs studied were provided by ANSMET, the US Antarctic Search for Meteorites. All the CCs were polished thin sections, used for petrographic analyses (SEM-EDS, Raman, EMPA), as well as unprocessed pieces of the original samples used for spectroscopy, XRD and for experiments.

2. Petrography and major element analysis

Petrographic analysis of TAM5.29, TAM18c.11 and TAM18c.13 were made using a field-emission scanning electron microscope (ESEM-FEG-STEM FEI Quanta 450), equipped with microanalytical EDS (Energy Dispersive Spectrometry) Bruker, QUANTAX 400 XFlash Detector 6|10, which has a 129eV spectral resolution and an intermediate size 10mm^2 detector plate, capable of rapid-data collection semi-quantitative results at the Centro Interdipartimentale di Scienza e Ingegneria dei Materali (CISIM), University of Pisa. All analyses were performed under high-vacuum and at a fixed working distance of 10.0mm (the optimal sample-to-pole-piece distance to maximise X-ray counts at the EDS detector on this instrument). Operating conditions are standardized for our lab and use an electron beam accelerating voltage of 15kV and an unmonitored beam current. Spectra were acquired with an acquisition time of 30s maintaining a deadtime of approximately 10%. EDS data reported are therefore uncalibrated and standard-less. Weight totals were determined using the Bruker's "*interactive oxides*" and are quoted as weight normalized values. Elemental detection limits for this instrument are on the order of 0.2-0.5wt%.

Other SEM-EDS analyses were carried out at the Department of Geosciences, University of Padova with a CamScan 2500 SEM equipped with a LaB6 source. Operation conditions were 25 mm working distance, 15 kV beam acceleration and 10 nA probe current.

Mineral phases were identified by Raman measurements at the Department of Geosciences, University of Padova, using a Thermo Scientific™ DXR™ Raman Microscope using a 532 nm laser excitation source. Analyses were performed using a 50x and 100x long working distance objective with ~2.5 cm^{-1} spectral resolution, ~1 µm spatial resolution and 25 µm pinhole operating at a minimum of 1 mW to a maximum of 5 mW of power. Low power (1 to 5 mW) coupled with short exposure times of 3-4 s was essential to avoid damage to minerals and carbonaceous phases. To minimise noise, each spectrum was acquired 10 to 15 times. Spectra were recorded in the frequency range from 100 to 3500 cm^{-1}. Spectral fitting was carried out using the Thermo Scientific™ OMNIC™ Spectra Software. Rectangular areas were analysed with the Raman *point-by-point* mapping technique – again each spectrum in the map was collected 10-15 times using an exposure time of 3 to 4 s and spectra were obtained from a grid of points spaced 2 µm along X axis and 2 µm along Y axis.

Raman spectroscopy for TAM5.30 was carried out using a Reinshaw inVia Raman microscope, hosted at the Diamond Lightsource synchrotron facility, UK (offline labs). A 473nm green Ar^+ laser was focused through a 50x objective lens providing a ~6 µm diameter spot. Care was taken to ensure an extremely low laser power (<80µW) in accordance with standard analytical protocol for analysis of highly disordered carbonaceous phases, thereby preventing modification and graphitisation of micrometeorite's organic matter (Bonal et al., 2007). The resulting Raman spectra were processed by fitting against a 6th order polynomial baseline and exponentially smoothing the subtracted

spectrum. Carbonaceous 'G' and 'D' bands were then modelled using a 2-part Lorentz/Voigt model. Peak parameters from each spectrum were averaged and their standard deviation (σ) calculated.

EBSD analysis was performed on a CamScan 2500 SEM (Department of Geosciences, University of Padova) equipped with a LaB6 source, a NordlysNano EBSD detector of Oxford Instruments and Channel 5.12 EBSD acquisition- and post-processing software. The sample was for one-hour Syton polished to remove surface damage related to conventional diamond polishing, and was then carbon coated (few nanometers of thickness) to improve conductivity. Operation conditions were 25 mm working distance, 15 kV beam acceleration and 10 nA probe current. Considered the small grain size of the olivine crystals, for EBSD mapping in automated mode a 0.1 µm step-size in X and Y directions was applied during acquisition of a 600 x 400 data grid. EBSD does not discriminate between solid-solutions of olivine, garnet and Cpx, therefore forsterite and diopside reflector files of the HKL database were used to index olivine and Cpx, whereas andradite of the American Mineralogist Crystal Structure Database (Downs and Hall-Wallace, 2003) was used to index andradite. Indexing of the EBSD-patterns was accepted when at least 6 Kikuchi bands were detected. EBSD data were processed using the Oxford Instruments HKL software package Channel 5.12, generating crystallographic orientation maps, band contrast maps, phase maps and pole figure plots after noise reduction. Latter was done by removing isolated misindexed data points using a wildspike correction, whereas all non-indexed points were infilled to a six nearest-neighbour crystallographic orientation by extrapolation. In the Channel 5.12 software package grain detection in EBSD maps is based on crystallographic orientation, using a misorientation angle of at least 10° between two adjacent pixels to identify grain boundaries. Grain orientation data from the entire map were plotted onto lower hemisphere equal area projections as one point per grain to avoid grain size related bias during contouring.

We determined bulk mineralogy through µXRD diffraction methods, using a Rigaku Rapid II micro-diffraction system, equipped with a 2D curved imaging plate detector, at the Department of Earth Science, The Natural History Museum in London. This was employed to collect in-plane diffraction pattern data from the TAM5.29 sample. A Cu X-ray source with an incident beam monochromator provided Kb filtered Cu-Kα radiation (1.5418 Å). This was collimated by a pinhole system to a beam spot of 100µm. Analysis ran for 10 hours, after which the 2D diffraction image was converted to a 1D XRD pattern following automated removal of the background signal and integration of the Debye rings. Data were collected on cross section samples using a constant ω angle of 16º2θ and a rotating φ axis to maximise the number of crystallites and the randomness of their orientations in the X-ray beam. Low-angle (<16°2θ) diffraction peaks could not be collected because the polished resin block, which holds the particles prevented the stage from rotating in the ω plane by <16°2θ. Peak positions in the converted 1D patterns were identified by comparison against a mineral reference database (PDF-4 database from ICDD).

EMPA spot analyses were carried out at the Department of Geosciences, University of Padova with a CAMECA SX50 instrument with 5 wavelength dispersive spectrometers. Data were acquired with a beam current of 20 nA, accelerating voltage of 20 kV, defocused beam diameter of 5 µm and we used for each element an acquisition time of 10 seconds. Amelia plagioclase, olivine, orthoclase, diopside, sphalerite (blenda), synthetic $MnTiO_3$ and Cr_2O_3 standards were used for instrumental calibration. The Pouchou-Pichoir procedure (PAP), supplied by the manufacturer, was used for raw

data reduction. Detection limits (wt%) are: Na_2O=0.04; MgO=0.02; Al_2O_3=0.02; SiO_2=0.3; SO_3=0.03; K_2O=0.02; CaO=0.02; TiO_2=0.02; Cr_2O_3=0.04; MnO=0.04; FeO=0.04. We also used EMPA spot analyses to obtain the bulk composition of TAM5.29 by averaging a grid of 122 randomly spaced EMPA analyses in a specific representative area chosen on the basis of EDX maps, especially to avoid areas with major terrestrial alteration.
For TAM5.30 we also collected high accuracy EMPA data were collected at the Natural History Museum (NHM), London using a Cameca SX100 SEM, equipped with 5 wave dispersive spectrometers. Analyses were conducted at 20kV accelerating voltage, with a 20nA beam current and a <4µm spot size. Prior to analysis, the system was calibrated using suite of mineral standards, specific to each element under detection and post analysis PAP matrix corrections were performed using the in-house Cameca software. This removed artefacts arising from atomic number, absorption and secondary fluorescence (ZAF) effects. Elemental detection limits for this instrument are on the order of 0.02-0.05wt% and elemental uncertainties vary between 0.01-0.03wt%, values quoted in Table.2 are given to 2 decimal places.

X-ray powder diffraction (XRD) patterns were acquired with an X´Pert PRO MPD (PANalytical) instrument in Bragg–Brentano geometry with iron-filtered Co-Kα radiation (40 kV, 40 mA, λ = 0.1789 nm), equipped with an X´Celerator detector at room temperature. The powders were placed onto a rotating metal slide; the angular range was set as 2θ = 3 – 85°, with a step size of 0.017° and scan speed of 0.0061° s^{-1}. The identification of the crystalline phases was obtained using the X'Pert High Score Plus software, which includes a PDF-2, Pan-ICSD and COD (Crystallography Open Database) databases.

3. Spectroscopy

Reflectance near-IR spectra of micrometeorites were acquired at the laboratories at the IAPS-INAF (Istituto di Astrofisica e Planetologia Spaziali – Istituto Nazionale di Astrofisica). We used a microscope Micro-IR Hyperion 2000 FTIR Vertex Bruker®. The spectra were acquired under ambient conditions in the spectral range between 1.3- 22 µm (here we focused and report only the range between 1.5 – 4.2 µm), with a MCT detector. Infragold (Labsphere®) has been used to calibrate spectral reflectance. The spectra were acquired with a spectral resolution of 2 cm^{-1} and an aperture on the sample of 150X150 µm.

For more precise and detailed reflectance spectra analyses of the micrometeorites we performed FTIR hyperspectral imaging measurements at the SMIS beamline of the SOLEIL synchrotron (France), using an Agilent Cary 670/620 micro-spectrometer equipped with a 128 x 128 pixels FPA (Focal Plane Array) detector (the system is described in more details by Dionnet et al., 2018 and Brunetto et al., 2018). We collected NIR-MIR from 4000 to 850 cm^{-1} (2.50–11.76 µm) spectra under ambient conditions using the internal globar source, but we focused on the 2.5-4 µm range sincewith this set up was not possible to acquire a continuous spectra in the 1.5-4 µm region like at IAPS-INAF). The spectral resolution was either 4 or 8 cm^{-1}. We acquired the MIR maps in reflectance geometry, with respect to gold references. In one complete acquisition we accumulated 512 or 1024 scans. In our setup, the FPA is projected on the focal plane through a 25x objective (numerical aperture 0.81), providing a field of view of about 420x420 µm2 and a projected pixel size of about 3.3 µm (spatial sampling of the MIR maps). We thus simultaneously collected 16384 spectra per acquisition without moving the X-Y stage of the microscope. In some cases, we acquired only 64x64 pixels to

select a smaller field of view of 210x210 µm2. Larger spectral mosaics were measured by moving the X-Y stage and acquiring several tiles, to cover mm-sized areas of the sample. In the case of the large mosaics, a 4-pixels bin was applied.

Experiments were carried out at the Planetary Spectroscopy Laboratory (PSL) of the German Aerospace Center (DLR: *Deutsches Zentrum für Luft- und Raumfahrt*) in Berlin. IR spectra of original CCs and of the resulting materials from the experiments were acquired under asteroid-like conditions using a Bruker Vertex80V FTIR spectrometer equipped with a bi-directional reflectance unit, a MIR global source, a liquid nitrogen cooled MCT detector and a KBr beamsplitter. Bi-directional reflectance was measured at room temperature under purging/vacuum conditions, covering the 1 to 25 µm spectral range with an illumination angle fixed at 30° and variable emission angles at 15°, 30° and 45°.

We compared the average mid-IR spectrum (8-13µm) of TAM5-30 against a suite of mineral standards publicly available as part of the RRUFF database (Lafuente et al., 2015) as well as dehydrated phyllosilicate spectra published in Che and Glotch (2012) and amorphous Mg-silicate spectra published in Hallenback et al., (1998). Using a simple linear mixing model fed with the above mineral standards we were able to reproduce a modelled spectrum for TAM5-30, which closely matches the empirical spectrum. This approach allows an approximate estimation of modal mineralogy and is valid for phases present at >5% [vol.] abundance and whose grain sizes are >50µm and thus unaffected by volume scattering effects (Ramsey and Christensen, 1998; Feely and Christensen, 1999).

The continuum removal in all the reflectance analyses has been carried out with the Origin software and has been done individually for each diagnostic band of the C-type asteroids: 2.7 µm, 3 µm, 3.4-3.5 µm and 4 µm bands. For the removal of the continuum we individually take into account the band shoulders for each spectrum of every sample (see an example in figure 3). The band centre of each band did not suffer substantial changes after the continuum removal. However the continuum removal is crucial for the determination of band depths and allows better comparisons among sample spectra, highlighting qualitative different abundances of various minerals.

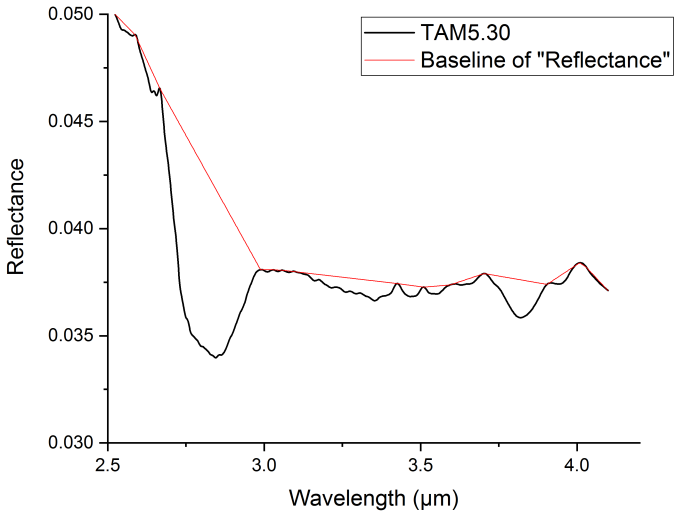

Fig. 3. Example of baseline creation for the continuum removal.

4. Organic matter analyses

n-alkane analyses were carried out with a single quadrupole GC-MS (Hewlett Packard-Agilent 6890 Series GC System, coupled with an Agilent 5973 inert Mass Selective Detector) operating in electron impact mode (EI, 70 eV) equipped with a 30 m long column (HP-5ms, 0.25 mm I.D., 0.25 µm film thickness). The MS source and analyzer were set to 230°C and 150°C respectively, while the transfer line was set to 300°C. The operating conditions of the GC were optimized and set as follows. Helium 5.5 (99.9995%) was used as carrier gas at a constant flow rate of 1.2 mL min^{-1}. The splitless mode inlet was set to 300°C. The oven was programmed from 50°C (holding time of 5min) to 315°C at 18°C min^{-1} with 6 min hold, for a total run time of 26 min. Acquisition was performed using selected ion monitoring (SIM) mode and PFTBA was chosen as reference compound.

In order to enhance repeatability and reduce contamination risks, automated instruments were used for analytes extraction and sample clean-up. Briefly, homogenized sub-samples of carbonaceous chondrite powders, as well as procedural blanks, were spiked with a known amount of hexatriacontane as internal standard. Aliphatic hydrocarbons were extracted by means of a Accelerated Solvent Extractor (ASE™ 350, Thermo Fisher Scientific Dionex) using a mixture of dichloromethane (DCM) and *n*-Hexane (HEX; 1:1; v/v). The extractions were carried out in the presence of anhydrous sodium sulphate, diatomaceous earth and Ottawa sand, and were performed at 100°C and 100 bar, with 5 static cycles of 5 min each. Clean-up was performed by direct injection of the sample in a Power-Prep™ system (FMS, Fluid Management System) into a disposable neutral silica column and by eluting with 30 mL of HEX followed by 30 mL of DCM-HEX (1:1; v/v). Purified samples were reduced to 100 µL under a gentle nitrogen flow at 23°C (Turbovap® II, Caliper Life Science). Results were corrected using the instrumental response factor and subtracting the procedural blank values.

Chapter 3

Hydrothermal activity on the CV parent body: new perspectives from the giant Transantarctic Mountains minimeteorite TAM5.29

Abstract

TAM5.29 is an extraterrestrial dust grain, collected on the Transantarctic Mountains (TAM). Its mineralogy is dominated by an Fe-rich matrix composed of platy fayalitic olivines and clasts of andradite surrounded by diopside-jarosite mantles, chondrules are absent. TAM5.29 records a complex geological history with evidence of extensive thermal metamorphism in presence of fluids at T<300°C. Alteration was terminated by an impact, resulting in shock melt veins and compaction-orientated foliation of olivine. A second episode of alteration at lower temperatures (<100°C) occurred post-impact and is either parent body or terrestrial in origin and resulted in the formation of iddingsite. The lack of chondrules is explained by random sub-sampling of the parent body, with TAM5.29 representing a matrix-only fragment. On the basis of bulk chemical composition, mineralogy and geological history TAM5.29 demonstrates affinities to the CV_{ox} group with a mineralogical assemblage in between the Allende-like and Bali-like subgroups (CV_{oxA} and TAM5.29 are rich in andradite, magnetite and FeNiS but CV_{oxA} lacks hydrated minerals, common in TAM5.29. Conversely CV_{oxB} are rich in hydrated phyllosilicates but contains almost pure fayalite, not found in TAM5.29). In addition, TAM5.29 has a slightly different metasomatic history, in-between the oxidised and reduced CV metamorphic grades whilst also recording higher oxidizing conditions as compared to the known CV chondrites. This study represents the third CV-like cosmic dust particle, containing a unique composition, mineralogy and fabric, demonstrating variation in the thermal metamorphic history of the CV parent body(-ies).

1. Introduction

The CV (Vigarano-like) carbonaceous chondrites (CCs) are a group of primitive meteorites sharing approximately equal ratios of chondrules and matrix, as well as the highest abundances of refractory phases (CAIs [Ca-Al-rich inclusions] and AOAs [ameboid olivine aggregate]) among any chondrite class (~10 vol%, McSween, 1977; Brearley and Jones, 1998; Weisberg et al., 2006). Chondrules in CVs are typically large (averaging 1 mm in diameter) type I, porphyritic olivine subtypes (~90%, Jones, 2012) and often surrounded by thick (~400μm) accretionary rims (King and King, 1991; Tomeoka and Ohnishi, 2010). Meanwhile, their matrices are rich in fayalitic olivine, Ca,Fe-pyroxenes and andradite (Krot et al., 1995-1998; Brearley and Jones, 1998; Weisberg et al., 2006).

The CV chondrite group most likely represent members of a single parent body, derived from an asteroid-sized planetesimal. Thermal remnant magnetism studies reveal a single coherent magnetic field among constituent chondrules (Carporzen et al., 2011). This requires the presence of a partially differentiated structure with a molten core and silicate mantle overlain by a cold chondritic "*lid*" as described by the model of Weiss and Elkins-tanton, (2013). Furthermore, isotopic signatures of CV chondrites (ε^{54}Cr vs. ε^{50}Ti and ε^{54}Cr vs. Δ^{17}O) fall within the carbonaceous supergroup, requiring an outer solar system origin or late accretion history (Warren, 2011). In addition to a partially differentiated interior, the CV chondritic "*lid*" attests to a protracted episode of parent body evolution with evidence for aqueous alteration (variously characterised by oxidation, hydration and replacement [e.g. phyllosilicate-rich chondrule rims, Tomeoka and Tanimura, 2000 or oxidized metal and mobilizied Na and K, Krot et al., 2004]) as well as recording the highest grade shock deformation

among the carbonaceous chondrites (commonly S2-S3 shock stages, Scott et al., 1992) and thermal metamorphism (~300°C, Krot et al., 1995; 1998).

The CV class is divided into two subgroups: a reduced (CV_{red}) and an oxidized group (CV_{ox}) – dependent on their ratio of metal/magnetite and on the Ni content of sulfide phases (Mcsween, 1977). The oxidised CVs are further classified into Bali-like (CV_{oxB}) and Allende-like (CV_{oxA}) subtypes, with the Bali-like population containing high abundances of hydrated minerals (up to 4.2 vol%, Howard et al., 2010) (including Fe-phyllosilicate) and nearly pure fayalite (Fa_{90}) (e.g. Kaba: Fo_{100}=20.9 vol% and Fo_{90}=23 vol%; Mokoia: Fo_{100}=19.3 vol% and Fo_{90}=13.3 vol%; Howard et al., 2010), while the Allende-like population lack hydrated minerals altogether and do not contain pure fayalite (Weisberg et al., 2006; MacPhearson & Krot 2014). Further differences are observed in the abundance and speciation of secondary minerals formed by metasomatic alteration (MacPhearson & Krot 2014). Fe-rich olivine and diopside-hedenbergite are found in all CVs. CV_{ox} and CV_{red} groups can be distinguished as CV_{ox} (especially the Allende-like members) contain nepheline, sodalite, andradite, magnetite and Fe-Ni-sulfides, whereas, these minerals are rare or absent in the CV_{red} group that instead contain kirschteinite (MacPhearson & Krot 2014).

These distinct petrographies require different alteration histories operating on the theoretical pristine CV material. The oxidised subgroup is enriched in alkali elements and Fe-rich silicates, attesting to Fe-alkali-halogen metasomatism (Krot et al., 1995; 1998). However, the formation of fayalite remains unresolved. Different processes have been invoked such as: alteration of low-Ca pyroxene into fayalitic olivine (Housley and Cirlin 1983), hydrothermal growth of fayalite (Krot et al., 2004) or the formation of fayalite through dehydration of phyllosilicates (Brearley 1999). At present, the most accredited mechanism of formation of fayalite is development during thermal metamorphism by growth from an amorphous precursor phase whilst in the presence of aqueous fluids (Abreu and Brearley 2011). Thermodynamic constraints on the formation of fayalite were delineated by Zolotov et al. (2006) who suggested that the presence of Ca-Fe-silicates (fayalite, nepheline, sodalite, diopside-hedenbergite, andradite, grossular, kirschteinite and phyllosilicates) are clear evidence of alteration from primary minerals held inside CAIs (i.e. melilite, anorthite, Al-Ti-diopside, hibonite, spinel and perovskite) (Krot et al 1995) with dissolution of anorthite and albite in chondrule mesostasis releasing CaO and SiO_2 for secondary mineral growth (Krot et al., 1995).

Among micrometeorite collections only two particles have previously been recognized as CV-like (Genge 2010 and van Ginneken et al. 2012), although neither were the subject of a detailed investigation into their parent body processing, a task that we discuss in this work with a more detailed characterisation of the CV-like TAM5.29 particle. Furthermore, the classification of these samples as a CV-like reveals some issues. The particle described by van Ginneken et al. (2012) contains wüstite instead of Fe-Ni metal and the magnetite composition does not fall in the CV magnetite field. On the other hand, the sample described by Genge (2010) show olivines with rounded morphologies and a high density of crystal defects, which are not typical characteristics of CVs. For this reason, van Ginneken et al. (2012) and Genge (2010) also suggested an affinity with CO chondrites. In addition TAM5.29 has andradite inclusions, diopside crystals and oriented petrofabric of olivine that were not detected in the two other CV-like particles described by Genge (2010) and van Ginneken et al. (2012), making TAM5.29 different and unique with an enhanced metasomatic history and with an undoubted metamorphosed CV-like mineralogy.

Micrometeorites from anhydrous CC groups are relatively rare, Although up to the 50% of the incoming micrometeorite flux have oxygen isotopic compositions related to the CO/CV/CK

anhydrous supergroup (Suavet et al., 2010). Thus, the characterisation of unique micrometeorites and those derived from rare parent bodies is crucial for our collective understanding of the near-Earth dust complex and the diversity of the asteroid belt.

Here we provide a detailed characterisation of the third CV-like cosmic dust particle with unique mineralogy and fabric, expanding knowledge in the compositional range of micrometeorites as well as investigating the thermal metamorphism and hydrothermal history of the CV parent body-(ies). Furthermore, given that micrometeorites originate from the asteroid belt (Genge et al., 2008; van Ginneken et al., 2012) and cometary sources (Noguchi et al., 2015), the study of this sample can be a useful support to recent and upcoming space missions to C-type asteroids (e.g. NASA-Dawn mission at [1] Ceres, Hayabusa 2 at [162173] Ryugu, Osiris-Rex at [101955] Bennu) giving possible insights into the surface and subsurface composition and geological events. In particular, TAM5.29 with its particular metasomatic history adds knowledge on aqueous alteration and hydrothermalism, that are known to characterise C-type asteroids, and the relative products: secondary mineral formation in particular hydrous minerals like phyllosilicates, the formation of opaque phases and post accretion processing of organic matter, especially aliphatic and aromatic hydrocarbons.

2. Results

2.1 Petrography and mineral chemistry

TAM5.29 is a ~300 µm x ~600 µm sized particle with a partial magnetite rim only found along the fusion crust. The melt layer is discontinuous and the texture is similar to the fusion crust found on meteorites (Fig.5A, Fig.S1). Voids are recognisable in the melt layer (fig. 5A). High resolution FE-SEM imagining demonstrates that the particle is composed primarily of lath-shaped olivine crystals with widespread andradite inclusions surrounded by dark halos composed of intermixed pyroxene and jarosite, which also occur as alteration veins (fig 1A-B). These inclusions form lenses with an augen-like texture (fig. 1A-B-E). A few of these lenses show a distinct asymmetrical shape (fig. 1B). Olivine is euhedral to subhedral with dimensions from a few micrometres up to ~10 µm. Andradite appears as sub-rounded crystals 5-10 µm in size, while the diopside and jarosite surrounding these are anhedral and difficult to distinguish from one another in backscattered electron images since they are small crystals (few micrometres) finely mixed and with similar greyscales. EDS spot analyses (table S1) reveal Fe-rich olivines, with heterogeneous grain compositions, ranging from $Fa_{42.5}$ to almost pure fayalite $Fa_{92.3}$. Rare crystals of forsterite are also present (Fo_{66-71}). Similarly, pyroxenes have heterogeneous grain compositions ($Fs_{1.8-60}$ $Wo_{0.7-48}$). Owing to the small grain size, pores and limitations with the spatial resolution and the interaction volume of the electron microprobe, spot analyses on some phases suffer from beam overlap with adjacent hydrated minerals, oxides and sulphides, thus analyses shown in table S1 may reveal low weight totals (olivine 89 wt%; andradite 95 wt%). We therefore supported mineral identification with spatially resolved Raman and bulk µXRD measurements.

Raman data revealed pyroxenes to be diopside (fig. 2) with sparsely distributed isolated enstatite grains. In fig. 2 a Raman map shows the typical microtexture of this particle. Furthermore, an aggregate of spinel crystals (mean Cr/(Cr+Al)=0.003 and Fe/(Fe+Mg)=0.34 based on EMPA analyses) are present (fig. 1C-10, Table.S1-S2), these co-occur with micron-sized Fe-oxides (mainly magnetite, spinel and ferrihydrite). Only minor FeNi alloys are found (Fig. 10 and Table S2) dispersed within the matrix (fig. 1). Raman analysis together with EDS, EMPA and EBSD suggest that a considerable

portion of the olivine has been altered resulting in a mixture of fine-grained hydrated Mg-Fe-sulphur-rich minerals and minor carbonates (likely Fe-carbonates) as suggested by the 3.9 µm band in TAM5.29 IR spectra (fig. 11), that we identify as iddingsite (see paragraph 3.3 for a more detailed description). Fine-grained phases are found as weathering films on fayalite and also scattered throughout the whole particle. Given their cryptocrystalline nature it is difficult to definitely resolve individual mineral phases, however, fibrous phyllosilicates are clearly resolved as dark haloes around andradite inclusions (fig. 1A-B-F). Micro-XRD revealed that these fibrous phyllosilicates are mainly antigorite and saponite (Fig. 8).

The bulk composition of TAM5.29 shown in table 1 is similar to that of CCs, being within 2 orders of magnitude of CI values, and similar to other unmelted fine-grained Antarctic micrometeorites (UMM) (fig. 3). However, TAM5.29 also demonstrates notable enrichment in Fe and depletion in Mg compared to the CCs, as also suggested by the 2.8 µm band (fig. 11) typical of Fe-rich hydrous phases (Takir et al, 2013). The aluminium content of TAM5.29 is similar to that of CV meteorites (table 1 and fig. 3) and is significantly higher than other CCs – consistent with the high concentrations of refractory elements found in CV and CK chondrites. Conversely Ca and Ti are depleted compared to CVs. The spider diagram in fig. 3 shows a strong enrichment in K in TAM5.29 compared to both CVs and other UMM. If we consider bulk composition of only the matrix of CVs (table 1 and Fig. 3) we see that FeO-MgO-CaO-TiO_2 values are closer to those of TAM5.29. On the contrary Al_2O_3 and Cr_2O_3 CVs matrix values are considerably different from the values of TAM5.29, which are closer to the average CVs (considering also chondrules). Slight depletion of Na_2O in TAM5.29 compared to both CVs and CVs matrix is also found.

Carbon is also ubiquitous, Raman analyses (fig. 2 and 6) identified characteristic “G” and “D” band peaks (located at ~1350 and ~1590 cm^{-1} respectively) and associated with disordered carbonaceous phases (Bonal et al., 2006). Poorly Graphitized Carbon (PGC) occurs as tiny inclusions of 100-200 nm in fayalite and as thin films surrounding crystals (Krot et al., 1998; Abreu and Brearley, 2011). It is interesting to note that Raman spectra of the various mineral phases (fayalite, andradite, diopside, jarosite and fine grained material) also have peaks around 2680 and 2930cm^{-1}. These peaks are second order peaks of C but also attest to the presence of OH as well as S-H and C-H functional groups within organic molecules. Sulphur is detected in all EMPA and EDS analyses, reflecting either S in jarosite, S-bearing organics or S-rich phyllosilicates. IR reflectance spectra (fig. 11) also show the presence of organic matter (i.e. CH compounds, aromatic and aliphatic hydrocarbons) with the 3.3 and 3.4 µm bands, the broad band between 3.6 and 3.8 µm can be instead indicative of S-H compounds. IR spectra also indicate the presence of carbonates with the 3.9 µm band (fig. 11). Furthermore, all EMPA and EDS analyses show low totals, indicating ubiquitous presence of OH and CH functional groups, in agreement with Raman observations.

Another important observation is a shock melt vein 136 µm in length and approximately 5µm in thickness (Fig.1D). This feature cross-cuts the fayalitic groundmass and is either deforms or displaces the primary features (an andradite-diopside vein Fig.1D). In addition, we observe a conjugate synthetic fracture and release band (fig. 1D). The displacement of these features appears to show a dextral shear sense, although this interpretation remains uncertain owing to significant variations in the width of the Jarosite/diopside band on either side of the melt vein. The lower margin of the linear feature (as seen in Fig.1D) shows an abrupt compositional contact with the host groundmass, while the upper margin is transitional over approximately 5µm. This feature is composed of a nanocrystalline or glassy matrix with a high porosity and hosting anhedral rounded small (<2µm) olivine crystallites and minor Fe-Ni oxides.

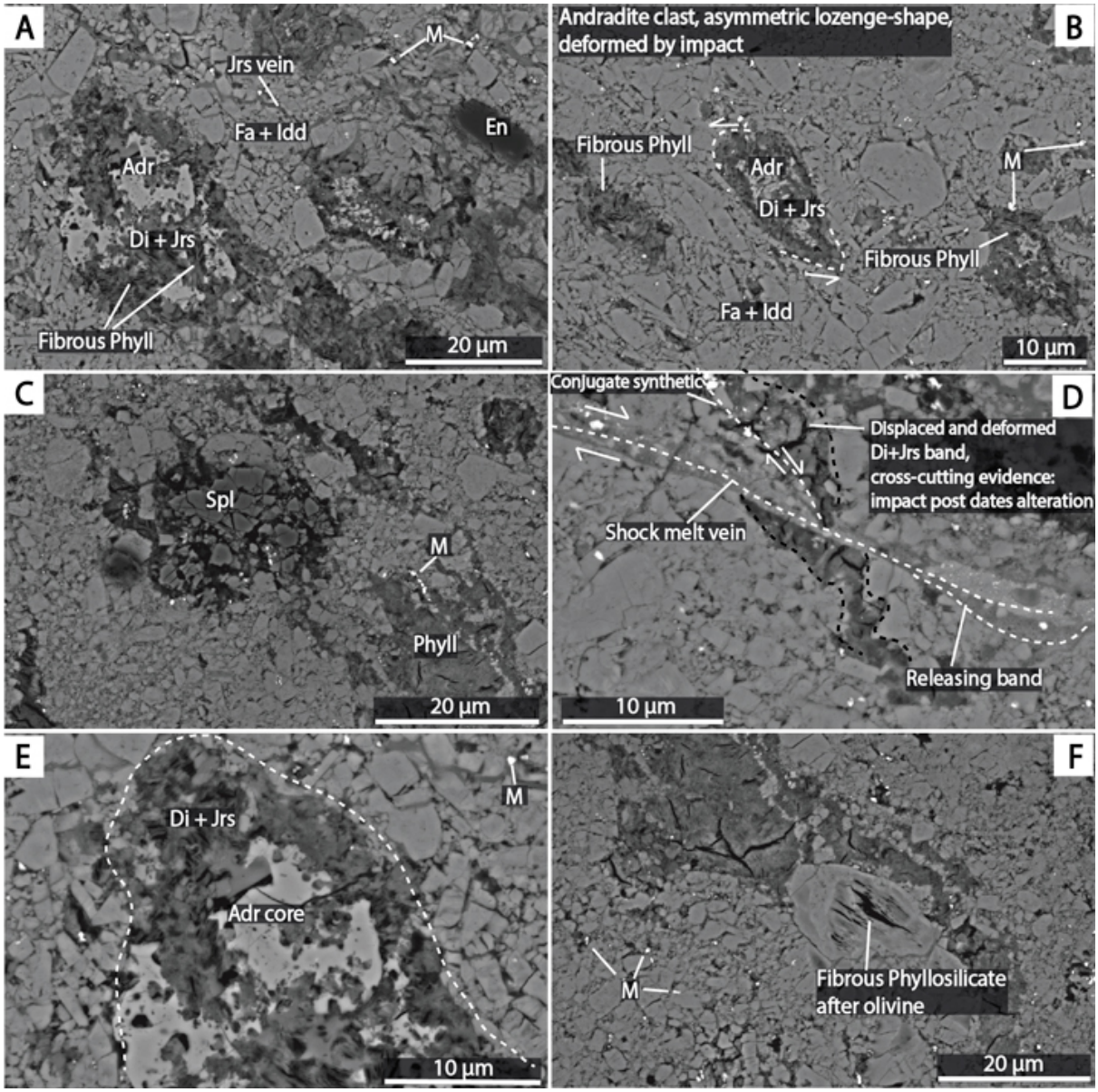

Fig.1. TAM5.29 FE-SEM BSE images. A-B-E) Typical mineral association of TAM5.29 with andradite surround by diopside, jarosite and fibrous phyllosilicates in a matrix made of iron rich olivine alterated in iddingsite. Many metal grains can be seen. C) Isolated spinel crystals. D) shock melt vein that sharply cuts other crystals. F) Fibrous phyllosilicates. Fa=fayalite, Di=diopside, Adr=andradite, Jrs=jarosite, En=enstatite, Phyll=phyllosilicate, M=metal alloys-oxides, Spl=spinel, Idd=iddingsite.

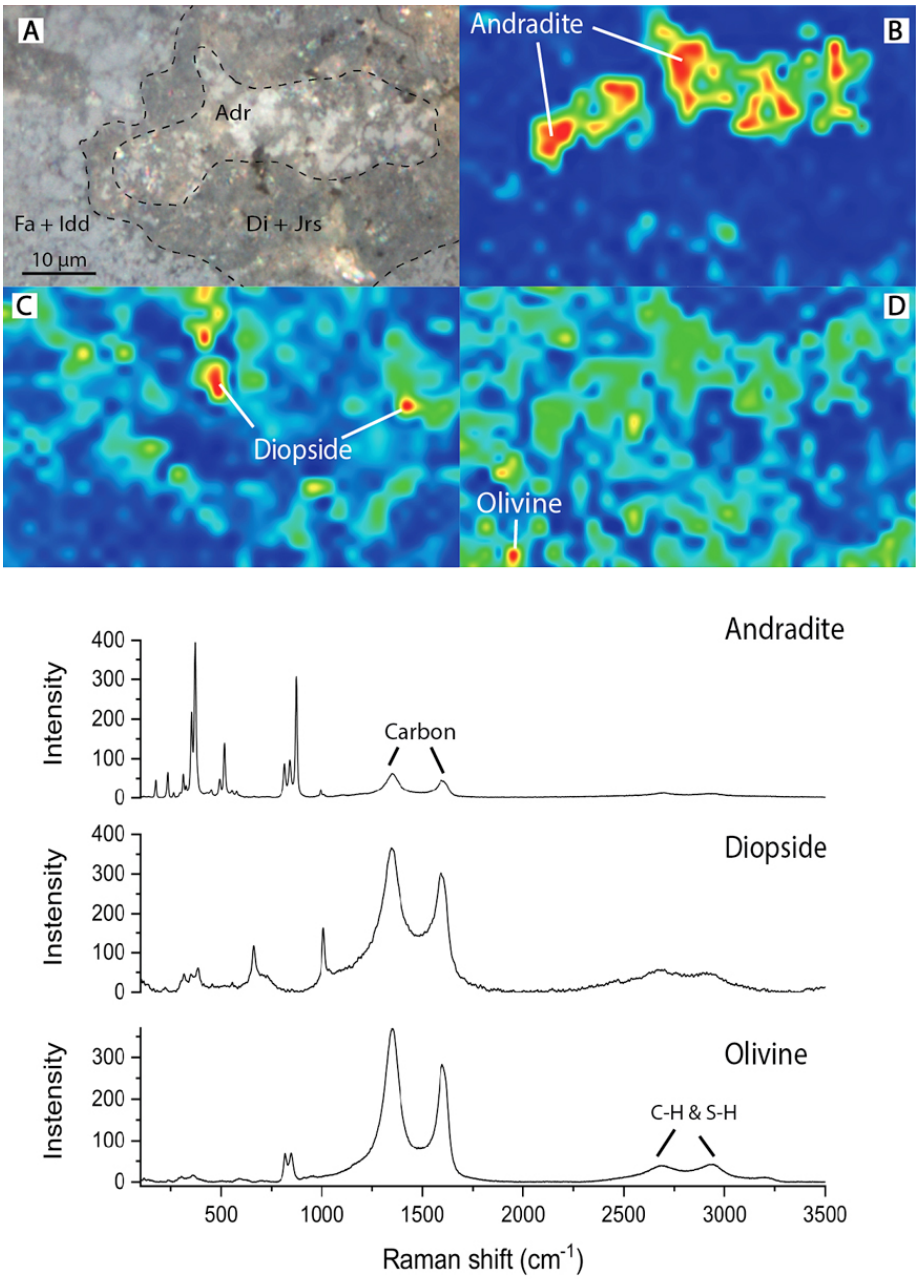

Fig. 2. Raman map showing a typical assemblage of TAM5.29 (A) consisting of andradite inclusions (B) surrounded by dark halos composed of intermixed pyroxene and jarosite (C), immersed in an olivine matrix (D). Abbreviations as in figure 1.

Table 1. Bulk composition obtained from 122 random EMPA analyses (oxide wt%) of TAM5.29 micrometeorite compared with bulk composition of carbonaceous chondrites and average composition of unmelted fine-grained Antarctic micrometeorites (UMMs).

	TAM5.29		CV*	CM*	CO*	CI*	CK*	CR*	UMMs**	CV matrix
	Mean	σ	Mean	Mean	Mean	Mean	Mean	Mean	Mean	Mean
Na_2O	0.26	0.18	0.46	0.48	0.47	1.13	0.42	0.31	0.44	0.46
MgO	12.6	3.23	23.3	20.9	23.9	19.1	24.4	17.4	16.8	18.8
Al_2O_3	4.93	8.34	4.02	2.55	2.98	2.02	2.98	2.31	4.28	2.49
SiO_2	29.2	4.95	33.2	30.1	33.9	27.3	34.2	31.9	33.9	28.6
P_2O_5	n.d.	-	0.28	0.27	0.25	0.28	0.25	0.29	0.40	n.d.
SO_3	2.17	2.22	3.96	8.6	2.34	17.9	2.9	2.7	1.9	3.29
K_2O	0.28	0.65	0.04	0.06	0.06	0.11	0.04	0.04	0.13	0.02
CaO	1.41	2.58	3.50	1.96	2.26	1.71	2.39	1.91	0.72	0.85
TiO_2	0.12	0.27	0.24	0.13	0.13	0.10	0.18	0.10	0.11	0.07
Cr_2O_3	0.53	0.42	0.50	0.47	0.52	0.42	0.53	0.53	0.49	0.36
MnO	0.15	0.05	0.19	0.24	0.23	0.28	0.18	0.22	0.23	0.23
FeO	40.1	6.61	28.9	29.5	31.3	28.5	30.3	30.4	29.6	37.6
NiO	n.d.	-	1.37	1.19	1.66	1.13	1.44	1.72	0.37	1.65
TOT.	91.8		100	96.5	99.9	100	100.2	89.9	89.4	94.5

n.d.: Not Determined
* from MetBase.
** from Genge et al., 1997.

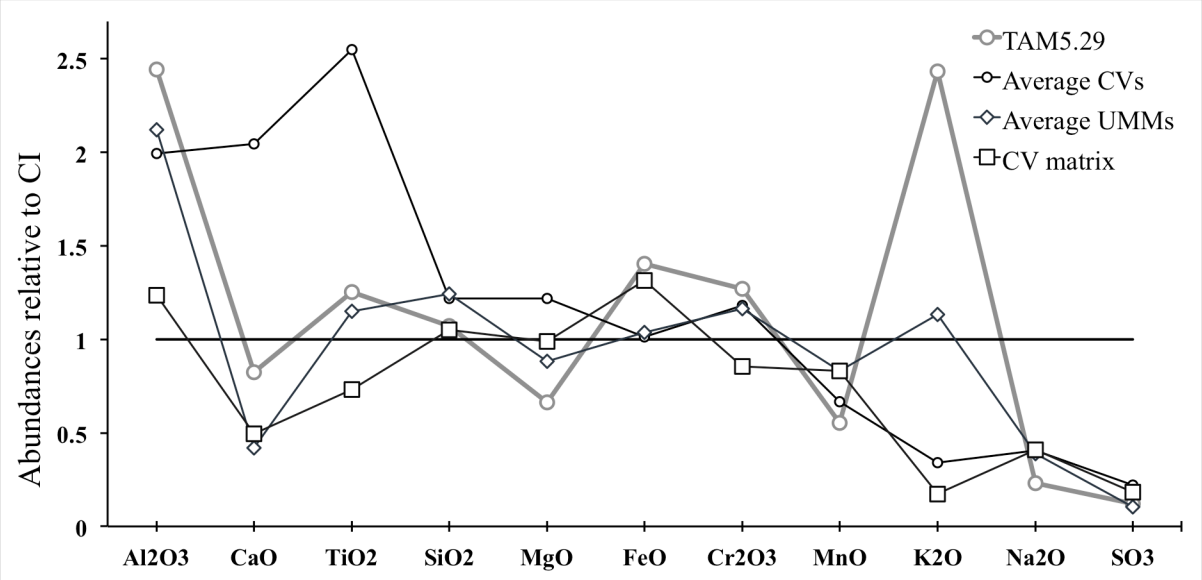

Fig. 3. Bulk composition of TAM5.29, average CVs (data from METDB database), average CV matrix and average Unmelted fine-grained Antarctic micrometeorites (UMMs) (data from Genge et al., 1997) relative to the CI chondrites composition.

Table 2. Oxide (wt%) EDS analyses of olivine, pyroxene, andradite and spinel of the TAM5.29 micrometeorite.

	Olivine		Pyroxene		Andradite		Spinel	
	Mean	σ	Mean	σ	Mean	σ	Mean	σ
Na_2O	0.11	0.08	0.49	0.33	0.12	0.11	0.23	0.10
MgO	15.2	2.50	21.9	15.1	0.76	0.77	17.1	1.54
Al_2O_3	1.27	1.46	3.27	3.00	0.65	0.54	65.2	1.65
SiO_2	27.6	2.70	52.7	5.07	33.6	1.61	0.97	0.85
K_2O	n.d.	0.96	0.44	0.58	0.05	0.05	0.03	0.02
CaO	0.35	0.09	7.55	9.15	28.3	9.06	0.16	0.19
TiO_2	0.07	0.14	0.20	0.10	0.02	0.06	0.15	0.04
Cr_2O_3	0.13	0.13	0.75	0.68	0.04	0.06	0.28	0.04
MnO	0.11	2.78	0.15	-	4.58	11.6	0.09	0.06
FeO	44.3	0.12	12.8	11.8	27.0	1.81	15.6	2.06
NiO	0.19	-	n.d		n.d		0.06	0.06
Tot	89.3*		100.3		95.11		99.82	
Fo/En	37.8	4.85	59.7	33.8				
Fa/Fs	62.0	4.85	24.0	24.6				
Wo			16.3	18.2				

n.d.: Not Determined

* Low total due to contamination of near-by hydrous minerals and inclusions of organic matter.

Table 3. Oxide wt% EDS analyses of metal oxides of TAM5.29. Due to the small size of the crystals (1-2 μm) analyses are contaminated by near-by phases giving high abundances of SiO_2 and S and low totals due to OH and C contamination. All analyses have high concentrations of Fe with the exception of Metal OX_5 that have high Cr instead. In all the analyses are also present minor quantities of Mg, Al and in Metal OX_5 also Ti. Thus, the most likely phases are: magnetite, chromite, spinel, ulvospinel etc.

	Metal OX_1	Metal OX_2	Metal OX_3	Metal OX_4	Metal OX_5
Na_2O	0.25	0.01	0.08	0.23	0.53
MgO	2.54	5.63	5.74	3.81	11.3
Al_2O_3	4.46	12.9	3.26	5.95	12.2
SiO_2	4.89	10.5	10.9	9.03	22.9
P_2O_5	n.d.	0.24	0.19	n.d.	0.72
S	0.32	2.83	1.46	1.59	7.92
K_2O	n.d.	0.24	n.d.	0.21	0.89
CaO	n.d.	0.20	0.14	0.02	0.65
TiO_2	n.d.	0.34	0.42	n.d.	2.50
Cr_2O_3	n.d.	0.76	0.30	0.21	24.5
MnO	n.d.	0.04	0.17	n.d.	n.d.
FeO	77.9	57.6	68.4	71.5	17.6
NiO	n.d.	0.11	0.01	0.01	n.d.
Tot	91.4	91.4	91.1	92.5	101.7

n.d.: Not Detected.

2.2 Preferred orientation of olivine

Figure 4 reports EBSD map data acquired on the same site shown in Fig. 1B where olivine crystals wrap around andradite-diopside/jarosite inclusions and form a foliation texture (Fig.1B). To investigate whether the olivine crystals show a crystallographic preferred orientation (CPO), a detailed EBSD map (fig. 4) was collected. In Figure 4A, a phase map, olivine (red), andradite (green) and diopside (yellow) is shown. The dark part of the map is material that was not indexed. It is unlikely that the material between the olivine crystals has not been indexed because of potential polishing problems, since micro-Raman, SEM, EMPA and micro-XRD analysis shows the presence of fine grained alteration products (see below).

The three pole figures (fig. 4B), lower hemisphere equal area projections, are obtained considering one point per olivine grain. This has been done to avoid a bias of the data distribution due to grain size effects. Pole figures in fig. 4B show the pertinent crystallographic orientation of every single olivine crystal. In these pole figures a clear trend is recognized, with the [100] axis forming a maximum in the NW periphery, suggesting a NW-SE preferred orientation of this direction, hence orthogonally to the foliation trace. Conversely, the [010] and the [001] directions are dispersed along girdles consistent with the overall trend of the foliation trace. This implies that the [100] axis is a rotation axis, and that the differently elongated shape of the olivine crystals is the result of crystals having their [010] and [001] directions at systematically changing angles within the foliation plane.

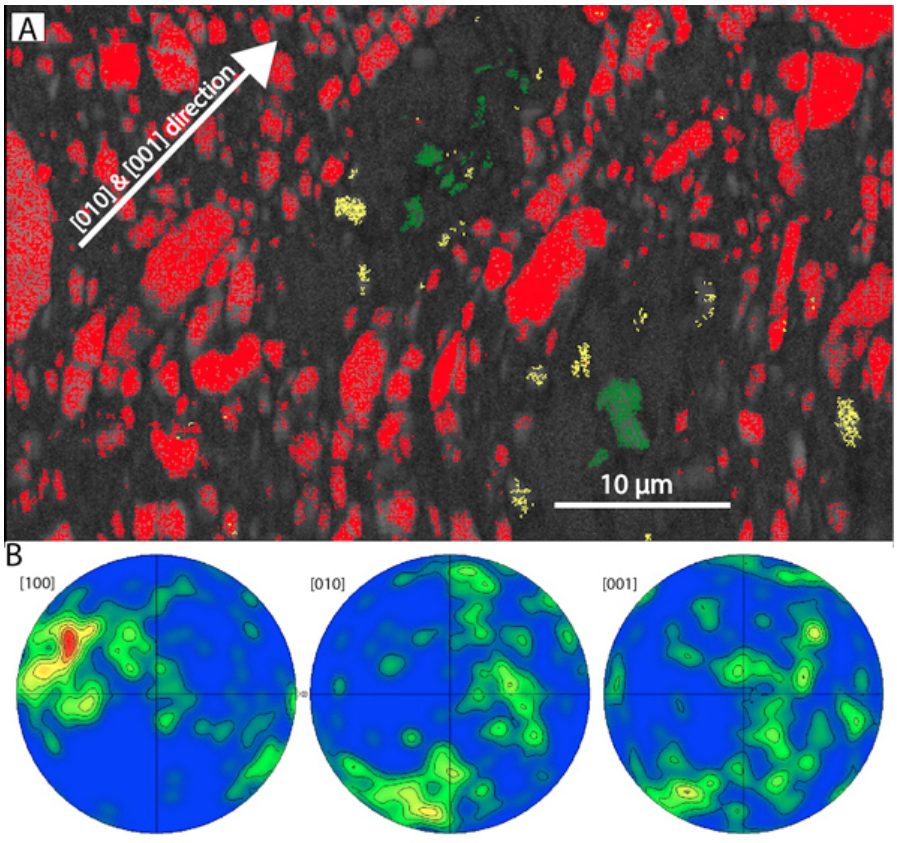

Fig. 4. A) EBSD phase map of the same area in fig. 1B with relative pole figures of olivine (panel B, one point per grain). Red=olivine, green=andradite, yellow=diopside and black-grey area are fine grained undetected material.

2.3 Fine-grained material

With EDS/EMPA, Raman and EBSD analyses widespread fine-grained cryptocrystalline phases are found in the TAM5.29 dust grain along with the previously described iddingsite. The EBSD map in fig. 4 was made with a step size of 100 nm (see methods). Under these conditions (see also paragraph 2.2) EBSD wasn't able to detect the fine-grained cryptocrystalline phases, thus we can infer that the fine-grained material phases are less than 100 nm. Likewise, Raman analyses produce mixed spectra suggesting the presence of sulfides, probably related to the S-H bands as well as poorly crystalline hydrated phyllosilicates (fig. 8). Micro-XRD data (fig. 9-10) are in agreement with this interpretation, revealing Fe-Ni sulfides, phyllosilicates and possibly oxides and hydroxides. Carbonates are not clearly detected by Raman and micro-XRD, but their presence is inferred by the 3.9 µm band in the IR spectra (fig. 11).

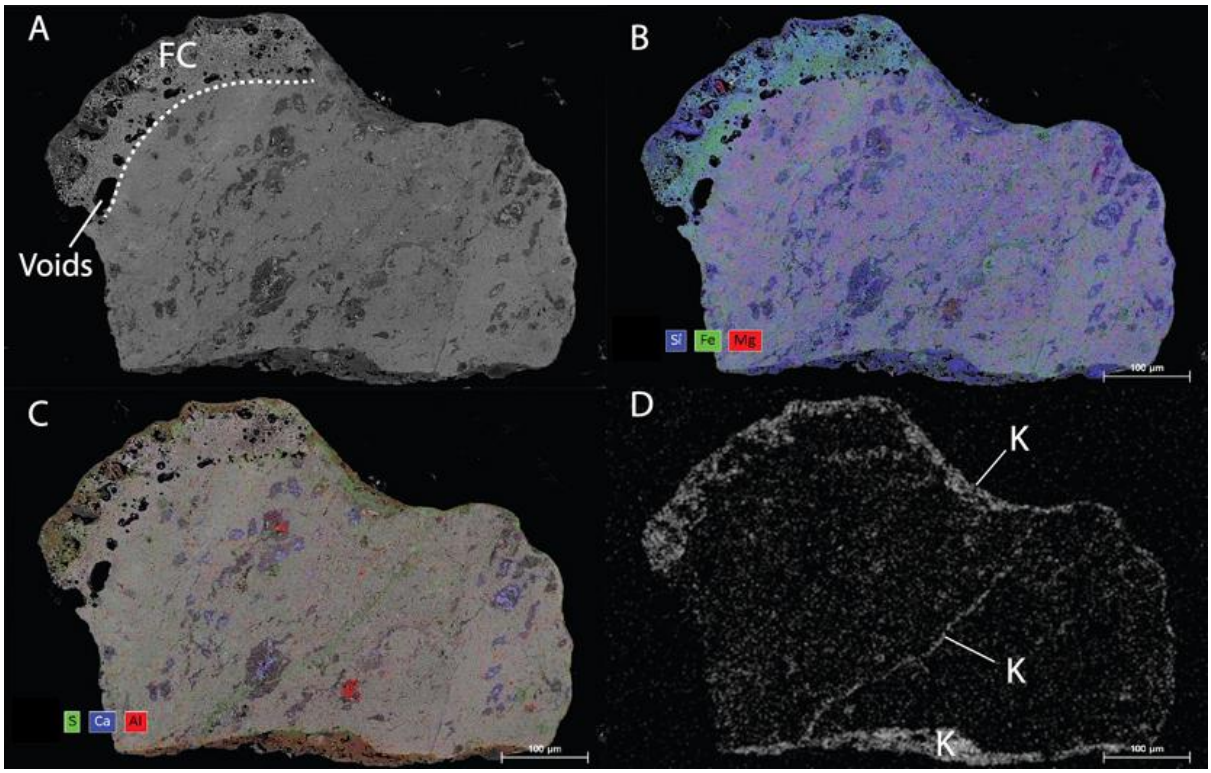

Fig. 5. EDX map of TAM5.29. A) Entire TAM5.29 particle. FC= Fusion Crust. B) Composite map showing Si-Fe-Mg abundances C) Composite map showing S-Ca-Al abundances. D) Map of K concentrations.

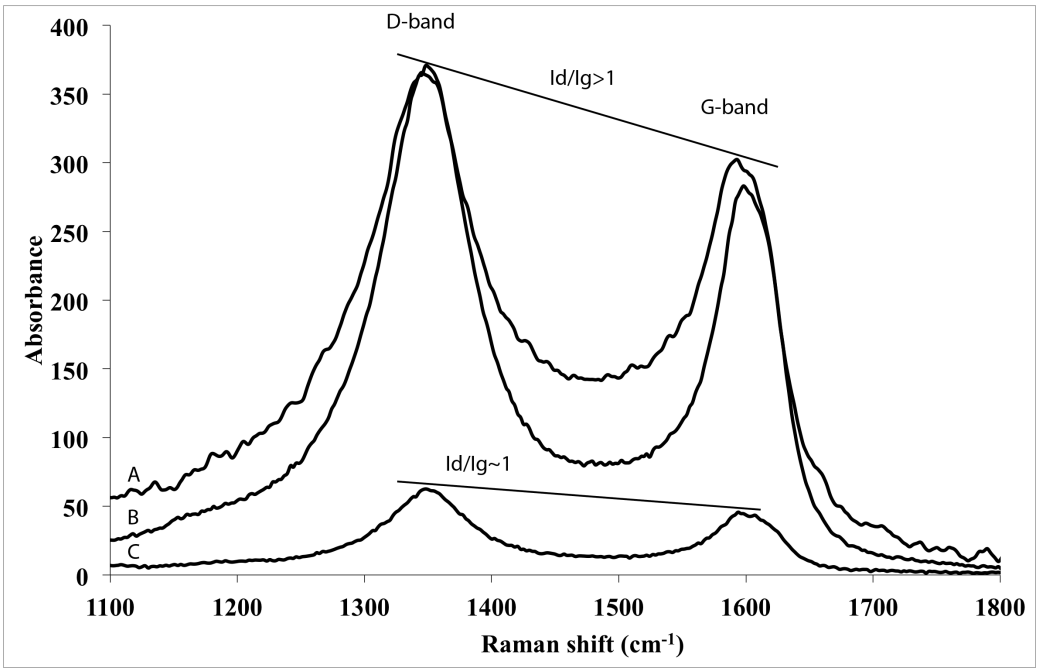

Fig. 6. D and G-bands of some representative analyses of TAM5.29. In case A and B D-band is higher than G-band giving a I_d/I_g ratio >1, indicating high carbon maturity and high metamorphic grade. In case C I_d/I_g ratio is ~1 related to a medium metamorphic grade.

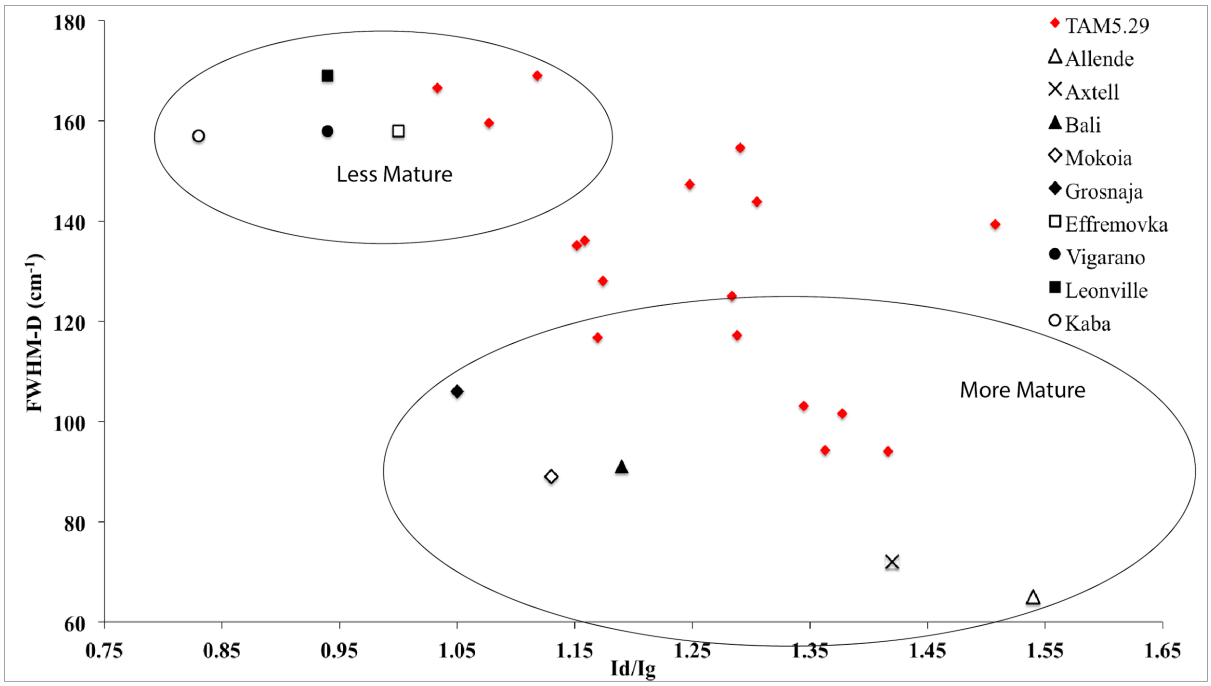

Fig. 7. Modified from Bonal et al. (2006). Id/Ig ratios are plotted versus FWHM of the D-band. The two groups represent more metamorphosed (more mature) and less metamorphosed (less mature) CVs. Red dots represent TAM5.29 spectral parameters.

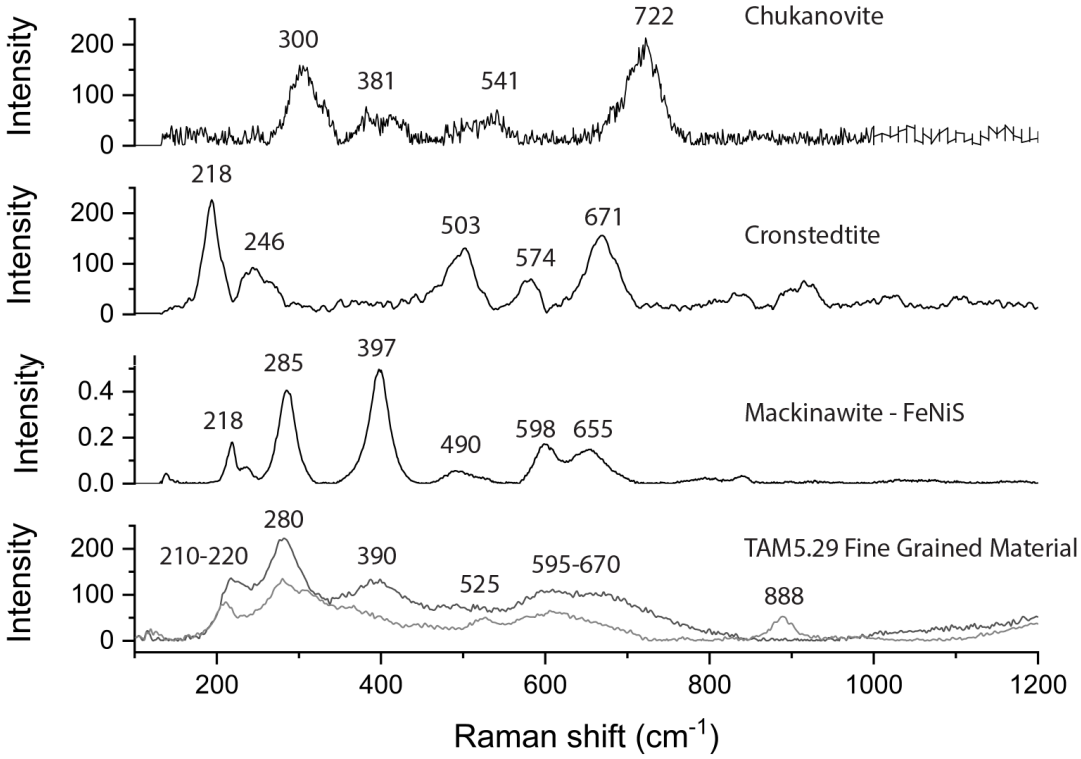

Fig. 8. Raman spectra of TAM5.29 fine-grained material compared to possible minerals that are contained within it.

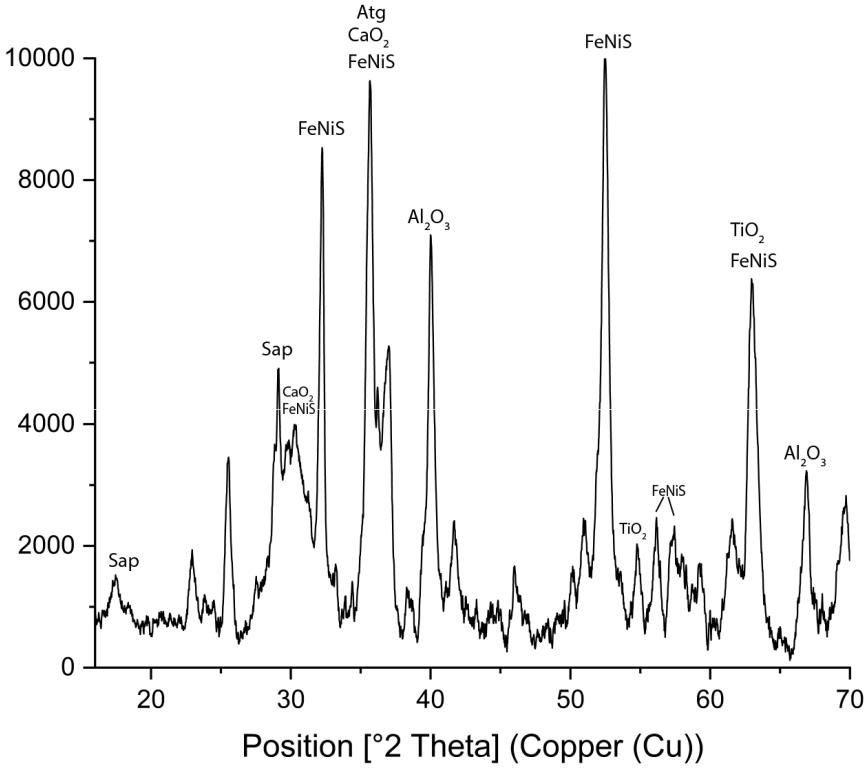

Fig. 9. µXRD analysis of TAM5.29. Sap: saponite; Atg: antigorite; FeNiS: iron-nickel sulfides (millerite and mackinawite); CaO_2-Al_2O_3-TiO_2: oxides from CAIs that survived alteration. Sap=saponite, Atg=antigorite.

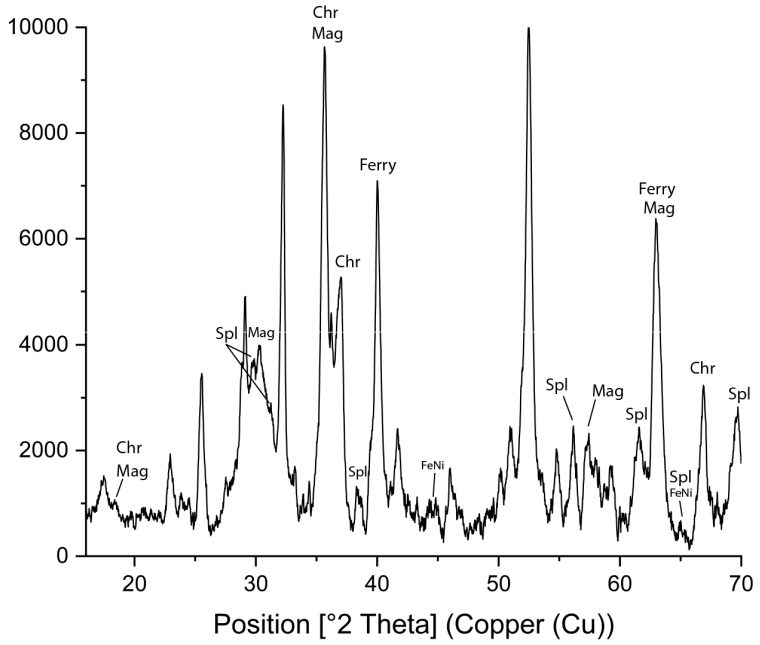

Fig. 10. µXRD analysis of TAM5.29. Mg: magnetite; Sp: spinel; FeNi: kamacite; Chr: chromite; Ferry: ferrihydrite. Micron sized metal-oxide grains in TAM5.29, in agreement with EDS data in table S1, are mainly magnetite, spinel, chromite and hydrated Fe-oxides such as ferrihydrite. Minor and rare FeNi alloys may be also present. The fact that TAM5.29 mainly contains metal-oxides is also in agreement with µXRD data in fig. 9 where CaO_2-Al_2O_3-TiO_2 are found. Furthermore this confirms the affinity of TAM5.29 with the CVox group. Mag=magnetite, Spl=spinel, Ferry=ferrihydrite, FeNi=metal alloys.

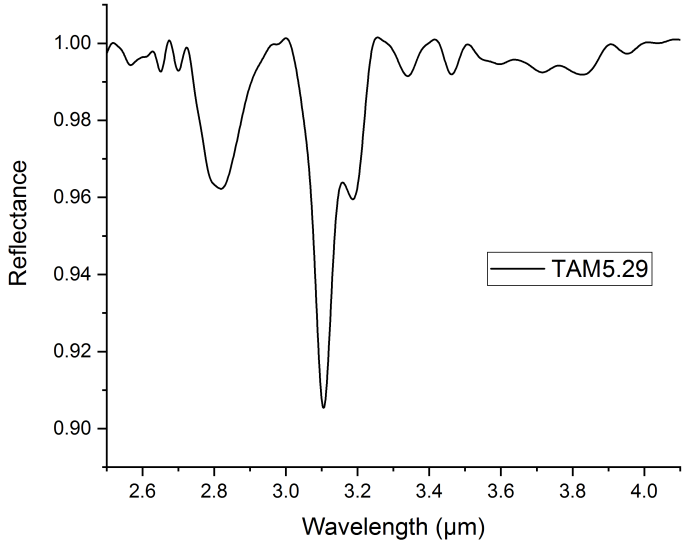

Fig. 11. IR reflectance spectra of TAM5.29. To be noticed the 2.8 µm band of Fe hydrous phyllosilicates, 3.3-3.4 µm band given by organic matter (i.e. CH compounds, aromatic and aliphatic hydrocarbons), a broad band between 3.6 and 3.8 µm likely related to SH functional groups and the 3.9 µm band of carbonates (likely Fe-carbonates). The 3.1 µm band is a very discussed band and attribution to a mineral phase is difficult, its nature will be discussed in chapter 2.

3.Discussion

3.1 TAM5.29: micrometeorite or meteorite?

TAM5.29 has a discontinuous melt layer with a texture similar to the fusion crust found on meteorites (Fig.5A, Fig.12). The presence of such a prominent melt layer is unusual for a micrometeorite exterior, which instead have a thin (~5-50µm) double-layered igneous rim and magnetite rim (Genge, 2006). This could imply that TAM5.29 is a fragment of a larger meteorite.

Although meteorite fusion crusts are highly variable in composition, texture and thickness (Genge and Grady, 1998) they are commonly >1000µm (that is 10x thicker than the crust on TAM5.29, Fig.S1). In addition, the bulk composition of CV fusion crust is also markedly different from bulk composition of TAM5.29 (Table.1). As reported by Genge and Grady (1998), they have MgO= 25.65 wt%; SiO_2= 34.5 wt%; FeO= 30.46 wt%; CaO= 2.39 wt% and Al_2O_3= 3.34 wt%. On the contrary TAM5.29 has major elements bulk composition (Table.1) of MgO= 12.6 wt%; SiO_2= 29.2 wt%; FeO= 40.1 wt%; CaO= 1.41 wt% and Al_2O_3= 4.93 wt%. Furthermore, because the melt layer on TAM5.29 is discontinuous, this requires that the particle fragmented whilst on the Earth's surface, as evidenced by the lack of fusion features on the remainder of the particle perimeter. We estimate that the pre-atmospheric particle diameter – assuming a spherical shape (a simplistic approximation given fusion crusts can show protrusions) at 1300-2000µm, approaching the size limit for micrometeorites. The pre-atmospheric particle diameter is derived assuming that the object was originally a sphere and that the micrometeorite, based on the curved fusion crust, sampled a portion of this sphere. We thus analysed how much of the sphere could be represented by TAM5.29 as shown in figure 13. Thus TAM5.29 may represent a different class of extraterrestrial material intermediate in size between micrometeorites (<2000 µm) and meteorites (~>1 cm). This size domain was previously described by Harvey and Maurette (1991), Kurat et al., (1994) and Folco and Rochette (2010) and termed "*minimeteorites*".

The hypothesis that TAM5.29 was a small particle in space is further supported by its unique petrology (chondrule-free nature and mixed metamorphic history). Owing to their unique delivery mechanism (P-R drag, operating on grains <1 cm, Gonczi et al., 1982) cosmic dust samples a more diverse collection of asteroid parent bodies than their larger meteorite counterparts. Thus, because TAM5.29 represents a new lithology, this adds to our confidence that this sample is not simply a fragment of a larger meteorite broken off during atmospheric entry but instead existed as a grain of dust in interplanetary space derived from a parent body not currently delivering meteorites to Earth and otherwise unsampled.

Finally, the preferential fragmentation of a heterogeneous material, with fractures following boundaries of chondrules and CAIs may explain their absence in this minimeteorite, thereby reflecting the unrepresentative sampling (of coarse-grained features within parent body), as previously argued by Genge et al., (2008).

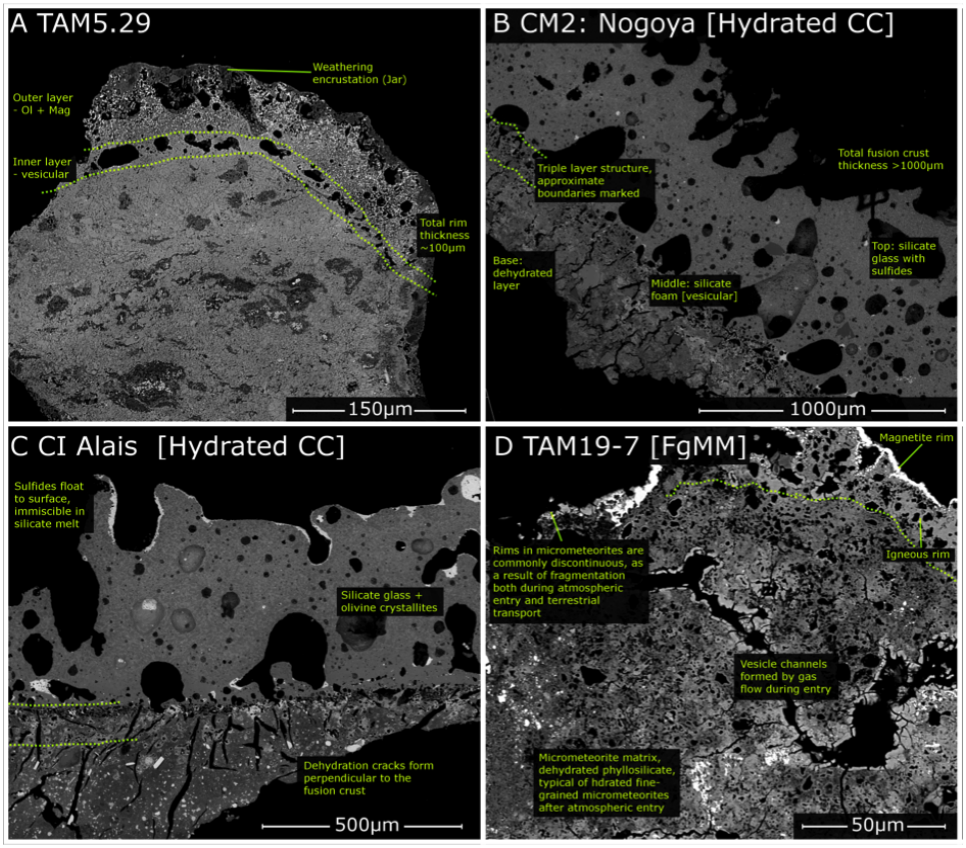

Fig.12. The melt layer on TAM5.29 developed during atmospheric entry and comparison against fusion crusts and igneous rims on micrometeorites.

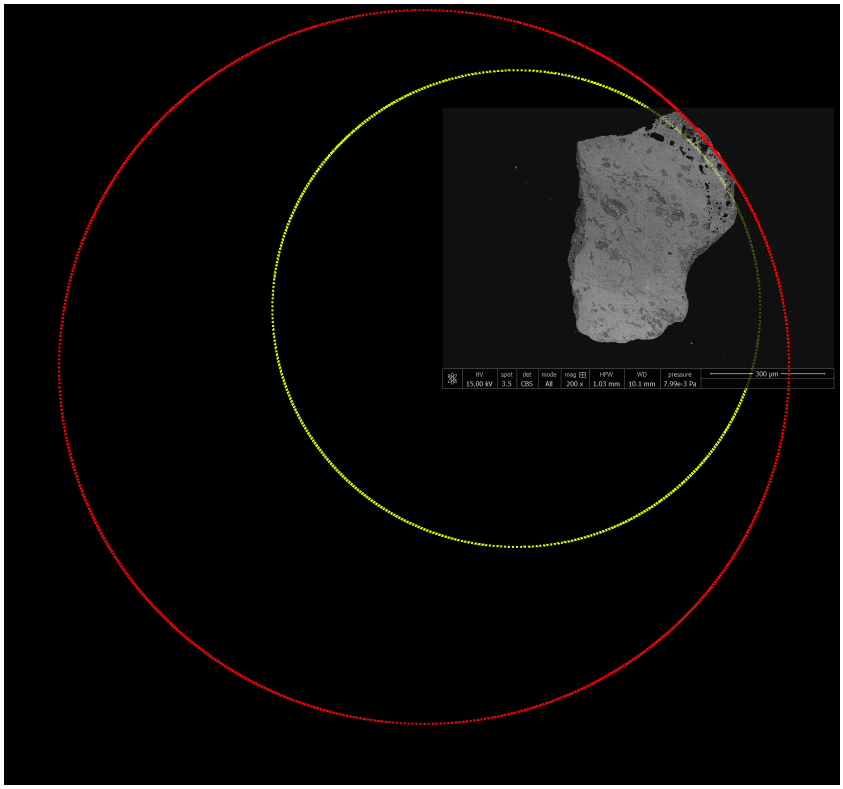

Fig. 13. TAM5.29 pre-atmospheric diameter estimate. Green circle reporesent the minimum possible dimension of the original TAM5.29. Red circle represent the maximum possible dimension of the original TAM5.29 particle.

3.2 Terrestrial weathering

Micrometeorites from the Transantarctic Mountains often show moderate to significant terrestrial weathering. In particular, jarosite is a common product of formed in subaerial Antarctic environments (van Ginneken et al., 2016). The EDX map in fig. 5C-D reveals co-occurrences of S and K, the main components of jarosite, concentrated along the particle border and in the fractures within TAM5.29. The effect of terrestrial weathering is however limited being confined to the fractures and margins. The EDX map in fig. 5C reveals that high Ca concentrations correspond to andradite inclusions, unaffected by replacement. In addition, Mg and Fe-element maps (fig. 5B) are well delineated, suggesting that these elements have not been leached by terrestrial fluids. It appears that TAM5.29 has therefore suffered limited weathering, retaining the majority of its pre-atmospheric mineralogy unaltered. Because the melt vein displaces a dark vein of diopside + jarosite (marked in Fig. 1D), we conclude that the shock event post-dates the metasomatic event. However, it remains unclear whether iddingsite is also intersected by the melt vein or if alteration that created the iddingsite overprints the shock vein. We favour the latter option assuming that iddingsite formed by fluids released by hydrous minerals as a consequence of the pressure exerted by the impact (because olivine in TAM micrometeorites typically weathers to jarosite and not iddingsite [van Ginneken et al., 2012]). Later fractures instead cut the shock melt vein creating possible localized terrestrial alteration also on the shock melt vein.

3.3 Petrogenesis – Record of hydrothermal environment on the Parent Body

The mineralogy displayed by TAM5.29, primarily composed of fayalitic olivine plus Ca-Fe rich pyroxenes, andradite, phyllosilicates and sulphides as well as the close matrix compositions demonstrate a clear affinity to the CV chondrite group. The mineralogy in TAM5.29 is, however, distinct from any currently reported CVs and also unique among reported micrometeorite studies.

TAM5.29's most common mineral – fayalite is associated with Fe-alkali-halogen metasomatism at temperatures <300°C (Krot et al., 1995-1998; Zolotov et al., 2006; MacPhearson and Krot, 2014). The preferred fayalite growing mechanism in CVs is during thermal metamorphism from an amorphous precursor phase in the presence of fluids (Abreu and Brearley 2011) and Ca-Fe-rich phases are derived from the aqueous alteration of CAIs and anorthitic-alibitic mesostasis (Krot et al., 1995).

Fe-rich olivine and diopside-hedenbergite assemblages are common in all CVs, while Ca-rich silicates (e.g. andradite) and Fe-Ni sulfides are almost absent in CV_{red}, which instead contain kirschteinite (MacPhearson and Krot, 2014). Nepheline and sodalite are typical of CV_{oxA} and absent in CV_{oxB}, which in turn contain phlogopite and saponite (MacPhearson and Krot, 2014; Krot et al., 1998). TAM5.29 is therefore consistent with the CV_{oxB} group's mineralogy, having several andradite inclusions plus phyllosilicates. This metasomatic alteration is similar to the terrestrial serpentinization-rodingitization process (Python et al., 2007; Bach and Klein, 2009). During serpentinization at temperatures <385°C clinopyroxene replaces tremolite and, at lower temperatures, below 275°C, clinopyroxene is in turn replaced by andradite (Python et al., 2007; Bach and Klein, 2009).

In summary, diopside and andradite grow at the expense of serpentine and, at lower temperatures (<275°C), andradite also replaces diopside (Python et al., 2007; Bach and Klein, 2009). Tremolite and disordered biopyriboles have been found in Allende chondrules and their presence represents a peak metamorphic temperature below 340°C (Brearley 1997). In TAM5.29 tremolite is not found. Furthermore, serpentine and diopside are small anhedral crystals that form dark haloes around andradite that appear to consume them. This provides a temperature constraint on the formation of secondary phases in TAM5.29, between 275 and 250°C, in agreement with temperatures estimated

by Krot et al. (1995-1998). Krot et al. (1995-1998) based the temperature range mainly on the CV tensile strength, liquid water can exist at a maximum temperature of 310°C. This limit of 310°C is also supported by textural observations of CVs, O-isotopic composition and thermodynamic analysis (Krot et al., 1995-1998).

The bulk composition of TAM5.29 supports the Fe-alkali-halogen metasomatism hypothesis. Significant enrichment of Fe and K are observed compared to average CVs bulk composition. The enrichment in Fe is indicative of highly oxidizing conditions. However, Fe value of CVs matrix is comparable with the concentration of Fe in TAM5.29. This is probably due to the higher concentration of Fe-oxides (i.e. magnetite and alloys) in the matrix of CVs. Instead, K is easily leached from minerals by fluids. The high concentration of K is explained with jarosite formed by terrestrial alteration (even if bulk analyses were made in areas were K enrichment due to terrestrial alteration was as low as possible based on EDX maps). It is also possible that part of the K is representative of hydrothermal fluid circulation rich in alkali elements, even if this alone cannot account for the very high K abundance in TAM5.29. In fact, localized heating on C-type bodies (e.g. Ceres) have been proposed to be due to leaching and re-deposition near the surface of long-lived radioisotopes like ^{40}K, which decays in ^{40}Ar (Castillo-Rogez et al., 2008). The Ca and Ti depletion compared to CVs is instead due to the absence of refractory inclusions in TAM5.29. However Ca and Ti concentration of TAM5.29 is higher than that in the CVs matrix. This enrichment is due to the higher concentration of Ca-rich minerals and Ti-oxides in TAM5.29, compared to the CVs matrix, formed during metasomatism. In addition, Ca depletion relative to CVs can also be related to Ca leaching that formed carbonate veins (not sampled by TAM5.29) in the parent body, a feature commonly found in terrestrial serpentinization processes (Python et al., 2007). Mg depletion in TAM5.29 is a consequence of the oxidising conditions and Fe enrichment. Na is easily depleted during aqueous alteration and TAM5.29 doesn't have nepheline and sodalite, the main carriers of Na. Al in TAM5.29 is higher than CVs and CV matrix. This high Al content is tricky to explain but is likely given by Al in the phyllosilicates derived from leached CAIs.
However, under these environmental conditions fayalite is not stable with andradite and Ni-sulfides (Krot et al., 1998; Zolotov et al., 2006; MacPhearson and Krot, 2014). Andradite is stable at higher temperatures than fayalite and the two phases can only coexist at equilibrium at T<100°C (Krot et al., 1998; MacPhearson and Krot, 2014). Temperature <100°C have also been proposed for the formation of iddingsite in the Lafayette meteorite (Treiman et al., 1993). Raman spectra and EDS analyses of TAM5.29 also show that andradite retain a certain amount of water (fig. 2 and table S1), thus the OH in andradite could represent a $(SiO_4)^{4-} \leftrightarrow (O_4H_4)^{4-}$ substitution reaction for which low temperature formations are also expected within a low-pressure post magmatic environment (Amthauer and Rossmann, 1998). However structural $(O_4H_4)^{4-}$ is expected to have Raman peaks at ~3560 cm^{-1} (Amthauer and Rossmann, 1998). In contrast, in TAM5.29 andradite Raman spectra show OH peaks at lower wavelengths between ~2680 and ~ 2930 cm^{-1} implying the presence of non-structural water (in addition to S-H and C-H bonds).
In support of a low temperature formation, the bulk composition of TAM5.29 shows considerable enrichment in Fe compared to all other CCs (table 1 and fig. 3). The majority of this Fe is held within the silicate minerals (rather than reduced Fe-Ni metal and) suggesting highly oxidizing conditions at low temperatures.
Serpentinization may also occur at lower temperatures but in this case lizardite is also expected, which is not detected in TAM5.29. Instead, in TAM5.29 the presence of antigorite can only be

formed by serpentinization at higher temperatures, in particular at ~310°C occurs the chrysotile breakdown to antigorite + brucite at low pressure (1 bar, which is also typical of minor bodies of the Solar System, Wunder et al., 2001). However in TAM5.29 there is no clear evidence of the presence of brucite probably due to the Fe-rich composition of the sample. In contrast, fayalite can form over a wide range of temperatures from 30°C to 300°C with W/R (water to rock ratio) between 0.06 and 0.2 (Zolotov et al., 2006) and thus does not provide significant temperature restrictions.
Thus, the alteration assemblage in TAM5.29 must have formed across a range of temperatures, with two distinct alteration periods with distinct environmental conditions. An initial alteration regime generated the fayalite, andradite, antigorite and diopside at temperatures of ~275-250°C under oxidising conditions. While, later, at a distinctly lower temperature (<100°C), the iddingsite formed. We conclude that fayalite-andradite-FeS-NiS assemblages derive from a retrograde metasomatism, inferred mainly by the andradite crystals consuming diopside and serpentine, at ~250°C, suggested by the mineral assemblage typical of serpentinization. Conversely, the formation of iddingsite appears to be related to an independent low-T event that will be discussed later.

3.4 Origin of preferred orientation of olivine

The CPOs seen in the EBSD map (Fig. 4) may at a first glance resemble the terrestrial "type D" fabric of olivines recognized in simple shear experiments by Bystricky et al. (2000). Olivine "Type D" fabric refers to high stress and water-poor conditions (Michibayashi et al., 2016), and Bystricky et al. (2000) associated this fabric to upper mantle conditions, for example in regions of extensional deformation in major detachment zones near the crust-mantel boundary, or in subduction zones where hot mantle convects past the upper side of cold slabs. Such deformation regimes are inconsistent with that recorded by TAM5.29. We believe that pole figures (fig. 4),showing a clear maximum in the [100] direction, while the [010] and [001] directions are scattered in two girdles, are describing a kind of olivine fibre texture that relate to an axially symmetric shortening regime in which the (100) plane of olivine orients orthogonally to the maximum compression direction (σ1) and relate to compaction rather than to shearing.
It is also interesting to note that the elongated olivine in TAM5.29 are generally not associated to the elongated [100] direction, but are randomly associated to the [010] and [001] directions. Further examination reveals that the longest olivine crystals show clear alignment around andradite inclusions. These preferential CPOs concentrated locally around coarse-grained inclusions were previously described in CV chondrites where olivine crystals wrap around chondrules or dark inclusions (Watt et al., 2006; Forman et al. 2017). These areas, around chondrules in CVs and around andradite crystals in TAM5.29, were probably characterised by a higher porosity compared to the rest of the matrix and thus suffered a more significant compression and pore collapse during impact. Such a scenario results in heterogeneous strain distribution with significant heat production (~575 °C) and locally high stress at the sites or pore collapse while the surrounding low-porosity matrix retains a lower degree of compaction and andradite inclusions records no compaction at all (Bland et al., 2014). The matrix therefore remains partially unaffected by the shock wave passage (Bland et al., 2014; Forman et al., 2017), while around andradite inclusions compaction is more enhanced with the creation of augen-like structures as predicted and observed in Allende by Bland et al. (2014). This process also produces a distinct heterogeneity in the CPOs (Forman et al. 2017), which is in agreement with our EBSD data.
Another intriguing fact is the dislocation of the diopside-jarosite vein in fig. 1D. This vein has a dextral displacement. This kind of deformation is typically non-uniaxial and is in contrast to the

theoretical uniaxial nature of the shock compaction. In support of the non-uniaxial deformation there's also the asymmetric andradite-diopside inclusion (fig. 1B), proof of a shear stress. It seems thus that the preferred orientation of olivine has been created in the instant when the impact occurred - a moment in which stress is uniaxial. Subsequent to the initial stage of the impact, simple shear deformations form radial to the impact area (Kenkmann et al., 2014). In this second stage, deformation has been accommodated along the shock vein melt and around andradite, the two areas of TAM5.29 where weakness is higher. In particular, maximum strain occurred along the upper part of the shock vein melt where crystals were forced into the melt vein creating the transitional upper limit, the conjugate synthetic displacement and the releasing band (fig. 1D).

Alternatively, non-impact processes may have generated the preferred orientation of olivine seen in TAM5.29. These include: sintering, sub-grain recrystallization, lithification and gravitational compaction (Forman et al., 2016-2017).

Sintering requires heating at temperatures higher than 360°C over long (>1 million years) timescales to achieve recrystallisation alignment (Gail et al., 2015). However, both the temperature and duration of heating are inconsistent with the formation conditions of TAM5.29, which require lower temperatures (~250°C) – as determined by the secondary mineral assemblage and shorter durations – as determined by Raman data and olivine crystal morphology. Likewise, the petrofabrics in TAM5.29 cannot have been formed by a plastic deformation processes such as sub-grain rotation, recrystallization and diffusion creep as these would result in significantly less elongation of olivine crystals and lower aspect ratios (Forman et al. 2017).

Petrofabrics formed by compression due to lithostatic forces cannot be ruled out, but it's less likely as also suggested by Watt et al. (2006), Format et al. (2016; 2017) and Bland et al. (2014). This is because the pressure on small protoplanets is negligible, especially on porous water-rich carbonaceous chondritic parent bodies. For example, at the centre of a 200 km diameter asteroid pressures are thought to reach a maximum of 1MPa (corresponding to a depth of a few tens of meters on Earth), far too low for lithostatic compaction (Weidenschilling and Cuzzi, 2006). Meanwhile, on larger Ceres-like bodies, pressure estimates vary between <0.2 GPa (Neumann et al., 2015) and 1220 MPa (Suttle et al., 2017). Even if sufficient pressures are possible, liberation would require an impact of an enormous magnitude, equivalent to the complete destruction of such a body. In both cases we would expect a brecciated texture of the resulting asteroid's chunks. In TAM5.29 brecciated texture is not observed. However TAM5.29 is a small fragment and does not necessarily sample an area with clasts boundaries. For this reason we cannot assume that TAM5.29 is not part of a breccia and we cannot completely rule out the possibility of lithostatic compression.

Finally, a gravitational compaction model, such as that proposed for Allende by Watt et al. (2006) may be possible. Here, a muddy outer layer of a parent body affected by sedimentary processes operating under microgravity result in the alignment of olivine. However, gravity is very low even on a Ceres-like body (Ceres gravity is ~0.28 m/s^2, around 1/35 Earth's gravity). The low gravity coupled with the chaotic [010] and [001] axis distribution of olivines in TAM5.29 (fig. 4), bring us to prefer an impact-induced compaction (Gattacceca et al., 2005; Bland et al., 2014; Forman et al., 2016-2017). Consequently, the process that most likely created the preferred orientation of olivines in TAM5.29 is impact compaction, and this is further supported by the presence of the shock melt vein within the micrometeorite.

3.5 Carbon and Poorly Graphitized Carbon (PGC)

Carbon, which is widely distributed in TAM5.29, is a powerful index of metamorphic grade. In particular the maturity of the organic matter is influenced by thermal metamorphism and can be used to establish petrologic types for individual meteorites (Bonal et al., 2006). The maturation grade of the organic matter can be determined by the study of the Raman D-band (~ 1350 cm^{-1}) and the G-band (~1580 cm^{-1}) peak parameters. In the least metamorphosed samples, the intensity of the G-band I_G is higher than the intensity of the D-band I_D, the opposite is seen in samples with higher metamorphic grade (Bonal et al., 2006). When the I_D/I_G ratio of the CV chondrites is compared to the FWHM (Full Width at Half Maximum) of the D-band (FWHD-D) two distinct groups are recognised (fig. 6) (Bonal et al., 2006). The oxidised CVs have the highest I_D/I_G ratio (1.05 to 1.55) and lowest FWHM-D (~60 to ~100 cm^{-1}) (lower right, fig. 6), they are known to have experienced the highest metamorphic grade (Bonal et al., 2006). In particular, these data show that Allende suffered the highest thermal metamorphism (Bonal et al., 2006). An exception to this is the meteorite Kaba, which is a CV_{oxB} that lies in the upper left group (fig. 6) showing a minor metamorphic grade typical of the reduced CVs (Bonal et al., 2006). Analysis of the I_d and I_g bands from TAM5.29 (Fig. 7) shows an R1 ratio $(I_d/I_g)>1$ and in some other cases I_d/I_g~1 (but never <1), thus TAM5.29 does not clearly belong to either group. Instead, TAM5.29 values tend towards the most metamorphosed group (CV_{ox}) although several values also lie in the less-metamorphosed group (fig. 6). This is proof of the highly unequilibrated nature of this micrometeorite and suggests that TAM5.29 is transitional between the Kaba-like CVs and the more evolved Allende-like CVs. The reason for this unspecified petrologic type are, however, not clear. It is known that within the CV parent body many different environmental conditions existed from oxidising fluid-enriched locations to the reducing fluid-poor localities. The TAM5.29 metamorphic grade is thus representative of a new lithology of the CV parent body that experienced more oxidising conditions (resulting in significant Fe enrichment) with an incomplete thermal metamorphism terminated by the impact that also created the shock melt vein and preferred orientation of olivine.

3.6 Origin of the fine-grained material

Iddingsite is a common alteration feature that affects olivine in terrestrial rocks and is also found as a native minor component in chondritic meteorites. Iddingsite forms as a weathering film and represents a complex mixture of secondary hydrated silicates as well as carbonates, sulphates halides and oxides. Iddingsite compositions in TAM5.29 are difficult to interpret because of their very small grain size (<100 nm) and mixed phase composition, which in turn gives averaged data when analysed with Raman, EDS and EMPA.

Lee et al. (2015) described iddingsite in the Lafayette meteorite as an alteration sequence affecting olivine and augite concurrent with the formation of hydrous Fe-Mg-phyllosilicates. These newly formed phyllosilicates are then partially replaced by siderite. During the growth of siderite Fe-oxides also begin to form (Abreu and Brearley 2011). The alteration sequence ends with saponite and other fibrous phyllosilicates replacing siderite. Tomeoka and Buseck (1985) described similar alteration features in the matrix of CM chondrites formed as an intergrowth of Fe-Ni-S-O phases and cronstedtite. Based on these findings we looked for possible constituent minerals of iddingsite within TAM5.29.

Raman spectra of the fine-grained material of TAM5.29 (Fig.8) show possible matches to mackinawite, cronstedtite, and chukanovite (from RRUFF database). The best match among these phases is the hydrated Fe-Ni sulfide mackinawite (the two peaks at 209 cm^{-1} and 279 cm^{-1} of TAM5.29 are also well matched by troilite), although this lacks characteristic peaks around 525 and

888 cm^{-1}. Mackinawite is a poorly crystalline precipitate formed by the reaction between HS^- and Fe (Lennie et al., 1997). In nature, mackinawite occurs as hydrothermal alteration product within serpentinized peridotites and has also been reported in meteorites. Conditions of formation of mackinawite are in agreement with the conditions of formation of TAM5.29, making this phase a plausible candidate.
Phyllosilicates are also present. Although cronstedtite can be ruled out due to a lack of diagnostic within the Raman spectra the µXRD data (fig. 9) revealed the presence of saponite and antigorite in TAM5.29. Phlogopite and clay minerals may also be present but, since diffraction data could not be collected below 16°2θ and clay minerals have their main peaks in this region it is not possible to obtain further details about these phases. In addition, the µXRD data also suggested the presence of Fe-Ni sulfides (fig. 9) (pentlandite in matrix olivine in Allende was reported by Brearley 1999) as well as tentative evidence of Fe-carbonates.

Collectively, these data imply that the fine-grained material in TAM5.29 is a mixture of fibrous phyllosilicates (antigorite, saponite and possibly phlogopite-cronstedtite), Fe-Ni sulfides and possibly Fe-oxy-hydroxides with a possibility of rare carbonates inferred from the 3.9 µm band in TAM5.29 IR spectra (fig. 11). This mineralogy is in agreement with the final stage of alteration described by Lee et al. (2015) from the Lafayette meteorite, and demonstrating that TAM5.29 records a protracted episode of intense post impact aqueous alteration. Fluids involved in the formation of iddingsite may therefore derive from the partial dehydration of phyllosilicates (previously formed during metasomatism) liberated after the impact event. In this scenario iddingsite formation occurs after the interruption of metasomatism at lower temperatures and in agreement with iddingsite temperature of formation proposed by Treiman et al. (1993) (<100°C).

However, low-temperature aqueous alteration of olivine alone cannot explain the entire fine-grained mineral assemblage. Evidence also exists for the loss of CAIs. Greshake et al. (1996) reported within four CAIs, several crystals of periclase (MgO), rutile (TiO_2), calcium oxide (CaO) and corundum (Al_2O_3) inside and at grain boundaries of the constituent minerals of the inclusions. These oxides have dimensions of 50-200 nm (most of them under 100 nm), a grain size similar to the fine-grained material of TAM5.29. Since Ca-rich minerals (andradite and diopside) derive from alteration of CAIs and PRCs (Plagioclase-rich chondrules [Krot et al., 2002]), it is possible that TAM5.29 preserves some of these residual oxides as described by Greshake et al. (1996). CaO, Al_2O_3 and TiO_2 in fact match some of the strongest peaks in the µXRD pattern of TAM5.29 (fig. 9). So, in addition to the previously listed minerals, we believe that residual Ca-Al-Ti oxides are present as relicts of the primary parent body CAIs and PRCs. However, there are no evidences of residual CAIs in TAM5.29. We thus infer that the residual CAIs and PRCs minerals were not in situ alteration but were mobilised by fluids circulation. In fact hibonite and spinel are two of the most resistant CAI crystals to metasomatic alteration and in strongly altered CAIs Al-Ti-diopside is replaced by ilmenite and phyllosilicates (Krot et al., 1995). Al_2O_3 may also be indicative of the presence of sericite, an alteration aggregate of fine-grained minerals such as illite, muscovite and palagonite (Al and K rich minerals) formed by hydrothermal fluids circulation. Palagonite and allophane on Earth are also alteration products volcanic glasses and water interaction. TAM5.29 had some glass content before the metasomatic event (that largely creater fayalite, see paragraph 4.3). It is possible that part of it was converted into palagonite-allophane. Allophane can also be enriched in Fe and Ti (Gerard et al., 2007). The Ti enrichment can explain the TiO_2 detection in TAM5.29. So, illite and palagonite-allophane can

explain the presence of Al_2O_3 and TiO_2, but not the presence of MgO and CaO oxides. Furthermore these minerals are also K-rich, which can explain part of the high K and Al bulk concentration of TAM5.29. The fine-grained material in TAM5.29 therefore requires two distinct alteration events and derived from two different processes: Fe-Ni sulfides and oxides are residues of the metasomatic event and iddingsite components (such as saponite) are derived from weathering at lower temperature (<100°C) in presence of fluids released from hydrous minerals by an impact.

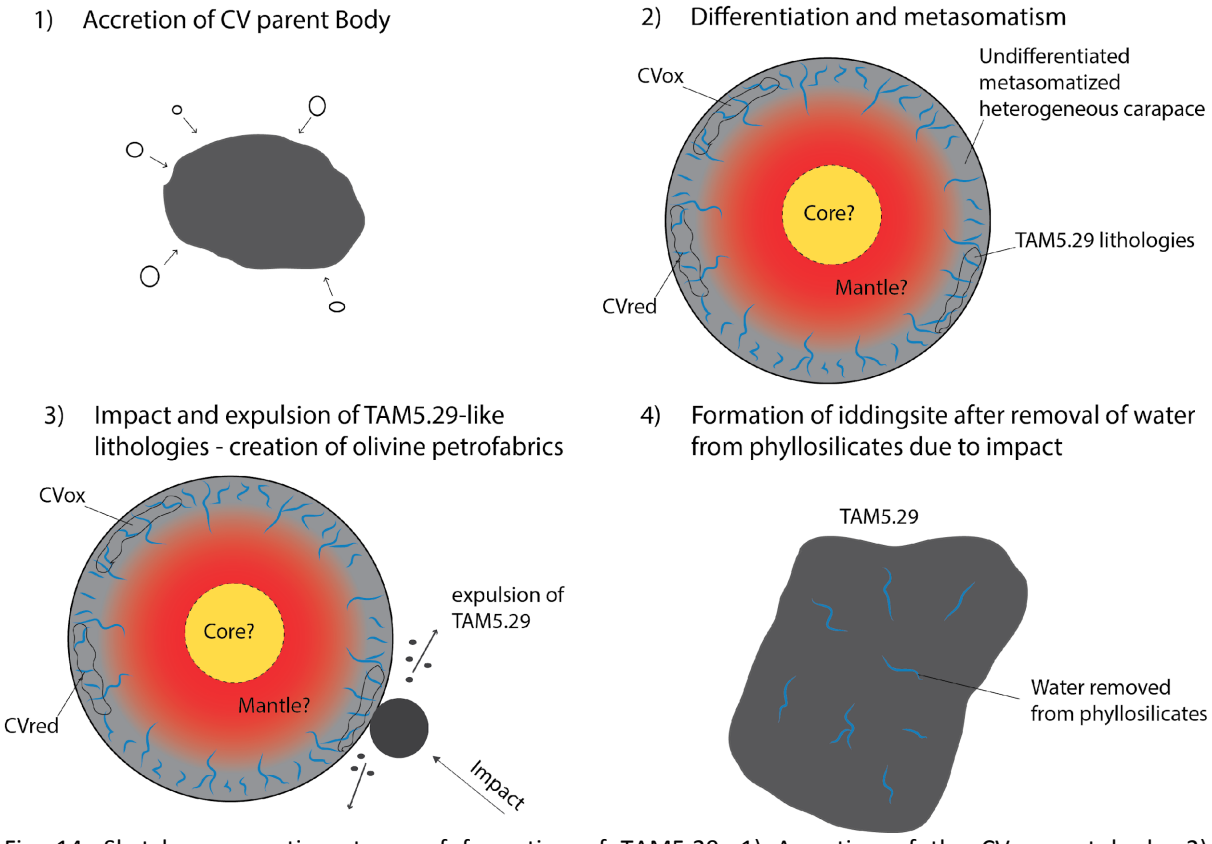

Fig. 14. Sketch representing stages of formation of TAM5.29. 1) Accretion of the CV parent body. 2) Differentiation into a core, mantle and an undifferentiated chondritic crust. The outer layer, or carapace, is heterogeneous in composition and suffer metasomatic alteration, hydrothermal activity and impact gardening. Different areas with different composition and environment cause the formation of the different types of CVs (CV_{ox}, CV_{red} and TAM5.29-like lithologies). 3) An impact occurs in the area where TAM5.29-like lithologies are found and TAM5.29 is expelled from the CV parent body. In this stage preferred orientation of olivine is created and the thermal metamorphism is terminated. 4) TAM5.29 is already separated from the parent body and water removed from hydrated minerals creates iddingsite at low temperature.

4.Conclusions

We document an unambiguous and unique minimeteorite from the CV chondrite group (a member of the CV_{OX} family), thereby expanding our collective knowledge of micrometeorite parent body diversity.

- Primary mineral phases of TAM5.29 are Fe-rich olivine, andradite and Ca-Fe-rich pyroxenes plus carbonaceous matter containing OH, S-H and C-H functional groups. Fayalite crystals grew during thermal metamorphism potentially from an amorphous precursor phase in presence of fluids.
- The fine-grained material is derived by two distinct alteration events. The metasomatic process created: Ni-Fe sulfides (e.g. mackinawite), Mg-Ca-Al-Ti oxides partly derived by residual CAIs constituents mobilised by fluids and partly derived by illite-palagonite-allophane derived by aqueous alteration, FeO-OH. Low temperature alteration created: Mg-Fe-phyllosilicates (saponite and possibly phlogopite) and possibly minor Fe carbonates.
- TAM5.29 mineralogy lies in between the CV_{oxA} and CV_{oxB}. CV_{oxA} are rich in andradite, magnetite and FeNiS like TAM5.29 but lacks of high abundances of hydrated minerals, common in TAM5.29. Conversely CV_{oxB} are rich in hydrated phyllosilicates but contains almost pure fayalite not found in TAM5.29. TAM5.29 retains a mineralogical assemblage that might be a link between the CV_{oxA} and CV_{oxB}.
- TAM5.29 retains a mineralogy dominated by thermal metamorphism products formed at ~275-250°C within the presence of Fe-alkali-halogens-rich fluids and under highly oxidizing conditions resulting in significant Fe enrichment.
- This may represent a newly described alteration environment on the CV parent body, similar to the conditions recorded by Allende-Axtell-Mokoia-Kaba etc. but with differences. These differences are: higher oxidizing conditions, heterogeneous thermal metamorphism that shows different degrees of alteration within only one micrometeorite and a different secondary alteration history enabled by a particular impact history.
- This is the proof of an even more heterogeneous CV parent body(-ies) thus adding a unique sample to the known CV lithologies.

In conclusion, the hypothesis of formation of the TAM5.29 micrometeorite may be divided in three main stages:

- Stage one: metasomatism at ~275-250°C with Fe-alkali-halogens-rich fluids occurred on the parent body.
- Stage two: the particle was involved in an impact that terminated the metamorphic event resulting in a strongly unequilibrated composition with cryptocrystalline and amorphous phases and generating a preferred orientation olivine petrofabric.
- Stage three: characterised by the formation of iddingsite at lower temperatures, possibly from fluid released by hydrated minerals during the impact.

Chapter 4

Insights on the composition of C-type asteroids revealed by Antarctic fine-grained micrometeorites showing the 3 µm band

Abstract

Many C-type asteroids are characterised by an IR reflectance spectra showing a 3 µm band with its centre varying between 3 to 3.15 µm and its shape from sharp to rounded. In this work we give new insights on the debated nature of this band and thus on the composition of C-type asteroids by studying Fine-Grained micrometeorites (Fg-MMs) showing a 3 µm band I.e. TAM5.29, TAM18c.11 and TAM18c.13. TAM5.29 is a CV-like minimeteorite characterised by a matrix of Fe-rich olivine largely altered into iddingsite, and clasts of andradite surrounded by diopside-jarosite-phyllosilicates assemblages. TAM18c.11 and TAM18c.13 are very similar in composition and both suffered a very strong alteration in Antarctica that replaced almost all the crystals with jarosite (ammoniumjarosite in the case of TAM18c.11). However, some phyllosilicates, metal alloys and tiny olivine crystals are still visible. The band centre of the 3 µm absorption of these samples varies between 3.07 µm up to 3.15 µm in the case of TAM5.29. The 3.15 µm band found in TAM5.29 is always associated with Fe-rich hydrous phases suggesting a close relationship between this feature and Fe-OH bonds. In a single spot in TAM5.29 and in TAM18c.11 the 3 µm band is found at shorter wavelengths, around 3.07 µm band. In the case of TAM5.29 particle is found together with the 3.4 and 3.5 µm absorptions of aliphatic hydrocarbons, while in TAM18c.11 is found scattered around the ammoniumjarosite-rich matrix. It thus seems that when found at shorter wavelengths (3.07 µm) the 3 µm band is indicative of organic matter, most likely CH and NH functional groups found in hydrocarbons or sulphates and salts. With these observations we infer that Europa-like asteroids (with a band centre at 3.15 µm) are Fe-rich hydrous worlds, while Ceres-like bodies (with a band centre at 3.05 ± 0.01) are organic rich worlds. In both cases we bring also evidences that these bodies went through an extensive period of hydrothermal alteration and a second period of low-temperature aqueous alteration.

1. Introduction

The 3 µm band has been detected on many minor bodies of the Solar System and its origin is still debated. Takir and Emery (2012) reported a complete list of the asteroids bearing the 3µm band, the main ones are: 1 Ceres, 10 Hygiea, 31 Euphrosyne, 52 Europa, 76 Freia, 107 Camilla, 153 Hilda, 190 Ismene, 324 Bamberga, 361 Bononia, 401 Ottilia, 451 Patientia, 790 Pretoria. Not all these bodies show the same 3 µm band characteristics. On the contrary four different groups can be recognised (Takir and Emery, 2012) and generally the 3 µm is interpreted as a hydration band attesting the presence of hydrated phyllosilicates and water ice (Takir and Emery, 2012; Hargrove et al., 2012-2015). The first group is called “sharp” and show a sharp 3 µm band given by hydrated phyllosilicates (Takir and Emery, 2012). The Second group is the “Ceres-like” and have a band centre at 3.05 ± 0.01 µm (Takir and Emery, 2012). The third group “Europa-like” exhibits a band 3.15 ± 0.01 µm also due to hydrated phyllosilicates and finally the fourth group called “rounded” due to the wide and curve 3 µm band related to water ice (Takir and Emery, 2012). However other interpretation for the 3 µm band have been proposed. One possibility is that the 3 µm bands is given by the water-iron bond in hydrated Fe-rich phyllosilicates (e.g. cronstedtite) (Rivkin et al., 2006) or given by goethite (Beck et al., 2011). Alternatively another carrier of the 3 µm band is a mixture of crystalline water ice and ion-

irradiated organics, mainly asphaltite (Vernazza et al., 2005). Finally, King et al. (1992) suggested that the 3 µm band on Ceres is due to ammonium bearing minerals. Lately this interpretation received a big consensus with the NASA-Dawn space mission at Ceres since the 3 micron absorption revealed by the VIR spectrometer has been indeed attributed to ammoniated phyllosilicates, in particular NH_4-smectites (NH_4-annite and NH_4-montmorillonite) (De Sanctis et al., 2015; Ferrari et al., 2019). More recently a 2.99-3 µm band was seen on Ceres spectra associated to the organics 3.4 µm band (De Sanctis et al., 2019). The nature of this band is not clear, it is probably given by NH functional groups contained in the organic matter (De Sanctis et al., 2019). De Sanctis et al. (2015) considered also other minerals as possible carriers of the 3 µm band: cronstedtite, in agreement with the hypothesis of Rivkin et al. (2006), and brucite as also suggested by Milliken and Rivkin (2009). Tochilinite may be another possibility since it is composed of Fe-sulphide interlayed with brucite (De Sanctis et al., 2015). However all these minerals do not show a good fit with the Ceres spectrum, especially brucite which is characterised by a 2.46 band not found on Ceres. Therefore brucite most probably is not a major component of C-type asteroids with 3 µm band (De Sanctis et al., 2015).

The 3 micron band is a feature detected not only on asteroids. Yang et al. (2009) found the 3 µm band on the 17P/Holmes comet during a massive outburst. The nature of this feature on the 17P comet was attributed to the presence of water ice, even though the other typical absorption of water ice at 1.5 µm was not observed (Yang et al., 2009). 3 µm band was either found in the centre of the proto-planetary nebula IRAS 22272+5435 and it is thought to be given by acetylene C_2H_2 and hydrogen cyanide HCN (Goto et al., 2003), two organics also found in some meteorites (Sephton, 2002). However, among the meteorite collections it has been found only one sample with a 3 µm band, the reduced CV chondrite Efremovka showing a 3.11 µm band probably related to aqueous alteration and/or the presence of metal (Takir et al., 2019). Hence we focused on searching among micrometeorites (MMs) as also suggested by Vernazza et al. (2015) who studied IDPs. Micrometeorites are sub-millimetre size dust grains (Genge et al., 2008) and represent the majority of the incoming extraterrestrial material on Earth, approximately between 20000 and 60000 tons per year (Love and Brownlee, 1993; Zolensky et al., 2006). Micrometeorites sample minor bodies especially from the asteroid belt (Genge et al., 2008; Carrillo-Sanchez et al., 2015) and are liberated from their parent bodies in many different ways: impacts (Nesvorny et al., 2003; Flynn et al., 2009), spontaneous disruption (Nesvorny et al., 2010), sublimation (Schulz et al., 2004; Yang et al., 2009) and mantle shedding events (Schulz et al., 2015). Based on oxygen isotopic composition and mineralogy, most of the micrometeorites (~75%) have an affinity to the carbonaceous chondrites (Suavet et al., 2010; van Ginneken et al., 2012; Taylor et al., 2012; Cordier et al., 2018). These micrometeorites are mainly friable material called fine-grained unmelted micrometeorites (Fg-MM) (Genge et al., 2008). The Fg-MMs are then divided into 3 groups based on the hydration degree: C1 particles have an extensively hydrated matrix, C2 is less aqueously altered and C3 anhydrous (Genge et al., 2008). With this work we report the first micrometeorites showing an unambiguous 3 µm band. The samples we studied labelled TAM5.29, TAM18c.11 and TAM18c.13 are fine-grained micrometeorites (between C1 and C2 groups) collected on the Transantarctic Mountains by the Italian expedition (PNRA – Programma Nazionale delle Ricerche in Antartide). Our observations suggest that the 3 µm absorption in the samples we studied is due to either Fe-rich hydrated minerals, in agreement with what found in Europa-like asteroids by Rivkin et al. (2006) and Beck et al. (2011), or organic matter, as already suggested by Vernazza et al. (2005) and Goto et al. (2003) for Ceres and the planetary nebula IRAS 22272+5435 respectively or a combination of both.

2. Results

2.1. Petrography and mineral composition

TAM5.29, TAM18c.11 and TAM18c.13 are fine-grained particles with dimensions of a few hundred of micrometres (fig. 1). TAM18c.11 and TAM18c.13 have the typical magnetite rim that distinguishes the micrometeorites (fig. 1), which is not present in TAM5.29. In fact TAM5.29 is a minimeteorite, a little piece of a larger meteorite (see chapter 1; Nava et al., accepted) (fig. 1). Another clear difference between TAM5.29 and the other two particles is that TAM18c.11 and TAM18c.13 have a very high porosity with voids reaching 100 µm, while TAM5.29 is characterised by a much lower porosity and no voids are observed (fig. 1). Furthermore TAM18c.11 and TAM18c.13 suffered a very strong alteration in Antarctica favoured by the interconnected porosity and a large part of the particles is replaced by jarosite (fig. 1-2); on the contrary TAM5.29 shows only minimal terrestrial alteration. More in detail, TAM5.29 is a CV-like minimeteorite composed of a Fe-rich olivine matrix with inclusions of andradite with diopside-jarosite halos (fig. 2A-B). Fibrous phyllosilicates, mainly serpentine, are also present as well as scattered tiny (less than 1 µm) metal alloys and an aggregated of spinel crystals (fig. 2A-B). This mineralogy is a record of hydrothermal process at ~250 °C that created TAM5.29 (Nava et al., accepted). After this phase of metasomatism TAM5.29 underwent a phase of low temperature (<100 °C) that altered almost completely the olivine and created iddingsite (<100 nm crystals), mainly composed of Fe-rich hydrous minerals (e.g clays, phlogopite, annite, saponite) and possibly carbonates (e.g. chukanovite-siderite) (see chapter 1; Nava et al., accepted). Analyses revealed also ubiquitous presence of SH and CH functional groups (see chapter 1; Nava et al., accepted). This detailed characterisation was not possible for the TAM18c.11 and TAM18c.13 samples because of their very high terrestrial alteration, that obliterated a considerable part of the particles, and their fine-grained mineralogy, resulting in mixed analytical values due to mineral phases overlapping. However, both in TAM18c.11 and TAM18c.13 remnants of fibrous phyllosilicates like those found in TAM5.29 are recognisable (fig. 2C-E-F). The three particles have also in common the presence of small metal alloys crystals scattered in the matrix (fig. 2C to F). In TAM18c.11 (fig. 2D) a portion of the matrix is recognisable and is very similar to the matrix of TAM5.29. In fact it is composed of lath-shaped olivine crystals with dimensions of 1-2 µm plus a mesostasis in between the olivine crystals and tiny metal-alloys. Furthermore, Raman analyses revealed that in TAM18c.11 there is also the ubiquitous presence of organic matter (peaks at 1340 and 1600 cm^{-1}), CH and SH functional groups (peaks at 2680 and 2910 cm^{-1}) (fig. 3). Another peak appears in TAM18c.11 at around 3412 cm^{-1} and can be due to NH functional groups (fig. 3).

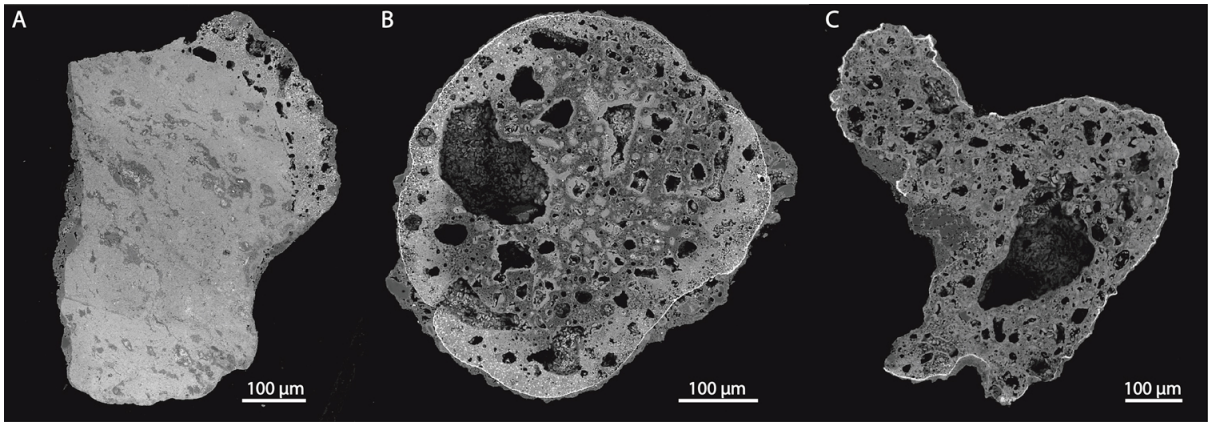

Fig. 1. FE-SEM backscattered images of A) TAM5.29, B) TAM18c.11 and C) TAM18c.13.

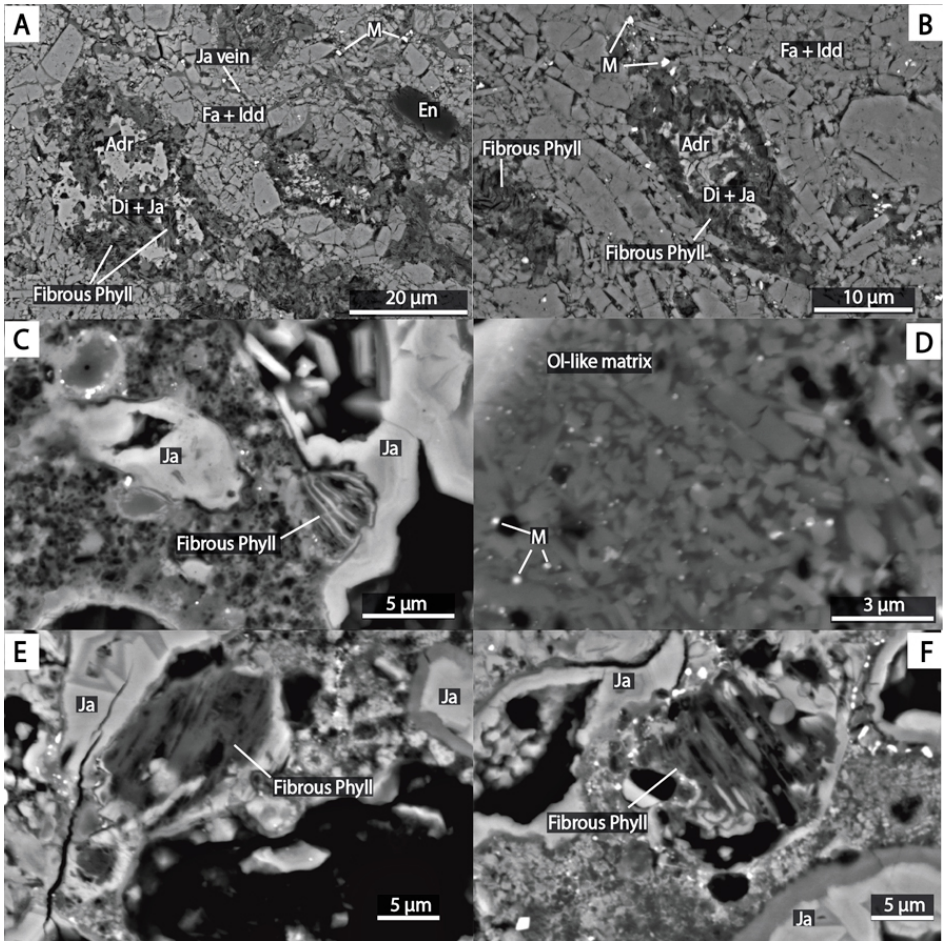

Fig. 2. FE-SEM backscattered images of A-B) TAM5.29, C-D) TAM18c.11 and E-F) TAM18c.13. Fa=fayalite; Idd=iddingsite; Adr=andradite; Di=diopside; Ja=jarosite; M=metal alloys; En=enstatite; Ol=olivine; Fibrous Phyll=fibrous phyllosilicates.

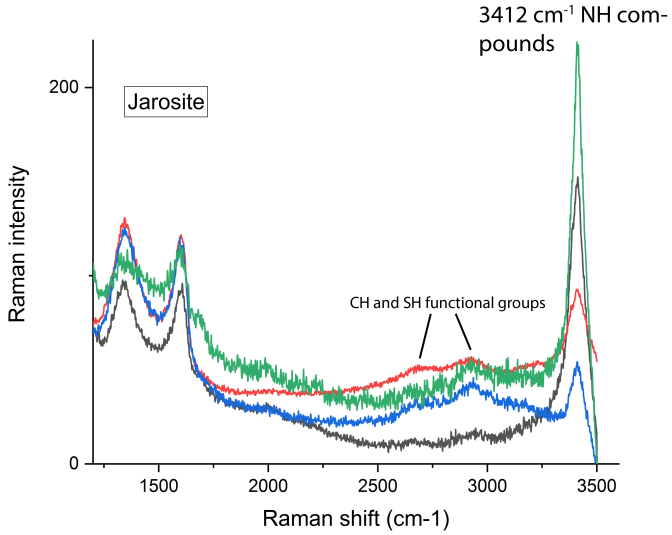

Fig. 3. Raman spectra of jarosite in TAM18c.11. To be noticed the peaks of carbon, the peaks of CH-SH functional groups and at ~3412 cm^{-1} the NH peak.

2.2. Spectroscopy

In figure 4 are reported the reflectance spectra of TAM5.29, TAM18c.11 and TAM18c.13. These spectra are with the continuum removed with origin software. All the particles have an absorption band centred at ~2.8 µm, consistent with the presence of Fe-rich hydrous phyllosilicates (Takir et al., 2013) (Fig. 4). The 3 µm absorption band has a band centre at ~3.15 µm for TAM5.29 and TAM18c.11 with a second minor absorption at 3.18 µm, while in TAM18c.13 the band centre is at lower wavelength around 3.07 µm (Fig. 4). All the samples show the absorption between 3.31 µm and 3.34 µm given by organic matter, likely aromatic hydrocarbons (Moroz et al., 1998; Cloutis, 2003; Quirico et al., 2016; De Sanctis et al., 2019), while the band at 3.4 µm is representative of aliphatic hydrocarbons (De Sanctis et al., 2017-2019) (Fig. 4). Another broadband between 3.5-3.6 µm can be seen in TAM18c.13 most likely related to organic matter (CH bonds) (De Sanctis et al., 2019). TAM18c.11 and TAM18c.13 respectively show absorptions at 3.7 µm and 3.8 µm (Fig. 4). These two bands are indicative of SH bonds (see chapter 1 and 5), consistent with the high content of jarosite due to Antarctic alteration. The carbonates related absorption band at 3.9 µm (De Sanctis et al., 2016; Tosi et al., 2017; Carrozzo et al., 2017) is evident in TAM18c.11 and TAM18c.13, while in TAM5.29 the band depth decreases and the 3.9 µm band is barely detected (Fig. 4).

The spectral maps made at the IAS-Orsay allows us to do a more detailed analysis of TAM5.29 in order to better understand the nature of the 3 µm band. We also made a spectral map of TAM18c.11, but its high degree of alteration made the interpretation very difficult. The same would have happened with TAM18c.13. For this reason we focused only on TAM5.29 and TAM18c.11. Scattered around the matrix of TAM5.29 we found different spots with spectra showing a prominent 3.15 µm band associated to the 2.8 µm and 3.3 µm band (fig. 5A). Another isolated spot of a few micrometres of TAM5.29 gave a different spectra characterised by a 3.04 µm band that always appears with the 3.4 µm and 3.5 µm band of the aliphatic organics (fig. 5B). In all these cases the 2.8 µm band was not detected. Unfortunately, we haven't been able to attribute the single spots with a specific mineral due to the fine-grained nature of the matrix of TAM5.29. In TAM18c.11 the 3 µm is shifted towards shorter wavelength at 3.05-3.06 µm (fig. 6). In this case the band is associated with the 2.8-2.9 µm band and a broad band at 3.8 µm (fig. 6).

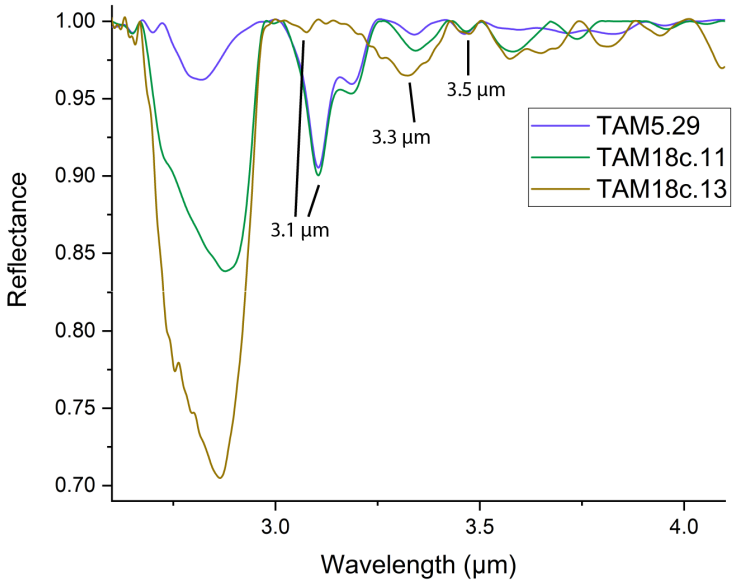

Fig. 4. Continuum removed IR reflectance spectra of TAM5.29, TAM18c.11 and TAM18c.13.

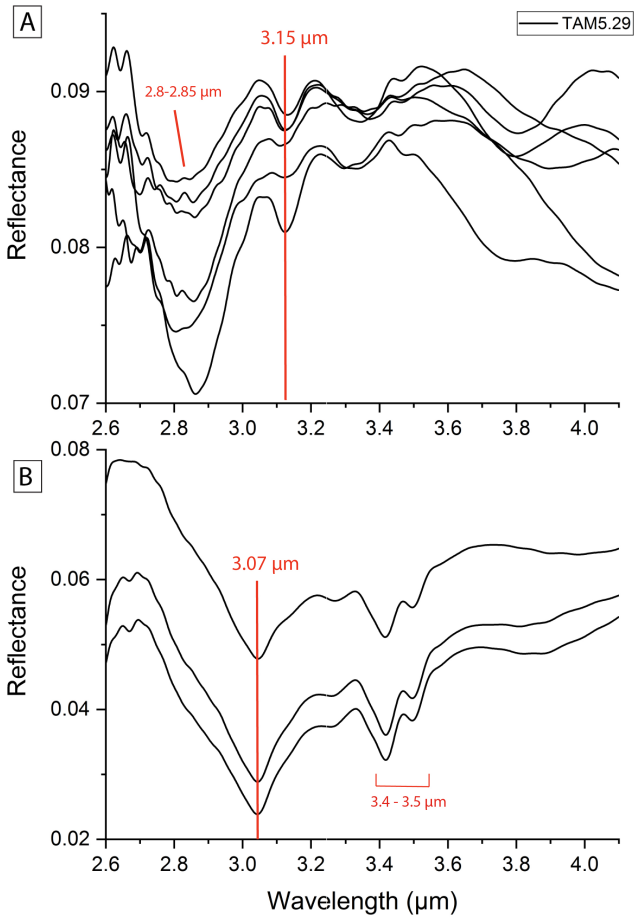

Fig. 5. IR reflectance spectra of TAM5.29. A) Spectra acquired in the Fe-rich hydrous matrix showing the 3.15 µm band. B) Spectra taken in the localized spot rich in aliphatic hydrocarbons (3.4 and 3.5

µm bands) with the 3.07 µm band. A minor contribution of the surrounding material may be possible, causing the very slight detection of the 3.15 µm band in the spectra in panel B.

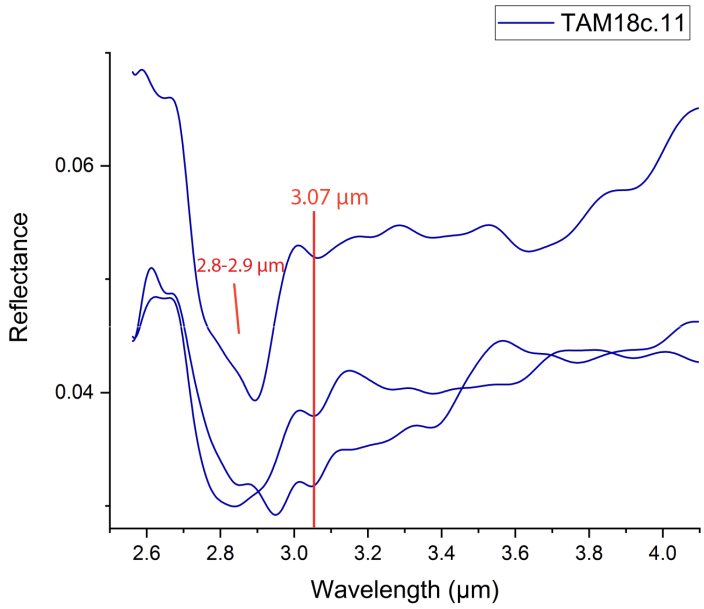

Fig. 6. IR reflectance spectra of TAM18c.11.

3. Discussion

3.1. Nature of the 3 µm band

Based on our findings the 3 µm band can be associated either to OH, in particular to Fe-OH, or to the organic matter. In the first case the 3 µm band is shifted towards longer wavelength around 3.15 µm (fig. 5A), and in the second case the 3 µm band centre is at around 3.07 µm (fig. 5B). The Fe-OH related 3.15 µm band is suggested by the fact that in the spectral map on TAM5.29 the 3.15 µm band is found scattered in the Fe-rich olivine matrix largely altered into iddingsite, which is in part made up by hydrated Fe-rich clays. Furthermore, in this scenario the 3.15 µm band is always associated to the 2.8 µm band, typical of Fe-rich phyllosilicates (e.g cronstedtite) (Takir et al., 2013). In the matrix of TAM5.29 magnetite is also found. Part of the magnetite has been altered into hematite and goethite during the second stage of low temperature aqueous alteration when iddingsite formed. These observations support the hypothesis of Rivkin et al. (2006) and Beck et al. (2011) on Europa-like asteroids who respectively attributed the 3 µm band to Fe-rich clays and goethite. In particular Cronstedtite, the Fe-rich end member of serpentine, have been proposed to be a major component of Ceres surface (along with brucite and Mg-carbonates) (Zolotov, 2014). In the second case shown in figure 5B, the spectrum shows a prominent 3.07 µm band along with 3.4 and 3.5 µm band but no 2.7-2.8 µm bands are found. The 3.4 and 3.5 µm bands are proof of the presence of aliphatic hydrocarbons, which coupled with the absence of the 2.7-2.8 µm band related to Mg-OH and Fe-OH bonds, suggest that in this context the 3.07 µm band is given by organic matter as also suggested by Vernazza et al. (2005) and Goto et al. (2003). A similar situation has been found on the aliphatic rich material around the Ernutet crater on Ceres. Around the Ernutet crater indeed evident the 3.4-3-5 µm aliphatic bands together with a 2.99-3 mm band attributed to NH compounds in the organic matter (i.e amine or salts) (De Sanctis et al., 2019). In our analyses of

TAM5.29 no NH has been detected, however this can be due to a very low abundance of NH, which is in the order of ppm localized in a very small spot.
It is worth to note that the only two known samples with a prominent 3 µm band, Efremovka (showing a 3.11 µm band, Takir et al., 2019) and TAM5.29, are both related to CV chondrites. This implies, on the contrary to what has been suggested so far (McSween et al., 2018), that aqueously altered C-type asteroids like Ceres might not only be parent bodies of the CM/CI chondrites but also of the CV ones. Takir et al. (2019) also suggest that the shift of the 2.7 µm band towards longer wavelengths is related to increasing aqueous alteration on the parent body. However in the samples we studied there is no clear evidence of this effect since the shift towards 2.8 µm in our samples is more likely due to changes in composition towards increasingly Fe-rich hydrous silicates.

On the contrary, the results of TAM18c.11 suggest that the 3.05-3.06 µm band can be given by NH found in ammonium-jarosite indicated by the 3412 cm^{-1} Raman peaks. The link between the 3.05 µm band and jarosite is also confirmed by the broad 3.8 µm band, which indicates the presence of SH functional groups. However, ammonium-jarosite is a product of terrestrial alteration in Antarctica. This environment of formation may give some insights on the parent body processing, discussed in the following 3.2 section.

3.2. Parent body environment

The 3.15 µm band in TAM5.29 can give insights on the parent body environment of the Europa-like asteroids (fig. 7), which either display a 3.15 µm band (Driss and Emery, 2012). As discussed above the carriers of the 3.15 µm band in TAM5.29 are Fe-rich phyllosilicates. These phyllosilicates were formed during metasomatism in presence of fluids on the parent body at a temperature around 250°C (Krot et al., 1995-1998). Additional Fe-rich clays and hematite-goethite were formed during a second phase of low temperature (well below 100°C) aqueous alteration (Tomeoka and Buseck, 1985; Abreu and Brearley, 2011; Lee et al., 2015). Thus, it is likely that the Europa-like asteroids such as Europa and Patientia underwent a phase of hydrothermal alteration that created Fe-rich anhydrous and hydrous minerals that have been subsequently altered by low temperature alteration. Unfortunately the spectra of Europa and Patientia (fig. 7) don't have any data acquired below 2.9 µm, thus we can not associate the 3.15 µm band that we infer related to Fe-OH to a possible 2.8 µm band attributed to the Fe-phyllosilicates (Driss et al., 2013).
On the other side, the 3.07 µm band of TAM5.29 can give insights on the Ceres-like asteroids (fig. 8). characterised by a 3.05 ± 0.01 band centre (Driss and Emery, 2012). The 3.07 µm of TAM5.29 can represent very well the 3 µm band found at the Ernutet crater on Ceres since both are found together with the aliphatic hydrocarbons absorption. However it fails to describe and explain the entire spectrum of Ceres and thus the Ceres-like bodies. If we consider a bulk spectroscopic analyses that comprises the spot where the 3.07 µm band is found in TAM.59 and the surrounding hydrous minerals we have a better match with the spectrum of Ceres since it displays a 2.8 µm band. However the 2.7-2.8 µm band on Ceres is found at 2.7 µm, suggesting that Ceres is less iron rich and is dominated by Mg-phyllosilicates. Even if we consider this scenario the 3.4 and 3.5 µm bands in aliphatic rich spot on TAM5.29 are not present on the average spectrum of Ceres and thus difficult to explain. In fact the average spectrum of Ceres (Fig. 8) has a broad organic band between ~3.25 µm up to ~3.6 µm with a minima towards at ~3.3 µm and not 3.4-3.5 µm. However, this broad 3.25-3.6 µm band may obliterate possible aliphatic absorptions. Broad bands between 3.2 µm and 3.7 µm have also been attributed to possible presence of aromatic CH bonds on the 67P/Churyumov-

Gerasimenko comet (Quirico et al., 2016). We thus assume a predominance of aromatic hydrocarbons over aliphatic chains and it is known that hydrothermalism can bring to an aromatization of the aliphatic hydrocarbons (Elsila et al. 2005; Galvin et al. 2010; Burton et al. 2012). Ceres went indeed through a period of hydrothermal alteration (Neveu et al., 2014; Hendrix et al., 2016) as well as TAM5.29, which also shows an average organics absorption at 3.3 µm (Fig. 5A) rather than at 3.4-3.5 µm (only found in a localized spot Fig. 5B). Thus, hydrothermal processes suffered by TAM5.29 may have destroyed the majority of the aliphatic hydrocarbons (typical absorption band at 3.4-3.5 only found in one spot) in favour of aromatic hydrocarbons (absorption at shorter wavelengths around 3.3 µm). This process on Ceres may lead to a liberation of NH compounds that may have been recycled by aromatic hydrocarbons or may have entered into the phyllosilicates lattice (i.e. ammoniated phyllosilicates, De Sanctis et al., 2015).

The presence of localized aliphatic-rich spots on Ceres around the Ernutet crater may be explained with recent mobilization of pristine material or by sublimation and outbursting (see chapter 3). Regarding TAM5.29 the aliphatic band is probably related to a remnant of pristine material since the micrometeorites underwent an incomplete heterogeneous metamorphism and still retains rare pristine phases such as enstatite and forsterite crystals (see chapter 1; Nava et al., accepted under review).

The 3.07 µm band described in TAM18c.11 is intimately linked to the presence of NH in the jarosite (as discussed in paragraph 3.1) and can cast light on in situ alteration at around 0°C in presence of ice on main belt asteroids and protoplanets like Ceres. Aqueous alteration or cryovolcanic processes can lead to the formation of evaporites on bodies like Ceres (De Sanctis et al., 2016; Nathues et al., 2017; Bu et al., 2018). Ammonium-jarosite found in TAM18c.11 as a product of terrestrial alteration can thus form also on bodies like Ceres. Indeed ammonium-jarosite crystallises in environments that are rich in organic material (fine-grained micrometeorites are in fact enriched in organic matter, see chapter 3) and C-type asteroids are rich in organics as well (Rivkin and Emery, 2010; Hendrix et al., 2016; Marchi et al., 2019), thus formation of ammonium bearing sulphates on C-type asteroids, like the case of TAM18c.11, is plausible. However, ammonium-jarosite in TAM18c.11 was formed under atmospheric conditions in which sulphates are stable, whereas the stability of hydrated sulphates on airless bodies is controversial considered that OH in vacuum is expected to sublimate (Nathues et al., 2015; Bu et al., 2018). If OH-sulphates are not likely to exist on the surface of asteroids, than NH-sulphates are even less likely given that NH is more volatile than OH. On the contrary Bu et al. (2018) suggest that minimally hydrated sulphates may be still be present on low-pressure atmosphere bodies. In addition, sulphates have been reported in CM and CI chondrites (Velbel, 1988; Zolotov, 2009-2016; Zolensky et al., 2016), meteorites with a composition closely related to that of C-type asteroids suggesting the presence of sulphates on CCs parent bodies. De Sanctis et al. (2019) proposed NH-salts as possible candidates for the 3.07 µm band on Ceres and NH-salts have been detected on Ceres in the Ceralia Facula (De Sanctis et al., 2016; Raponi et al., 2019). Thus, NH-bearing sulphates as carriers of the 3 µm band may be another explanation and may give some contribution to the 3 µm band, especially in localized spots were upwelling of evaporites and salts occurs (i.e. Ceralia Facula, De Sanctis et al., 2016, Raponi et al., 2019).

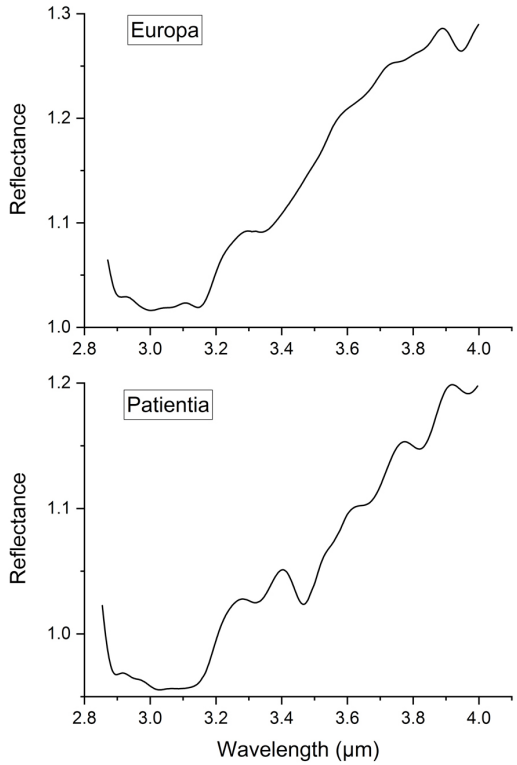

Fig. 7. IR reflectance spectra of Europa and Patietia, two of the Europa-like C-type asteroids (Takir et al., 2012).

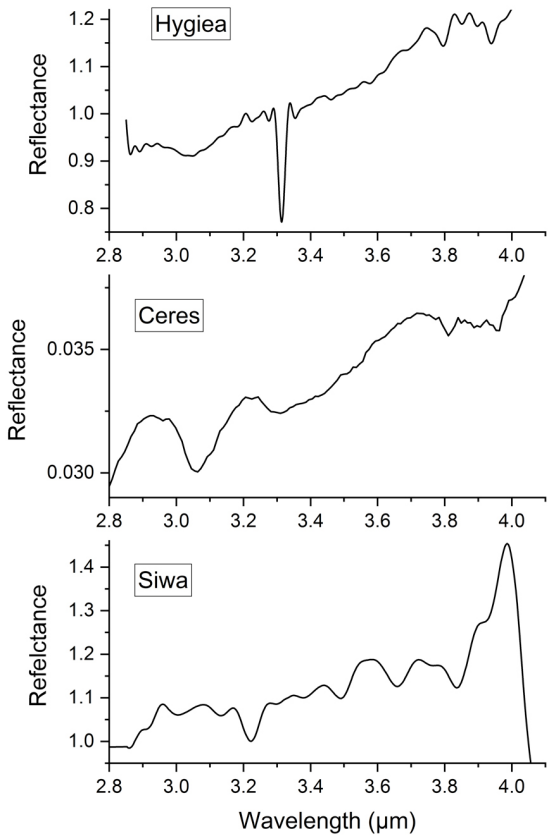

Fig. 8. IR reflectance spectra of Hygiea, Ceres and Siwa, three of the Ceres-like C-type asteroids (Takir et al., 2012).

3.3. Anhydrous pyroxene presence on Ceres and C-type asteroids

Previous studies on IDPs as possible analogues for icy bodies revealed the presence of anhydrous pyroxene in IDPs (Vernazza et al., 2017). This seems to be inconsistent with the hydrous nature of icy bodies as well as C-type asteroids (Vernazza et al., 2017). However, a minimum presence of anhydrous pyroxene, mainly enstatite, has been reported on Ceres and Eugenia with an abundance of around 20 vol% mixed with hydrated minerals (Vernazza et al., 2017). The best explanation for the presence of enstatite is an exogenous origin, in particular from pyroxene-rich dust (Vernazza et al., 2017). Our results on TAM5.29 give important insights on the nature of anhydrous pyroxene on C-type asteroids. Enstatite as a relict mineral, not affected by metasomatism, has been found in TAM5.29 (fig. 2A). At the same time diopside is found in TAM5.29 (fig. 2A-B) and is a product of metasomatism. As discussed above under a spectroscopic point of view TAM5.29 may be a possible analogue of C-type asteroids, especially the Europa-like bodies. TAM5.29 also is the result of geological processes like hydrothermalism and metasomatism at ~250°C, similar to those proposed for bodies like Ceres (Neveu et al., 2014; Hendrix et al., 2016). Thus, we bring evidences that the presence of anhydrous pyroxene can be an original feature of C-type asteroids. In particular enstatite may represent remnants of the original pristine material from which C-type asteroids formed and diopside-hedenbergite may be products of endogenous processing. We also suggest that not only pyroxene but also olivine can be actually largely present on C-type asteroids. The majority of the olivine is altered into iddingsite by low-temperature aqueous alteration, like the fayalite in TAM5.29, explaining the fact that in the spectra of C-type asteroids olivine is not detected.

4. Conclusions

We document the micrometeorite samples TAM5.29, TAM18c.11 and TAM18c.13 showing a clear 3 µm band in their reflectance spectra, which together with the Efremovka CV chondrite found by Takir et al. (2019) are the first samples found with a prominent 3 µm band. All the three samples have a composition closely related to the carbonaceous chondrites. TAM18c.11 and TAM18c.13 are in fact fine-grained micrometeorites, while TAM5.29 is a CV-like minimeteorite. The high Antarctic alteration and fine-grained matrix of TAM18c.11 and TAM18c.13 put some limitations on the mineralogical and spectroscopic study of these samples. Phyllosilicates and tiny metal alloys are still found in the olivine-like matrix of TAM18c.11 and TAM18c.13. However the majority of these samples is replaced by jarosite formed by terrestrial alteration in Antarctica. In particular, in TAM18c.11 is characterised by the presence of ammonium-jarosite. On the contrary TAM5.29 has a minimal alteration and an interesting mineralogy that records hydrothermal alteration on the parent body. TAM5.29 is composed by a Fe-rich olivine matrix plus andradite inclusions with haloes of diopside-jarosite intimately mixed formed by metasomatism at 250°C. In addition iddingsite replaced the fayalite during a secondary phase of low temperature aqueous alteration. Iddingsite is a mixture of nano-proportion Fe-rich hydrous phyllosilicates, Fe-oxy-hydroxes like hematite-goethite and possibly minor Fe-carbonates like siderite and chukanovite. CH and SH functional groups are found scattered all around the TAM5.29 particle. The bulk reflectance spectra of the three samples has band centre at around 3.15 µm, but a more detailed spectral map on TAM5.29 revealed the presence of two bands with minima at 3.15 µm and 3.07 µm. The 3.15 µm band is found closely mixed with Fe-rich altered matrix, while the 3.07 µm is found together with the 3.4 and 3.5 µm bands of aliphatic hydrocarbons. Combining petrographic and spectral information and comparing them to the spectra of C-type asteroids we conclude that:

1. The 3.15 µm band is given by Fe-OH bonds. Thus the Europa-like asteroids, characterised by a 3.15 µm band, are Fe-rich hydrous worlds characterised by Fe-clays and phyllosilicates created by a period of extensive hydrothermal alteration and/or low-temperature aqueous alteration.
2. The 3.15 µm band of TAM5.29 coupled with the 3.11 µm band of the CV chondrite Efremovka (Takir et al., 2019) point to a CV-like composition of the Europa-like asteroids. Thus Europa-like bodies may be the CV chondrites parent bodies.
3. The 3.07 µm band is related to organic matter, in particular CH and NH functional groups found in aromatic or aliphatic hydrocarbons or in the phyllosilicates lattice. This suggests that the Ceres-like asteroids, which have a 3.05 ± 0.01 µm band, are bodies enriched in organic matter.
4. The 3.05-3.06 µm band revealed by TAM18c.11 is probably related to terrestrial NH-jarosite. This suggests that on bodies with past or active aqueous alteration and cryovolcanism (e.g. Ceres) creating evaporites, the NH compounds may also be found in the sulphates and salts. However, the high instability of sulphates on low-pressure atmosphere bodies makes this hypothesis less likely or at least the contribution of NH-sulphates to the 3 µm band is only minimal and localized.

Finally, our observations bring evidence that anhydrous pyroxene (enstatite and diopside-hedenbergite) can be present on C-type asteroids as remnants of the pristine material and product of hydrothermal alteration. Olivine can also be present on C-type asteroids, largely replaced by iddingsite. Thus, pyroxene and olivine may be also endogenous materials and not only an exogenous contribution of dust and meteorites.

Chapter 5

Outburst nature of hydrocarbons on icy bodies of the Solar System

Abstract

Outbursts can be generated by cryovolcanism in many different planetary bodies such as asteroids, satellites, TransNeptunian Objects (TNOs) and by irradiation and sublimation on cometary nuclei. Mechanisms driving cryovolcanic activity and ice-rock interaction are poorly understood. For this reason we made some experiments in laboratory with Carbonaceous Chondrites (CCs) and ices with the intent of simulating cryovolcanic processes and eventually study outbursting products. We powdered 3 CCs samples and individually mixed them with deionized or ammoniated waters and subsequently froze them at -80°C. Once frozen the mixtures were put in a vacuum chamber and heated from ~ -195°C up to ~ 100°C. We acquired reflectance spectra in the NIR range before and after the experiment. The powders started sublimating fine particles at around -40°C and between -20 °C and -10°C a violent outburst occurred. We divided the sublimated powders from the ejected powders during the outburst and compared with the original ones. In the ejected powders the 3.4 µm and 3.5 µm bands of aliphatic hydrocarbons appeared in two of the 3 samples, while in the original and sublimated powders this feature was not found. Gas chromatography analyses showed that in the sublimated powders two new *n*-alkanes, the C_{19} and C_{21}, formed (not enough to be detected by reflectance spectroscopy). Even more interestingly in the ejected powders the C_{19} and C_{21} were found in higher abundance with respect to the sublimated and original powders and another *n*-alkane, the C_{17}, appeared in very high quantities. Hence we find out that aliphatic hydrocarbons can form in presence of ice during short-duration sublimation-outburst at temperature as low as -40°C. This finding is able to explain the organic-rich composition of bodies like Ceres, Themis and most importantly implies that cometary activity is capable of creating new organic materials which can not anymore considered only as unprocessed remnant of the Solar Nebula. Our results can also explain the high organic matter abundances in micrometeorites (MMs) if we consider sublimation-outburst as a delivery mechanism for MMs.

1. Introduction

Outbursting either related to sublimation by irradiation or cryovolcanism deeply shape the surface of a variety of planetary and minor bodies such as dwarf planets like Ceres (Ruesch et al., 2016), satellites like Europa (Quick et al., 2017), Enceladus (Postberg et al., 2009), Ganymede (Kay and Head, 1999; Head et al., 2002) and Charon (Desch and neveu, 2017), and cometary nuclei (Miles, 2016; Vincent et al., 2016). Although prerequisites for cryovolcanism have been delineated by Kargel (1991) and Neveu et al. (2015) cryovolcanic processes and their related products are still not well understood. Volatiles are crucial for the generation of outbursts, in particular carbon monoxide (CO) and other volatiles (CO_2, N_2, CH_4 and H_2) that can be produced by other mechanism such as hydrothermal activity (Neveu et al., 2015). Cracks formation and propagation is another crucial aspect that control cryovolcanism (Neveu et al., 2015). Cracks propagation is in turn controlled by the internal structure of planetesimals, a hydrated core facilitates the formation of cracks while in an undifferentiated body cracks are less likely to form (Neveu et al., 2015). The Petrogenesis of the brines involved in the cryovolcanic processes has been described in the system H_2O-Mg_SO_4-Na_2SO_4, where the main solutes are Mg_SO_4 and Na_2SO_4 plus minor sulphates of K, Ni, Mn and Ca (Kargel, 1991). Carbon-nitrogen-sulphur species as well as hydrogen are also very important, in particular CO,

CO_2, N_2, CH_4 and H_2 exsolution may lead to a gas-driven activity resulting in an explosive cryovolcanic event (Neveu et al., 2015). Surface expressions of outbursting and cryovolcanism are multiple: conical mountains found in depressions like the Kubrick Mons on Charon (Desch and Neveu, 2017), Domes found on Europa (Pappalardo and Barr, 2004; Quick et al., 2017), Enceladus (Helfenstein et al., 2005; Spencer et al., 2009) and Ceres (Ruesch et al., 2016), salt rich water fountains like the case of Occator bright spots on Ceres (Ruesch et al., 2019), cryogenic flow features on Ceres (Krohn et al., 2016) and on comets (1P/Halley, 9P/Tempel 1 and 19P/Borrelly; Belton, 2010), ejecta curtain-like deposits on the 9P/Tempel 1 comet (Belton and Melosh, 2009), low–lying and low-albedo smooth surfaces on Europa (Fagents, 2003) and pits from sinkhole collapse in several comet such as Wild2 and 67P comets (Vincent et al., 2015). Outburst may be driven by gas exsolution, in particular CO release (Belton and Melosh, 2009), by post impact heating (Krohn et al., 2016), rapid change of temperatures due to solar heating (Jewitt, 2004; Belton, 2010; Vincent et al., 2016), rapid release of pressure (e.g. cliff collapse) (Vincent et al., 2016; Pajola et al., 2017) or by a subsurface energy source given by the phase transition of amorphous to crystalline ice (Tancredi et al., 1994; Vincent et al., 2015). These models imply that outbursting effects are confined to the surface and subsurface of a planetary body. However outburst might imply brines and volatiles mobilization from depth. On planetary bodies this can be hallowed by endogenic heating due to long-lived radioisotopes (McCord et al., 2011), tidal stress (Neveu et al., 2015) or ascent of liquids and brines due to natural buoyancy (Desch and Neveu, 2017). On cometary bodies mobilization of volatiles is rather due to thermal stress induced by the changing conditions of solar illumination (De Sanctis et al., 2015) or fluidization created by internal pressure of super-volatiles (Belton, 2010). Different types of cometary activity have been proposed (Belton and Melosh, 2009; Belton et al., 2008; Belton, 2010-2017; De Sanctis et al., 2015), all of them involving H_2O, CO and CO_2 as main drivers of jets and outbursts. Cometary outburst may be either a low-intensity widespread sublimation process or localized destructive episodes (Belton, 2010; Vincent et al., 2015-2016; Pajola et al., 2017). The general consensus is that low-intensity process are driven by sunlight (Belton, 2010; De Sanctis et al., 2015) and involve mainly water sublimation, while violent outbursts are due to super-volatiles release induced by internal process and only partially stimulated by illumination (Belton, 2010; Vincent et al. 2015).

The role of rock-ice interactions is still to be clarified. Carbonaceous chondrites (CCs) are the closest icy-bodies analogues. CCs are rich in soluble salts and unstable anhydrous minerals. These minerals can react with water even at low temperatures modifying the composition of the cryomagma, and thus its rheology giving birth to different cryogenic morphologies (domes in case of viscous cryomagma, ejecta-like in case of explosive eruptions in case of viscous and volatile-rich cryomagmas or flows in case of volatile-poor cryomagma) (Kargel, 1991). Hence we carried out laboratory experiments involving CCs and ices to shed light on the mechanism and products of outburst processes in our Solar System showing that sublimation of fine particles begins at temperatures as low as -40°C and are followed by outburst at temperatures between -20°C and -10°C depending on the composition of the ice. Temperature is indeed dependent on ice composition since ammoniated ices sublimate at lower temperatures than deionized water ones. With these experiments we show that outbursting is a main mechanism capable of creating and processing organic matter on icy bodies in our Solar System, being able of generating long chains of aliphatic hydrocarbons.

Our experiments shed light also on one possible mechanism that can remove micrometeorites from their parent bodies. Micrometeorites originate from the asteroid belt (Genge et al., 2008; van Ginneken et al., 2012) and cometary sources (Noguchi et al., 2015), however it is not well

understood the way they are delivered from their parent bodies to Earth. The majority of the micrometeorites with a composition similar to the carbonaceous chondrites (Suavet et al., 2010; van Ginneken et al., 2012; Taylor et al., 2012) are called fine-grained unmelted micrometeorites (Fg-MM) (Genge et al., 2008). However substantial differences between MMs and CCs exist, being MMs particularly enriched in organic matter (Bonal et al., 2019). Our experiments can reconcile this compositional difference if we assume that the majority of the micrometeorites are expelled from their parent bodies via sublimation and outbursts, a process that we have demonstrated is able to enrich the ejected material in the specific organic matter underling the difference between CCs and the analysed Antarctica Fg-MMs.

2. Experimental details

For the experiments we used 5 CCs: FRO99040, FRO90006, FRO95002, DaG521 and MCY14001. FRO99040, FRO95002 and FRO90006 are CO3 chondrites while MCY14001 is a CM2 and DaG521 is a CV3 (Fig. 1) (described also in chapter 4 and in Frattin et al., 2019 in the appendix). The CO3 chondrites have a similar mineralogy and abundant chondrules (~45 vol%) with a mean diameter of 0.2 mm. They are mainly composed of olivine and pyroxene with compositions $Fa_{1\text{-}59}$ and $Fs_{1\text{-}7}$ (enstatitic low-Ca pyroxenes only) respectively. Fe-Ni alloys and troilite are abundant (~5 vol%) as well as CAIs (~10 vol%) containing fassaite, garnets, spinel and melilite. FRO90006 was originally misclassified as a L/LL3. Lately FRO90006 has been reclassified as a CO3 (Folco and Rastelli, 2002), this sample has indeed a magnetic susceptibility of 4.64 compatible with a fresh CO3 sample (Prof. L. Folco personal communication). MCY14001 has a higher content of matrix than chondrules, which are only ~20 vol% with a mean diameter of 0.2 mm. Olivines have fayalite content of $Fa_{0.3\text{-}57}$ and low-Ca pyroxenes and a ferrosilite content of $Fs_{0.6\text{-}5}$. Phyllosilicates are widespread replacing chondrules mesostasis and in the matrix, minor calcite crystals often associated to troilite, FeNi alloys are generally rare. CAIs builds up ~7 vol% of the MCY 14001 meteorite. All the samples show low shock stage (S1-S2) and very low to totally absent terrestrial alteration. DaG521 is a CV3 chondrite and is the only meteorite of our set with reddish colour, probably due to iron oxide generated by weathering in the Lybian desert. For the experiments we powdered the sample and mixed FRO99040, FRO95002 and DaG521 with deionized water and FRO90006 and MCY14001 with ammoniated water (mixtures were around 20-30% water and 80-70% rock) to simulate icy bodies conditions as well as composition since carbonaceous chondrites are the closest analogue of icy-primitive bodies. We put the mixtures in the dryer for ~ 30 minutes to avoid the formation of atmospheric frost and then we froze them at -80°C. Once frozen the mixtures were put in a cup with liquid nitrogen to preserve the temperature and then transferred into the emissivity chamber of the PSL-DLR and heated in vacuum using the induction system. Samples were heated from around ~ -195°C (due to liquid nitrogen) up to 100°C, a temperature range which encompass icy bodies environments (e.g. Ceres surface temperature varies between ~-170°C and ~-70°C (Formisano et al., 2015); 67P/Churyumov-Gerasimenko comet surface temperature ranges between a minimum of ~-170°C to a maximum of ~70°C (Keller et al., 2015; Pajola et al., 2017). The duration of the heating process for each mixture was about 30 minutes. During the experiments, the samples were monitored using a webcam installed in the chamber and a temperature sensor located at the base of the sample holder. Once the experiments finished, we acquired reflectance spectra in the NIR range and compared them with spectra of the original samples acquired before the experiment.

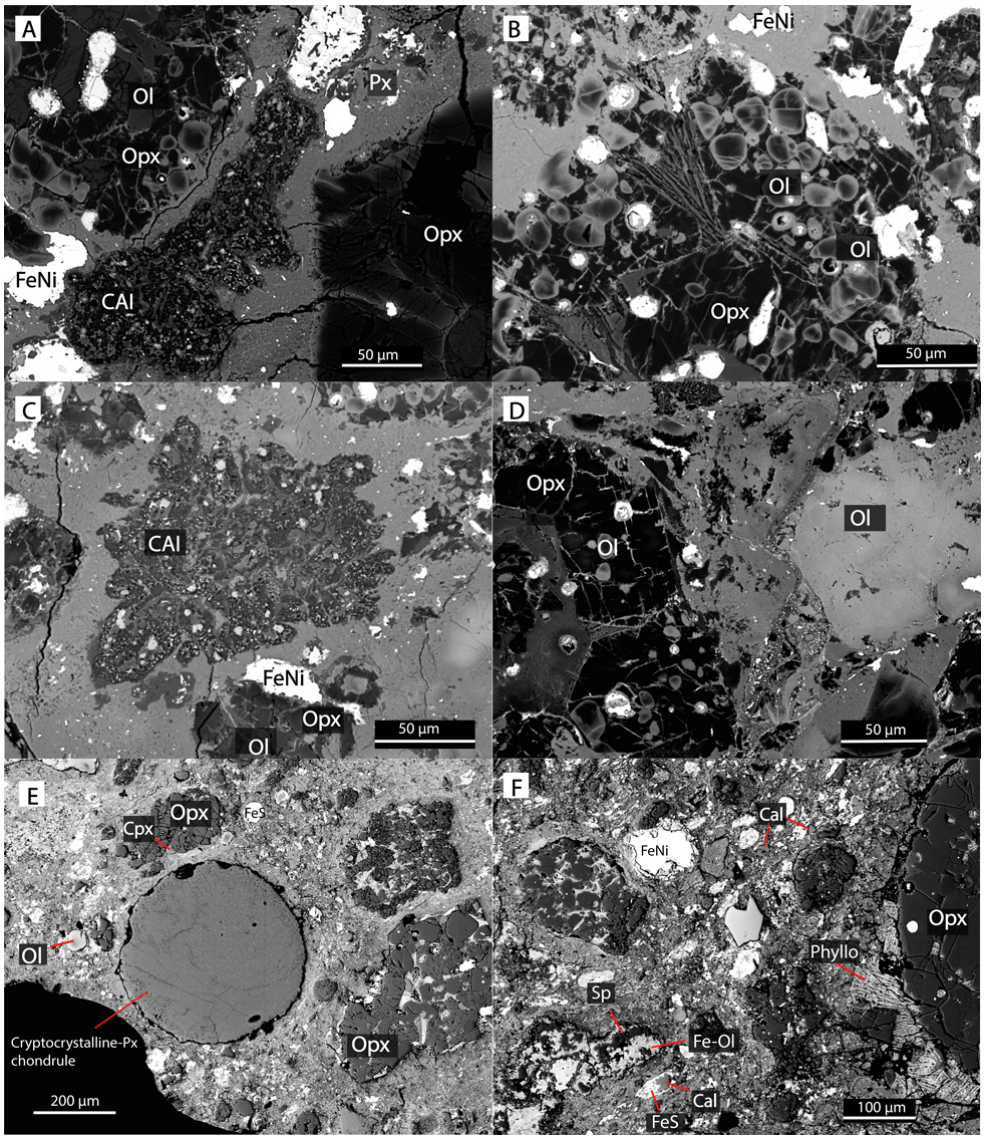

Fig. 1. SEM backscattered images of A-B) FRO99040; C-D) FRO90006 and E-F) MCY14001. Ol=Olivine; Opx=orthopyroxene (Low-Ca pyroxene); Cpx=clinopyroxene; FeNi=metal alloys (kamacite-taenite); CAI=Calcium-Auminium inclusions; Cal=calcite; Phyllo=phyllosilicates; FeS=troilite; Sp=spinel.

3. Results

3.1. Experiment results

During the heating process the samples started sublimating fine particles at T~ -40°C. Between around -20°C and -10°C MCY14001, FRO99040 and FRO95002 also experienced a violent episode of outburst, after which sublimation of fine particles ceased. In particular FRO99040 showed a localized outburst in a circular area of the sample (Fig. 2), leaving a crater-like morphology, while MCY14001 and FRO95002 experienced a more catastrophic outburst that affected the entire samples and didn't left any particular structure. A violent outburst was not observed during FRO90006 and DaG521 heating, which only ejected fine particles. The sublimation gradually decreased and stopped once ice was completely exhausted. The ejected outgassed powders of FRO90006, FRO99040, FRO95002 and DaG521 always show absorption bands at 3.4 µm and 3.5 µm while in the original unprocessed powders and on the powders that remained in the sample holder (sublimated powders) this feature is not found (Fig. 3). FRO95002 and DaG521 show absorption bands at 3.4 and 3.5 µm after the experiments in the ejected powders like in the case of FRO99040 and FRO90006 (Fig. 4). In addition

in FRO95002 the 3.4-3.5 µm features appear also in the sublimated powders (Fig. 4). Ejected powders of MCY14001 still show the absorption at 3.4 µm and 3.5 µm, but much less prominently than on the other four samples (Fig. 3). As already known from literature, these absorption bands can be ascribed to the symmetric and antisymmetric stretching frequencies of methyl (-CH_3) and methylene (-CH_2-) functional groups, characteristic of hydrogenated sp^3 carbon (Orthus-Daunay et al., 2013; De Sanctis et al., 2017). Therefore, GC/MS analyses were conducted on FRO99040, FRO95002 and DaG521 to identify and quantify the possible presence of saturated aliphatic hydrocarbons (*i.e. n*-alkanes). Such analyses showed that there are some differences between the ejected powders (hereafter _EJ), hence more closely related to the outgassing event, and the non-ejected lag part, which experienced sublimation (here after _SB). In particular, in FRO99040_EJ appears a new aliphatic hydrocarbon at a relatively high concentration (4510 ng g^{-1}): the heptadecane ($C_{17}H_{36}$), which is not present in FRO99040_SB and in the pristine original FRO99040 (Fig. 5). In addition, in FRO9940_EJ other two aliphatic hydrocarbons, nonadecane ($C_{19}H_{40}$) and henicosane ($C_{21}H_{44}$), were found in quantities one order of magnitude higher than in FRO99040_SB, (i.e. 221 and 31 ng g^{-1} vs 1386 and 183,1 ng g^{-1} respectively) (Fig. 5), whereas in the original FRO99040 the same *n*-alkanes are absent or eventually lower than the instrumental detection limits (thus excluding any biological or terrestrial contamination). In FRO95002 and DaG521, as expected from the spectral features acquired after the experiment showing 3.4 and 3.5 µm bands in all the powders, the three compounds heptadecane, nonadecane and henicosane have been detected in both the ejected and sublimated powders, whereas they were absent in the pristine ones. As previously observed, in FRO95002 the *n*-alkanes found in the sublimated powders clearly increase in FRO95002_EJ, doubling their concentrations, while 112.5 and 267.2 ng g^{-1} of docosane ($C_{22}H_{46}$) were found in FRO95002_SB and FRO95002_EJ powders respectively. Lastly, in both experiments traces of undecane ($C_{11}H_{24}$) and pentadecane ($C_{15}H_{32}$) were detected in the original CC powders. Irrespective of their origin, that can be ascribed to terrestrial or handling contamination as well as to an endogenous origin, their behavior follow the same trend of the other compounds and strongly increase in the sublimated and (for FRO95002) ejected powders (Fig. 5).

Another aspect to take into account is the change in the reflectance of the different sample powders. MCY14001 reflectance doesn't change in the 3 powders. FRO90006 reflectance substantially decreases in the ejected powders while on the contrary FRO99040 and FRO95002 reflectance increases in the sublimated and ejected powders. The reasons for these changes are likely related to either grain size or to the fact that sublimated-ejected powders are less mixed with the original dark matrix (these powders have been physically separated from the lag powders). However the reflectance changes do not follow a common path, the reason for this different behavior remains unsolved and needs to be investigated with further analyses.

3.2. CCs and Fg-MMs spectroscopy results

CCs and Fg-MMs show substantial differences in their spectra (fig. 7). As shown in figure 7 CCs spectra have a deep (0.1-0.5 band depth) and wide 2.7-2.8 µm band related to Mg-OH bonds and between 2.9 and 4 µm are almost featureless with only shallow 3.4-3.5 µm organic matter bands (< 0.01 band depth). On the contrary Fg-MMs show systematically bands at 3.4 µm ranging from ~3.35 µm and ~3.42 µm and at 3.5 µm that shifts between ~3.47 and ~3.5 µm. Only MCY14001 has an absorption at 2.9 µm, probably also related to hydrated minerals, and around 3.9 µm due to carbonates.

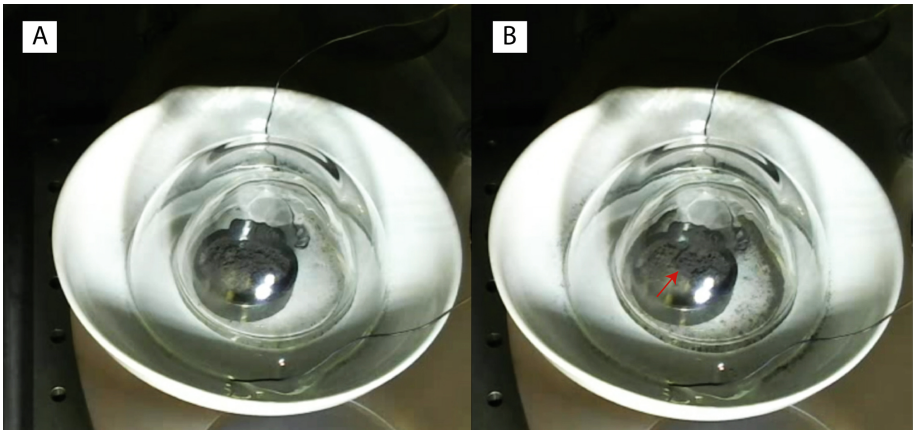

Fig. 2. Localized outburst with the creation of a crater-like rounded morphology (indicated by the red arrow). A) Before the outburst; B) after the outburst. Close to the border of the transparent cups sublimated and outbursted powders can be seen.

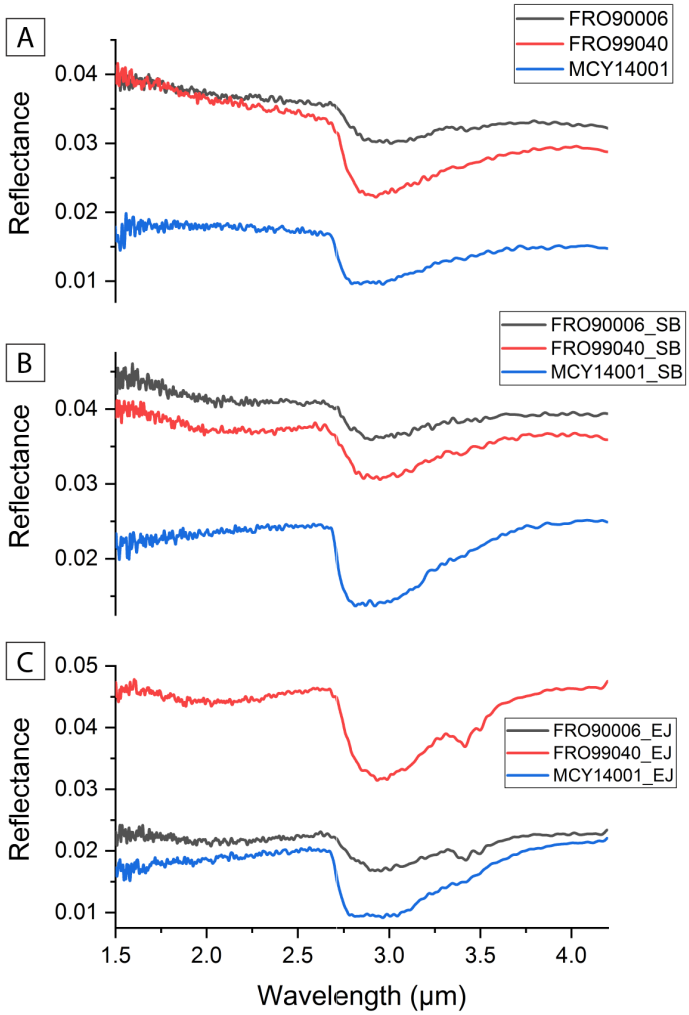

Fig. 3. IR reflectance spectra of A) unprocessed samples; B) sublimated powders (SB) and C) ejected powders (EJ).

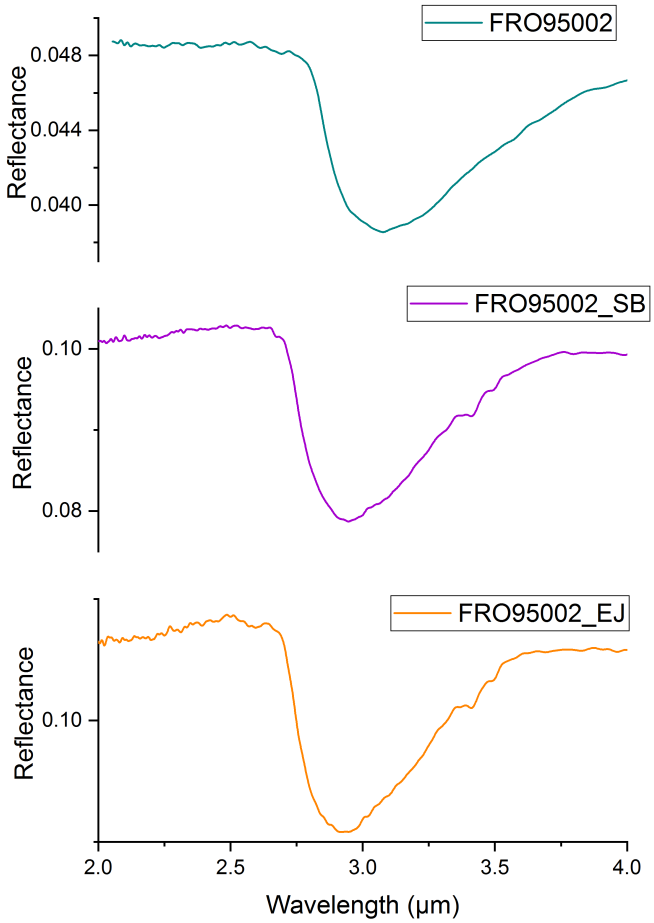

Fig. 4. IR reflectance spectra of FRO95002 used to replicate the experiments for confirmation of the results. FRO95002 are the non-processed original powders, SB sublimated powders and EJ ejected powders.

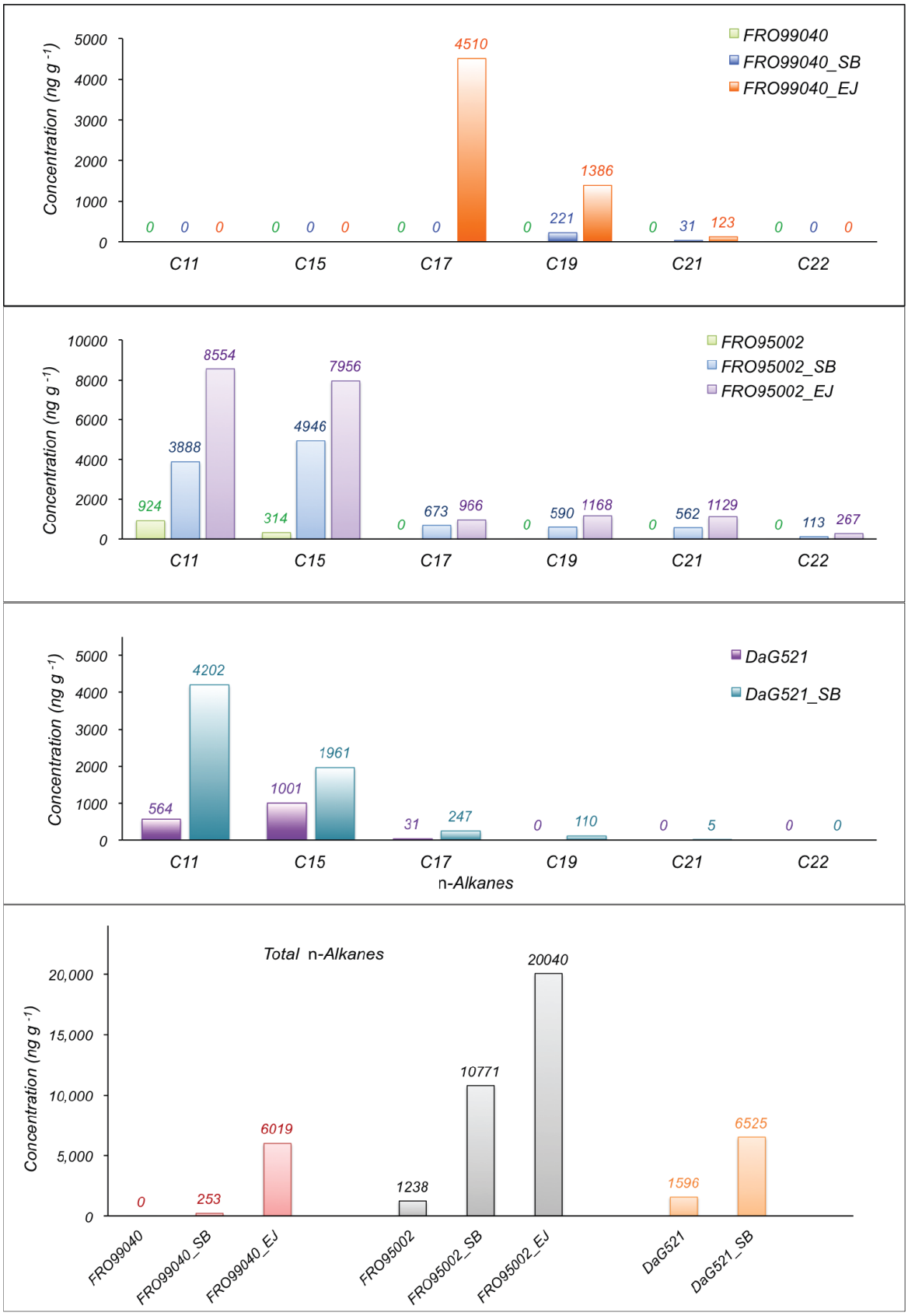

Fig. 5. GC/MS data showing abundance of undecane - $C_{11}H_{24}$, pendadecane - $C_{15}H_{32}$, heptadecane - $C_{17}H_{36}$, nonadecane - $C_{19}H_{40}$, henicosane - $C_{21}H_{44}$ and docosane – $C_{22}H_{46}$ in powders of pristine original meteorites: A) FRO99040; B) FRO95002; C) DaG521, their sublimated powders (_SB) and ejected ones (_EJ). Finally total n-alkanes concentration for the original, sublimated and ejected chondrite powders are reported.

4. Discussion

4.1. Formation of aliphatic hydrocarbons via sublimation and outburst

The analytical results exclude by themselves any kind of contamination. The organic species ratios in figure 6 strongly support their petrogenic origin, it is thus reasonable to think that organics are derived from meteorites only. In addition other evidences suggest that no contamination: 1) sublimated and ejected powders were treated exactly in the same way, if contamination occurred we would expect to find it in both samples, which is not found; 2) ejected powders of MCY14001 barely show 3.4 µm and 3.5 µm bands contrary to the prominent ones on the other four samples, again if contamination occurred we would expect it to be equal in all samples; 3) n-alkanes ratios indicate a petrogenic source as shown in figure 6, thus coming from the meteorites only.

Hence with our experiments we have found a process capable of creating aliphatic hydrocarbons through outbursting, which on planetary and minor bodies is induced by cryovolcanism and sublimation induced by solar irradiation. Organic Material (OM) with related absorption bands at ~3.4 µm has been indeed found in different Solar System bodies: 67P/Churyumov-Gerasimenko, Ceres, 24 Themis, 65 Cybele, Phoebe, Iapetus and Enceladus (De Sanctis et al., 2017 and references therein). OM is also found in CCs (Sephton et al., 2002), in particular presence of n-alkanes in the C_{15}-C_{27} range has been reported by Kissin (2003) (however this is not the case of the chondrites we studied, which do not originally contain such alkanes). The origin of the OM is not clear, but it is now widely accepted that modifications of OM in icy bodies is related to internal processes, such as hydrothermal activity or relative low-temperature aqueous alteration (Schulte and Shock, 2004 report a temperature range between 2-250°C, while Vinogradoff et al., 2017 infer a temperature lower than 100°C). In high-temperature environments (~250°C) both short-duration (10 s; Yabuta et al., 2010) and long-duration (week-long and more; Wang and Lipschutz, 2010) heating have been invoked for the formation of organics (Orthus-Daunay et al., 2013). At low-temperature (20-50°C), a short-duration shock heating producing minimal alteration, local melting of cometary ice and organics dissolution was proposed for the formation of UltraCarbonaceous Antarctic Micrometeorites (UCAMM) (Yabuta et al., 2017). Another post-accretional process affecting organics, proposed for the 67P/Churyumov-Gerasimenko comet, is the solar irradiation of ices or the polymerization of mixtures of ices (water ice, methane ice and nitrogen ices) at low temperatures (which vary in relation to the ice composition) (De Bergh et al., 2008). Our experiments favour a low-temperature of formation of OM and a short-duration heating event, created by cryovolcanism or solar irradiation, inducing sublimation and outbursting of fine particles. Indeed, outgassing of particles started at T ~ -40°C with an explosive event in a temperature range between -20°C and -10°C. Considering that on icy-bodies brines and salts capable of lowering the melting point of a liquid are also involved in cryovolcanism (Kargel et al., 1991; Neveu et al., 2015), these temperatures may be even lower. For example on the 67P comet the most active areas have a temperature of ~-63°C (Keller et al., 2015; De Sanctis et al., 2015). In fact the MCY14001 sample, mixed with ammoniated water ice, experienced the outburst at a temperature 10°C lower than FRO99040, FRO95002 and DaG521 mixed with deionized water ice. We discard high temperature formation even though in our experiment we raised the temperature up to 100°C. In fact, sublimated and ejected powders were processed under the same conditions and only ejected powders have very high concentration of aliphatic hydrocarbons, thus, formation of aliphatic hydrocarbons must be related to sublimation and outburst that took place between -40°C and -10°C. Furthermore the shallow 3.4 and 3.5 µm band in the MCY14001 sample compared to the prominent ones in FRO99040, FRO90006, FRO95001 and DaG521 suggest that the primary mineralogies play an important role on the formation of

organics, while the composition of the fluid (deionized water versus ammoniated water) does not seem to strongly affect the formation of aliphatic hydrocarbons. Pressure also has a crucial role. We worked in vacuum (10^{-4} bar) to reproduce the surface conditions of minor bodies of the Solar System. In vacuum ice sublimates and melts at lower temperatures. For this reason we infer that outbursts and formation of aliphatic hydrocarbons via outbursting at temperatures below zero can only happen on planetary bodies with weak atmosphere, thus low pressure, if not any. Higher pressure would however facilitate the formation of hydrocarbons, but at the same time would inhibit sublimation at temperatures below 0°C.

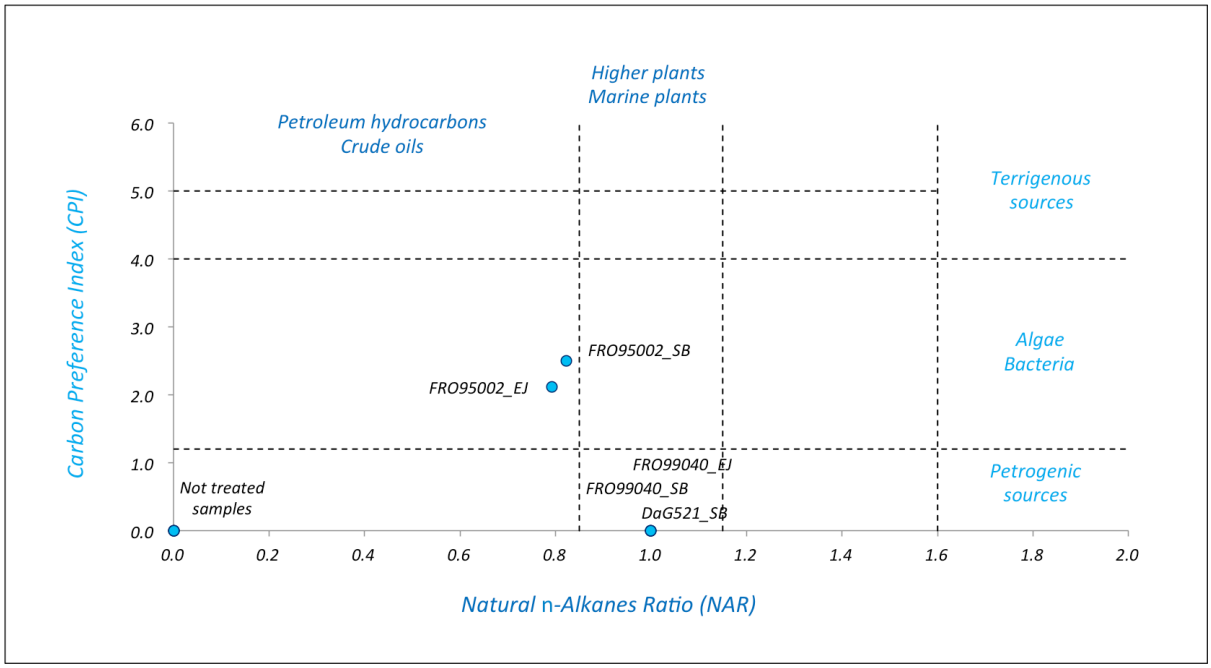

Fig. 6. Origin and sources of *n*-alkanes . Distribution of CPI/NAR ratio for powders of carbonaceous chondrites. CPI = Carbon Preference Index); NAR = Natural *n*-Alkane Ratio.

4.2. Mechanism of formation and enrichment of hydrocarbons

Although further studies are needed to fully understand the reaction mechanism, there are the thermodynamic conditions for the hydrocarbon formation to take place. The basic reagents can be supplied from the rocky substrate of the CCs (carbon) and from the ice (hydrogen), which can be joined in reducing atmosphere such as that present inside our reactor. Furthermore, given the presence of CAIs and Fe-Ni alloys providing elements such Fe-Ni-Al, we cannot exclude the possibility that such components work as catalysts in the syntheses of organic species like *n*-alkanes. By increasing the temperature, some alkanes might have formed (*i.e.* nonadecane and henicosane), probably in concentrations that are too low to be visible in the NIR spectra. Forcing the reaction conditions until reaching the sublimation and outburst, the concentrations of $C_{19}H_{40}$ and $C_{21}H_{44}$ increased considerably and the thermodynamic conditions that allow the formation of heptadecane are reached. The reaction mechanism appears to be well-ordered and strongly directed to the formation of odd-chain compounds, thus in contrast with a Fischer-Tropsch-like process, often suggested in literature as the possible formation process of aliphatic hydrocarbons (Hayatsu and Anders, 1981). Indeed, the Fischer-Tropsch reaction mechanism would lead to the formation of even- and odd-carbon chains with the same degree of probability and, therefore, to a mixture of them. The reaction also seems to show a certain shape-selectivity, given the formation of only

alkanes at 17, 19 and 21 carbon atoms, perhaps related to the crystalline structure of the meteorite and/or the high porosity of CCs. Indeed, the dimension of the unit cells can act selectively as a trap for molecules of a certain lengths, whereas short-chain alkanes are more volatile can disperse within the reaction system. Determining the dimension of long chain aliphatic hydrocarbons is not straightforward since they tend to bend and roll. However, the heptadecane has a theoretical linear dimension around 24.64 Å, nonadecane around 27.72 Å and henicosane around 30.80 Å. Among the most common minerals in the CCs, antigorite has the *a* dimension of the unit cell that can reach 40 Å and clay minerals like vermiculite has the *c* direction of 29 Å. Kamacite also has a quite big unit cell with a *b* direction that can be as big as 54 Å. These minerals can accommodate and trap the *n*-alkanes, in particular vermiculite and kamacite also provide high quantities of Fe and Al, good catalysts of the reaction. Experimental evidences from FRO95002 and DaG521 lead to the same hypothesis formulated for FRO99040 experiment with the exception for the even-carbon chain of the docosane detected in the FRO95002 powders, which in any case have dimensions comparable to that of the other odd-carbon chains. Nevertheless, many important questions still remain unanswered, especially considering that in literature bacteria, algae and fungi are listed as the main producer of *n*-alkanes in the range C_{14}-C_{22} and in particular, heptadecane is generally considered to be a biomarker indicator for algae and photosynthetic bacteria (Han and Calvin, 1969; Grimalt and Albaiges, 1987; Ficken et al., 1998; Aichner et al., 2010). Thus the detection of such *n*-alkanes on planetary hydrous bodies can be used as a very important biomarker and can provide considerable advantages in the astrobiology research.

4.3. Implications for planetary and minor bodies

Our findings on the relationship between cryovolcanism-sublimation-outbursting and organics can be applied on many bodies of the Solar System. Indeed outbursts by sublimation were seen on different cometary nuclei (i.e. 29P/Schwassman-Wachmann (Miles, 2016), 9P/Tempel-1 (Belton and Melosh, 2009) and 67P/Churyumov-Gerasimenko (Vincent et al., 2016)) where organics have been detected (Soderblom et al., 2002; A'Hearn et al., 2011; Capaccioni et al., 2015; Fray et al., 2016). The only analogue materials suggested for Cometary organics have been coals, bitumens and aliphatich-rich tholins (Filacchione et al., 2019), but our findings imply that specific aliphatic C_{17}, C_{19} and C_{21} alkanes species are very likely present (in addition to other oganics) on cometary nuclei because derived by volatile driven outburst and sublimation triggered by either sunlight or endogenous heat. Comets have always been considered as unaltered bodies with remnants of pre-solar materials (Mumma and Charnley, 2011; de Niem et al., 2018). As a consequence, organics on comets are thought to derive directly from the Solar Nebula with no post-accretional processing (Mumma and Charnley, 2011). On the contrary, our findings provide evidences that not all the organics on comets are pristine materials inherited from the Solar Nebula since cometary activity can produce newly formed organics even at low temperatures and without significant heating and metasomatism.

On dwarf planets and asteroids cryovolcanism and organics are closely related. For example high concentration of organics on Ceres were found on a restricted area near the Ernutet crater (De Sanctis et al., 2017-2019). These organic compounds are randomly scattered around the crater without a clear association to morphology, however these molecules are thought to derive from a not well understood endogenous activity (De Sanctis et al., 2017-2019). Our results perfectly fit in this scenario. Aliphatic-rich material on Ceres might indeed derive from an outburst due to a pocket of mixed ice-fine particles below the Ernutet crater. In addition, the whole composition of Ceres is rich in organics (less than the aliphatic-rich area of Ernutet, but higher than the average

concentration of organics in meteorites) (De Sanctis et al., 2019; Marchi et al., 2019). Water vapour has been found around Ceres, probably derived by a comet-like sublimation (Küppers et al., 2014). Such sublimation could be the main process that created the high amount of organics, as suggested by our experiments. It is interesting to notice that this sublimation on Ceres is confined at the mid-latitudes and the majority of the heat is probably due to insulation (Küppers et al., 2014). These areas and the equatorial ones are the smoothest on Ceres. This suggests that the equatorial and mid-latitudes areas were resurfaced by sublimation and at the equatorial area, where temperatures are higher, surface-subsurface ice available for sublimation is already exhausted. We thus also expect an enrichment of organics towards the equator and depletion at the poles, where sublimation is minimal or absent. The case of Ernutet also suggests that ice pockets have a heterogeneous distribution.

Our results do not only apply to Ceres. For example on the C-type asteroid 24 Themis ice and organics have been found and steady-state outgassing have also been proposed, even though clear evidence of outgassing were not found (Rivkin and Emery, 2010). Indeed 24 Themis has the right ingredients (carbonaceous composition and presence of ice) to create the detected organics via sublimation. We can thus extend the organic genesis from comet-like sublimation even to minor bodies of the Solar System, contributing to blurry the line between asteroids and comets.

However on planetary bodies expressions of cryovolcanism are not often clear. For example on 1P, 9P and 19P there are no clear association between outbursts and topography (Belton, 2010). The same is true for the case of Ceres (De Sanctis et al., 2017). In these cases our results can be used the way round. In fact high abundances of organics may be tracers of cryovolcanic-sublimation processes.

4.4. Sublimation: a mechanism for micrometeorites delivery

As described in paragraph 3.2, MMs have 3.4-3.5 µm bands much deeper than those of the CCs, indicating strong organic matter enrichment. Up to the 50% of the incoming micrometeorite flux have oxygen isotopic compositions related to the CO/CV/CK anhydrous supergroup (Suavet et al., 2010) and the majority of the micrometeorites income flux has a mineral composition related to the carbonaceous chondrites (van Ginneken et al., 2012; Taylor et al., 2012). However, substantial differences between CCs and Fg-MMs exist. Differences regard hydration state, mineralogy and especially the organic matter abundances and composition (Bonal et al., 2019). In particular, Fg-MMs are enriched in organic matter (Bonal et al., 2019). Bonal et al. (2019) showed that heating during atmospheric entry can lower the organics concentration and can dehydrate the micrometeorites. The Fg-MMs we studied record very low atmospheric entry modification, deduced especially by the prominent 2.7-2.8 µm bands (fig. 7). These are hydration bands that tend to disappear if thermal modifications happened. Fg-MMs have much deeper absorption bands (0.03-0.05 band depth) around 3.3-3.4 and 3.5 µm compared to the ones of CCs (<0.01 band depth). Some CCs spectra don't have organics absorption bands at all. Band centres varies between ~3.35 µm and ~3.42 µm and between ~3.47 and ~3.5 µm. This attests to compositional differences of the parent bodies as also suggested by Bonal et al. (2019). Our experiments also suggest that different starting compositions result in different organics compositions and abundances. In particular this is proven by the MCY14001 sample, which have very shallow 3.4-3.5 µm bands compared to the ones of FRO99040, FRO90006, FRO95002 and DaG521. Concluding, our findings can also explain the organic matter enrichment and composition of Fg-MMs. In fact, sublimation and outburst are possible mechanism capable of expelling micrometeorites from their parent bodies and deliver them to

Earth. At the same time this process creates organic matter, explaining the OM-rich composition of Fg-MMs.

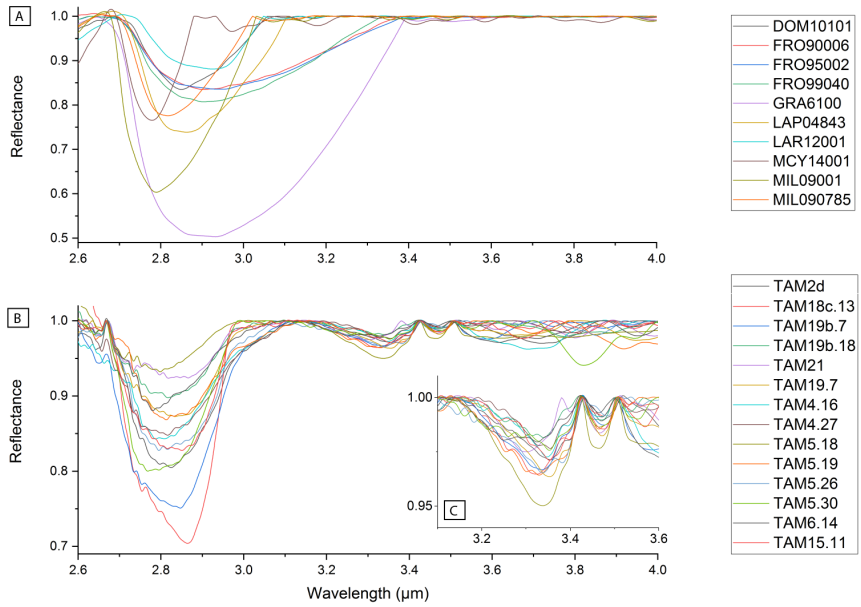

Fig. 7. Continuum removed IR reflectance spectra of carbonaceous chondrites and fine-grained micrometeorites. A) IR spectra of CCs. 3.4-3.5 μm band of organics are almost absent. 2.8 μm hydration bands are in turn very prominent. B) IR spectra of Fg-MMs. 3.3-3.4 μm and 3.5 μm bands related to organic matter are always present. These absorptions have a band depth higher (0.03-0.05) than that of CCs (<0.01 when present). 2.8 μm hydration band is also present. C) Zoomed in spectra of Fg-MMs in the 3.1-3.6 μm region.

5. Conclusions

With this work we demonstrate hydrocarbons formation during post-accretional processing. Aliphatic hydrocarbons may form during very short duration sublimation-outburst processes. Temperatures of formation can be as low as -40°C. A precise mechanism of formation is difficult to describe with the current knowledge. The carbon is provided by the CCs, hydrogen by the ice and a reducing environment, consistent to that of airless minor bodies, is required. It is likely that there is a relation between *n*-alkanes and the mineral structure dimensions of mineral such antigorite, vermiculite and probably also FeNi alloys, which can act as a trap for the organic molecules and also provide catalyst elements (Fe-Ni-Al). These findings are very important for the understanding of Cometary composition as well as that of C-type asteroids, dwarf planets and icy bodies of the Solar System. A very important advance we bring is the evidence that on comets organics are not only remnants of the Solar Nebula, but cometary activity can itself create new organic species. On bodies like Ceres and Themis sublimation-outburst can explain the organic-rich composition without involving exogenous carbonaceous-like material. Furthermore organics detection is a useful way to find possible cryovolcanic activity on those bodies or areas where cryovolcanic surface expressions are absent. Presence of cryovolcanism is in turn evidence of the presence of water on a variety of Solar System bodies such as asteroids, dwarf planets satellites and comets. Presence of water coupled with the fact that *n*-alkanes in the C_{14}-C_{22} range are used as tracers of photosynthetic

bacteria makes the long chain aliphatic hydrocarbons produced by sublimation-outburst possible biomarkers, which can be useful for astrobiology researches. Finally, sublimation-outburst processes are a possible mechanism for fine grained micrometeorites expulsion from the parent body, explaining at the same time the high organic matter concentration in Fg-MMs compared to the CCs.

Chapter 6

Hydrothermal experiments on the MCY14001 CM2 and FRO95002 CO3 chondrites with H_2O and ammoniated-H_2O - close affinities with Ceres-like asteroids

Abstract

We investigate the hydrothermal alteration of minor bodies of the Solar System carrying out experiments on two carbonaceous chondrites (CCs): CO3 FRO95002 and CM2 MCY14001. After being powdered the two CCs were put in two distinct autoclaves with different water to rock ratios (W/R) and different fluid compositions to simulate two distinct scenarios. In particular FRO95002 was mixed with deionized water with W/R=0.1 and MCY14001 with ammoniated water with W/R=1. Both the samples were heated at 240°C for two months. Mineralogical changes were studied by taking IR reflectance spectra and carrying out XRD analyses before and after the experiments. FRO95002 altered powders did not show major changes except a dehydration revealed by the loss of the 2.7 µm hydration band and of hydrotalcite. On the contrary MCY14001 IR spectrum reveals a 2.9 and 3.03 µm bands in the altered powders, indicative of an ammoniation process, mainly of serpentine (the only phyllosilicate present in the sample) and of the newly formed analcime-natrolite crystals. MCY14001 went indeed through substantial mineralogical changes reflecting the changing environment conditions during the experiment from oxidizing to reducing. We report the formation of magnetite during an initial oxidising phase. As the oxygen was consumed a second reducing alteration phase followed, characterized by the formation of sulfides (pentlandite and pyrrhotite). Na-carbonates and hydrotalcite were completely leached releasing Na and Al that contribute to the formation of ammoniated analcime-natrolite. The carbon released by leached Na-carbonates forms calcite and magnesite during the oxidising phase and aromatic hydrocarbons when the environment became reducing. Finally we report the formation of Fe-enstatite and diopside, suggesting that silicates are enriched in Ca and Fe during fluid assisted thermal metamorphism at temperatures around 250°C. These results give important insights in the composition of Ceres-like C-type asteroids, suggesting that these bodies went through a period of strong hydrothermalism with the ammoniation of serpentine and creation of other ammoniated phases like analcime-natrolite at the expanses of Na-rich phases such as Na-carbonates that we're detected in several bright spots on Ceres (e.g. of Occator and Haulani craters).

1. Introduction

The composition of C-type Ceres-like asteroids is still a debated topic. One of the main difficulties is due to the lack of analogue samples among the meteorites collections. C-type asteroid composition is similar to that of carbonaceous chondrites (CCs) (McCord and Gaffey, 1974), however these pristine materials went through different secondary processes on the parent body, the major one being hydrothermal alteration (Grimm and McSween, 1989; Krot et al., 1998-2005). Hydrothermal activity on CCs parent bodies is generated by impact and mostly by decay of ^{26}Al and ^{40}K that heat a pristine homogeneous mixture of ice and rock (Grimm and McSween, 1989; Castillo-Rogez et al., 2008). Evidences of hydrothermal alteration is widely recognised in CV chondrites, where secondary mineral assemblages like fayalite-andradite/grossular-diopside/hedenbergite-magnetite has been detected (Krot et al., 1998). Hydrothermal experiments on CCs to investigate mineral changes have

been already done by Nomura and Miyamoto 1998; Jones and Brearley, 2006; Palmer and Lauretta, 2011. Nomura and Miyamoto (1998) made experiments on typical CAIs minerals such as gehlenite, spinel and diopside discovering that most of the secondary minerals in CAIs are produced by alteration of gehlenite. In particular, gehlenite releases Ca-Al-Si (Nomura and Miyamoto 1998), Ca reacts with CO_3 in the fluids to produce calcite and Na (mainly from the mesostasis), Al and Si (from both gehlenite and mesostasis) react to crystallize hydrated nepheline and sodalite, and analcime (Nomura and Miyamoto 1998). If CO_3^{2-} is absent also hydrogrossular can crystallize (Nomura and Miyamoto 1998). Jones and Brearley (2006) made experiments on the CV3 Allende at 100-150-200°C with water/rock (W/R) ratios between 1:1 and 9:1 showing that Ca-Mg salts are the first phases affected by alteration. With increasing alteration Fe-olivines are replaced with interlayered serpentine-saponite and Fe-oxy-hydroxides assemblages (Jones and Brearley, 2006). The FeNi alloys (i.e. kamacite-taenite), one of the main constituents of CCs, follow an alteration path in presence of fluids based on the S and Si activity (Palmer and Lauretta, 2011). In case of a high activity of S kamacite alters into tochilinite, P-sulfides, eskolaite and schreibersite (Palmer and Lauretta, 2011), whereas with high Si activity kamacite turns into sulfide-bearing cronstedtite. In case of low S and Si activity altered kamacite crystallizes magnetite (Palmer and Lauretta, 2011).

It is also widely accepted that the dwarf planet Ceres experienced a long period geothermal aqueous alteration (Neveu et al., 2015; Hendrix et al., 2016), which caused the ammoniation of some mineral phases, in particular phyllosilicates (De Sanctis et al., 2015). On Earth ammoniated minerals occur in proximity of hydrothermal or metamorphic zones within organic-rich host rocks (Krohn et al., 1993; Beran et al., 1992; Sucha et al., 1998; Nieto, 2002; Ruiz Cruz and Sanz de Galdeano, 2008) and ammonia is found mainly in the phyllosilicate lattice, in the interlayer site or adsorbed (Ehlmann et al., 2018). In meteorite samples ammoniation has never been found as a natural product, making the study of this process particularly difficult. Some ammoniation experiments runned at room temperature and for the very short time of 72 hours showed that the main minerals that can be ammoniated are smectites, in particular Mg-saponite (Ehlmann et al., 2018; Ferrari et al., 2019). These experiments however failed to recreate ammoniation of serpentine, which is the main phyllosilicate in CCs and thus on C-type asteroids. However, ammoniated micas are known to exist in nature (Nieto, 2002; Ruiz Cruz and Sanz de Galdeano, 2008) and probably ammoniation of other phyllosilicates is possible with higher temperatures or pressures or for longer exposure to hydrothermal alteration (Ferrari et al. 2019). For these reasons we performed hydrothermal experiments on two CCs (the CO3 FRO95002 and the CM2 MCY14001) at 240°C and the samples were left to react into two distinct autoclaves for two months. We also used two distinct fluids composition (deionized water and ammoniated water) and two different W/R ratios to investigate the role of different fluids. We show that serpentine ammoniation is possible at higher temperature and long lasting experiments. We also give further insights on hydrothermal processes with the evidence of alteration of Na-carbonates into Na-ammoniated phases like analcime-natrolite, and discuss the implications of our findings for minor bodies like Ceres.

2. Experimental setup

For the experiments we powdered the FRO95002 and MCY14001 meteorites. The powders of FRO95002 were mixed with deionized water into an autoclave. The water to rock ratio (W/R) of this mixture was 0.1. The MCY14001 samples was also powdered and mixed with ammoniated water with W/R=1 and put in a distinct autoclave. We put the two mixtures in an oven and heated at 240°C for nearly two months. The initial oxygen fugacity was the same of that of the Earth atmosphere (i.e.

at the beginning of the experiment the environment was oxidising) and during the alteration process we had no control on the oxygen fugacity and on the pH. We decided to use two very different W/R ratios as well as fluid composition to have two end members as different as possible. The temperature choice is based on the average temperature inferred for fluid assisted thermal metamorphism on minor bodies (Krot et al., 1998; Keil 2000; Travis and Schubert, 2005). In particular 250°C was the autoclaves safe temperature indicated by the manufacturer, so for safety reasons we decided not to excessively approach that temperature.

3. Results

3.1. Petrography and mineral composition

The FRO95002 (fig. 1A-B) chondrite is a CO3. It has abundant chondrules (~45 vol%) with a mean diameter of 0.2 mm. The two major phases are olivine, with composition $Fa_{1\text{-}59}$, and pyroxene with composition $Fs_{1\text{-}7}$ (enstatitic low-Ca pyroxenes only). Fe-Ni alloys and sulfides, like troilite and pyrrhotite, are abundant (~5 vol%) and also CAIs (~10 vol%). The main constituents of CAIs are fassaite, garnets, spinel and melilite. In addition, XRD analyses indicate that in FRO95002 there are also minor quantities of nepheline and sodalite (fig. 2). Nepheline and sodalite are record of minor mild temperature aqueous alteration (Krot et al., 1998; Nomura and Miyamoto, 1998; Krot et al., 2005), but no phyllosilicates have been detected. MCY14001 is a CM2 chondrite (fig. 1C to F) and has a higher content of matrix than chondrules, which are only ~20 vol% with a mean diameter of 0.2 mm. The content of fayalite in olivines is $Fa_{0.3\text{-}57}$ and ferrosilite in low-Ca pyroxenes $Fs_{0.6\text{-}5}$. MCY14001 has a composition more heterogeneous than FRO95002, being clinoenstatite and Fe-olivines also present (fig. 1C-D). Phyllosilicates are widespread replacing chondrules mesostasis and in the matrix (fig. 1F). XRD revealed that the phyllosilicates are mainly serpentine (fig. 3). Calcite crystals are also found and are often associated to troilite (fig. 1E). Calcite crystals are not the only carbonates found since XRD shows that Na-carbonates (i.e. natron) are also present in MCY14001 (Fig.3). FeNi alloys are generally rare. CAIs constitute around the 7 vol% of the MCY14001 meteorite. Finally, hydrotalcite has been detected with XRD as an additional hydrated phase in both FRO95002 and MCY14001. All the samples are pristine since secondary processing like shock stage and terrestrial alteration are very low, more precisely the shock stage recorded is S1-S2.

After the experiments bulk XRD analyses shows different alteration histories of FRO95002 and MCY14001. During FRO95002 alteration no substantial changes were seen being the main one a loss of hydrotalcite (fig. 2). On the other side, in the alteration process of MCY14001 several changes have been highlighted by the XRD analyses. Magnetite, pyrrhotite and pentlandite form as new phases (fig. 4A). Furthermore in the altered MCY14001 Na-carbonates and hydrotalcite disappear and are replaced by Na-phases, likely analcime-natrolite (fig. 4B). Finally Fe-enstatite and diopside also crystallize during the alteration process (fig. 4C).

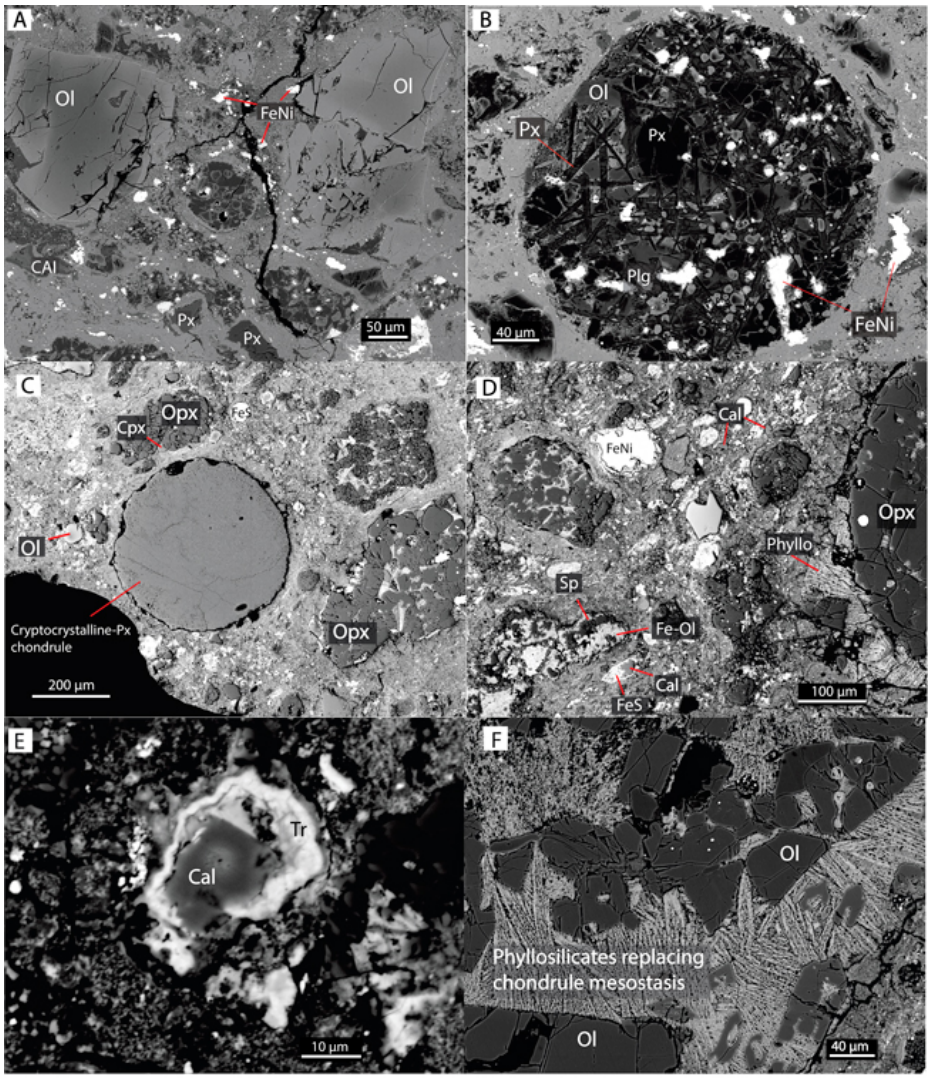

Fig. 1. SEM backscattered images of A-B) FRO95002; C to F) MCY14001. Ol=Olivine; Opx=orthopyroxene (Low-Ca pyroxene); Cpx=clinopyroxene; Px=pyroxene; FeNi=metal alloys (kamacite-taenite); CAI=Calcium-Auminium inclusions; Cal=calcite; Phyllo=phyllosilicates; FeS=troilite; Sp=spinel; Plg=plagioclase.

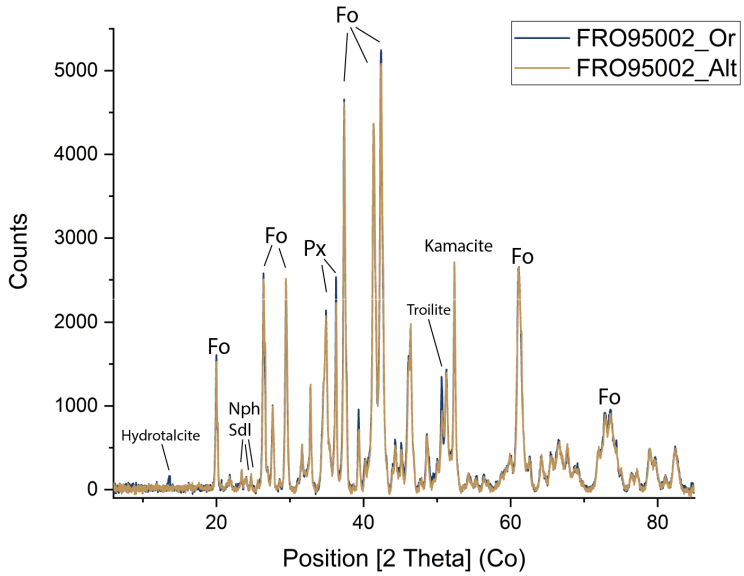

Fig. 2. XRD pattern of FRO95002 original powders (FRO95002_Or) compared to the XRD pattern of the altered ones (FRO95002_Alt). Fo=forsterite; Px=pyroxene; Nph=nepheline; Sdl=sodalite.

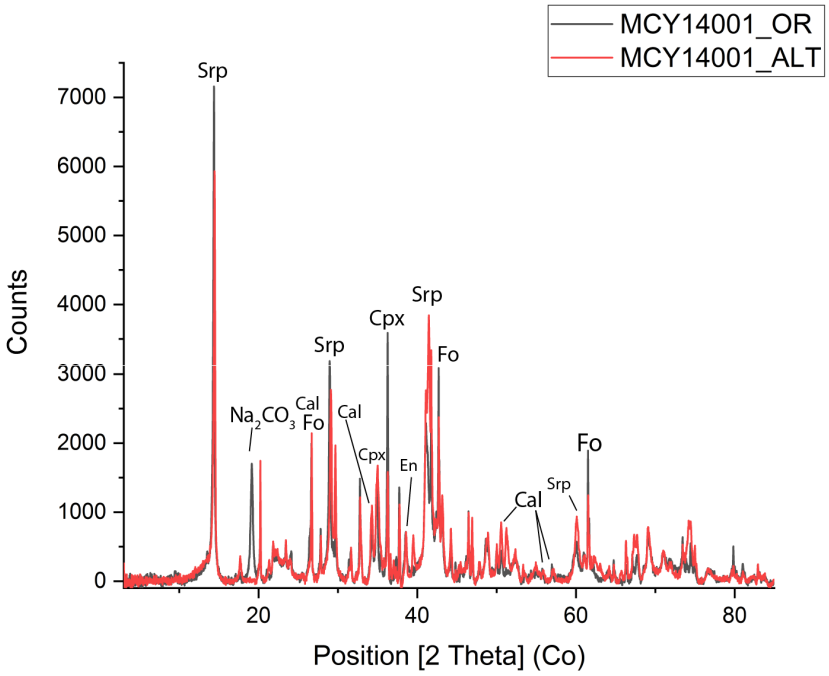

Fig. 3. XRD pattern of MCY14001 original powders (MCY14001_Or) compared to the XRD pattern of the altered ones (MCY14001_Alt). Fo=forsterite; Cpx=clinopyroxene; Srp=serpentine; En=enstatite; Cal=calcite; Na_2CO_3=natron.

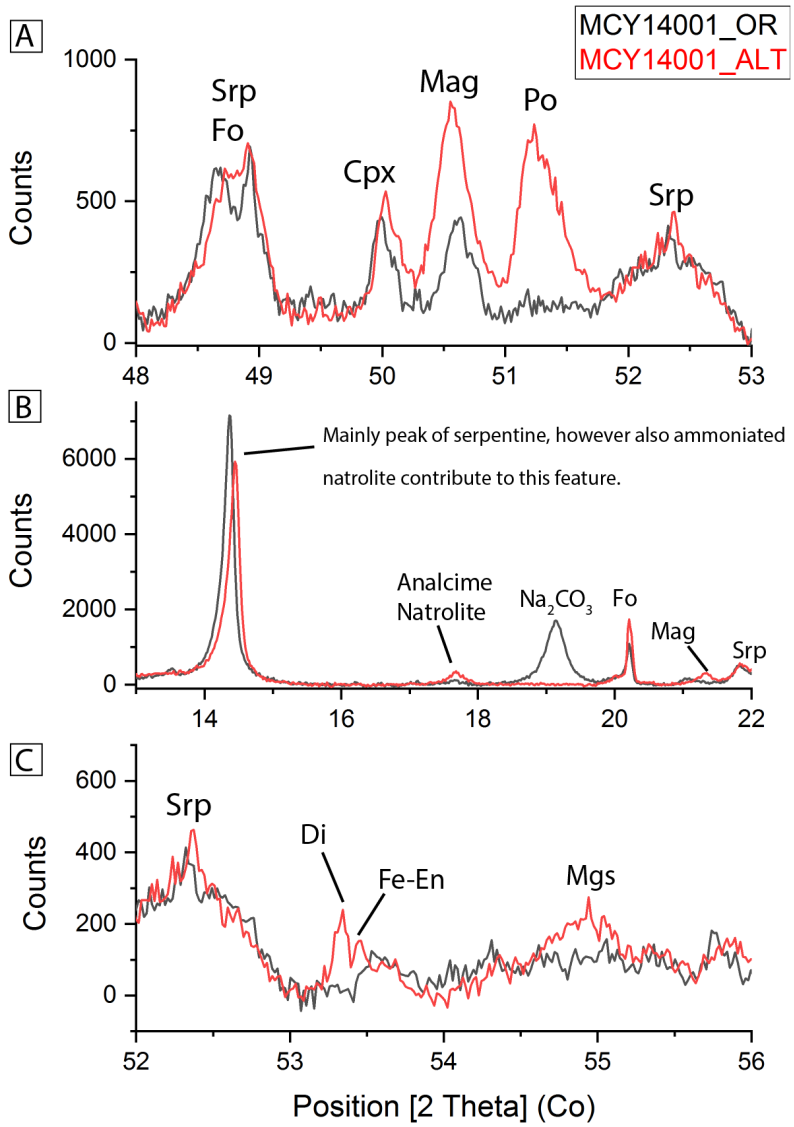

Fig. 4. Selected regions of the XRD patterns of the MCY14001 pristine powders (MCY14001_Or) and MCY14001 altered powders (MCY14001_Alt). Fo=forsterite; Srp=serpentine; Fe-En=iron enstatite; Di=diopside; Mgs=magnesite; Mag=magnetite; Po=pyrrhotite; Cal=calcite; Na_2CO_3=natron.

3.2. Spectroscopy

The IR reflectance spectra of the original samples FRO95002_Or and MCY14001_Or are typical spectra of carbonaceous chondrites (fig. 5A-B). The Spectra of FRO95002_Or is indeed characterised by a very broad band from 2.7 µm up to around 3.7 µm, which obliterates any other possible feature (fig. 5A). The same for MCY14001_Or spectrum where the broad band between 2.7 and 3 µm extends up to around 3.6-3.7 µm (fig. 5B). The altered powders of FRO95002 (hereafter FRO95502_Alt) show a very noisy spectrum (fig. 5C) probably due to poorly crystalline and disordered phases, making the interpretation tricky. The major difference from the original sample spectra is the loss of the hydration band between 2.7 and 3.7 µm. Replacing this broad band we see three band at 2.8 µm, 2.87 µm and 2.93 µm. In the 3 µm region there is an absorption at 3.03 µm and at longer wavelengths there is a band at 3.8 µm. To verify whether these bands are representative of minerals phase and what kind of minerals further SEM-EDS analyses will be carried out, at the moment XRD data do not indicate new mineral species formed after the experiment. The

spectra of the alterated MCY14001 (MCY14001_Alt) show a sharp 2.7 µm band and other two bands at 2.95 and 3.03-3.04 µm appear (fig. 5D). The spectrum between 3.3 and 4 µm is noisy, but slightly enhanced 3.5 µm, 3.75-3.8 µm and 3.9 µm bands can be seen. Furthermore, MCY14001 reflectance slightly increases from the original to the altered powders (Fig. 5B-D) reflecting a smaller grain sizes and/or the production of bright carbonates.

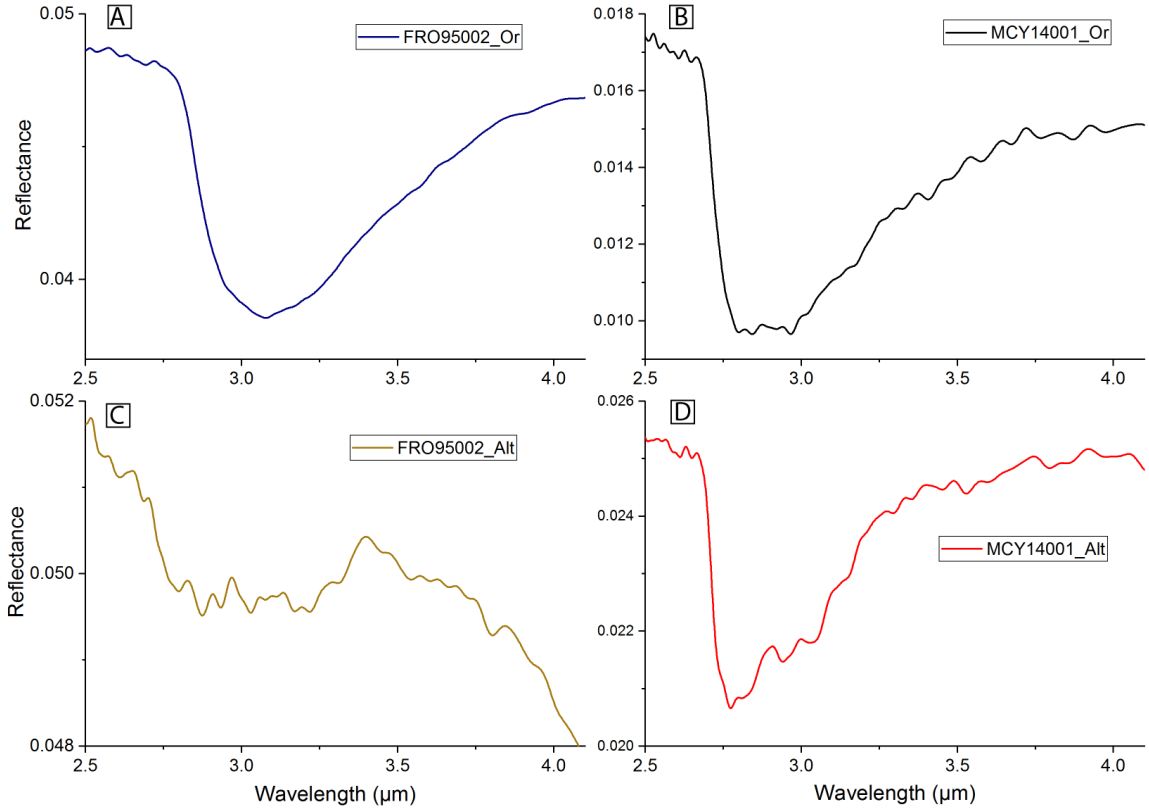

Fig. 5. IR reflectance spectra of A-B) FRO95002 and MCY14001 original unaltered powders respectively; C-D) spectra of FRO95002 and MCY14001 after the alteration processes. MCY14001 reflectance is higher in the altered powders. This is probably due to slightly different grain sizes, likely being the ejecta material of smaller grain sizes. Compositional differences might also be involved with a production of brighter carbonates in the altered powders (see paragraph 4.1).

4. Discussion

4.1. Mineralogical changes

The lack of any substantial change in mineralogy of FRO95002_Alt is most likely due to the low W/R ratio. Low abundance of water coupled with high temperatures brought the sample to dehydration, suggested by the disappearing of hydrotalcite and by the loss of the broad 2.7-3.7 µm hydration band. In addition, FRO95002 was originally already nearly anhydrous indicated by the absence of evident phyllosilicates as they were not clearly detected by XRD analyses. In FRO95002 phyllosilicates are thus a minor phase and the broad 2.7 µm hydration band in figure 5A is most likely due to the presence of other hydrated phases (i.e. hydrotalcite) whilephyllosilicates have a minor contribution. Probably the major effect of heating FRO95002 with low W/R besides dehydration is an increased textural and chemical equilibrium. This is similar to the thermal metamorphism suffered by chondrites and is defined by the petrologic type (see introduction,

chapter 1) (Brearley and Jones, 1998). Chodnrites with high petrologic types have homogeneous composition of olivine and pyroxene, pyroxene changes from monoclinic to orthorhombic, matrix and glass recrystallize and chondrules become porly defined (Brearley and Jones, 1998). Further compositional analyses (SEM-EDS and EMPA analyses) will be planned to investigate whether there has been any compositional change like an enrichment of Fe in the olivines, chemical homogeinization of silicates and recrystallization of matrix and glass. Indeed, Zolotov et al. (2006) suggested that fayalite may form with a W/R ratio of 0.1 in a wide range of temperatures below 350°C, although the pressure needed to crystallize fayalite at 240°C is almost 100 bar (Zolotov et al., 2006). We did not have control on the pressure inside the hydrothermal autoclaves, however they are designed to support a maximum of 30 Bar, it is thus very unlikely that we reached 100 Bar. For this reason we speculate that pure fayalite couldn't form, but an enrichment in Fe is possible derived by reduction of magnetite (Zolotov et al., 2006) or by growth from an amorphous precursor phase (Abreu and Brearley 2011), dehydration of serpentine is instead ruled out being absent in FRO95002.

MCY14001 gave more interesting results. In the altered samples magnetite and sulfides like pentlandite and pyrrhotite were produced. This indicates a changing in the oxidizing and reducing conditions. The autoclaves were sealed under room conditions, thus the starting environment was oxidising. Once the alteration begun started to form magnetite. After the oxygen has been exhausted by the formation of magnetite, the environment conditions changed in reducing ones and pentlandite and pyrrhotite formed. The iron was probably leached from FeNi alloys in an environment where activity of Si and S was low (Palmer and Lauretta, 2011). Other sources of Fe can be Fe-rich olivine or the Fe in mesostasis. However Fe from these sources tends to create cronstedtite instead of magnetite (Palmer and Lauretta, 2011). Unfortunately XRD analyses don't allow an accurate discrimination between antigorite, lizardite and cronstedtite. However XRD data point to enrichment in Fe in the silicates. The 53.4 XRD peak in MCY14001_Alt suggests that part of the Fe brought to the formation of Fe-enstatite (fig. 4C). This new peak is found together with another new one at 53.3 indicative of diopside (fig. 4C). The crystallization of diopside is allowed by the presence of Ca leached from CAIs, mesostasis and hydrotalcite. This Fe-rich composition and formation of diopside recall the observation made on the TAM5.29 minimeteorite in chapter 1 (Nava et al., accepted under review). We thus bring more evidences that fluid assisted thermal metamorphism at around 250°C can bring to the formation of Ca and Fe-rich silicates.
Another very interesting result is the disappearing of the natron and the minor phase hydrotalcite in the processed MCY14001 meteorite. Na-carbonates are known to be stable at low temperatures (Marion, 2000). Eutectic temperatures for $NaCO_3$ can be as low as -21.6°C (Marion, 2000), in fact it is detected on icy bodies like Europa and Ceres (McCord et al., 2001; De Sanctis et al., 2016). The Na released by the dissolved natron is than recycled by Na-phases like analcime and natrolite that forms as indicated by the XRD peaks at around 17°2θ (fig. 4B). Aluminium needed to form analcime-natrolite is probably leached from the mesostasis, from CAIs minerals as suggested by Nomura and Miyamoto (1998) and from the alteration of hydrotalcite that liberates Mg and Al. Furthermore the XRD peak at around 14°2θ (fig. 4B) can receive some contribution from NH_4-natrolite. Ammoniated natrolite has indeed the major XRD peak at 14.5°2θ, which is absent in normal natrolite. From these experiments is thus clear that also zeolites like analcime-natrolite can be NH-bearing phases that contributing to the 2.9 - 3 µm band,. Since at the same time no clays were found in the original and altered MCY14001 powders, we conclude that the only other mineral phase that can be ammoniated is serpentine.

4.2. Fate of CO_3

The fate of CO3 derived from leaching of natron and hydrotalcite is not clear. During the oxidising phase of the alteration CO_3 can contribute to the formation of carbonates. In fact, carbonates in terrestrial hydrothermal and serpentinization processes are known to co-crystallize with high temperature phases like diopside and tremolite (Python et al., 2007) and diopside is indeed found as a new phase in MCY14001_Alt. The presence of carbonates is further constrained by the fact that the 3.9 µm band (typical of carbonates) in the altered MCY14001 spectrum is still found (fig. 5D). XRD data also bring evidences of the presence of carbonates (Fig. 3 and 4C). Dehydration of hydrotalcite coupled with the Al leaching can turn hydrotalcite into magnesite, inferred from the newly formed 54.7°2θ XRD peak in the altered MCY14001 powders (fig. 4C). It thus appears that Ca-Mg-carbonates are stable during hydrothermal alteration and new crystals are also created, in agreement with observations of Python et al. (2007). On the contrary Na-carbonates are lost during hydrothermalism and are instead stable at lower temperatures as predicted by Marion (2000).

When the conditions change from oxidising to reducing the carbon left is then free to combine with H and NH. This leads to the formation of aromatic hydrocarbons, the preferred organic species created during hydrothermal alteration (Elsila et al. 2005; Galvin et al. 2010; Burton et al. 2012). The aromatic hydrocarbons formation is indeed attested by the slight deepening of the broad 3.3-3.5 µm band in the MCY14001_Alt spectrum (Fig. 5D). Giving the presence of nitrogen it is also likely that amino acids formed during the reducing phase of alteration, we will verify the presence of such compounds with gas chromatography analyses.

4.3. Comparison of MCY14001 with Ceres

Ammoniation experiments to match the composition of Ceres and all the Ceres-like asteroids have already been done on carbonaceous chondrites, clays and phyllosilicates (Ehlmann et al., 2018; Ferrari et al., 2019). However these experiments failed to recreate ammoniation of serpentine, the most common phyllosilicate in CCs and thus on C-type asteroids. This is probably due to the fact that previous experiments have been done at room temperature (25°C) and lasted for no more than a few days. In addition, no other minerals were considered in the experiments of Ehlmann et al. (2018) and Ferrari et al. (2019).

In figure 6 we compare the spectra of MCY14001_Alt with the average spectra of Ceres acquired by the Dawn spacecraft. In the 2.7-2.8 µm region Ceres show a band centre at 2.72 µm, while MCY14001_Alt has a band centre at 2.77 µm. Longer wavelengths are related to Fe-rich phyllosilicates and shorter wavelengths to Mg-rich phyllosilicates (Takir et al., 2013), MCY14001_alt is thus more enriched in Fe than Ceres. However it is known that with increasing hydrothermal alteration cronstedtite, the most common Fe-serpentine in CM chondrites, reacts with Mg and Si and becomes more enriched in Mg (Tomeoka and Buseck, 1985; Lauretta et al., 2000; Zega and Buseck, 2003; Palmer and Lauretta, 2011). We think that with longer experiments the 2.77 µm band of MCY14001_Alt can reach lower wavelengths.

The 2.94 µm band in MCY14001_Alt is very similar to that of Ceres centred at 2.96µm. On Ceres a more evident 2.9 µm band, centred at 2.99 µm, was detected by De Sanctis et al. (2019) in the organic-rich area of the Ernutet crater. The nature of this band is related to ammoniated salts or organics (De Sanctis et al., 2019). According to our experiments, we suggest that possible phases responsible for the 2.9 µm are instead ammoniated natrolite-analcime. As our experiments show, the formation of natrolite-analcime occurs with the alteration of Na-carbonates. Ceres is dominated by Ca-Mg-carbonates (Carrozzo et al., 2017) with localized spots enriched in Na-carbonates (e.g.

Occator bright spots, Haulani crater – De Sanctis et al., 2016; Tosi et al., 2017; Carrozzo et al., 2017). We suggest that Na-carbonates were probably in higher concentrations on Ceres before the occurrence of the period of extensive hydrothermal alteration (Neveu et al., 2015; Hendrix et al., 2016), which turned the majority of Na-phases in ammoniated natrolite. The 3 µm band on Ceres was attributed to ammoniated phyllosilicates (De Sanctis et al., 2015) and has a band centre at 3.05 ± 0.01 (Takir and Emery, 2012), close to the band centre displayed by MCY14001_Alt (3.03 µm). As discussed in section 4.1, in MCY14001_Alt there are no clays and no phyllosilicates other than serpentine. Thus, the only carriers of ammonia are serpentine crystals, which must have taken NH functional groups in their structures in relatively high temperature environments (240°C in the case of our experiments).

In the region of organic material (3.3-3.5 µm) no evident bands are seen in MCY14001_Alt, there is only one weak 3.5 µm band that can attest the presence of CH compounds. However, as pointed out in paragraph 4.2 it is likely that aromatic hydrocarbons formed. Leaving the powders in the autoclaves for a longer period of time would probably resolve the lack of the expected 3.3-3.5 µm bands in MCY14001_Alt.

In the 3.9-4 µm region characteristic of carbonates, we found absorption bands both in Ceres and in MCY14001_Alt. We report the presence of carbonates, mainly calcite, in the pristine MCY14001 sample. XRD than revealed also the presence of natron. In the altered MCY14001 powders other carbonates form (likely calcite and magnesite) and natron, as widely discussed, disappears. This is largely consistent with the overall composition of Ceres, inferred to be enriched in Ca-Mg-carbonates (Carrozzo et al., 2017).

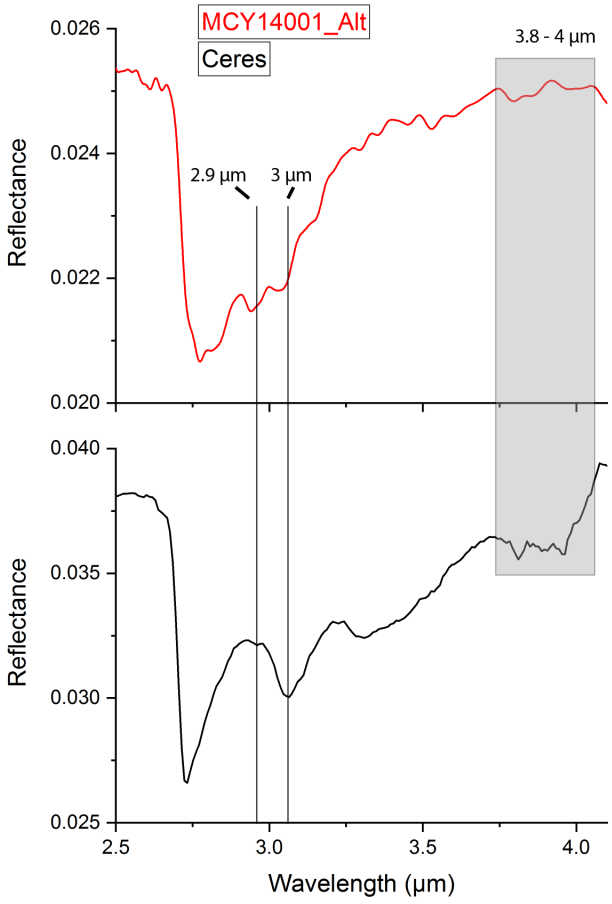

Fig. 6. IR reflectance spectra of altered powders of MCY14001 (MCY14001_Alt) compared with the spectra of the average spectrum of Ceres acquired by the Dawn spacecraft.

5. Conclusions

With this work we report new insights for hydrothermal alteration on minor bodies of the Solar System, with a special attention to C-type Ceres-like asteroids. In particular:

1. The Experiment with Low W/R ratios (~0.1) brings to a dehydration of the sample as a major change.
2. The Experiment with High W/R ratios (~1), ammonia-rich fluids and CM chondrite-like composition is more consistent with the composition of C-type Ceres-like asteroids.
3. During the experiment on the CM-MCY14001 chondrite a change in oxidising to reducing conditions was recorded by the formation of magnetite and sulfides respectively.
4. We add new evidences that in fluid assisted metamorphism at ~250°C there is an enrichment in Ca and Fe of the silicates, with the formation of Fe-enstatite and diopside mainly.
5. During hydrothermal alteration of MCY14001 CM chondrite at 240°C Na-carbonates become unstable and are turned into Na-rich phases like analcime-natrolite. Furthermore ammoniated-natrolite has been detected, suggesting that these mineral phases can be present on Ceres-like asteroids and accounts for their 2.9-3 μm absorption band.
6. CO_3 resulting from the dissolution of Na-carbonates form new carbonates stable at high temperature like calcite and magnesite during the oxidising phase. This process can explain the rarity of Na-carbonates as well as the high abundance of Ca-Mg-carbonates on Ceres surface. In addition during the reducing phase the liberated carbon combines with H to likely form aromatic hydrocarbons detected on Ceres.
7. We report indirect evidence for ammoniation of serpentine, the only phyllosilicate detected in the MCY14001 chondrite. This was never achieved before and we infer that this process can take place at relative high temperatures (240°C) in long lasting experiments and thus also on Ceres-like asteroids, which went through extensive hydrothermal alteration during their evolution. Thus ammoniated-serpentine is another phase that can explain the 3 μm band on Ceres-like asteroids

Chapter 7

An aqueously altered, thermally metasomatized CO chondritic micrometeorite – a new intermediate member covering the CO-CM gap

Abstract

The CO and CM chondrites form a meteorite clan, representing two closely related groups. However, the petrography and isotopic differences between these classes are increasingly blurred by the discovery of new intermediate members, which share affinities to both groups and are currently classed as ungrouped C2 representatives. We describe a new enigmatic member of this population, found amongst the TAM micrometeorite collection. We use Raman spectroscopy, mid-IR spectroscopy, mineral chemistry and particle textures to establish a strong parent body link and to trace the geological history of this micrometeorite. This sample (TAM5-30) is a "*wet*" CO chondrite, containing abundant hydrated phases, partially replaced chondrules and a high phyllosilicate fraction (~0.4) – equivalent to the hydrated CR chondrites and less altered than most CM chondrites. In addition, TAM5-30 records a two-part processing history characterised by an initial episode of low-temperature CM-like aqueous alteration leading to the formation of Fe-phyllosilicate, Cr-spinel and Fe-oxides, which later transitioned into higher temperature (~300°C) CV-like thermal metasomatic alteration, resulting in the formation of abundant fayalite, apatite, diffusion profiles in mafic silicates and "*cooked*" organic matter. This sample therefore reflects a dual petrologic subtype ranging from C2.2 to C3.6 – as based two independent petrographic metrics and demonstrates how the complex asteroidal histories of chondrites defy simple petrologic subtypes.

We speculate that meteorites intermediate between the CO and CM groups potentially formed as small asteroids in-between the main growth stages of larger CO and CM planetesimals. Thus, the COs, intermediate members and CMs represent a progressive continuum of petrographic and isotopic characteristics reflecting a chronological sequence of planetesimal formation from an evolving and increasingly hydrated region of the nebula.

1. Introduction

The asteroid belt, situated at ~ 2.06 and 3.27 AU between the orbits of Mars and Jupiter, contains approximately 128,000 members with diameters >1km (JPL, SSD – Nasa, 2019). This region is composed of early solar system remnants, including disintegrated planetesimals, early generation protoplanets and primitive nebula accretion products. The asteroid belt's diversity is progressively resolved through a combination of spectroscopy (DeMeo and Carry, 2014), space missions (Barucci et al., 2011) and meteoritics and this in-turn informs our understanding of the solar system's formation and evolution.

Within the field of meteoritics, extraterrestrial samples are studied primarily by microanalytical methods and the resulting information is used to classify samples into geochemically and isotopically distinct classes. Meteorite classification is hierarchical, with divisions tracing shared formation histories. For example, the classification of C, O, E and R chondrites are generally considered a reflection of the different large-scale formation regions within the solar nebula, while chondrite groups are assumed to trace different parent bodies with subgroups cataloguing the style and extent of parent body processing via mechanisms such as aqueous alteration, thermal metamorphism and igneous differentiation (Weisberg et al., 2006).

Meteorite classification is also an evolving field, dependent upon the discovery of new extraterrestrial samples. Anomalous meteorites (and more recently micrometeorites [Gounelle et al., 2009; Cordier et al., 2018]) with transitional properties or unique mineralogies are therefore potentially members of new and otherwise unknown parent bodies (Krot et al., 2000; Choe et al., 2010; Jacquet et al., 2016). Alternatively, anomalous samples could represent outliers closely associated with an established group and whose discovery forces us to expand the definition of a given chondrite group to reflect an enhanced understanding of the diversity and variability within a single body (Choe et al., 2010). This later scenario remains problematic since it is unclear how much variability is possible within a single asteroid. As such the question of whether a carbonaceous chondrite group represents a single parent body or multiple parent bodies is a pertinent and unresolved question. This is particularly true for the CO-CM chondrite clan, which represents one of the largest and most studied carbonaceous chondrite groups and whose component meteorites exhibit a wide range of properties (Krot et al., 2000; Schrader and Davidson, 2017; Alexander et al., 2018).

In this study, we examine a new and anomalous giant micrometeorite, whose petrographic properties suggest a close affinity to the CO chondrites but with an otherwise anomalously high abundance of phyllosilicate and fayalite, and therefore a partially hydrated mineralogy, recording a significant episode of parent body aqueous alteration and subsequent thermal metasomatism, inconsistent with the known geological history of the CO or CM chondrite groups. The discovery of this micrometeorite, along with an increasing number of anomalous ungrouped C2 representatives with similarly moderate degrees of hydration appear transitional between the CO and CM groups, suggesting a continuum in petrographic properties and a diverse range of processing histories. This has implications for the number of parent bodies formed from a single source region of the solar nebula as well as for the general parent body processing pathways for chondritic samples.

2. Results

2.1 TAM5-30: This is a large composite Antarctic micrometeorite (Fig.1A), containing no igneous rim and a discontinuous magnetite rim – which is observable across the exterior of the particle (Fig. 1A, 1C) and whose partial covering is attributed to terrestrial weathering and attrition. This particle has a rounded subspherical shape and average diameter of 780µm (Fig.1C). The exposed cross-section studied here measures: 680x590µm (approximate maximum dimensions) with a total surface area of ~0.315mm^2 (as measured using the ImageJ software).

2.2. Bulk composition: Terrestrial alteration is localised, primarily affecting the particle perimeter and regions of the matrix within 100µm of the particle edge (Fig.1B), as determined by EDX mapping, which shows locally enriched concentrations of K, S and Na (Fig.2). These are in fact known to indicate of the occurrence of weathering products of the Jarosite-Alunite series in Antarctic micrometeorites (van Ginneken et al. 2016). We therefore discarded matrix analyses with clear evidence of terrestrial alteration collected from these zones. The resulting weathering-corrected bulk composition for TAM5-30 (Fig.3A) is chondritic within 1 order of magnitude of CI values and produce a close match to oxidised anhydrous chondrites such CO Kainsaz and CV Allende, whilst being distinct from the hydrated CM group and the reduced CV chondrites.

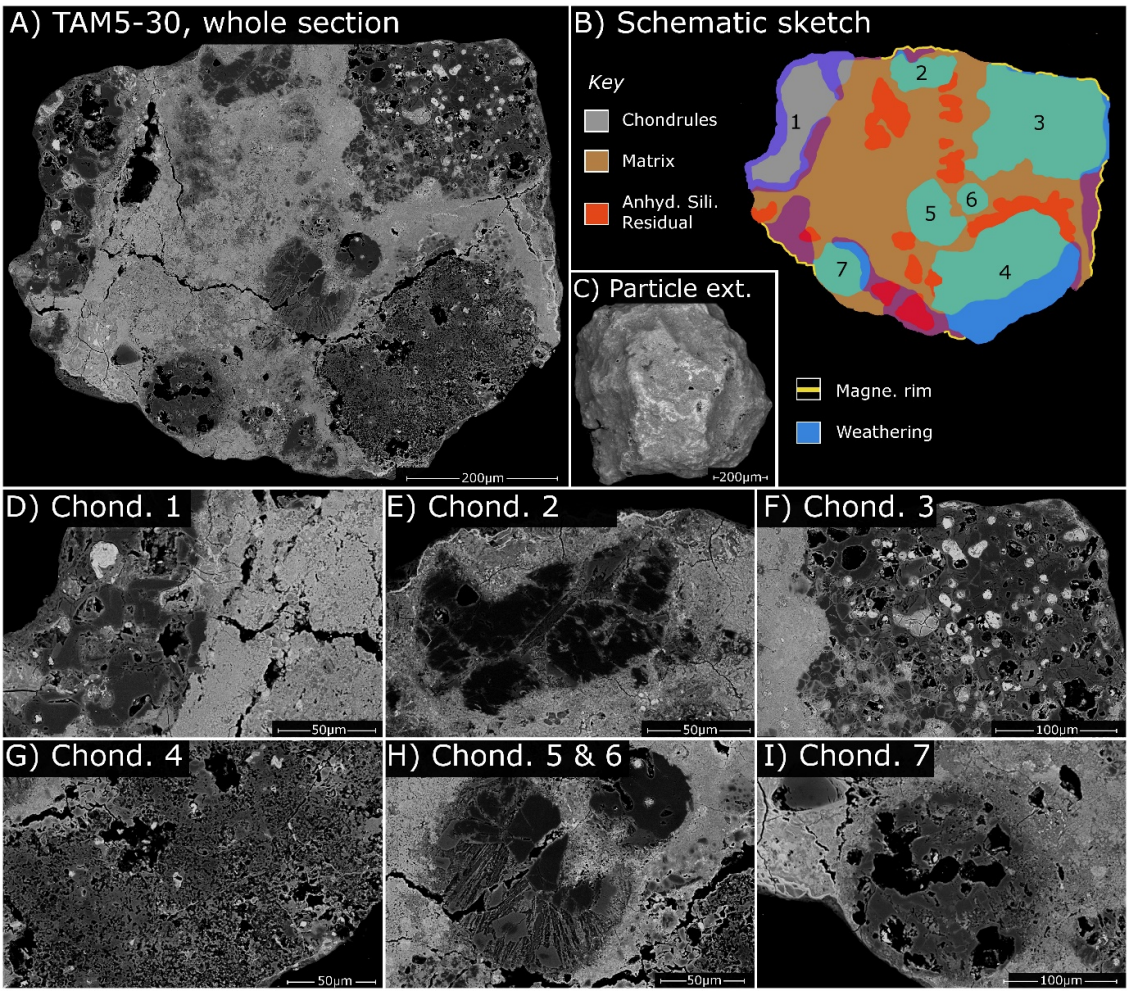

Fig.1. TAM5-30, a giant chondritic composite micrometeorite (A-C), containing seven chondrules embedded within a fine-grained matrix. Chondrules are small (<350µm) and are affected by significant parent body aqueous alteration and partial replacement. A Schematic sketch aids the readers interpretation, illustrating zones of localized terrestrial weathering, as well as numbering of chondrules.

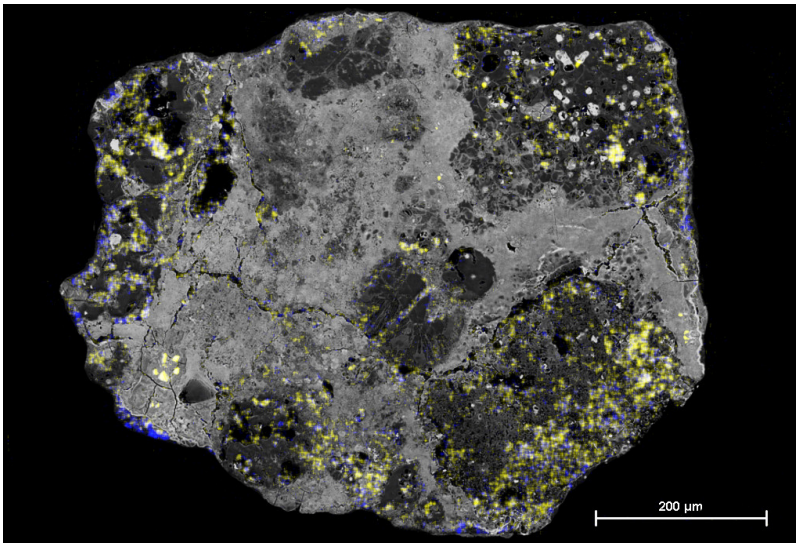

Fig.2. EDX maps of TAM5-30 highlighting localised zones of terrestrial weathering at the particle's margins, as traced by the co-occurrence of K (blue) and S (yellow), indicating the presence of Jarosite a diagnostic weathering mineral formed in TAM micrometeorites during terrestrial alteration.

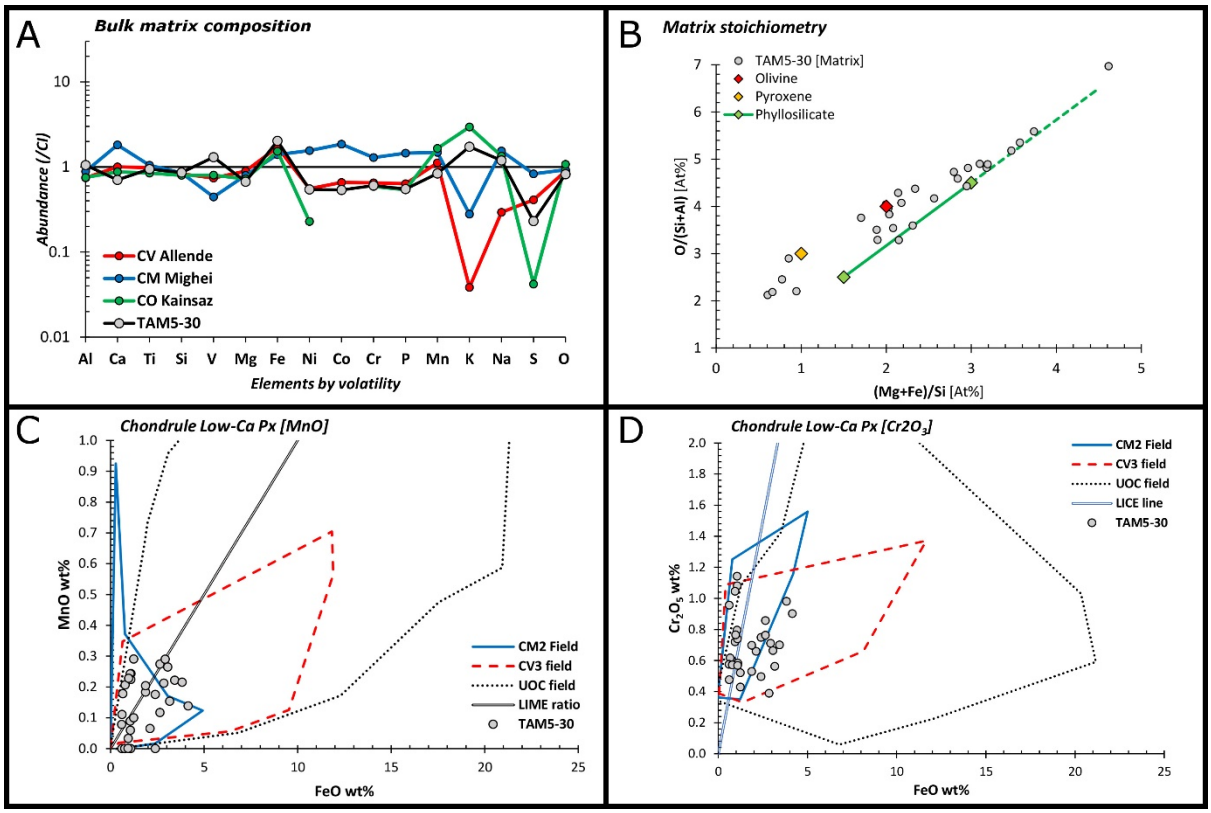

Fig.3. Geochemical panel, displaying bulk matrix and chondrule silicate minor element compositions

2.3. Chondrules: The particle interior contains clearly defined chondrules (Fig.1B-I), which lack fine-grained rims and compose ~53% of the particle (by area). There are seven chondrules in total which range in size between 60µm and 245µm and include porphyritic (PP and POP), radiating pyroxene (RP), cryptocrystalline (CC) and glassy subtypes. Chondrules in this micrometeorite are therefore small, with an average size of just 150µm – while the smallest of these extend towards the field of microchondrules (previously defined as <40µm, Krot et al., 1997). Chondrules are dominated by low-Ca pyroxene (En>93 for 88% of analyses), however, if Type I chondrules are characterised by mafic silicates with Mg#>90%, regardless of texture – TAM5-30 is found to contain three type I chondrules and 4 type II chondrules – and which do not correlate with the presence of reduced metal beads. They have minor element contents (MnO and Cr_2O_3) consistent with a CM chondrite parent body (Fig.3C and D). Olivine and high-Ca pyroxene are likewise present but relatively rare components. Olivine displays near-identical compositions to the low-Ca pyroxene (Fo72-95, MnO<0.54 and Cr_2O_3<0.56) while the high-Ca pyroxene (En50-57, Fs1-7, Wo40-42) has correlated MnO-Cr_2O_3 contents (0-1wt%), potentially formed by condensation growth from a solar nebula gas phase at moderately refractory conditions. Minor chondrule phases include metal, Fe-oxides and Fe-sulfides (~1.9% [area]) and a single grain of apatite.

2.4. Matrix and aqueous alteration: The particle's fine-grained matrix is a complex mix olivine and phyllosilicate, with minor low-Ca pyroxene as determined by mid-IR spectroscopy, stochiometry and high-resolution BSE imaging. Although some of the phyllosilicate has experienced incomplete thermal decomposition (possibly) during atmospheric entry, resulting in dehydroxylated phyllosilicates, diagnostic phase textures (Fig.4) and spectroscopic signatures remain (Fig.5). The matrix modal matrix mineralogy was estimated from randomly spaced EDS analyses (Fig.4B) as well by use of a mid-IR linear mixing model (Fig.5A) and revealed approximately equal proportions of olivine and phyllosilicate (~40-50%) as well as minor ~10% low-Ca pyroxene. This suggests a phyllosilicate fraction (phyllosilicate/total silicate [anhydrous, hydrous & amorphous]) of ~40%

(Fig.6B) which plots on the aqueous alteration petrologic subtype scheme of Howard et al., (2015) with a grade of C2.2.

The near-IR spectrum for TAM5-30 (Fig.5A) reveals a complex, hydrated mineralogy, with several distinct absorption bands. These include a 1.7 µm band produced by the Mg-OH functional group – indicating the presence of brucite. Meanwhile, the 2.7 µm band in TAM5-30 is deep, narrow and "*U-shaped*" with a band centre located at 2.8µm. This feature is distinct from the 2.7 µm bands typically observed in carbonaceous chondrites, which are otherwise broad and asymmetric with a steep low-wavelength side and a shallow long-wavelength shoulder (Fig.5A and Takir et al., 2013) and band centres between 2.7-2.9 µm. This 2.8 µm band is due to phyllosilicates with relative Fe-rich compositions, likely minerals of the serpentine group (i.e. antigorite or lizardite). TAM5-30 also has a prominent doublet peak at 3.3 µm 3.4-3.5 µm and 3.9-4.0 µm associated with organics (aromatic and aliphatic hydrocarbons in particular) and carbonates respectively. These features are commonly also observed in most carbonaceous chondrites, as demonstrated in Takir et al., (2013) although curiously were not detected in our reference chips of CM, CO, CR and CV chondrites (Fig.5A). Finally, TAM5.30 also shows a band at 3.8 µm, not found in the spectra of the other CCs. This feature can be related to either carbonates or the S-H functional group.

Matrix silicates are Fe-enriched (Mg#:3-62) in comparison to chondrule silicates (Mg#:72-99). Grains have rectangular euhedral morphologies and sizes <4µm. In contrast, the phyllosilicates have characteristic fibrous morphologies and form short, mis-orientated stacks (Fig.4D-F). They form locally abundant clusters which co-occur with micron-sized Fe-oxide grains but are also dispersed throughout the matrix at lower concentrations. This results in a highly variable matrix texture, with significant variations in porosity, grain size and composition.

In addition to the matrix phyllosilicates, the chondrules and isolated anhydrous silicates within the matrix have experienced hydration and partial replacement by phyllosilicate. Alteration veins penetrate the chondrules following crystallographic and microstructural anisotropies within the host crystals, resulting in significant localised replacement by serpentine (Fig.1) as previously described by Lee and Lindgren (2016). Chondrules within this micrometeorite therefore preserve variable degrees of alteration, with chondrules 2, 5 and 7 displaying the most severe parent body aqueous alteration.

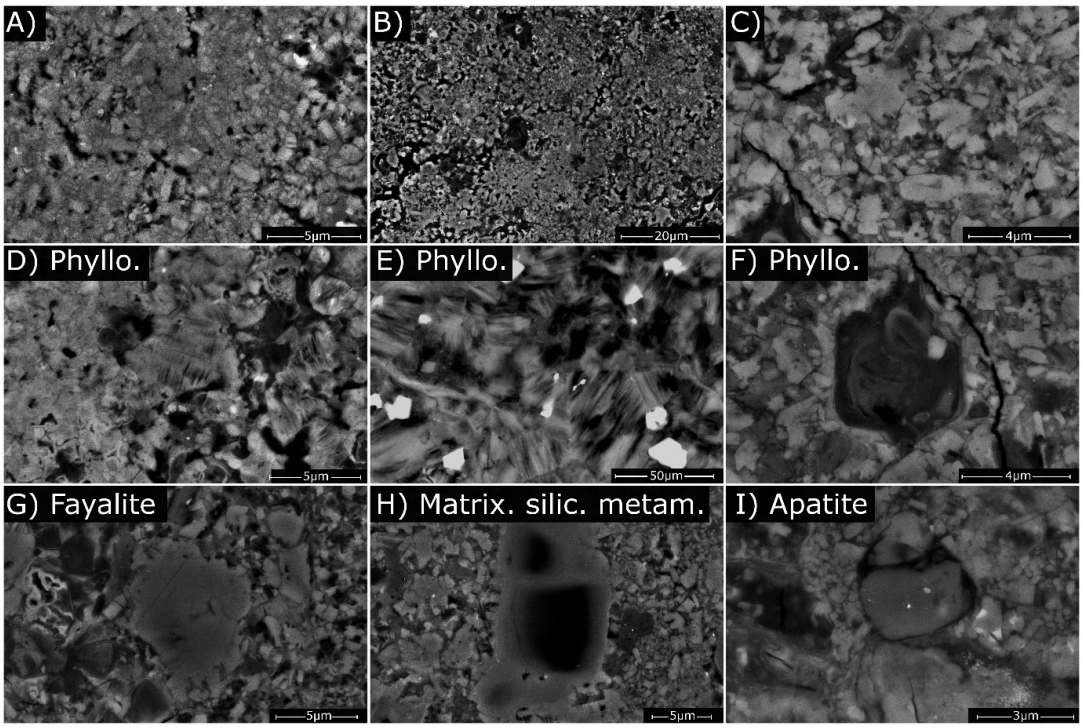

Fig.4. High magnification BSE images illustrating the diversity of grain textures and morphologies present within TAM5-30. The matrix of this micrometeorite is dominated by fayalite and Fe-rich phyllosilicates.

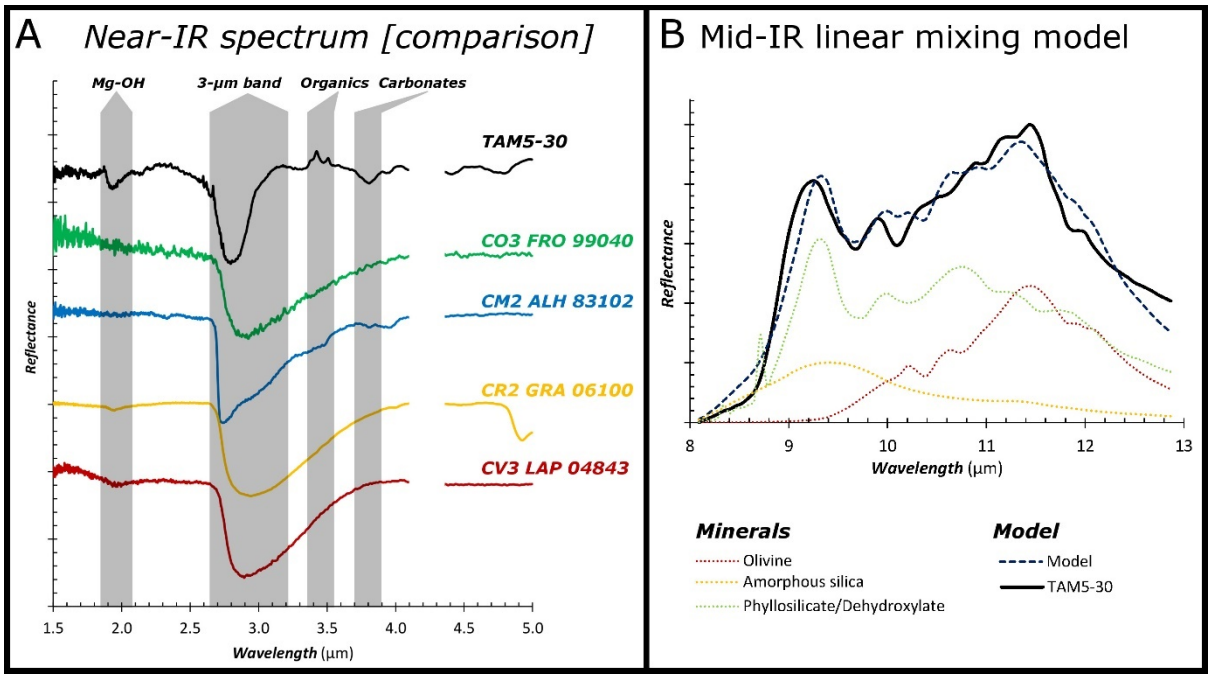

Fig.5. Infrared reflectance spectroscopic data for TAM5-30. Including an estimate of modal mineralogy over mid-IR wavelengths and comparison against reflectance spectra of carbonaceous chondrites over the near-IR 3 μm-region. Comparison meteorites are PNRA/ANSMET samples loaned for this study and mineral spectra from the RRUFF database, from Che and Glotch (2012) and Hallenback (1998). Reflectance is arbitrary in order to make the comparison between samples easier, for this reason units are not shown.

2.5. Carbonaceous and organic phases: Raman spectra collected from TAM5-30 are dominated by signals from disordered carbonaceous matter, containing prominent G and D bands (Fig.7). Average peak parameters from six high-quality spectra yielded values of R_1 – I_D/I_G (band height) of 1.22 (±0.16) and an average FWHM-D of 111cm^{-1} (±20). These values plots close to the CO metamorphic trendline previously established by Bonal et al., (2007) using data from eight CO chondrites (Fig.6A) and imply that the metamorphic grade or petrologic subtype for TAM5-30 is ~C3.6.

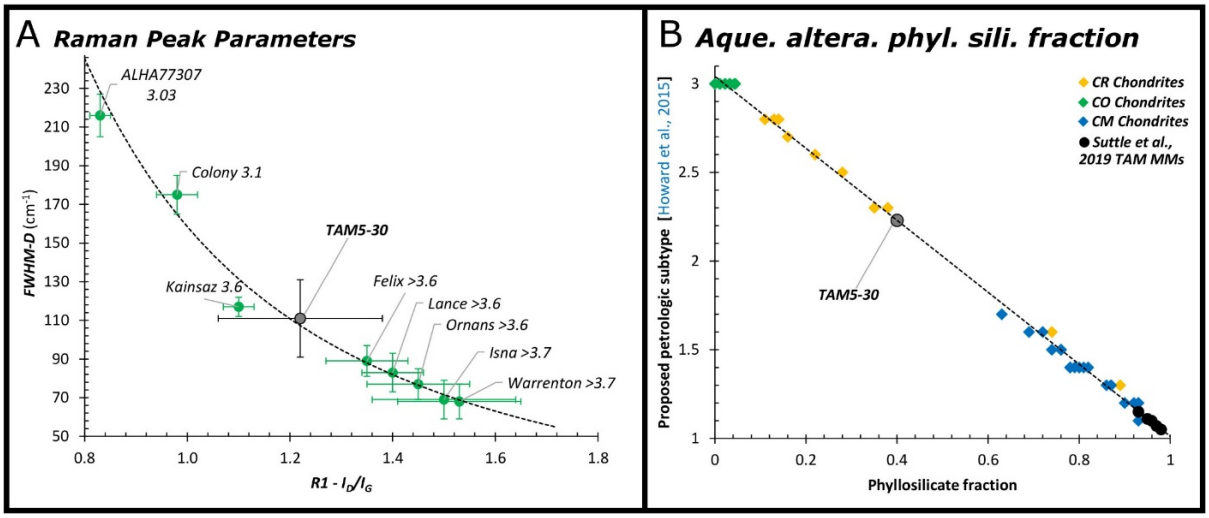

Fig.6. Parent body alteration recorded in TAM5-30, petrologic subtype estimated using Raman spectroscopy (A) and modal mineralogy (B). Metrics and model data after Bonal et al., (2007) and Howard et al., (2015) respectively. We also display additional modal mineralogy data from Alexander et al., (2018) [CO chondrites] and Suttle et al., (2019a) [giant fine-grained hydrated micrometeorites].

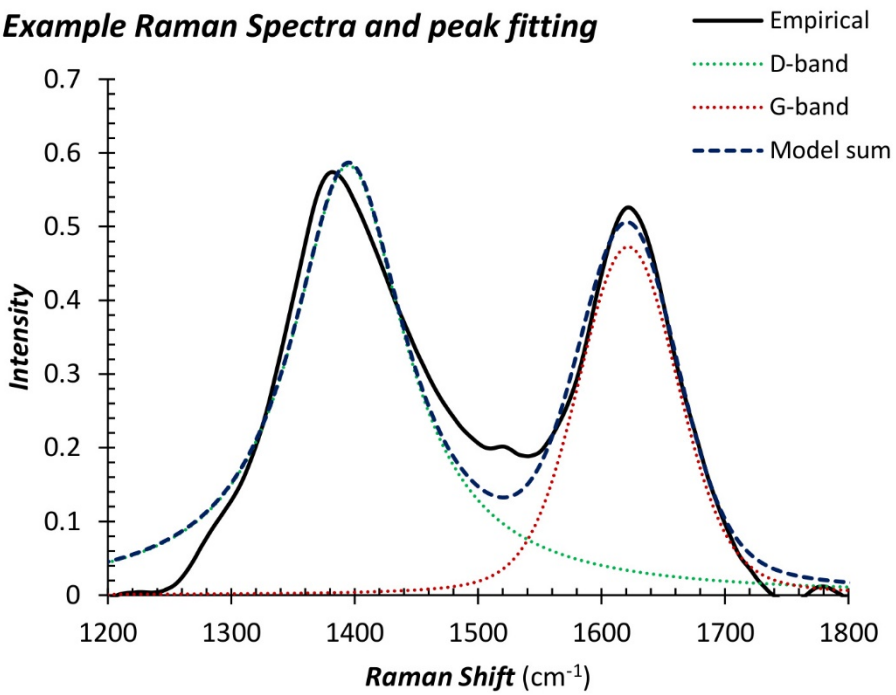

Fig.7. An example Raman spectrum from TAM5-30, demonstrating the peak fitting model (Lorentz-Voigt)

3. Discussion

3.1. Identification, entry heating and terrestrial modification: The presence of a magnetite rim confirms that TAM5-30 is a micrometeorite rather than a fragment of a larger meteorite. This particle was therefore liberated from its parent body as a small grain and resided in space as cosmic dust before being captured by Earth's gravity and surviving atmospheric entry (Genge et al., 2008).

The lack of an igneous rim, as well as disordered carbonaceous matter preserved within the fine-grained matrix and hydrated phyllosilicate (some of which may be partially altered dehydroxylate) demonstrate that atmospheric entry heating was minimal, temperature gradients were steep and that sustained peak temperatures were most likely between 300-400°C and certainly <<800°C (Nozaki et al., 2006; Suttle et al., 2017). This is highly unusual for large micrometeorites, which typically suffer significantly higher peak temperatures (Love and Brownlee, 1994). Currently no studies have attempted to model the heating profiles of micrometeorites larger than ~100µm, as such the entry dynamics of giant (>400µm) micrometeorites – found among the TAM collection (Rochette et al., 2008) – are unknown. However, given the strong control particle size plays on peak temperature and duration of heating, logically one would expect giant micrometeorites to rarely survive atmospheric entry. This indeed appears to be the true, because unmelted micrometeorite abundance decreases as particle size increases (Taylor et al., 2007). Thus, particles like TAM5-30, which are only minimally affected by flash heating must have experienced highly favourable entry conditions.

Finally, TAM5-30 was affected by terrestrial weathering while in Antarctica. The environmental conditions at Miller Butte result in the progressive replacement of extraterrestrial material with weathering phases, notably jarosite ($KFe^{3+}_3(OH)_6(SO_4)_2$), calcite, palagonite and ferrihydrite (van Ginneken et al., 2016). In TAM5-30 jarosite is clearly present, traced by the co-occurrence of K and S in EDX maps, however, its extent is limited and localised to the particle perimeter (Fig.1B and Fig.2).

TAM5-30 is therefore an exceptionally rare find being unmelted, essentially unheated and mildly affected by later terrestrial weathering, this permits a thorough investigation of the particle's parent body affinities and geological history.

3.2. Parent body affinities of TAM5-30 and the CO-CM gap:

TAM5-30 shares many petrographic similarities with the CO chondrites (Table.1). This includes average chondrule size (150µm), chondrule size range (60-245µm), chondrule abundance (~53%), metal abundance (<1.9% [area]), bulk matrix composition (Fig.3A), relict chondrule silicate compositions (Fig.3C & 3D) and matrix mineralogy. Based on these features TAM5-30 thus appears to be an unambiguous member of the CO group. However, the relatively high abundance of phyllosilicate (~40%) in TAM5-30, which is primarily concentrated within the matrix as well as the presence of carbonates are inconsistent with a CO chondrite. Most CO chondrites are anhydrous, containing variable proportions of crystalline and amorphous silicate within their matrix and no hydrated silicates (Fig.5B and Alexander et al., 2018). In contrast, in CO chondrites which do contain phyllosilicates these appear at very low concentrations, as Fe-rich serpentine varieties with low-degrees of crystallinity and in close association with oxidised Fe^{3+}-bearing Fe-oxides (Keller and Buseck, 1990). Modal mineralogy by PSD-XRD (position sensitive X-ray diffraction) conclude that most CO chondrites contain close to 0vol% phyllosilicate and certainly <5vol% (Alexander et al., 2018). Thus, although phyllosilicate species are present in CO chondrites, they are significantly lower than those observed in TAM5-30.

The CO chondrites share a close petrographic relationship with the CM chondrites forming a chondrite clan united by similar chondrule properties, isotopic signatures and volatile element

abundances (Kallemeyn and Wasson, 1981; Schrader and Davidson, 2017; Alexander et al., 2018). Their O-isotopic signatures define a single trendline (ranging between values δ^{18}O=-5‰, δ^{17}O=-10‰ and δ^{18}O=10‰, δ^{17}O=4‰) with a slope of 0.7 (and a δ^{17}O intercept of -4.23‰, Clayton and Mayeda, 1999; Greenwood et al., 2019). However, CO and CM chondrites plot as end-members leaving an isotopic "*gap*" in-between. Similar well-defined isotopic lines with various linear slope functions characterize all of the carbonaceous chondrite groups (but not the non-carbonaceous chondrites, Alexander, 2019). For example, the CRs also plot along a parallel slope 0.7 mixing line, but this is offset from the CO-CM line, with a δ^{17}O intercept of -2.25‰ (Schrader et al., 2011). Each of these trendlines records mixing between an inner solar system ^{16}O-rich and an outer solar system ^{16}O-poor component. This relationship was interpreted by Clayton and Mayeda (1999) as a dust and gas component respectively while others (Chaumard et al., 2018; Marrocchi et al., 2018; Alexander, 2019) favor mixing of ^{16}O-rich anhydrous silicates and ^{16}O-poor water-ice.

The CO-CM clan most likely grew from the same initial geochemical reservoir and formation region. Recently, Chaumard et al., (2018) suggested that the CO chondrite parent body may have accreted first with the CM parent body (or bodies) forming later. In between these events the solar system's snowline appears to have migrated inwards crossing their common formation region and thereby explaining the significant increase in water content among the CM chondrites as a product of water-ice condensation, partitioning into the volatile-bearing matrix. This suggestion has the advantage of explaining the distinct difference in hydration and water-to-rock ratios of two groups while maintaining their close isotopic and petrographic relationships, including near-identical chondrule chemistries. If the CMs formed later, then their consistent chondrules could have experienced longer growth times in the solar nebula, and assuming growth time correlates with chondrule size (for example by mechanisms such as sticking of molten droplets [Jacquet, 2014] or by periodic accretion of dust layers and subsequent melting cycles [Ruzicka, 2012]) this would potentially explaining their larger average sizes, in comparison to COs.

The dichotomy between the CO and CM end-members is however, increasingly blurred by the discovery of new intermediate members with transitional petrographic (Choe et al., 2010; Alexander et al., 2018) and isotopic properties (Clayton and Mayeda 1999; Greenwood et al., 2019). They are primarily a product of new Antarctic and hot desert finds. Most new intermediate members (Table.2) are categorized as C2-ungrouped, anomalous CM or CM-like chondrites and have relatively dry mineralogy with phyllosilicate contents <60vol% – that are otherwise typical for the CM family (Howard et al., 2009; 2015). Likewise, they have small chondrules, commonly in-between the CO and CM average size. Notable examples include: NWA 5958 (Jacquet et al., 2016), which is similar to the least altered CMs, containing modest quantities of coarse phyllosilicate, a larger volume of matrix but greater volatile depletion than the CM group; Acfer 094 with a uniquely pristine petrology potentially similar the precursor unaltered CM lithology (Newton et al., 1995; Choe et al., 2010); and LEW 85311 (Choe et al., 2010). TAM5-30 shares many similarities to this intermediate chondrite population being both CO and CM like, with similar chondrule sizes and alteration degrees. However, this micrometeorite is perhaps most similar to the C2-ungrouped meteorite MAC 88107, as the matrix in both samples contains Fe/Mg-phyllosilicates and fayalitic olivine, representing a distinct alteration history to that found in CM chondrites and instead more similar to the CVs (Krot et al., 2000).

Table.1. Geochemical data – EMPA & Standard-less EDS, spot and wide-beam analyses of various mineral phases within TAM5-30. Elements are normalized Wt%. Uncorrected Wt% totals are also reported.

	Na	*Mg*	*Al*	*Si*	*P*	*S*	*Cl*	*K*	*Ca*	*Ti*	*Cr*	*Mn*	*Fe*	*Ni*	*O*	*Unco.Tot. Wt%*	*End-member composition*
Low-Ca Px	-	22.93	0.46	27.36	-	0.02	-	-	0.36	0.13	0.41	0.07	0.82	0.01	47.4	101.43	En98, Fs2, Wo1
Low-Ca Px	0.04	19.8	0.93	26.78	0.02	0.02	-	-	1.97	0.12	0.47	0.11	3.22	0.02	46.5	102.37	En88, Fs6, Wo5
Low-Ca Px	0.04	21.99	0.56	27.01	0.04	0.14	-	0.07	0.86	0.11	0.34	0.05	1.64	0.02	47.11	99.23	En95, Fs3, Wo2
Low-Ca Px	*0.1*	*26.7*	*0.4*	*31*	-	-	-	-	*0.3*	-	*0.6*	*0.1*	*0.5*	*0.3*	*39.9*	*96.3*	En98, Fs1, Wo1
Low-Ca Px	-	*25.7*	*0.5*	*31.6*	-	-	*0.1*	-	*0.4*	-	*0.4*	-	*0.9*	*0.2*	*40.1*	*97.9*	En97, Fs2, Wo1
Low-Ca Px	*0.1*	*26.6*	*0.2*	*30.9*	-	-	-	-	*0.2*	-	*0.3*	*0.2*	*1.7*	-	*39.8*	*96*	En97, Fs3, Wo0
Olivine	0.06	18.96	2.82	18.26	0.02	0.41	-	0.03	2.26	0.1	0.29	0.13	14.78	0.04	41.85	103.11	Fo75
Olivine	*0.2*	*31.1*	*0.2*	*20*	-	*0.2*	-	-	*0.6*	-	*0.1*	*0.1*	*12.9*	*0.1*	*34.6*	*97.6*	Fo85
High-Ca Px	0.8	3.19	8.04	24.03	0.02	0.6	-	0.4	8.33	0.04	0.05	0.05	10.18	0.05	44.23	102.54	En25, Fs35, Wo40
High-Ca Px	0.05	11.03	2.36	24.26	0.02	0.25	-	0.14	13.71	0.65	0.84	0.6	1.61	0.05	44.41	104.56	En55, Fs3, Wo41
Apatite	-	*0.5*	*0.7*	*3*	*16.8*	*0.5*	-	-	*37.6*	-	*0.2*	-	*3.7*	*0.1*	*36.8*	*85.9*	-
Fe-sulfide	*0.1*	*0.1*	*0.2*	*0.4*	*0.2*	*31.8*	-	-	*0.1*	-	*0.5*	-	*59.3*	*0.1*	*7.1*	*89.4*	-
Bulk matrix	**0.4**	**9.65**	**1.4**	**14.95**	**0.1**	**0.77**	**0.17**	**0.06**	**0.35**	**0.04**	**0.24**	**0.14**	**36.41**	**0.95**	**34.38**	**86.95**	**-**
Matrix	*0.2*	*14.5*	*1.3*	*15.8*	-	*0.5*	*0.2*	*0.1*	*0.2*	-	*0.2*	*0.3*	*34.1*	*0.9*	*32*	*83.9*	-
Matrix	*0.1*	*5.7*	*1.2*	*12.8*	*0.3*	*1.1*	*0.5*	*0.1*	*1.9*	-	*0.1*	-	*42.2*	*1.4*	*32.6*	*80.22*	-
Fayalite	-	*9.3*	*0.2*	*14.1*	*0.2*	*0.4*	*0.1*	-	*0.2*	-	-	*0.2*	*36.8*	*0.1*	*38.2*	*92.3*	Fo37
Fayalite	-	*11.4*	*0.2*	*16.4*	*0.3*	*0.3*	-	-	*0.1*	-	-	*0.2*	*33.4*	*0.1*	*37.5*	*85.2*	Fo44
Fayalite	*0.1*	*11*	*0.2*	*16.1*	*0.3*	*0.3*	-	-	*0.1*	-	*0.1*	*0.3*	*33.6*	*0.1*	*37.9*	*88*	Fo43
Dark phyllosi.	*0.1*	*1.3*	*3.2*	*25.6*	*0.7*	*2*	*0.3*	*0.1*	*1.9*	-	*0.2*	*0.1*	*33.4*	*1.2*	*29.9*	*86.1*	-
Phyllosilicate	*0.1*	*0.6*	*1.2*	*6.8*	*0.7*	*2.5*	*0.7*	-	*0.4*	-	*0.5*	-	*47.6*	*1.9*	*37.1*	*94.1*	-
Cr-spinel	*0.2*	*1*	*5.6*	*3.6*	*0.2*	*1*	*0.2*	-	-	-	*17.3*	*0.3*	*36.3*	*0.5*	*33.8*	*89.1*	-
Fe-Sulfide	*0.1*	*0.2*	*0*	*0.5*	*0.1*	*34.4*	*0.1*	-	-	-	-	*0.1*	*62.1*	*0.2*	*2.2*	*87*	-
Apatite	*0.1*	*0.2*	*0.2*	*1.3*	*15.2*	*0.2*	*0.2*		*41.6*		*0.3*	*0.1*	*3.6*	*0.1*	*36.8*	*98*	Also: F-2.92wt%

Table.2. Comparison between the physical properties of CO and CM chondrites as well as ungrouped intermediate members and TAM5-30. Data sourced from a range of publications, as indicated by the following footnote symbols: *Weisberg et al., 2006, †Jones, 2012, ‡Jacquet et al., 2016, §Howard et al., 2015, Alexander et al., 2018, ¶Krot et al., 2000, #Choe et al., 2010, ΔFredrich et al., 2015, ^Davy et al., 1978, ◊Meteoritical Bulletin and •Newton et al., 1995.

Property	***CO chondrites****†Δ*	***Transitional varieties***						***CM chondrites****†Δ*
		TAM5-30	***MAC 88107****¶◊*	***NWA 5958****‡*	***LEW 85311****#*	***Acfer 094****#•*	***Adelaide****^◊*	
Avg. Chond. size *(μm)*	150	***150***	300	180	190	240	300-500	270-300
Chond. Size range *(μm)*	100-450	***60-245***	-	<100-1000	-	30-500	100-1000	0-500
Chond. Abund. *(%)*	48	***53***	-	19	30	<37.5	65	20
Metal abund. *(%)*	1-5	***1.9***	-	<1	0.3	-	minimal	0.1
Dominant chond. Type	-	***~equal***	-	Type I: 87%	-	Type I	-	-
Phyllo. Silic. Frac. *(0-1)*	<0.05	***0.4***	Low (<0.1) w/ fayalite	<0.05	Probably <0.3	<0.02	-	>0.7§
Classified as:	CO3.0-C3.7	Anom. CO 2.2-3.6	C3.1	C3.0	Anom. CM 2.6-2.7	C3.0	C2-UNGR	CM2 & CM1

3.3. Reconstructing the parent body environment: In terrestrial metamorphic petrology, prograde and retrograde paths are reconstructed using diagnostic index minerals to resolve the approximate metamorphic conditions experienced by a rock sample or rock suite. Similarly, meteorites can be analysed by an equivalent approach. Chondritic matrix mineralogy serves as a sensitive record of the parent body processing and can thus be used to constrain the environmental evolution of its parent body – or at least the local conditions of formation for a specific meteorite.

The unaltered starting material from which TAM5-30 evolved can be inferred, assuming that the low petrologic subtype CO3.0s represent the original precursor mineralogy or "*protolith*" for this sample. We deem this a reasonable assumption given their close petrographic relationship (Sect.4.2). The CO3.0s are dominated by amorphous Fe-rich silica (Keller and Buseck, 1990; Howard et al., 2015; Alexander et al., 2018), which is metastable and easily altered to secondary phases. In contrast, the matrix of TAM5-30 contains fayalite and Fe-phyllosilicates, most likely Fe-serpentine (cronstedtite) coexisting with accessory low-Ca, Fe-rich pyroxene (hedenbergite) and dark phyllosilicates (*Al,Si-rich*), while minor phases include Fe-sulfides, Cr-spinel and apatite. TAM5-30 therefore demonstrates evidence of both aqueous alteration (phyllosilicates replacing anhydrous silicates) and thermal metasomatism (development of fayalitic olivine matrix groundmass, cation diffusion removing the compositional zoning of mafic anhydrous silicates found within the matrix [Fig.4H] and maturiation of organic matter). Given this sample's close affinities to both the CM and CO chondrites a dual processing history is not necessarily surprising and potentially reflects a two-stage alteration environment.
Below we explore how each matrix mineral provides clues to the processing history of this sample:

3.3.1. Fayalite: Fayalite is a major secondary mineral found within the matrix of both the CV and CK chondrites, and its formation is evidence of oxidising conditions linked to both fluid-assisted metamorphism and low-temperature aqueous alteration (Krot et al., 2000; 2004). Zolotov et al., (2006) demonstrated using thermodynamic modelling that fayalite growth occurs between 30-350°C within a narrow range of W/R (water-to-rock) ratios (between 0.07-0.11) and at pressures typically >10 Bar – this corresponds to the transition between low-temperature aqueous alteration and thermal metamorphism. Furthermore, lower pressures, lower W/R ratios and higher temperatures progressively increase the Mg content of fayalite. Average fayalite contents in TAM5-30 range between Fa47-63, which is Mg-enriched in comparison to CV chondrites (Fa>80, Zolotov et al., 2006) and suggests that alteration occurred at either lower W/R ratios or higher temperatures than the CV chondrites. Furthermore, modelling calculations suggest that fayalite develops in equilibrium with Cr-spinel, both Fe-metal and Fe-oxides, Fe-rich pyroxenes and Fe-phyllosilicates, which is consistent with the observed mineralogy of TAM5-30.

3.3.2. Fe/Mg-phyllosilicates: In chondrites, phyllosilicates form over a wide range of environmental conditions. Initially Fe-rich serpentine develops within the matrix by the alteration of primitive GEMS (glass with embedded metal sulphides) or other amorphous silica-rich and phases (Leroux et al., 2015). This can occur rapidly (<24hrs) even at low temperatures (25-160°C) once liquid water is liberated and alkaline conditions (pH>7) prevail (Nakamura-messenger et al., 2011). However, progressive increases in the Mg content of phyllosilicate occur as Mg from anhydrous silicates is mobilized. Thus, Mg-rich phyllosilicate reflect the replacement of chondrule silicates (Howard et al., 2009; Velbel and Palmer, 2011). In TAM5-30 matrix phyllosilicates are Fe-rich (Mg#3-20). However, we also observe significant secondary replacement of chondrule silicates (Fig.1D-I) whose phyllosilicates have nearly pure Mg-serpentine compositions (Mg#~98) – as supported by the near-IR observations of Mg-phyllosilicates (potentially antigorite and lizardite species), indicating more

advanced alteration, consistent with higher temperatures, higher W/R ratios and increasingly alkaline conditions.

Temperature estimates for aqueous alteration in CM chondrites typically range from -20°C to 125°C, with a narrower range of 0-35°C favoured by most studies (Velbel et al., 2012 and references therein). In addition, the W/R ratios estimated for CM chondrites are higher than those for CR, CV or CO chondrites at approximately 0.3-0.4, as inferred from O-isotopic mixing between reservoir endmembers (Sect.4.2. and Marrocchi et al., 2018). Given that TAM5-30 is both less-altered than CM chondrites and contains phyllosilicate fractions equivalent to most CR chondrites (Sect.4.2), this micrometeorite likely accreted a similar initial W/R ratio to the CR chondrites, between 0.1-0.4 (Marrocchi et al., 2018).

3.3.3. Aqueously generated Cr-spinel: Chromite and Cr-spinel are known to form during aqueous alteration, precipitating from fluids, as reported by Tomeoka and Buseck (1985) within CM chondrites. Likewise, fluid-generated Cr-spinel was reported in micrometeorites by Suttle et al., (2019) and van Ginneken et al., (2012) within fine-grained hydrated particles. In TAM5-30, Cr-spinel is found within the matrix as dispersed grains (<3µm in size) with rounded morphologies and in close association with a coarse phyllosilicate cluster, suggesting both phases may have formed together during the replacement of a primary Cr-alloy or chromite grain. If alteration occurred together with phyllosilicate precipitation, their environmental conditions would be identical. Modelling by Zolotov et al., (2006) suggests that chromite can form either at low temperature (<40°C) and low W/R ratios (<0.03) or at higher temperatures (>280°C) and higher W/R ratios (~0.1) and thus Cr-spinel remains stable during both the formation windows of fayalite and Fe-phyllosilicate. Given the constraints of combined low W/R ratios and low temperatures, Cr-spinel in TAM5-30 most probably formed as an early secondary phase concurrent with the onset of water-ice melting.

3.3.4. Apatite: TAM5-30 also contains isolated grains of Cl, F-bearing apatite (Table.1). Apatite is a secondary mineral, whose high volatile contents are associated with fluid metasomatism (Zhang et al., 2016). In chondrites, mild parent body alteration converts P-bearing Fe/Ni-metal into merrillite [$Ca_9NaMg(PO_4)_7$]. However, with progressive alteration, increasing temperature and water-poor, Cl-rich fluids merrillite reprecipitates as apatite (Jones et al., 2014; Zhang et al., 2016). Apatite is therefore a late-stage secondary mineral. In TAM5-30, the matrix-hosted apatite grain (Fig.4l) is anhedral and appears to be growing within a void, potentially reflecting the pseudomorphic replacement of merrillite, itself a replacement of a former isolated Fe-Ni(P)-metal grain. Jones et al., (2014) estimate that apatite formation in LL3-4 chondrites occurs at temperatures >300°C concurrent with dehydration and breakdown of phyllosilicates and within a Cl-rich system. We therefore expect apatite generation in TAM5-30 to represent the last secondary mineral formed.

3.3.5 Carbonaceous matter, sulphides and carbonates: Raman spectroscopy revealed the presence of organic matter containing disordered but heated carbon (Fig.7). They act as a record of thermal processing on the parent body (Bonal et al, 2006). The D and G Raman bands from TAM5.30 have nearly the equal intensity (height), although the D-band is slightly taller than the G-band. Highly mature organic matter has D-bands significantly higher than the G-bands, while the opposite is true for immature organic matter (Bonal et al., 2006). TAM5.30 therefore represents an intermediate situation, which attest for a moderate thermal metamorphism. There is no clear dominance of aromatic over aliphatic hydrocarbons or *vice versa* in TAM5-30 also confirmed by the presence of both 3.3 µm and 3.4 µm IR bands. Aromatic hydrocarbons are commonly derived from aliphatic hydrocarbons during hydrothermal alteration. Thus the presence of both hydrocarbons attests to mild-temperature hydrothermal activity and again reflects the intermediate moderate metamorphism (Alexander et al., 2017).

In addition, the 3.8 and 3.9-4.0μm bands correspond to the presence of SH functional groups and carbonates respectively. The presence of sulfur is confirmed however by EDS spot analyses within the matrix that reveal relatively high S concentration in association with phyllosilicate (Table.1) and implies hydrothermal alteration resulting in the reaction of HS^- anions with Fe to form minerals such as Mackinawite ($[Fe,Ni]_{1+0-0.11}S$, Lennie et al., 1997). This is similar to the formation of pentlandite found within matrix olivines in the CV chondrite Allende (Brearley 1999). Metal and sulfides are in fact the first components to alter during fluid interaction with the subsequent creation of H_2 and H_2S (Alexander et al., 2017) Thus, presence of SH functional groups and possibly sulphides also supports the hypothesis of moderate thermal metamorphism.
Finally, carbonates may be present in TAM5-30 as a minor component, they are inferred from the IR data but were not confirmed as present under SEM. Carbonate formation is common during aqueous alteration, forming at both low temperature and relatively high temperatures. In the iddingsite formation process described by Lee et al. (2015), siderite forms in olivine fractures and also begins to replace phyllosilicates – this is a low-temperature route. In contrast, high temperature carbonates (primarily calcite) are formed during serpentinization reactions (Python et al., 2007). Both carbonate species are common but minor components with the CM lithology.

3.3.6. Summary of parent body processing inferred from matrix mineralogy (Fig.8):
Using the combined matrix mineralogy observed in TAM5-30 we infer the parent body processing history of this sample. TAM5-30 initially accreted with a moderate W/R ratio, intermediate between the CO and CM chondrites and equivalent to the CRs, this was approximately 10-40%. The onset of heating resulted in the formation of Fe-phyllosilicate, Cr-spinel, and Fe-oxides (possibly also carbonates as well) during an episode of low-temperature (<125°C) aqueous alteration similar to the histories of CM chondrites. However, progressively higher temperatures combined with the loss of water, consumed in alteration reactions and/or lost by de-gassing resulted in the transition to thermal metasomatic conditions more similar to those found in CV and CK chondrites. In this second episode, significantly lower W/R ratios (<0.1) combined with temperatures between 100-300°C resulted in the formation of Mg-phyllosilicates and fayalite, potentially converting pre-existing Fe-phyllosilicate to olivine as well as converting any remaining amorphous silica. Finally, at around 300°C, phyllosilicate may have begun to dehydrate as apatite recrystalized after merrillite.

3.4. Assigning a petrologic subtype to TAM5-30, aqueous alteration and thermal metasomatism: In the current system of meteorite taxonomy samples are classified by parent body group followed by a numerical designation (referred to as a petrologic subtype) which indicates the type and degree of parent body alteration. In principal, meteorites which record only nebulae processes, and following their accretion entirely avoided further parent body processing are classified as 3.0 (e.g. Acfer 094, Choe et al., 2010). Conversely, hydrated and aqueous altered samples are given lower petrographic subtypes (e.g. CM's between 2.0-2.6 [Rubin et al., 2007]) while those that are affected by thermal metamorphism receive progressively higher petrolographic subtypes (e.g. CO's between 3.0-3.7 [Rubin, 1998]). A stark contrast is therefore drawn between the CO population which record moderate degrees of thermal metamorphism (Greenwood and Franchi, 2004; Bonal et al., 2007) and the CM chondrites which are heavily affected by aqueous alteration (Rubin et al., 2007; Howard et al., 2015).

Petrologic subtypes therefore offer an alternative method for characterising the parent body processing history of TAM5-30. We employed two independent and well-established petrographic metrics – (1) the phyllosilicate fraction as a proxy for the degree of aqueous alteration, previously developed by Howard et al., (2015) and shown in Fig.5A, and (2) characterisation of carbonaceous

Raman G/D band peak parameters – using organic matter as a sensitive tracer of metamorphic grade, as established for CO chondites by Bonal et al., (2007) and shown in Fig.5B.

These metrics demonstrated that aqueous alteration in TAM5-30 is relatively advanced (C2.2) while the degree of thermal metamorphism is also relatively high (C3.6) but similar to many other CO chondrites (e.g. Kainsaz, Felix and Lance). Bonal et al., (2007) estimated that petrologic subtypes <C3.7 correspond to peak metamorphic temperatures below 330°C – this is approximately the temperature threshold above which phyllosilicates begin to dehydrate and breakdown. As such, the metamorphic temperature estimated here from Raman data is essentially identical to the estimated peak temperature conditions required to generate the fayalitic groundmass (Sect.4.3). Furthermore, the later thermal metasomatism conditions are sufficiently low temperature that they allow for the co-existence of early-formed phyllosilicate and thus prevent significant overprinting of the initial aqueous alteration processing history. The perspective from petrologic subtypes therefore supports our processing history inferred from matrix mineralogy and results in a high confidence reconstruction of this micrometeorite's asteroidal history.

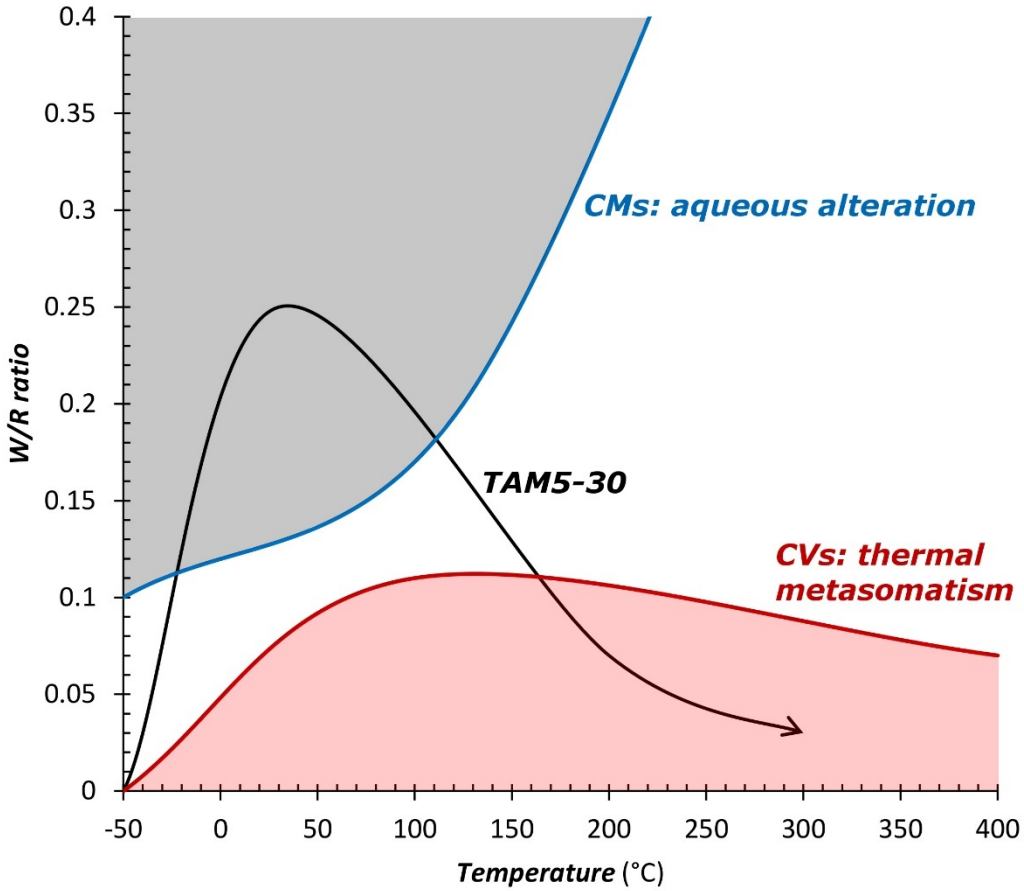

Fig.8. Reconstructed parent body processing history for TAM5-30, estimated using constraints from the particle's mineralogy and textures. Initially W/R ratios rise as water-ice melts and the parent body warms (due to radiogenic or impact heating), up to a maximum value of the total accreted water. However, progressively water is consumed in alteration reactions primarily as Fe-phyllosilicates (and also oxides) are formed (in addition water loss may be driven by de-gassing). Rising temperatures combined with lower W/R ratios transition the alteration environment into a thermal metasomatic regime, more similar to the alteration in CV chondrites and thereby resulting in the formation of fayalite and finally apatite.

4. Implications

The existence of intermediate chondritic samples such as TAM5-30 and other anomalous meteorites (e.g. MAC 88107), whose petrographic and isotopic properties are essentially transitional between the CO and CM end-members, suggests the formation of a series of related but separate parent bodies from a single geochemically and isotopically distinct region of the solar nebula. A region which itself was evolving as each parent body accreted, in a batch formation scenario. Logically, then the anhydrous CO chondrites with low volatile contents and minimal aqueous alteration (a direct consequence of minimal accreted water) should represent the earliest formed asteroids from this region. Likewise, the intermediate members and subsequently the CMs represent later-formed parent bodies which inherited progressively higher volatile contents.

Building upon the idea of a single CO-CM formation region affected by progressively increased addition of volatile δ^{18}O-rich water-ice (Chaumard et al., 2018; Marrocchi et al., 2018; Alexander, 2019), here we propose that the anomalous intermediate meteorites most likely represent asteroids formed during the critical period, after the COs and prior to the CMs. Parent bodies like those sampled by MAC 88107 and TAM5-30 therefore accreted sufficient water to experience pronounced aqueous alteration and phyllosilicate replacement, meanwhile their relatively early formation windows ensured that the energy released from accreted short-lived radioisotopes provided sufficient heat to drive thermal metasomatic alteration, resulting in higher temperature CV-like alteration histories. This would be in contrast to the CMs, whose later formation windows correlate with in higher water contents and less significant heating by radioactive decay. Instead then, the heat driving their aqueous alteration appears to be impact-driven (Lindgren et al., 2015). We also note that progressively later accretion ages could explain the general trend of larger average chondrule diameters (Table.2) among the intermediate CO/CM-like members and CM chondrites (as compared to the COs), as a direct consequence of longer chondrule growth periods prior to accretion. Such ideas can be tested by future geochronology tests using extinct short-lived radioisotope studies to constrain the timing of formation and alteration among different chondrite groups and anomalous meteorites.

5. Conclusions

The micrometeorite studied here (TAM5-30) is an anomalous hydrated carbonaceous chondrite with close petrographic and geochemical similarities to the CO and CM chondrites. This sample also records an unusual two-part post-accretion alteration history whose initial stages are CM-like, dominated by phyllosilicate formation and the replacement of chondrule silicates, occurring at high W/R ratios (~0.2) and low temperatures (<100°C). Later alteration forming fayalitic olivine, dehydrating phyllosilicate, precipitating apatite and "*cooking*" organic matter appears distinctly CV-like and corresponds to lower W/R ratios (<0.1) and higher temperatures (100-350°C). We explain both the petrographic and alteration features as a product of a unique accretion window, occurring in-between the formation of the CO and CM chondrites and therefore acquiring characteristics of both bodies. The relationship to CV chondrites is also noteworthy and reflects how a single parent body's alteration environment can evolve with time, overprinting the initial history.

Accreted water may be the most important factor controlling the alteration environment of early-formed asteroid planetesimals. Furthermore, their evolution may change significant and meteorite classification systems should be modified to accommodate their complex and multi-stage alteration histories.

Chapter 8

Discussion and conclusions

The open questions and objectives we had at the beginning of the project were the attribution of the different 3 µm band of C-type asteroid to specific mineral phases and the post accretion processing of organic matter for what concerns the compositional aspect. We also wanted to shed light on the main geological processes involving minor bodies of the Solar System, which are hydrothermal alteration and cryovolcanic processes and sublimation-outburst. Results on micrometeorites TAM5.29, TAM18c.11 and TAM18c.13 and MCY14001 chondrite gave very important advances in the understanding of the 3 µm band. TAM5.29 and TAM5.30 also provide interesting insights in the hydrothermal and aqueous alteration of the CCs parent bodies giving evidences of different and new processes found in between the already known fluid assisted alteration mechanisms. Hydrothermal experiments on MCY14001 also bring new perspectives in the hydrothermal alteration as well as on the 3 µm band nature. It thus seems that hydrothermalism and the 3 µm band are closely related. Finally we discover that cryovolcanism and sublimation-outburst are able to affect organic matter synthesis.

3 µm band nature

The TAM5.29, TAM18c.11 and TAM18c.13 are the first reported samples in the meteorite and micrometeorite collections showing a clear 3 µm band in their reflectance spectra. TAM18c.11 and TAM18c.13 are fine-grained micrometeorites with compositional affinities with the CCs, while TAM5.29 is a CV-like minimeteorite. TAM5.29 is composed by a Fe-rich olivine matrix plus andradite inclusions with haloes of diopside-jarosite formed by Fe-alkali-halogen metasomatism at 250°C. A secondary phase of low temperature aqueous alteration replaced fayalite with iddingsite, which is a pseudomorph composed by a mixture of Fe-rich hydrous phyllosilicates, Fe-oxy-hydroxes like hematite-goethite and possibly minor Fe-carbonates like siderite and chukanovite. CH and SH functional groups are found scattered all around the TAM5.29 particles. TAM5.29 revealed the presence of two bands, one with a centre at 3.15 µm and one centred at 3.07 µm. The 3.15 µm band is found closely mixed with Fe-rich altered matrix. It thus seems that the 3.15 µm band is given by Fe-OH bonds. For this reason we suggest that the Europa-like asteroids, characterised by a 3.15 µm band, are Fe-rich hydrous bodies characterised by Fe-clays and phyllosilicates created by a period of extensive hydrothermal alteration and/or low-temperature aqueous alteration.

The high Antarctic alteration and fine-grained matrix of TAM18c.11 and TAM18c.13 made the mineralogical and spectroscopic study of these samples quite difficult. Some of the original mineralogies are still recognisable (i.e. phyllosilicates and tiny metal alloys immersed in an olivine-like matrix). The majority of these samples is replaced by jarosite formed by terrestrial alteration in Antarctica. In particular, in TAM18c.11 is characterised by the presence of ammonium-jarosite. TAM18c.11 is characterised by a band centre at 3.07 µm, which, contrary to what observed in TAM5.29, is not found together with the 3.4 and 3.5 µm bands of aliphatic hydrocarbons. Thus the nature of the 3.07 µm band in TAM18c.11 is linked to the presence of the terrestrial ammonium-jarosite, the only possible mineral phase that can create this feature (and the major phase found in TAM18c.11). This suggests that on bodies with past or active aqueous alteration and cryovolcanism (e.g. Ceres) with consequent production of evaporites, the NH compounds may also be found in

sulphates and salts. However, the high instability of sulphates on low-pressure atmosphere bodies makes this hypothesis less likely or at least the contribution of NH-sulphates to the 3 µm band is most probably minimal and localized. In any case these observations suggest that the 3.07 µm band is likely related to organic matter, in particular CH and NH functional groups found in aromatic or aliphatic hydrocarbons, in the phyllosilicates lattice or in salts and sulphates, meaning that Ceres-like asteroids (which have a 3.05 ± 0.01 µm band) are bodies enriched in organic matter.

Hydrothermal experiments on the MCY14001 CM2 chondrites also contribute to the understanding of the 3 µm band. The altered powders of MCY14001 were treated with ammoniated water and their spectra show two bands at 2.9 and 3.04 µm. During hydrothermal alteration at 240°C Na-carbonates were leached from MCY14001 and turned into Na-rich phases like analcime-natrolite. Ammoniated natrolite has the major XRD peak at 14.5°2θ, one of the main peaks in the MCY14001 XRD pattern, absent in normal natrolite. This result suggests that these new mineral phases may be present on Ceres-like asteroids as ammoniated phases in addition to phyllosilicates, organic matter and salts-sulphates and that can be related to the 2.9-3 µm band.
Another remarkable result of the hydrothermal experiments is the possible ammoniation of serpentine, the only phyllosilicate detected in the MCY14001 chondrite. This was never achieved before and we infer that this process can take place at relative high temperatures (240°C) in long lasting alteration processes, comparable to those that affected Ceres.

Summarizing, the nature of the 3.15 µm band is clearly related to Fe-OH compounds. The origin of the shorter wavelength 3.04-3.07 µm band has been addressed to a series of materials like hydrocarbons, sulphates and salts, zeolite and phyllosilicates. It is difficult to conclude which one of these is actually found on C-type asteroids, but what is definitely clear is that organic compounds (in particular NH functional groups) are the main carries of this band, no matter in which phases they are found.

Cryovolcanism and organics processing

Cryovolcanism and sublimation-outburst understanding and the questions regarding organic matter post-accretional processing were initially approached separately. During the cryovolcanism experiments turned out that actually these two aspects are closely related. We demonstrated aliphatic hydrocarbons formation during very short duration sublimation-outburst processes. Temperatures of formation can be as low as -40°C and can be even lower considering the presence of anti-freezing compounds on icy bodies (e.g. salts, ammonia, chlorides). A precise mechanism of formation of aliphatic hydrocarbons in this context is still difficult to describe with the current knowledge. However it is plausible and there are the basic environmental conditions for the synthesis. We are giving energy to the system (heating the samples), we are in reducing conditions (experiments were done in vacuum) consistent to that of airless minor bodies as well as temperatures ranges (e.g. Ceres surface temperature varies between ~-170°C and ~-38°C (Formisano et al., 2015); 67P/Churyumov-Gerasimenko comet surface temperature ranges between a minimum of ~-170°C to a maximum of ~70°C (Keller et al., 2015; Pajola et al., 2017). The carbon is provided by the CCs, hydrogen by the ice and metal alloys, oxides and CAIs provide high amount of Fe, Ni and Al, which are very good catalyst of the reaction. The hydrocarbons formed in our experiments are predominantly long chain and odd chain aliphatic hydrocarbons, suggesting a shape selectivity probably exerted by mineral structures or porosity. It is very likely that there is a relation between *n*-

alkanes and the mineral structure dimensions of antigorite, vermiculite and FeNi alloys, which can either act as a trap for the organic molecules or provide catalyst elements (Fe-Ni-Al). These findings are very important for the understanding of Cometary composition as well as that of C-type asteroids, dwarf planets and icy bodies of the Solar System and other materials like micrometeorites since provide the following implications:

- Organic matter on comets is not only a direct remnant of the Solar Nebula, but cometary activity can itself create new organic species.
- On primitive minor bodies like Ceres and Themis sublimation-outburst can explain the organic-rich composition without involving exogenous carbonaceous-like material.
- Organics detection is a useful way to find possible past or present cryovolcanic activity on those bodies or areas where cryovolcanic surface expressions are absent or dubious.
- Presence of cryovolcanism is in turn evidence of the presence of water on a variety of Solar System bodies such as asteroids, dwarf planets satellites and comets. Presence of water coupled with the fact that *n*-alkanes in the C_{14}-C_{22} range are used as tracers of photosynthetic bacteria makes the long chain aliphatic hydrocarbons produced by sublimation-outburst possible biomarkers, which can be useful for astrobiology researches.
- Finally, sublimation-outburst processes are a possible mechanism for fine grained micrometeorites expulsion from the parent body, explaining at the same time the high organic matter concentration in Fg-MMs compared to the CCs.

Organic matter can also be processed by hydrothermal alteration. Hydrothermal experiments on the MCY14001 chondrites showed that CO_3 resulting from the dissolution of Na-carbonates follows two different paths depending on the oxidising or reducing conditions. Released CO_3 form new carbonates stable at high temperature like calcite and magnesite during the oxidising phase. This process can explain the overall absence of Na-carbonates on Ceres as well as the high abundance of Ca-Mg-carbonates on its surface. During the reducing phase the liberated carbon combines with H to form aromatic hydrocarbons.

Hydrothermal and aqueous alteration

Very new insights in the CCs parent bodies are inferred from the TAM5.29 and TAM5.30 micrometeorites for the CV and the CO-CM parent body respectively.

TAM5.29 is an unambiguous and unique minimeteorite from the CV chondrite group, belonging to the CV_{OX} family. This samples record three different stages: metasomatism, impact compaction and low-temperature aqueous alteration. It retains a mineralogy dominated by thermal metamorphism products formed at ~275-250°C within the presence of Fe-alkali-halogens-rich fluids and under highly oxidizing conditions resulting in significant Fe enrichment. Primary mineral phases of TAM5.29 are Fe-rich olivine, andradite and Ca-Fe-rich pyroxenes plus carbonaceous matter containing OH, SH and CH functional groups. Fayalite crystals grew during thermal metamorphism potentially from an amorphous precursor phase in presence of fluids.

The fine-grained material is derived by two distinct alteration events. The metasomatic process created Ni-Fe sulfides (e.g. tochilinite and mackinawite), Mg-Ca-Al-Ti oxides and, FeO-OH compounds.

Low temperature alteration is instead responsible for the formation of Mg-Fe-phyllosilicates, mainly saponite and possibly phlogopite, and minor Fe carbonates (e.g. chukanovite-siderite).

TAM5.29 mineralogy is unique among the micrometeorites and minimeteorites and is also partly different from the known CV chondrites. TAM5.29 lies in between the CV_{oxA} and CV_{oxB}. CV_{oxA} are rich in andradite, magnetite and FeNiS like TAM5.29 but lacks of high abundances of hydrated minerals, common in TAM5.29. Conversely CV_{oxB} are rich in hydrated phyllosilicates but contains almost pure fayalite not found in TAM5.29. TAM5.29 retains a mineralogical assemblage, which is the up to date missing link between the CV_{oxA} and CV_{oxB}.
This intermediate mineralogy may represent a new alteration environment on the CV parent body, similar to the conditions recorded by other CVs but with differences consisting in: higher oxidizing conditions, heterogeneous thermal metamorphism that shows different degrees of alteration even within one single small micrometeorite and a different secondary alteration history enabled by the following impact history.
This is the proof of more heterogeneous CV parent body(-ies) thus adding a unique sample to the known CV lithologies.

The three main stages that created TAM5.29 can be schematized as follows:

- Stage one: metasomatism at ~275-250°C with Fe-alkali-halogens-rich fluids occurred on the parent body.
- Stage two: the particle was involved in an impact that terminated the metamorphic event resulting in a strongly unequilibrated composition with cryptocrystalline and amorphous phases and generating a preferred orientation in the olivine petrofabric.
- Stage three: formation of iddingsite at lower temperatures, possibly from fluid released by hydrated minerals during the impact.

Further information on the combined hydrothermal and low-temperature aqueous alteration on the CCs parent bodies and relative heterogeneities were studied on the TAM5-30 micrometeorite. TAM5.30 is an anomalous hydrated carbonaceous micrometeorite with close petrographic and geochemical similarities to the CO and CM chondrites. This sample also records an unusual post-accretion alteration history divided into two parts. The initial stage is similar to the alteration displayed by CM chondrites, dominated by phyllosilicate formation and the replacement of chondrule silicates, occurring at high W/R ratios (~0.2) and low temperatures (<100°C). A second later stage of alteration recalls distinctly a CV-like process forming fayalitic olivine, dehydrating phyllosilicate, precipitating apatite and "*cooking*" organic matter and corresponds to lower W/R ratios (<0.1) and higher temperatures (100-350°C). We explain both the petrographic and alteration features as a product of a unique accretion window, occurring in-between the formation of the CO and CM chondrites and therefore acquiring characteristics of both bodies. The relationship to CV chondrites is also noteworthy and reflects how a single parent body's alteration environment can evolve with time, overprinting the initial history with multi-stage alterations recorded by an high heterogeneity.

The hydrothermal experiments on CCs point to a CM-like composition of Ceres-like asteroids rather than a CO chondrites composition. High W/R ratios (~1) and ammonia-rich fluids appeared to be necessary for a hydrothermal alteration consistent with that of C-type Ceres-like asteroids. In the MCY14001 chondrite experiment there has been a change in oxidising to reducing conditions, with formation of magnetite and sulfides respectively. This suggests that changing conditions may take

place in one single body, giving rise to the observed heterogeneities also reported by TAM5.29 and TAM5.30. Another common observation between TAM5.29 and the hydrothermal experiments on MCY14001 is that fluid assisted metamorphism at ~250°C is responsible for the enrichment in Ca and Fe of the silicates, with the formation of Fe-enstatite and diopside. Carbonates are another active component in the hydrothermal alteration process. During hydrothermal alteration Na-carbonates become unstable and are replaced by Na-rich phases like analcime-natrolite. This process can explain the overall absence of Na-carbonates on Ceres and instead the high abundance of Ca-Mg-carbonates whose formation is favoured by hydrothermal alteration.

Conclusions

With this study we describe a very complex geology of primitive icy bodies of the Solar System. The micrometeorites studied show new intermediate compositions between CV, CM and CO chondrite groups. This assumption implies that meteorite classification systems should be modified to accommodate their complex and multi-stage alteration histories.

Hydrothermal alteration and aqueous alteration create Fe-rich hydrous phases, carriers of longer wavelengths 3 μm bands (3.15 μm), as well as other phases that can be ammoniated via hydrothermalism like phyllosilicates and zeolites that are related to shorter wavelengths 3 μm bands (3.05 ± 0.01). Cryovolcanism, sublimation and outbursts are the main mechanism creating aliphatic hydrocarbons that can be processed during metasomatism to produce aromatic hydrocarbons, which can be in turn ammoniated in a NH-rich fluids reducing environment.

This work adds new important perspectives on the primitive icy bodies of the Solar System, but can also give new ideas for further projects of investigations, especially regarding organic matter. In particular further knowledge can be achieved by irradiation experiments on organic-rich samples made in laboratory to assess the post-formation fate of organics when exposed to solar radiation on airless planetary bodies. Organics-minerals relations can be investigated as well as changing in starting composition of meteorites and fluid during cryovolcanism and hydrothermalism experiments. Finally direct observations on icy bodies surfaces to detect hydrothermal and cryovolcanic features as well as sublimation sites will be pivotal for looking for organic matter on different environments assessing their formation process and age.

Acknowledgements

Europlanet 2020 Research Infrastructure (EPN2020-RI) has received funding from the European Union's Horizon 2020 research and innovation programme under grant agreement No 654208.

We are grateful to the MNA (Museo Nazionale dell'Antartide, Siena, Italy) for the loan of the meteorite samples, in particular we want to thank Sonia Sandroni for the support.

Thank also to the ANSMET (The US Antarctic search for meteorites) for the loan of part of the carbonaceous chondrites, in particular to Kevin Righter for the help during the request.

Thanks to Cristian Carli and Stefania Stefani for the support and access to the laboratories at the INAF-Rome. A special thank to Cristian Carli for his expertise, support and helpful discussions in the spectroscopic study of micrometeorites and chondrites. Thank also to Francesca Zambon for her suggestions and useful discussion on the spectroscopy of minor bodies.

All the micrometeorites petrographic analyses and interpretations were made with the very important help and essential collaboration of Martin Suttle, to whom we are very grateful.

Special thank to Richard Spiess for the important EBSD analyses and interpretations.

Another special thank goes to Alessandro Maturilli for the IR spectra analyses of carbonaceous chondrites and for the cryovolcanism and hydrothermal experiments, his help and laboratory expertise have been crucial for the realization of this project. Thank also to Joern Helbert for the access at the PSL laboratory and to Giulia Alemanno for the help with the experiments.

We also want to thank Raul Carampin for the EMPA analyses and Leonardo Tauro for the help with the SEM-EDS analyses. Thanks to Gabriella Salviulo and Federico Zorzi for the support and access to the XRD laboratory.

Thank to Jens Najorka for the μXRD analyses of TAM5.29 and their interpretation.

We are also grateful to Randa Anis Ishak and to Fabrizio Campanale for the support with the FE-SEM-EDS analyses.

We are very grateful to Sarah Pizzini and Patrizia Ferretti for the gas chromatography analyses and especially for the great and very helpful discussions on organic matter.

Thank to Sofia Genovesi, undergraduated student at the University of Bologna, who helped us acquiring bulk composition during her internship at the University of Padua.

We also want to thank Mathias van Ginneken who prepared the resin block containing the micrometeorite samples.

Thanks to Harald Hiesinger and Jan Hendrik Pasckert for the visiting period in Münster, for providing us Framing Cameras images of Ceres and for the help with the mapping and crater chronology.

We are grateful to Maria Cristina De Sanctis for providing us the average spectrum of Ceres acquired by the NASA-Dawn spacecraft and to Driss Takir for the C-type asteroids spectra.

This work was also supported by MIUR grants: Meteoriti Antartiche (PI# PNRA16_00029) and Cosmic Dust (PI# PRIN2015_20158W4JZ7).

References

A'Hearn, M. F., Belton, M. J., Delamere, W. A., Feaga, L. M., Hampton, D., Kissel, J., ... & Schultz, P. H. 2011. EPOXI at comet Hartley 2. *Science*, *332*(6036), 1396-1400.

Abreu N. M. & Brearley A. J. 2011. Deciphering the nebular and asteroidal record of silicates and organic material in the matrix of the reduced CV3 chondrite Vigarano. Meteoritics & Planetary Science, 46:252-274.

Aichner, B., Herzschuh, U., & Wilkes, H. 2010. Influence of aquatic macrophytes on the stable carbon isotopic signatures of sedimentary organic matter in lakes on the Tibetan Plateau. *Organic Geochemistry*, *41*(7), 706-718.

Alexander, C.M.D., 2019. Quantitative models for the elemental and isotopic fractionations in chondrites: The carbonaceous chondrites. *Geochim. Cosmochim. Acta* 254, 277-309, doi:10.1016/j.gca.2019.02.008

Alexander, C. O. D., Cody, G. D., De Gregorio, B. T., Nittler, L. R., & Stroud, R. M. 2017. The nature, origin and modification of insoluble organic matter in chondrites, the major source of Earth's C and N. *Chem Erde-Geohem*, 77, 227-256, doi:10.1016/j.chemer.2017.01.007.

Alexander, C.M.O'D., Greenwood, R.C., Bowden, R., Gibson, J.M., Howard, K.T. and Franchi, I.A., 2018. A mutli-technique search for the most primitive CO chondrites. *Geochim. Cosmochim. Acta* 221, 406-420, doi:10.1016/j.gca.2017.04.021.

Amthauer G. & Rossman G. R. 1998. The hydrous component in andradite garnet. *American Mineralogist*, *83*(7-8):835-840.

Bach W. & Klein F. 2009. The petrology of seafloor rodingites: insights from geochemical reaction path modeling. *Lithos*, *112*(1-2):103-117.

Barucci, M.A., Dotto, E. and Levasseur-Regourd, A.C., 2011. Space missions to small bodies: asteroids and cometary nuclei. *Astron. Astrophys. Rev*, 19, doi:10.1007/s00159-011-0048-2.

Beck, P., Quirico, E., Sevestre, D., Montes-Hernandez, G., Pommerol, A., & Schmitt, B. 2011. Goethite as an alternative origin of the 3.1 μm band on dark asteroids. *Astronomy & Astrophysics*, *526*, A85.

Belton, M.J.S. & Melosh, J. 2009. Fluidization and multiphase transport of particulate cometary materials an explanation of the smooth terrains and repetitive outbursts on 9P/Tempel 1. *Icarus,* 200, 280-291.

Belton, M. J., Feldman, P. D., A'Hearn, M. F., & Carcich, B. 2008. Cometary cryo-volcanism: Source regions and a model for the UT 2005 June 14 and other mini-outbursts on Comet 9P/Tempel 1. *Icarus*, *198*(1), 189-207.

Belton, M. J. S. 2010. Cometary activity, active areas and a mechanism for collimated outflows on 1P, 9P, 19P and 81P. *Icarus* 210, 881-897.

Belton, M. J. 2017. Hyperactivity in 103P/Hartley 2: Chunks from the sub-surface in Type IIa jet regions. *Icarus*, *285*, 58-67.

Benedix, G. K., Haack, H., & McCoy, T. J. 2014. Iron and stony-iron meteorites. *Meteorites and cosmochemical processes*, Volume 1 of Treatise on Geochemistry (Second Edition). Elsevier, edited by Andrew M. Davis, p.267-285.

Bland, P. A. 2001. Quantification of meteorite infall rates from accumulations in deserts, and meteorite accumulations on Mars. In *Accretion of extraterrestrial matter throughout Earth's history*(pp. 267-303). Springer, Boston, MA.

Bland P.A., Collins G.S., Davidson T.M., Abreu N.M., Ciesla F.J., Muxworthy A.R. and Moore J. 2014. Pressure-temperature evolution of primordial Solar System solids during impact-induced compaction. Nature Communications, 5:5451.

Beran, A., Armstrong, J., & Rossman, G. R. 1992. Infrared and electron microprobe analysis of ammonium ions in hyalophane feldspar. *European Journal of Mineralogy*, *4*(4), 847-850.

Bonal L., Quirico E., Bourot-Denise M. & Montagnac G. 2006. Determination of the petrologic type of CV3 chondrites by Raman spectroscopy of included organic matter. Geochimica et Cosmochimica Acta, 70:1849-1863.

Bonal, L., Bourot-Denise, M., Quirico, E., Montagnac, G. and Lewin, E., 2007. Organic matter and metamorphic history of CO chondrites. *Geochim. Cosmochim. Acta* 71, 1605-1623, doi:10.1016/j.gca.2006.12.014.

Bonal L., Battandier M., Beck, P. and Quirico, E. 2019. Study of a series of fine-grained AMMs: multi-analytical

characterization and comparison with carbonaceous chondrites. 82nd Annual Meeting of The Meteoritical Society.

Brearley A.J. 1999. Origin of graphitic carbon and pentlandite in matrix olivines in the Allende meteorite. Science, 285:1380-1382.

Brearley, A. J., & Jones, R. H. 1998. Planetary materials. *Reviews in Mineralogy and Geochemistry*, *36*, 3-1.

Brearley, A. J. 2014. Nebular versus parent body processing. Meteorites and Cosmochemical Processes, Volume 1 of Treatise on Geochemistry (Second Edition). Elsevier. Edited by Andrew M. Davis, p.309-334.

Brunetto, R., Lantz, C., Dionnet, Z., Borondics, F., Aléon-Toppani, A., Baklouti, D., ... & Pilorget, C. 2018. Hyperspectral FTIR imaging of irradiated carbonaceous meteorites. *Planetary and Space Science*, *158*, 38-45.

Bu, C., Rodriguez Lopez, G., Dukes, C. A., Ruesch, O., McFadden, L. A., & Li, J. Y. 2018. Search for sulfates on the surface of Ceres. *Meteoritics & Planetary Science*, *53*(9), 1946-1960.

Burbine, T. H., Buchanan, P. C., Binzel, R. P., Bus, S. J., Hiroi, T., Hinrichs, J. L., ... & McCoy, T. J. 2001. Vesta, Vestoids, and the howardite, eucrite, diogenite group: Relationships and the origin of spectral differences. *Meteoritics & Planetary Science*, *36*(6), 761-781.

Burbine, T.H., 2013. Asteroids. Planets, Asteriods, Comets and The Solar System, Volume 2 of Treatise on Geochemistry (Second Edition). Edited by Andrew M. Davis. Elsevier, 2014., p.365-415.

Burton, A. S., Stern, J. C., Elsila, J. E., Glavin, D. P., & Dworkin, J. P. 2012. Understanding prebiotic chemistry through the analysis of extraterrestrial amino acids and nucleobases in meteorites. *Chemical Society Reviews*, *41*(16), 5459-5472.

Bystricky M, Kunze K, Burlini M., & Burg J.-P., 2000. High Shear Strain of Olivine Aggregates: Rheological and Seismic Consequences. Scienze, 290, 1564-1567.

Capaccioni, F. A., Coradini, A., Filacchione, G., Erard, S., Arnold, G., Drossart, P., ... & Leyrat, C. 2015. The organic-rich surface of comet 67P/Churyumov-Gerasimenko as seen by VIRTIS/Rosetta. *Science*, *347*(6220), aaa0628.

Carporzen L., Weiss B.P., Elkins-Tanton L.T., Shuster D.L., Ebel D. and Gattacceca J. 2011. Magnetic evidence for a partially differentiated carbonaceous chondrite parent body. Proceedings of the National Academy of Sciences, 108:6386-6389, doi:10.1073/pnas.1017165108.

Carrillo-Sánchez, J. D., Plane, J. M. C., Feng, W., Nesvorný, D., & Janches, D. 2015. On the size and velocity distribution of cosmic dust particles entering the atmosphere. *Geophysical research letters*, *42*(15), 6518-6525.

Carrozzo, F. G., De Sanctis, M. C., Raponi, A., Ammannito, E., Castillo-Rogez, J., Ehlmann, B. L., ... & Capaccioni, F. 2018. Nature, formation, and distribution of carbonates on Ceres. *Science advances*, *4*(3), e1701645.

Castillo-Rogez J. C., Matson D. L., Kargel J. S., Vance S. D. & Johnson T. V. 2008. Role of hydrothermal geochemistry in the geophysical evolution of icy bodies. In *Lunar and Planetary Science Conference* (Vol. 39, p. 2461).

Chaumard, N., Defouilloy, C. and Kita, N.T., 2018. Oxygen isotope systematics of chondrules in the Murchison CM2 chondrite and implications for the CO-CM relationship. *Geochim. Cosmochim. Acta* 228, 220-242, doi:10.1016/j.gca.2018.02.040.

Che, C. and Glotch, T.D., 2012. The effect of high temperatures on the mid-to-far-infrared emission and near-infrared reflectance spectra of phyllosilicates and natural zeolites: Implications for Martian exploration. *Icarus*, 218, 585-601, doi:10.1016/j.icarus.2012.01.005.

Choe, W.H., Huber, H., Rubin, A.E., Kallemeyn, G.W. and Wasson, J.T., 2010. Compositions and taxonomy of 15 unusual carbonaceous chondrites. *Meteorit. Planet. Sci.* 45, 531-554, doi:10.1111/j.1945-5100.2010.01039.x.

Clayton, R.N. and Mayeda, T.K., 1999. Oxygen isotope studies of carbonaceous chondrites. *Geochim. Cosmochim. Acta* 6, 2089-2104, doi:10.1016/S0016-7037(99)00090-3.

Clayton, R.N., Onuma, N., Grossman, L. and Mayeda, T.K., 1977. Distribution of the pre-solar component in Allende and other carbonaceous chondrites. *Earth Planet. Sci. Lett.* 34, 209-224, doi:10.1016/0012-821X(77)90005-X.

Cloutis, E. A. 2003. Quantitative characterization of coal properties using bidirectional diffuse reflectance spectroscopy. *Fuel*, *82*(18), 2239-2254.

Cordier, C., Baecker, B., Ott, U., Folco, L., & Trieloff, M. 2018. A new type of oxidized and pre-irradiated micrometeorite. *Geochimica et Cosmochimica Acta*, *233*, 135-158.

Davy, R., Whitehead, S.G. and Pitt, G., 1978. The Adelaide meteorite. *Meteoritics* 13, 121-140, doi:10.1111/j.1945-5100.1978.tb00802.x.

De Bergh, C., Schmitt, B., Moroz, L.V., Quirico, E. and Cruikshank, D.P. 2008. Laboratory data on ices, refractory carbonaceous materials, and minerals relevant to transneptunian objects and Centaurs. *The Solar System Beyond Neptune*, A. Barucci, H. Boehnhardt, D. Cruikshank, A. Morbidelli, Eds. (Univ. of Arizona Press, Tucson, AZ), 483–506.

DeMeo, F. E., Binzel, R. P., Slivan, S. M., & Bus, S. J. 2009. An extension of the Bus asteroid taxonomy into the near-infrared. *Icarus*, *202*(1), 160-180.

DeMeo, F.E. and Carry, B., 2014. Solar System evolution from compositional mapping of the asteroid belt. *Nature* 505, 629-634, doi:10.1038/nature12908.

de Niem, D., Kührt, E., Hviid, S. & Davidsson, B. 2018. Low velocity collisions of porous planetesimals in the early solar system. *Icarus* 301, 196-218.

De Sanctis, M. C., Ammannito, E., Raponi, A., Marchi, S., McCord, T. B., McSween, H. Y., ... & Longobardo, A. 2015. Ammoniated phyllosilicates with a likely outer Solar System origin on (1) Ceres. *Nature*, *528*(7581), 241.

De Sanctis, M. C., Raponi, A., Ammannito, E., Ciarniello, M., Toplis, M. J., McSween, H. Y., ... & Tosi, F. 2016. Bright carbonate deposits as evidence of aqueous alteration on (1) Ceres. *Nature*, *536*(7614), 54.

De Sanctis, M. C., Ammannito, E., McSween, H. Y., Raponi, A., Marchi, S., Capaccioni, F., ... & Formisano, M. 2017. Localized aliphatic organic material on the surface of Ceres. *Science*, *355*(6326), 719-722.

De Sanctis, M. C., Vinogradoff, V., Raponi, A., Ammannito, E., Ciarniello, M., Carrozzo, F. G., ... & Russell, C. T. 2019. Characteristics of organic matter on Ceres from VIR/Dawn high spatial resolution spectra. *Monthly Notices of the Royal Astronomical Society*, *482*(2), 2407-2421.

Desch, S. J. & Neveu, M. 2017. Differentiation and cryovolcanism on Charon: A view before and after New Horizons. *Icarus* 287, 175-186.

Dionnet, Z., Aleon-Toppani, A., Baklouti, D., Borondics, F., Brisset, F., Djouadi, Z., ... & Brunetto, R. 2018. Organic and mineralogic heterogeneity of the Paris meteorite followed by FTIR hyperspectral imaging. *Meteoritics & Planetary Science*, *53*(12), 2608-2623.

Downs R.T, & Hall-Wallace M. 2003. The American Mineralogist Crystal Structure Database. American Mineralogist 88, 247-250.

Ehlmann, B. L., Hodyss, R., Bristow, T. F., Rossman, G. R., Ammannito, E., De Sanctis, M. C., & Raymond, C. A. 2018. Ambient and cold-temperature infrared spectra and XRD patterns of ammoniated phyllosilicates and carbonaceous chondrite meteorites relevant to Ceres and other solar system bodies. *Meteoritics & Planetary Science*, *53*(9), 1884-1901.

Elkins-Tanton L.T., Weiss B.P. and Zuber M.T. 2011. Chondrites as samples of differentiated planetesimals. Earth and Planetary Science Letters, 305:1-10, doi:10.1016/j.epsl.2014.11.019.

Elsila, J. E., de Leon, N. P., Buseck, P. R., & Zare, R. N. 2005. Alkylation of polycyclic aromatic hydrocarbons in carbonaceous chondrites. *Geochimica et Cosmochimica Acta*, *69*(5), 1349-1357.

Fagents, S.A. 2003. Considerations for effusive cryovolcanism on Europa: the post-Galileo perspective. *Journal of Geophysical Research* 108(E12).

Feely, K.C. and Christensen, P.R., 1999. Quantitative compositional analysis using thermal emission spectroscopy: Application to igneous and metamorphic rocks. *J. Geophys. Res.* 104, 24195-24210, doi:10.1029/1999JE001034.

Ferrari, M., De Angelis, S., De Sanctis, M. C., Ammannito, E., Stefani, S., & Piccioni, G. 2019. Reflectance spectroscopy of ammonium-bearing phyllosilicates. *Icarus*, *321*, 522-530.

Ficken, K. J., Street-Perrott, F. A., Perrott, R. A., Swain, D. L., Olago, D. O., & Eglinton, G. 1998. Glacial/interglacial variations in carbon cycling revealed by molecular and isotope stratigraphy of Lake Nkunga, Mt. Kenya, East Africa. *Organic Geochemistry*, *29*(5-7), 1701-1719.

Filacchione, G., Groussin, O., Herny, C., Kappel, D., Mottola, S., Oklay, N., ... & Moroz, L. 2019. Comet 67P/CG nucleus composition and comparison to other comets. *Space Science Reviews*, *215*(1), 19.

Flynn, G. J., Durda, D. D., Sandel, L. E., Kreft, J. W., & Strait, M. M. 2009. Dust production from the hypervelocity impact disruption of the Murchison hydrous CM2 meteorite: Implications for the disruption of hydrous asteroids and the production of interplanetary dust. *Planetary and Space Science*, *57*(2), 119-126.

Folco, L. and Rastelli, N. 2002. The meteorite collection of the Museo Nazionale dell'Antartide in Siena–December 2002 update.

Folco, L., Rochette, P., Perchiazzi, N., D'Orazio, M., Laurenzi, M. A., & Tiepolo, M. 2008. Microtektites from Victoria land transantarctic mountains. *Geology*, *36*(4), 291-294.

Folco L. and Rochette P. 2010. Minimeteorites from the Transantarctic Mountains. Meteoritics and Planetary Science Supplement, 73.

Forman L. V., Bland P. A., Timms N. E., Collins G. S., Davison T. M., Ciesla F. J., Benedix G.K., Daly L., Trimby P.W., Yang L. & Ringer, S. P. 2016. Hidden secrets of deformation: Impact-induced compaction within a CV chondrite. *Earth and Planetary Science Letters*, *452*, 133-145.

Forman L. V., Bland P. A., Timms N. E., Daly L., Benedix G. K., Trimby P. W., Collins G.S. & Davison, T. M. 2017. Defining the mechanism for compaction of the CV chondrite parent body. *Geology*, *45*:559-562.

Formisano, M., De Sanctis, M. C., Magni, G., Federico, C., & Capria, M. T. 2015. Ceres water regime: Surface temperature, water sublimation and transient exo (atmo) sphere. *Monthly Notices of the Royal Astronomical Society* 455(2), 1892-1904.

Fray, N., Bardyn, A., Cottin, H., Altwegg, K., Baklouti, D., Briois, C., ... & Grün, E. 2016. High-molecular-weight organic matter in the particles of comet 67P/Churyumov–Gerasimenko. *Nature*, *538*(7623), 72.

Friedrich, J.M., Weisberg, M.K., Ebel, D.S., Biltz, A.E., Corbett, B.M., Iotzov, I.V., Khan, W.S. and Wolman, M.D., 2015. Chondrule size and related physical properties: A compilation and evaluation of current data across all meteorite groups. *Chemie der Erde-Geochemistry* 75, 419-443, doi:10.1016/j.chemer.2014.08.003.

Gail H. P., Henke S. & Trieloff M. 2015. Thermal evolution and sintering of chondritic planetesimals-II. Improved treatment of the compaction process. Astronomy & Astrophysics, 576, A60.

Gattacceca J., Rochette P., Denise M., Consolmagno G. & Folco L. 2005. An impact origin for the foliation of chondrites. *Earth and Planetary Science Letters*, *234*(3-4), 351-368.

Glavin, D. P., Callahan, M. P., Dworkin, J. P., & Elsila, J. E. 2010. The effects of parent body processes on amino acids in carbonaceous chondrites. *Meteoritics & Planetary Science*, *45*(12), 1948-1972.

Genge M. J., Grady M. M. & Hutchison R. 1997. The textures and compositions of fine-grained Antarctic micrometeorites: Implications for comparisons with meteorites. *Geochimica et Cosmochimica Acta*, *61*(23):5149-5162.

Genge M.J. and Grady M.M. 1998. The fusion crusts of stony meteorites: Implications for the atmospheric reprocessing of extraterrestrial materials. Meteoritics & Planetary Science, 34:341-356, doi:10.1111/j.1945-5100.1999.tb01344.x.

Genge M. J. 2006. Igneous rims on micrometeorites. *Geochimica et Cosmochimica Acta*, *70*(10):2603-2621.

Genge, M. J., Engrand, C., Gounelle, M., & Taylor, S. 2008. The classification of micrometeorites. *Meteoritics & Planetary Science*, *43*(3), 497-515.

Genge M.J. 2010. A Primitive Micrometeorite with Affinities to CV3 Chondrite Matrix. Meteoritics and Planetary Science Supplement, 73.

Gérard M., Caquineau S., Pinheiro J. & Stoops G. 2007. Weathering and allophane neoformation in soils developed on volcanic ash in the Azores. *European journal of soil science*, *58*(2), 496-515.

Goto, M., Gaessler, W., Hayano, Y., Iye, M., Kamata, Y., Kanzawa, T., ... & Takato, N. 2003. Spatially resolved 3 micron spectroscopy of IRAS 22272+ 5435: Formation and evolution of aliphatic hydrocarbon dust in proto-planetary nebulae. *The Astrophysical Journal*, *589*(1), 419.

Greshake A., Bischoff A., Putnis A. & Palme H. 1996. Corundum, rutile, periclase, and CaO in Ca, Al-rich inclusions from carbonaceous chondrites. Science, 272(5266):1316-1318.

Grimm, R. E., & McSween Jr, H. Y. 1989. Water and the thermal evolution of carbonaceous chondrite parent bodies. *Icarus*, *82*(2), 244-280.

Grimalt, J., & Albaigés, J. 1987. Sources and occurrence of C12 C22n-alkane distributions with even carbon-number preference in sedimentary environments. *Geochimica et Cosmochimica Acta*, *51*(6), 1379-1384.

Gonczi, R., Froeschlé, C., & Froeschle, C. 1982. Poynting-Robertson drag and orbital resonance. *Icarus*, *51*(3), 633-654.

Gounelle, M., Chaussidon, M., Morbidelli, A., Barrat, J.A., Engrand, C., Zolensky, M.E. and McKeegan, K.D., 2009. A unique basaltic micrometeorite expands the inventory of solar system planetary crusts. *Proc. Natl. Acad. Sci. U.S.A.* 106, 6904-6909, doi:10.1073/pnas.0900328106.

Greenwood, R.C. and Franchi, I.A., 2004. Alteration and metamorphism of CO3 chondrites: Evidence from oxygen and carbon isotopes. *Meteorit. Planet. Sci* 39, 1823-1838, doi:10.1111/j.1945-5100.2004.tb00078.x.

Greenwood, R.C., Howard, K.T., King, A.J., Lee, M.R., Burbine, T.H., Franchi, I.A., Anand, M., Findlay, R. and Gibson, M., 2019. Oxygen Isotope Evidence for Multiple CM Parent Bodies: What Will We Learn from the Hayabusa2 and OSIRIS-REx Sample Return Missions?. 50th *Lunar and Planetary Science Conference*, held 18th-22nd March, 2019 at The Woodlands, Texas. LPI Contribution No. 2132 (abstract#3191).

Hallenbeck, S.L., Nuth III, J.A. and Daukantas, P.L., 1998. Mid-infrared spectral evolution of amorphous magnesium silicate smokes annealed in vacuum: Comparison to cometary spectra. *Icarus* 131, 198-209, doi:10.1006/icar.1997.5854.

Han, J., & Calvin, M. 1969. Hydrocarbon distribution of algae and bacteria, and microbiological activity in sediments. *Proceedings of the National Academy of Sciences*, *64*(2), 436-443.

Hargrove, K. D., Kelley, M. S., Campins, H., Licandro, J., & Emery, J. 2012. Asteroids (65) cybele,(107) camilla and (121) hermione: Infrared spectral diversity among the cybeles. *Icarus*, *221*(1), 453-455.

Hargrove, K. D., Emery, J. P., Campins, H., & Kelley, M. S. 2015. Asteroid (90) Antiope: Another icy member of the Themis family?. *Icarus*, *254*, 150-156.

Harvey R. P. & Maurette M. 1991. The origin and significance of cosmic dust from the Walcott Névé, Antarctica. In *Lunar and Planetary Science Conference Proceedings* (Vol. 21, pp. 569-578).

Hayatsu, R., & Anders, E. 1981. Organic compounds in meteorites and their origins. In *Cosmo-and geochemistry* (pp. 1-37). Springer, Berlin, Heidelberg.

Head, J., Pappalardo, R., Collins, G., Belton, M. J., Giese, B., Wagner, R., ... & Moore, J. 2002. Evidence for Europa-like tectonic resurfacing styles on Ganymede. *Geophysical Research Letters*, *29*(24), 4-1.

Helfenstein, P., Thomas, P. C., Veverka, J., Squyres, S., Rathbun, J. A., Denk, T., ... & Turtle, E. 2005. Geological features and terrains on Enceladus as seen by Cassini ISS. In *Bulletin of the American Astronomical Society* (Vol. 37, p. 701).

Hendrix, A. R., Vilas, F., & Li, J. Y. 2016. Ceres: Sulfur deposits and graphitized carbon. *Geophysical Research Letters*, *43*(17), 8920-8927.

Hiesinger, H., Marchi, S., Schmedemann, N., Schenk, P., Pasckert, J. H., Neesemann, A., ... & Bland, M. T. 2016. Cratering on Ceres: Implications for its crust and evolution. *Science*, *353*(6303), aaf4759.

Housley R.M. and Cirlin E.H. 1983. On the alteration of Allende Chondrules and the formation of matrix. In Chondrules and Their Origins (ed. E. D. King), pp. 145-161. Lunar and Planetary Institute, Houston, Texas, USA.

Howard, K.T., Benedix, G.K., Bland, P.A. and Cressey, G., 2009. Modal mineralogy of CM2 chondrites by X-ray diffraction (PSD-XRD). Part 1: Total phyllosilicate abundance and the degree of aqueous alteration. *Geochim. Cosmochim. Acta* 73, 4576-4589, doi:10.1016/j.gca.2009.04.038.

Howard K. T., Benedix G. K., Bland P. A. & Cressey G. 2010. Modal mineralogy of CV3 chondrites by X-ray diffraction (PSD-XRD). *Geochimica et Cosmochimica Acta*, *74*(17), 5084-5097.

Howard, K.T., Alexander, C.O.D., Schrader, D.L. and Dyl, K.A., 2015. Classification of hydrous meteorites (CR, CM and C2 ungrouped) by phyllosilicate fraction: PSD-XRD modal mineralogy and planetesimal environments. *Geochim. Cosmochim. Acta* 149, 206-222, doi:10.1016/j.gca.2014.10.025

Jacquet, E., 2014. The quasi-universality of chondrule size as a constraint for chondrule formation models. *Icarus* 232, 176-186, doi:10.1016/j.icarus.2014.01.012.

Jacquet, E., Barrat, J.A., Beck, P., Caste, F., Gattacceca, J., Sonzogni, C. and Gounelle, M., 2016. Northwest Africa 5958: A weakly altered CM-related ungrouped chondrite, not a CI 3. *Meteorit. Planet. Sci* 51, 851-869, doi:10.1111/maps.12628.

Jet Propulsion Laboratory, Solar system dynamics, Nasa 2019 (accessed on 26/05/2019) available at: https://ssd.jpl.nasa.gov/

Jewitt, D. C. 2004. From cradle to grave: The rise and demise of the comets. *Comets II*, 659-676.

Jones, C. L., & Brearley, A. J. 2006. Experimental aqueous alteration of the Allende meteorite under oxidizing conditions: constraints on asteroidal alteration. *Geochimica et Cosmochimica Acta*, *70*(4), 1040-1058.

Jones, R.H. 2012. Petrographic constraints on the diversity of chondrule reservoirs in the protoplanetary disk. Meteoritics and Planetary Science, 47:1176-1190, doi:10.1111/j.1945-5100.2011.01327.x.

Jones, R.H., McCubbin, F.M., Dreeland, L., Guan, Y., Burger, P.V. and Shearer, C.K., 2014. Phosphate minerals in LL chondrites: A record of the action of fluids during metamorphism on ordinary chondrite parent bodies. *Geochim. Cosmochim. Acta* 132, 120-140, doi:10.1016/j.gca.2014.01.027.

Jung H., Katayama I., Jiang Z., Hiraga T. & Karato S. I. 2006. Effect of water and stress on the lattice-preferred orientation of olivine. Tectonophysics, 421:1-22.

Kallemeyn, G.W. and Wasson, J.T., 1981. The compositional classification of chondrites—I. The carbonaceous chondrite groups. *Geochim. Cosmochim. Acta* 45, 1217-1230, doi:10.1016/0016-7037(81)90145-9.

Kargel, J.S. 1991. Brine volcanism and the interior structures of asteroids. *Icarus* 94, 368-390.

Kay, J. E., & Head III, J. W. 1999. Geologic mapping of the Ganymede G8 Calderas region: Evidence for cryovolcanism. In *Lunar and Planetary Science Conference* (Vol. 30).

Keil, K. 2000. Thermal alteration of asteroids: evidence from meteorites. *Planetary and Space Science*, *48*(10), 887-903.

Keller, L.P. and Buseck, P.R., 1990. Matrix mineralogy of the Lancé CO3 carbonaceous chondrite: A transmission electron microscope study. *Geochim. Cosmochim. Acta* 54, 1155-1163, doi:10.1016/0016-7037(90)90446-R.

Keller, H. U., Mottola, S., Davidsson, B., Schröder, S. E., Skorov, Y., Kührt, E., ... & Scholten, F. 2015. Insolation, erosion, and morphology of comet 67P/Churyumov-Gerasimenko. *Astronomy & Astrophysics*, *583*, A34.

Kenkmann T., Poelchau M. H. & Wulf G. 2014. Structural geology of impact craters. *Journal of Structural Geology*, *62*:156-182.

King, T. V., & King, E. A. 1981. Accretionary dark rims in unequilibrated chondrites. *Icarus*, *48*(3), 460-472.

King, T. V., Clark, R. N., Calvin, W. M., Sherman, D. M., & Brown, R. H. 1992. Evidence for ammonium-bearing minerals on Ceres. *Science*, *255*(5051), 1551-1553.

Kissin, Y. V. 2003. Hydrocarbon components in carbonaceous meteorites. *Geochimica et cosmochimica acta*, *67*(9), 1723-1735.

Krohn, M. D., Kendall, C., Evans, J. R., & Fries, T. L. 1993. Relations of ammonium minerals at several hydrothermal systems in the western US. *Journal of volcanology and geothermal research*, *56*(4), 401-413.

Krohn, K., Jaumann, R., Stephan, K., Otto, K. A., Schmedemann, N., Wagner, R. J., ... & Schulzeck, F. 2016. Cryogenic flow features on Ceres: Implications for crater-related cryovolcanism. *Geophysical Research Letters*, *43*(23), 11-994.

Krot A.N., Scott E.R.D. and Zolensky M.E. 1995. Mineralogical and chemical modification of components in CV3 chondrites: nebular or asteroidal processing?. Meteoritics, 30:748-775.

Krot, A.N., Rubin, A.E., Keil, K. and Wasson, J.T., 1997. Microchondrules in ordinary chondrites: Implications for

chondrule formation. *Geochim. Cosmochim. Acta* 61, 463-473, doi:10.1016/S0016-7037(96)00342-0.

Krot A.N., Petaev M.I., Scott E.R.D., Choi B-.G., Zolensky M.E. and Keil K. 1998. Progressive alteration in CV3 chondrites: more evidence for asteroidal alteration. Meteoritics & Planetary Science, 33:1065-1085.

Krot, A.N., Brearley, A.J., Petaev, M.I., Kallemeyn, G.W., Sears, D.W., Benoit, P.H., Hutcheon, I.D., Zolensky, M.E. and Keil, K., 2000. Evidence for low-temperature growth of fayalite and hedenbergite in MacAlpine Hills 88107, an ungrouped carbonaceous chondrite related to the CM-CO clan. *Meteorit. Planet. Sci* 35, 1365-1386, doi:10.1111/j.1945-5100.2000.tb01522.x.

Krot A. N., Hutcheon I. D. & Keil K. 2002. Plagioclase-rich chondrules in the reduced CV chondrites: Evidence for complex formation history and genetic links between calcium-aluminum-rich inclusions and ferromagnesian chondrules. *Meteoritics & Planetary Science*, *37*(2):155-182.

Krot A.N., Petaev M.I. and Bland P.A. 2004. Multiple formation mechanism of ferrous olivine in CV carbonaceous chondrites during fluid-assisted metamorphism. Antarctic Meteorite Research, 17:153-171.

Krot, A. N., Hutcheon, I. D., Brearley, A. J., Pravdivtseva, O. V., Petaev, M. I., & Hohenberg, C. M. 2005. *Timescales and settings for alteration of chondritic meteorites* (No. UCRL-BOOK-217207). Lawrence Livermore National Lab.(LLNL), Livermore, CA (United States).

Krot, A. N., Keil, K., Scott, E. R. D., Goodrich, C. A., & Weisberg, M. K. 2014. Classification of meteorites and their genetic relationships. *Meteorites and cosmochemical processes*, Volume 1 of Treatise on Geochemistry (Second Edition). Elsevier. Edited by Andrew M. Davis, p.1-63.

Küppers, M., O'Rourke, L., Bockelée-Morvan, D., Zakharov, V., Lee, S., von Allmen, P., ... & Crovisier, J. 2014. Localized sources of water vapour on the dwarf planet (1) Ceres. *Nature*, *505*(7484), 525.

Kurat G., Koeberl C., Presper T., Brandstätter F. & Maurette M. 1994. Petrology and geochemistry of Antarctic micrometeorites. *Geochimica et Cosmochimica Acta*, *58*(18), 3879-3904.

Lafuente B, Downs R T, Yang H, Stone N. 2015. The power of databases: the RRUFF project. In: Highlights in Mineralogical Crystallography, T Armbruster and R M Danisi, eds. Berlin, Germany, W. De Gruyter. 1-30

Lauretta, D. S., Hua, X., & Buseck, P. R. 2000. Mineralogy of fine-grained rims in the ALH 81002 CM chondrite. *Geochimica et Cosmochimica Acta*, *64*(19), 3263-3273.

Lee M. R., Tomkinson T., Hallis L. J. & Mark D. F. 2015. Formation of iddingsite veins in the Martian crust by centripetal replacement of olivine: Evidence from the nakhlite meteorite Lafayette. Geochimica et Cosmochimica Acta, 154:49-65.

Lee, M.R. and Lindgren, P., 2016. Aqueous alteration of chondrules from the Murchison CM carbonaceous chondrite: Replacement, pore filling, and the genesis of polyhedral serpentine. *Meteorit. Planet. Sci* 51, 1003-1021, doi:10.1111/maps.12644.

Lee, M.R., Cohen, B.E., Mark, D.F. and Boyce, A., 2018. Ephemeral Nebular Components in the Mildly Aqueously Altered CM Carbonaceous Chondrite LEW 85311, In Lunar and Planetary Science, (abstr. #1287).

Lennie A. R., Redfern S. A., Champness P. E., Stoddart C. P., Schofield P. F. & Vaughan D. J. 1997. Transformation of mackinawite to greigite; an in situ X-ray powder diffraction and transmission electron microscope study. *American Mineralogist*, *82*(3-4):302-309.

Leroux, H., Cuvillier, P., Zanda, B. and Hewins, R.H., 2015. GEMS-like material in the matrix of the Paris meteorite and the early stages of alteration of CM chondrites. *Geochim. Cosmochim. Acta* 170, 247-265, doi:10.1016/j.gca.2015.09.019.

Lindgren, P., Hanna, R.D., Dobson, K.J., Tomkinson, T. and Lee, M.R., 2015. The paradox between low shock-stage and evidence for compaction in CM carbonaceous chondrites explained by multiple low-intensity impacts. *Geochim. Cosmochim. Acta* 148, 159-178, doi:10.1016/j.gca.2014.09.014.

Love, S. G., & Brownlee, D. E. 1993. A direct measurement of the terrestrial mass accretion rate of cosmic dust. *Science*, *262*(5133), 550-553.

Love, S.G. and Brownlee, D.E., 1994. Peak atmospheric entry temperatures of micrometeorites. *Meteoritics*, 29, 69-70, doi:10.1111/j.1945-5100.1994.tb00653.x.

MacPherson, G. J. 2003. Calcium-aluminum-rich inclusions in chondritic meteorites. *Treatise on Geochemistry*, *1*, 711.

MacPherson G.J. and Krot A.N. 2014. The formation of Ca-Fe-Rich silicates in reduced and oxidised CV chondrites: the roles of impact-modified porosity and permeability, and heterogeneous distribution of water ices. Meteoritics & Planetary Science, 49:1250-1270, doi: 10.1111/maps.12316.
MacPherson G.J. and Krot A.N. 2014. The formation of Ca-Fe-Rich silicates in reduced and oxidised CV chondrites: the roles of impact-modified porosity and permeability, and heterogeneous distribution of water ices. Meteoritics & Planetary Science, 49:1250-1270, doi: 10.1111/maps.12316.
Marchi, S., Raponi, A., Prettyman, T. H., De Sanctis, M. C., Castillo-Rogez, J., Raymond, C. A., ... & Palomba, E. 2019. An aqueously altered carbon-rich Ceres. *Nature Astronomy*, *3*(2), 140.

Marion, G. M. 2001. Carbonate mineral solubility at low temperatures in the Na-K-Mg-Ca-H-Cl-SO4-OH-HCO3-CO3-CO2-H2O system. *Geochimica et Cosmochimica Acta*, *65*(12), 1883-1896.

Marrocchi, Y., Bekaert, D.V. and Piani, L., 2018. Origin and abundance of water in carbonaceous asteroids. *Earth Planet. Sci. Lett* 482, 23-32, doi:10.1016/j.epsl.2017.10.060.

Mauler A., Bystricky M., Kunze K. & Mackwell S. 2000. Microstructures and lattice preferred orientations in experimentally deformed clinopyroxene aggregates. *Journal of Structural Geology*, *22*(11-12):1633-1648.

McCord, T. B., & Gaffey, M. J. 1974. Asteroids: Surface composition from reflection spectroscopy. *Science*, *186*(4161), 352-355.

McCord, T. B., Orlando, T. M., Teeter, G., Hansen, G. B., Sieger, M. T., Petrik, N. G., & Van Keulen, L. 2001. Thermal and radiation stability of the hydrated salt minerals epsomite, mirabilite, and natron under Europa environmental conditions. *Journal of Geophysical Research: Planets*, *106*(E2), 3311-3319.

McCord, T.B., Castillo-Rogez, J. & Rivkin, A. 2011. Ceres: its origin, evolution and structure and Dawn's potential contribution. *Space Science Reviews* 163, 63-76.

McSween Jr, H.Y. 1977. Petrographic variations among carbonaceous chondrites of the Vigarano type. Geochimica et Cosmochimica Acta, 41:1777-1790, doi:10.1016/0016-7037(77)90210-1.

McSween Jr, H. Y., Binzel, R. P., De Sanctis, M. C., Ammannito, E., Prettyman, T. H., Beck, A. W., ... & Raymond, C. A. 2013. Dawn; the Vesta–HED connection; and the geologic context for eucrites, diogenites, and howardites. *Meteoritics & Planetary Science*, *48*(11), 2090-2104.

McSween Jr, H. Y., Emery, J. P., Rivkin, A. S., Toplis, M. J., C. Castillo-Rogez, J., Prettyman, T. H., ... & Russell, C. T. 2018. Carbonaceous chondrites as analogs for the composition and alteration of Ceres. *Meteoritics & Planetary Science*, *53*(9), 1793-1804.

Michibayashi, K., Mainprice, D., Fujii, A., Uehara, S., Shinkai, Y., Kondo, Y., Ohara, Y., Ishii, T., fryer P., Bloomer, S.H., Ishiwatari, A., Hawkins, J.W. & Ji, S. 2016. Natural olivine crystal-fabrics in the western Pacific convergence region: A new method to identify fabric type. *Earth and Planetary Science Letters*, *443*, 70-80.

Miles, R. 2016. Discrete sources of cryovolcanism on the nucleus of comet 29P/Schwassmann-Wachmann and their origin. *Icarus* 272, 387-413.

Milliken, R. E., & Rivkin, A. S. 2009. Brucite and carbonate assemblages from altered olivine-rich materials on Ceres. *Nature Geoscience*, *2*(4), 258.

Mittlefehldt, D. W. 2003. Achondrites. *Treatise on geochemistry*, Volume 1. Editor: Andrew M. Davis. Executive Editors: Heinrich D. Holland and Karl K. Turekian. pp. 711.

Moroz, L. V., Arnold, G., Korochantsev, A. V., & Wäsch, R. 1998. Natural solid bitumens as possible analogs for cometary and asteroid organics:: 1. reflectance spectroscopy of pure bitumens. *Icarus*, *134*(2), 253-268.

Mumma, M. J. & Charnley, S. B. 2011. The chemical composition of comets—Emerging taxonomies and natal heritage. *Annual Review of Astronomy and Astrophysics* 49, 471-524.

Nakamura-Messenger, K., Clemett, S.J., Messenger, S. and Keller, L.P., 2011. Experimental aqueous alteration of cometary dust. *Meteorit. Planet. Sci* 46, 843-856, doi:10.1111/j.1945-5100.2011.01197.x.

Nathues, A., Hoffmann, M., Schaefer, M., Le Corre, L., Reddy, V., Platz, T., ... & Mengel, K. 2015. Sublimation in bright spots on (1) Ceres. *Nature*, *528*(7581), 237.

Nathues, A., Platz, T., Thangjam, G., Hoffmann, M., Mengel, K., Cloutis, E. A., ... & Crown, D. A. 2017. Evolution of Occator crater on (1) Ceres. *The Astronomical Journal*, *153*(3), 112.

Nesvorný, D., Bottke, W. F., Levison, H. F., & Dones, L. (2003). Recent origin of the Solar System dust bands. *The Astrophysical Journal*, *591*(1), 486.

Nesvorný, D., Jenniskens, P., Levison, H. F., Bottke, W. F., Vokrouhlický, D., & Gounelle, M. 2010. Cometary origin of the zodiacal cloud and carbonaceous micrometeorites. Implications for hot debris disks. *The Astrophysical Journal*, *713*(2), 816.

Neumann W., Breuer D. & Spohn T. 2015. Modelling the internal structure of Ceres: coupling of accretion with compaction by creep and implications for the water-rock differentiation. Astronomy & Astrophysics, 584, A117.

Neveu, M., Desch, S. J., & Castillo-Rogez, J. C. 2015. Core cracking and hydrothermal circulation can profoundly affect Ceres' geophysical evolution. *Journal of Geophysical Research: Planets*, *120*(2), 123-154.

Neveu, M., Desch, S. J., Shock, E. L. & Glein, C. R. 2015. Prerequisites for explosive cryovolcanism on dwarf planet-class Kuiper belt objects. *Icarus* 246, 48-64.

Newton, J., Bischoff, A., Arden, J.W., Franchi, I.A., Geiger, T., Greshake, A. and Pillinger, C.T., 1995. Acfer 094, a uniquely primitive carbonaceous chondrite from the Sahara. *Meteoritics* 30, 47-56, doi:10.1111/j.1945-5100.1995.tb01211.x.

Nieto, F. 2002. Characterization of coexisting NH4-and K-micas in very low-grade metapelites. *American Mineralogist*, *87*(2-3), 205-216.

Noguchi, T., Ohashi, N., Tsujimoto, S., Mitsunari, T., Bradley, J. P., Nakamura, T., Tho, S., Stephan, T., Iwata, N. & Imae, N. 2015. Cometary dust in Antarctic ice and snow: Past and present chondritic porous micrometeorites preserved on the Earth's surface. Earth and Planetary Science Letters 410, 1-11.

Nomura, K., & Miyamoto, M. 1998. Hydrothermal experiments on alteration of Ca-Al-rich inclusions (CAIs) in carbonaceous chondrites: Implication for aqueous alteration in parent asteroids. *Geochimica et Cosmochimica Acta*, *62*(21-22), 3575-3588.

Nozaki, W., Nakamura, T. and Noguchi, T., 2006. Bulk mineralogical changes of hydrous micrometeorites during heating in the upper atmosphere at temperatures below 1000 C. *Meteorit. Planet. Sci* 41, 1095-1114, doi:10.1111/j.1945-5100.2006.tb00507.x.

Orthous-Daunay, F. R., Quirico, E., Beck, P., Brissaud, O., Dartois, E., Pino, T., & Schmitt, B. 2013. Mid-infrared study of the molecular structure variability of insoluble organic matter from primitive chondrites. *Icarus*, *223*(1), 534-543.

Pajola, M., Höfner, S., Vincent, J. B., Oklay, N., Scholten, F., Preusker, F., ... & Feller, C. 2017. The pristine interior of comet 67P revealed by the combined Aswan outburst and cliff collapse. *Nature Astronomy*, *1*(5), 0092.

Palmer, E. E., & Lauretta, D. S. 2011. Aqueous alteration of kamacite in CM chondrites. *Meteoritics & Planetary Science*, *46*(10), 1587-1607.

Pappalardo, R. T., & Barr, A. C. 2004. The origin of domes on Europa: The role of thermally induced compositional diapirism. *Geophysical Research Letters*, *31*(1).

Postberg, F., Kempf, S., Schmidt, J., Brilliantov, N., Beinsen, A., Abel, B., ... & Srama, R. 2009. Sodium salts in E-ring ice grains from an ocean below the surface of Enceladus. *Nature*, *459*(7250), 1098.

Python M., Ceuleneer G., Ishida Y., Barrat J. A. & Arai S. 2007. Oman diopsidites: a new lithology diagnostic of very high temperature hydrothermal circulation in mantle peridotite below oceanic spreading centres. *Earth and Planetary Science Letters*, *255*(3-4):289-305.

Quick, L. C., Glaze, L. S. & Baloga, S. M. 2017. Cryovolcanic emplacement of domes on Europa. *Icarus* 284, 477-488.

Quirico, E., Moroz, L. V., Schmitt, B., Arnold, G., Faure, M., Beck, P., ... & Erard, S. 2016. Refractory and semi-volatile organics at the surface of comet 67P/Churyumov-Gerasimenko: Insights from the VIRTIS/Rosetta imaging spectrometer. *Icarus*, *272*, 32-47.

Ramsey, M.S. and Christensen, P.R., 1998. Mineral abundance determination: Quantitative deconvolution of thermal emission spectra. *J. Geophys. Res* 103, 577-596, doi:10.1029/97JB02784.

Raponi, A., De Sanctis, M. C., Carrozzo, F. G., Ciarniello, M., Castillo-Rogez, J. C., Ammannito, E., ... & Zambon, F. 2019. Mineralogy of Occator crater on Ceres and insight into its evolution from the properties of carbonates, phyllosilicates, and chlorides. *Icarus*, *320*, 83-96.

Rivkin, A. S., Volquardsen, E. L., & Clark, B. E. 2006. The surface composition of Ceres: Discovery of carbonates and iron-rich clays. *Icarus*, *185*(2), 563-567.

Rivkin, A. S., & Emery, J. P. 2010. Detection of ice and organics on an asteroidal surface. *Nature*, *464*(7293), 1322.

Rochette, P., Folco, L., Suavet, C., Van Ginneken, M., Gattacceca, J., Perchiazzi, N., Braucher, R. and Harvey, R.P., 2008. Micrometeorites from the Transantarctic Mountains. *Proc. Natl. Acad. Sci. U.S.A* 105, 18206-18211, doi:10.1073/pnas.0806049105.

Rubin, A.E., 1998. Correlated petrologic and geochemical characteristics of CO3 chondrites. *Meteorit. Planet. Sci* 33, 385-391, doi:10.1111/j.1945-5100.1998.tb01644.x.

Rubin, A.E., Trigo-Rodríguez, J.M., Huber, H. and Wasson, J.T., 2007. Progressive aqueous alteration of CM carbonaceous chondrites. *Geochim. Cosmochim. Acta* 71, 2361-2382, doi:10.1016/j.gca.2007.02.008.

Ruesch, O., Platz, T., Schenk, P., McFadden, L. A., Castillo-Rogez, J. C., Quick, L. C., ... & Williams, D. A. 2016. Cryovolcanism on Ceres. *Science*, *353*(6303), aaf4286.

Ruesch, O., Quick, L. C., Landis, M. E., Sori, M. M., Čadek, O., Brož, P., ... & Hiesinger, H. 2019. Bright carbonate surfaces on Ceres as remnants of salt-rich water fountains. *Icarus*, *320*, 39-48.

Ruiz Cruz, M. D., & De Galdeano, C. S. 2008. High-temperature ammonium white mica from the Betic Cordillera (Spain). *American Mineralogist*, *93*(7), 977-987.

Ruzicka, A., 2012. Chondrule formation by repeated evaporative melting and condensation in collisional debris clouds around planetesimals. *Meteorit. Planet. Sci* 47, 2218-2236, doi:10.1111/j.1945-5100.2012.01412.x.

Schrader, D.L., Franchi, I.A., Connolly Jr, H.C., Greenwood, R.C., Lauretta, D.S. and Gibson, J.M., 2011. The formation and alteration of the Renazzo-like carbonaceous chondrites I: Implications of bulk-oxygen isotopic composition. *Geochim. Cosmochim. Acta* 75, 308-325, doi:10.1016/j.gca.2010.09.028.

Schrader, D.L. and Davidson, J., 2017. CM and CO chondrites: A common parent body or asteroidal neighbors? Insights from chondrule silicates. *Geochim. Cosmochim. Acta* 214, 157-171, doi:10.1016/j.gca.2017.07.031.

Schulz, R., Stüwe, J. A., & Boehnhardt, H. 2004. Rosetta target comet 67P/Churyumov-Gerasimenko-Postperihelion gas and dust production rates. *Astronomy & Astrophysics*, *422*(1), L19-L21.

Schulte, M. & Shock, E. 2004. Coupled organic synthesis and mineral alteration on meteorites parent bodies. *Meteoritics &Planetary Science* ***39***, 1577-1590.

Schulz, R., Hilchenbach, M., Langevin, Y., Kissel, J., Silen, J., Briois, C., ... & Cottin, H. 2015. Comet 67P/Churyumov-Gerasimenko sheds dust coat accumulated over the past four years. *Nature*, *518*(7538), 216.

Scott E.R., Keil K. and Stoeffler D. 1992. Shock metamorphism of carbonaceous chondrites. Geochimica et Cosmochimica Acta, 56:4281-4293, doi:10.1016/0016-7037(92)90268-N.

Scott, E. R. D., & Krot, A. N. 2003. Chondrites and their components. *Treatise on geochemistry*, Volume 1. Editor: Andrew M. Davis. Executive Editors: Heinrich D. Holland and Karl K. Turekian. pp. 711. ISBN 0-08-043751-6. Elsevier, p.143-200.

Sephton, M. A. 2002. Organic compounds in carbonaceous meteorites. *Natural product reports*, *19*(3), 292-311.

Soderblom, L. A., Becker, T. L., Bennett, G., Boice, D. C., Britt, D. T., Brown, R. H., ... & Hicks, M. D. 2002. Observations of Comet 19P/Borrelly by the miniature integrated camera and spectrometer aboard Deep Space 1. *Science*, *296*(5570), 1087-1091.

Spencer, J. R., Barr, A. C., Esposito, L. W., Helfenstein, P., Ingersoll, A. P., Jaumann, R., ... & Waite, J. H. 2009. Enceladus: An active cryovolcanic satellite. In *Saturn from Cassini-Huygens* (pp. 683-724). Springer, Dordrecht.

Suavet, C., Alexandre, A., Franchi, I. A., Gattacceca, J., Sonzogni, C., Greenwood, R. C., ... & Rochette, P. 2010. Identification of the parent bodies of micrometeorites with high-precision oxygen isotope ratios. *Earth and Planetary Science Letters*, *293*(3-4), 313-320.

Šucha, V., Elsass, F., Eberl, D. D., Madejová, J., Gates, W. P., & Komadel, P. 1998. Hydrothermal synthesis of ammonium illite. *American Mineralogist*, *83*(1), 58-67.

Suttle M.D., Genge M.J. and Russell S.S. 2017. Shock fabrics in fine-grained micrometeorites. Meteoritics & Planetary Science, 52:2258-2274, doi:10.1111/maps.12927.

Suttle, M.D., Genge, M.J., Folco, L. and Russell, S.S., 2017. The thermal decomposition of fine-grained micrometeorites, observations from mid-IR spectroscopy. *Geochim. Cosmochim. Acta* 206, 112-136, doi:10.1016/j.gca.2017.03.002.

Suttle, M.D., Folco, L., Genge, M.J., Russell, S.S., Najorka, J. and van Ginneken, M., 2019a. Intense aqueous alteration on C-type asteroids: Perspectives from giant fine-grained micrometeorites. *Geochim. Cosmochim. Acta* 245, 352-373, doi: 10.1016/j.gca.2018.11.019.

Suttle, M.D., Genge, M.J., Salge, T., Lee, M.R., Folco, L., Góral, T., Russell, S.S. and Lindgren, P., 2019b. A microchondrule-bearing micrometeorite and comparison with microchondrules in CM chondrites. *Meteorit. Planet. Sci* 54, 1303-1324, doi:10.1111/maps.13279.

Takir, D., & Emery, J. P. 2012. Outer main belt asteroids: Identification and distribution of four 3-µm spectral groups. *Icarus*, *219*(2), 641-654.

Takir, D., Emery, J. P., Mcsween Jr, H. Y., Hibbitts, C. A., Clark, R. N., Pearson, N., & Wang, A. 2013. Nature and degree of aqueous alteration in CM and CI carbonaceous chondrites. *Meteoritics & Planetary Science*, *48*(9), 1618-1637.

Takir, D., Stockstill-Cahill, K. R., Hibbitts, C. A., & Nakauchi, Y. 2019. 3-µm reflectance spectroscopy of carbonaceous chondrites under asteroid-like conditions. *Icarus*, *333*, 243-251.

Tancredi, G., Rickman, H., & Greenberg, J. M. 1994. Thermochemistry of cometary nuclei. 1: The Jupiter family case. *Astronomy and Astrophysics*, *286*, 659.

Taylor, S., Matrajt, G., Lever, J.H., Joswiak, D.J. and Brownlee, D.E., 2007. Size distribution of Antarctic micrometeorites. *Dust in Planetary Systems*, 643, 145-148.

Taylor, S., Matrajt, G., & Guan, Y. 2012. Fine-grained precursors dominate the micrometeorite flux. *Meteoritics & Planetary Science*, *47*(4), 550-564.

Tomeoka K. & Buseck P. R. 1985. Indicators of aqueous alteration in CM carbonaceous chondrites: Microtextures of a layered mineral containing Fe, S, O and Ni. Geochimica et Cosmochimica Acta, 49(10):2149-2163.

Tomeoka, K., and Tanimura, I., 2000. Phyllosilicate-rich chondrule rims in the Vigarano CV3 chondrite: Evidence for parent-body processes. Geochimica et Cosmochimica Acta, 64:1971-1988.

Tomeoka K. and Ohnishi I. 2010. Indicators of parent-body processes: hydrated chondrules and fine-grained rims in the Mokoia CV3 carbonaceous chondrite. Geochimica et Cosmochimica Acta, 74:4438-4453, doi:10.1016/j.gca.2010.04.058.

Tosi, F., Carrozzo, F. G., Raponi, A., De Sanctis, M. C., Thangjam, G., Zambon, F., ... & Ammannito, E. 2018. Mineralogy and temperature of crater Haulani on Ceres. *Meteoritics & Planetary Science*, *53*(9), 1902-1924.

Travis, B. J., & Schubert, G. 2005. Hydrothermal convection in carbonaceous chondrite parent bodies. *Earth and Planetary Science Letters*, *240*(2), 234-250.

Treiman A. H., Barrett R. A. & Gooding J. L., 1993. Preterrestrial aqueous alteration of the Lafayette (SNC) meteorite. *Meteoritics*, *28*:86-97.

van Ginneken, M., Folco, L., Cordier, C., & Rochette, P. 2012. Chondritic micrometeorites from the Transantarctic Mountains. *Meteoritics & Planetary Science*, *47*(2), 228-247.

van Ginneken M., Genge M.J., Folco L. and Harvey R.P. 2016. The weathering of micrometeorites from the Transantarctic Mountains. Geochimica et Cosmochimica Acta, 179:1-31, doi:10.1016/j.gca.2015.11.045.

Velbel, M. A. 1988. The distribution and significance of evaporitic weathering products on Antarctic meteorites. *Meteoritics*, *23*(2), 151-159.

Velbel, M.A. and Palmer, E.E., 2011. Fine-grained serpentine in CM2 carbonaceous chondrites and its implications for the extent of aqueous alteration on the parent body: A review. *Clays Clay Min.* 59, 416-432, doi:10.1346/CCMN.2011.0590405.

Velbel, M.A., Tonui, E.K. and Zolensky, M.E., 2012. Replacement of olivine by serpentine in the carbonaceous chondrite Nogoya (CM2). *Geochim. Cosmochim. Acta* 87, 117-135, doi:10.1016/j.gca.2012.03.016.

Vernazza, P., Mothé-Diniz, T., Barucci, M. A., Birlan, M., Carvano, J. M., Strazzulla, G., Fulchignoni, M. & Migliorini, A. 2005. Analysis of near-IR spectra of 1 Ceres and 4 Vesta, targets of the Dawn mission. *Astronomy & Astrophysics*, *436*(3), 1113-1121.

Vernazza, P., Marsset, M., Beck, P., Binzel, R. P., Birlan, M., Brunetto, R., ... & Mousis, O. 2015. Interplanetary dust particles as samples of icy asteroids. *The Astrophysical Journal*, *806*(2), 204.

Vernazza, P., Castillo-Rogez, J., Beck, P., Emery, J., Brunetto, R., Delbo, M., ... & Lamy, P. 2017. Different origins or different evolutions? Decoding the spectral diversity among C-type asteroids. *The Astronomical Journal*, *153*(2), 72.

Vincent, J. B., Bodewits, D., Besse, S., Sierks, H., Barbieri, C., Lamy, P., ... & Agarwal, J. 2015. Large heterogeneities in comet 67P as revealed by active pits from sinkhole collapse. *Nature*, *523*(7558), 63.

Vincent, J. B., A'Hearn, M. F., Lin, Z. Y., El-Maarry, M. R., Pajola, M., Sierks, H., ... & Rickman, H. 2016. Summer fireworks on comet 67P. *Monthly Notices of the Royal Astronomical Society*, *462*(Suppl_1), S184-S194.

Vinogradoff, V., Le Guillou, C., Bernard, S., Binet, L., Cartigny, P., Brearley, A. J., & Remusat, L. 2017. Paris vs. Murchison: Impact of hydrothermal alteration on organic matter in CM chondrites. *Geochimica et Cosmochimica acta*, *212*, 234-252.

Wang, M. S., & Lipschutz, M. E. 1998. Thermally metamorphosed carbonaceous chondrites from data for thermally mobile trace elements. *Meteoritics & Planetary Science*, *33*(6), 1297-1302.

Warren P.H. 2011. Stable-isotopic anomalies and the accretionary assemblage of the Earth and Mars: A subordinate role for carbonaceous chondrites. Earth and Planetary Science Letters, 311:93-100, doi:10.1016/j.epsl.2011.08.047.

Watt L. E., Bland P. A., Prior D. J. & Russell S. S. 2006. Fabric analysis of Allende matrix using EBSD. *Meteoritics & Planetary Science*, *41*(7):989-1001.

Weidenschilling S. J. & Cuzzi J. N. 2006. Accretion dynamics and timescales: Relation to chondrites. Meteorites and the early solar system II, 1, 473-485.

Weisberg M.K., McCoy T.J. and Krot A.N. 2006. Systematics and evaluation of meteorite classification. In Meteorites and the Early Solar System II, D. S. Lauretta and H. Y. McSween Jr. (eds.), University of Arizona Press, Tucson, 943:19-52.

Weiss B.P. and Elkins-Tanton L.T. 2013. Differentiated planetesimals and the parent bodies chondrites. Annual review of Earth and Planetary Science, 41:529-560, 10.1146/annurev-earth-040610-133520.

Wilson, L., Keil, K., Browning, L. B., Krot, A. N., & Bourcier, W. 1999. Early aqueous alteration, explosive disruption, and reprocessing of asteroids. *Meteoritics & Planetary Science*, *34*(4), 541-557.

Wunder B., Wirth R. & Gottschalk M. 2001. Antigorite pressure and temperature dependence of polysomatism and water content. *European Journal of Mineralogy*, *13*(3):485-496.

Yabuta, H., Alexander, C. M. O. D., Fogel, M. L., Kilcoyne, A. D., & Cody, G. D. 2010. A molecular and isotopic study of the macromolecular organic matter of the ungrouped C2 WIS 91600 and its relationship to Tagish Lake and PCA 91008. *Meteoritics & Planetary Science*, *45*(9), 1446-1460.

Yabuta, H., Noguchi, T., Itoh, S., Nakamura, T., Miyake, A., Tsujimoto, S., ... & Okubo, A. 2017. Formation of an ultracarbonaceous Antarctic micrometeorite through minimal aqueous alteration in a small porous icy body. *Geochimica et Cosmochimica Acta*, *214*, 172-190.

Yang, B., Jewitt, D., & Bus, S. J. 2009. Comet 17P/Holmes in outburst: the near infrared spectrum. *The Astronomical Journal*, *137*(5), 4538.

Young, E. D. 2001. The hydrology of carbonaceous chondrite parent bodies and the evolution of planet progenitors. *Philosophical Transactions of the Royal Society of London. Series A: Mathematical, Physical and Engineering Sciences*, *359*(1787), 2095-2110.

Zega, T. J., & Buseck, P. R. 2003. Fine-grained-rim mineralogy of the Cold Bokkeveld CM chondrite. *Geochimica et Cosmochimica Acta*, *67*(9), 1711-1721.

Zhang, A.C., Li, Q.L., Yurimoto, H., Sakamoto, N., Li, X.H., Hu, S., Lin, Y.T. and Wang, R.C., 2016. Young asteroidal fluid activity revealed by absolute age from apatite in carbonaceous chondrite. *Nat. comm.* 7, 12844, doi:10.1038/ncomms12844.

Zinner, E. K. 2003. Presolar grains. *Treatise on Geochemistry*, *1*, 711.

Zolensky, M., Bland, P., Brown, P., & Halliday, I. 2006. Flux of extraterrestrial materials. *Meteorites and the early solar system II*, 869-888.

Zolotov M. Y., Mironenko M. V. & Shock E. L. 2006. Thermodynamic constraints on fayalite formation on parent bodies of chondrites. Meteoritics & Planetary Science, 41:1775-1796.

Zolensky, M., Chan, Q. H., Gounelle, M., & Fries, M. 2016. Bright Stuff on Ceres= Sulfates and Carbonates on CI Chondrites.

Zolotov, M. Y. 2009. On the composition and differentiation of Ceres. *Icarus*, *204*(1), 183-193.

Zolotov, M. Y. 2014. Formation of brucite and cronstedtite-bearing mineral assemblages on Ceres. *Icarus*, *228*, 13-26.

Zolotov, M. Y. 2016. Formation of sulfates on parent bodies of carbonaceous chondrites, Ceres, Europa, and other icy bodies. In *Lunar and Planetary Science Conference* (Vol. 47, p. 1778).

Appendix

Monthly Notices
of the
ROYAL ASTRONOMICAL SOCIETY

MNRAS **484,** 2198–2211 (2019)
Advance Access publication 2019 January 12

doi:10.1093/mnras/stz129

Experimental phase function and degree of linear polarization of cometary dust analogues

E. Frattin,[1,2]★ O. Muñoz,[3,4] F. Moreno,[3] J. Nava,[5] J. Escobar-Cerezo,[6] J. C. Gomez Martin,[3] D. Guirado,[3] A. Cellino,[7] P. Coll,[8] F. Raulin,[8] I. Bertini,[1] G. Cremonese,[2] M. Lazzarin,[1] G. Naletto[9,10,11] and F. La Forgia[1]

[1]*Department of Physics and Astronomy 'G. Galilei', University of Padova, Vicolo dell'Osservatorio 3, I-35122 Padova, Italy*
[2]*INAF, Astronomical Observatory of Padova, Vicolo dell'Osservatorio 5, I-35122 Padova, Italy*
[3]*Instituto de Astrofísica de Andalucía, CSIC, Glorieta de la Astronomia s/n, E-18008 Granada, Spain*
[4]*Advanced Optical Imaging Group, School of Physics, University College Dublin, Dublin 4, Ireland*
[5]*Department of Geosciences, University of Padova, Via G. Gradenigo 6, I-35131 Padova, Italy*
[6]*Department of Physics, University of Helsinki, FI-00014 Helsinki, Finland*
[7]*INAF – Astrophysical Observatory of Torino, Via Osservatorio 20, I-10025 Pino Torinese (TO), Italy*
[8]*Laboratoire Inter-Universitaire des Systemes Atmospheriques, Universites Paris 12 – Paris 7, CNRS, France*
[9]*Department of Physics and Astronomy 'G. Galilei', University of Padova, Via Marzolo 8, I-35131 Padova, Italy*
[10]*Center of Studies and Activities for Space (CISAS), 'G. Colombo', University of Padova, Via Venezia 15, I-35131 Padova, Italy*
[11]*CNR-IFN UOS Padova LUXOR, Via Trasea 7, I-35131 Padova, Italy*

Accepted 2018 December 22. Received 2018 December 20; in original form 2018 July 19

ABSTRACT

We present experimental phase function and degree of linear polarization curves for seven samples of cometary dust analogues namely: ground pieces of Allende, DaG521, FRO95002, and FRO99040 meteorites, Mg-rich olivine and pyroxene, and a sample of organic tholins. The experimental curves have been obtained at the IAA Cosmic Dust Laboratory at a wavelength of 520 nm covering a phase angle range from 3° to 175°. We also provide values of the backscattering enhancement for our cometary analogue samples. The final goal of this work is to compare our experimental curves with observational data of comets and asteroids to better constrain the nature of cometary and asteroidal dust grains. All measured phase functions present the typical behaviour for μm-sized cosmic dust grains. Direct comparison with data provided by the OSIRIS/Rosetta camera for comet 67P/Churyumov–Gerasimenko reveals significant differences and supports the idea of a coma dominated by big chunks, larger than one micrometer. The polarization curves are qualitatively similar to ground-based observations of comets and asteroids. The position of the inversion polarization angle seems to be dependent on the composition of the grains. We find opposite dependence of the maximum of the polarization curve for grains sizes in the Rayleigh-resonance and geometric optics domains, respectively.

Key words: scattering.

1 INTRODUCTION

Dust is a fundamental constituent of planetary systems in all their stages of development. For example, the origin of planetary systems involves a phase of aggregation of submicron-sized dust grains by streaming instability into protoplanetary discs (Johansen & Youdin 2007; Blum & Wurm 2008; Blum et al. 2014). In our mature Solar system, dust can be found in the interplanetary medium orbiting around the Sun as a product of the disintegration of comets and asteroidal collisional cascading (the Zodiacal Cloud), as well as in the rings of the giant planets. In addition, dust is present in the regolith surfaces of planets, asteroids and comets, and in dense atmospheres (e.g. Venus, the Earth, Mars, Titan) in the form of aerosol. Because of the ubiquity of dust and its involvement in countless physical phenomena, from atmospheric radiative transfer to cometary activity through the tracing of Solar system primitive materials, it is important to study its nature and properties.

Comets are the most appropriate targets to study the early Solar system, since they are among the most pristine objects orbiting

★ E-mail: elisa.frattin@gmail.com

the Sun. Because of their low velocity, gentle accretion process, some of their most primitive constituents (the grains) have remained intact, i.e. as they were when the comets formed (Fulle et al. 2016). During their passage at perihelion, these objects release refractory materials driven by the sublimation of trapped ices, generating a bright dust coma dominated by μm-sized particles composed of silicate minerals and organics. Comets unveil the composition of the primordial material from which they accreted, namely material located in the outer regions of the Solar system, and put some constraints to the processes involved in its origin. The flyby missions that first revealed the nature of cometary dust with *in situ* measurements were the *Giotto* (Reinhard 1986) and *Vega* (Sagdeev et al. 1986) missions to 1P/Halley in 1986. The 'Halley Armada' was followed up by the Deep Space 1 mission to comet 19P/Borrelly in 2001 (Soderblom et al. 2002). A major breakthrough came with the *Stardust* mission flyby of comet 81P/Wild in 2004 (Hörz et al. 2006), and subsequent return to Earth of samples of dust collected directly from the coma of the comet. Later, missions to comet 9P/Temple in 2005 (Deep Impact 2005; A'Hearn et al. 2005) and to comet 103P/Hartley in 2010 (EPOXI) (A'Hearn et al. 2011) provided new insights of these two objects. More recently, the Rosetta mission has been able, for the first time, to follow the trajectory of the cometary nucleus and observe its evolution during its trajectory before and after perihelion. The coma of comet 67P/Churyumov–Gerasimenko (hereafter 67P) was observed during two entire years (2014–2016) from the very inside, reaching distances of few km from the nucleus. The astonishing images obtained by the OSIRIS instrument onboard the spacecraft have shed new light into the properties of cometary dust (Sierks et al. 2015) . There is now evidence that 67P was formed by gentle accretion of pebbles smaller than 1 cm at velocities of the order of 1 $\mathrm{m\,s^{-1}}$ (Fulle & Blum 2017). Moreover, photometric analysis of the overall coma and single grains reveal that the majority of the material has similar spectral properties to those of nucleus surface (Frattin et al. 2017), which enables using the dust coma as a proxy indicator of nucleus properties.

The sunlight incident on a cometary dust envelope is partly absorbed and partly scattered by the particle cloud. Spacecraft and ground-based observations of scattered light show characteristics strictly dependent on the nature and physical properties (composition, size distribution, shape, roughness, etc.) of the material composing the coma. Since each material has characteristic scattering signatures, scattering theory can be used to interpret observations and retrieve from them some of the properties of the dust. Experimental data of the angular distribution of the scattered intensity and degree of linear polarization of clouds of cosmic dust analogues assist in the interpretation of *in situ* and remote sensing observations. Since these quantities are intimately related to the nature of the particles, laboratory data are used as a reference for comparison and interpretation, allowing a correct analysis of the observational data (Muñoz et al. 2000; Volten et al. 2006; Muñoz et al. 2017). Modelling of the interaction between electromagnetic radiation and particles in turn, supports the experiments, helping to discriminate unambiguously dust features corresponding to specific observables (Liu, Yang & Muinonen 2015; Zubko 2015; Escobar-Cerezo et al. 2017). All these different approaches (observations, laboratory experiments, and theoretical simulations) provide essential contributions to the investigation of the behaviour of dust particles as radiation scatterers.

In this work we present experimental phase function and degree of linear polarization curves as functions of the observational phase angle of a selected set of cometary dust analogues: four meteoritic samples, two minerals (Mg-rich olivine and pyroxene), and a sample of organic particles (tholins). Light scattering measurement has been performed at the Cosmic Dust Laboratory (CODULAB; Muñoz et al. 2011) at the Instituto de Astrofísica de Andalucía (IAA), spanning a phase angle range from 3° to 175° at a wavelength of 520 nm. We combine the new measurements presented in this work with the scattering matrices at 442 and 633 nm of a sample of the Allende meteorite and of size-segregated Mg-rich olivine samples that have been previously presented by Muñoz et al. (2000). Finally, we compare the experimental data with observations of asteroids and cometary dust envelops, with special emphasis on the observations of 67P by Rosetta, in order to put constraints on the nature of cometary dust.

2 LIGHT SCATTERING THEORY

A beam of quasi-monochromatic light is physically defined by the Stokes vector $\boldsymbol{I}= \{I, Q, U, V\}$, where I is proportional to the total flux of the light beam and Q is related to the linear polarization of the light beam, representing the difference between the two components of the flux along the x-axis and the y-axis. U is defined by the difference of the two components of the flux along the directions rotated by 45° from the x- and y-axis. V is related to the circular polarization, defined as the difference between the left-handed and the right-handed polarized components of the flux.

The interaction between a light beam and a cloud of particles results in scattering of the incident light. The Stokes vector of the scattered beam $\boldsymbol{I}_{sc}$ is related to the one of the incident beam $\boldsymbol{I}_{in}$ by the so-called scattering matrix $\mathbf{F}$, through the following expression:

$$\begin{pmatrix} I_{\rm sc} \\ Q_{\rm sc} \\ U_{\rm sc} \\ V_{\rm sc} \end{pmatrix} = \frac{\lambda^2}{4\pi^2 D^2} \begin{pmatrix} F_{11} & F_{12} & F_{13} & F_{14} \\ F_{21} & F_{22} & F_{23} & F_{24} \\ F_{31} & F_{32} & F_{33} & F_{34} \\ F_{41} & F_{42} & F_{43} & F_{44} \end{pmatrix} \begin{pmatrix} I_{\rm in} \\ Q_{\rm in} \\ U_{\rm in} \\ V_{\rm in} \end{pmatrix}, \quad (1)$$

where λ is the wavelength of the incident beam and D is the distance of the detector from the particles. The 16 dimensionless elements of the matrix depend on physical characteristics of the particles such as their number, shape, dimension (through the size parameter $x = 2\pi r/\lambda$) and refractive index, as well as on geometrical parameters such as their orientation in the space and scattering direction.

When the particles are randomly oriented all scattering planes are equivalent. Therefore, the scattering direction is fully described by the scattering angle, θ, defined by the angle between the directions of propagation of the incident and scattered beams. To facilitate direct comparison with astronomical observations of comets and asteroids we use the phase angle, $\alpha = 180^\circ - \theta$, throughout the text. Furthermore, when the particles present mirror symmetries, and are randomly oriented, the scattering matrix has six parameters (van de Hulst 1957):

$$\mathbf{F} = \begin{pmatrix} F_{11} & F_{12} & 0 & 0 \\ F_{12} & F_{22} & 0 & 0 \\ 0 & 0 & F_{33} & F_{34} \\ 0 & 0 & -F_{34} & F_{44} \end{pmatrix}. \quad (2)$$

3 EXPERIMENTAL APPARATUS

The CODULAB facility is dedicated to measuring the elements of the scattering matrix (equation 1 and 2) as a function of the scattering angle of clouds of randomly oriented cosmic dust analogues. This is

achieved by means of a gonio-nephelometer that has been described in detail previously by Muñoz et al. (2010). In the experiments carried out for this work we employed an Argon–Krypton laser tuned to 520 nm as our light source. The laser beam passes through a polarizer and an electro-optic modulator before encountering a jet stream of randomly oriented particles produced by an aerosol generator (Muñoz et al. 2011). The powder under analysis is contained in a cylindrical reservoir, and is pushed by a piston in a controlled manner towards a rotating brush, which disperses the particles into a flow of air which carries them through a nozzle to the scattering volume. The particle density in the scattering volume, which is controlled by the speed of the piston, must be high enough to produce a detectable scattering signal, but low enough to avoid multiple scattering. In this way it better approximates the low-density cometary coma. The scattered light passes through optional optics before being detected by a photomultiplier, the *detector*, which is mounted on a 1 m ring rail centred at the aerosol jet. In the measurements presented in this paper we have covered the phase angle range from 3° to 175° in steps of 5° within the 10°–20° and 40°–175° ranges, and in steps of 1° within the 3°–10° and 25°–40° ranges. Sinusoidal electro-optic modulation combined with lock-in detection allows determining all elements of the scattering matrix from eight different configurations of the optical components (equation 1) and the assumption of reciprocity of the sample (see further details in Muñoz et al. 2010). In order to keep the scattered intensity within the linearity range of the detector, a wheel of neutral density filters is placed between the laser head and the polarizer, which allows adapting the beam intensity to the scattering behaviour of the aerosol sample at each particular angle. A second photomultiplier placed at a fixed angle, the *monitor*, corrects for fluctuations in the aerosol beam. For each position of the detector, 1000 measurements are conducted in about 2 s. The final value at each phase angle is obtained from the average of such measurements, with an associated error given by the standard deviation. Three measurement runs are carried out for each optical configuration in order to achieve further noise reduction. Due to the limited amount of material, we did not measure the complete scattering matrix but only the elements F_{11} and F_{12}. For unpolarized incident light the F_{11} is proportional to the scattered flux. The measured values of the F_{11} are arbitrarily normalized so that they are equal to 1 at $\alpha = 150°$. The F_{11} normalized in this way is called the *phase function*. The $-F_{12}/F_{11}$ ratio (where the value of F_{11} is not normalized) is equal to the degree of linear polarization, P, for unpolarized incident light, expressed in terms of Stokes parameters as $P = -Q_{sc}/I_{sc}$.

4 MATERIALS

We have selected four Carbonaceous Chondrites (CCs), two silicate minerals, and one organic powder as sources of cometary dust analogues. Bulk samples of the meteorites DaG521, FRO95002, and FRO99040 were provided by the Museo dell'Antartide Felice Ippolito, Siena especially for this work. Batches of particulate tholins were synthesized at the Laboratoire Inter-Universitaire des Systemes Atmospheriques (LISA), Paris. The Allende, olivine, and pyroxene samples belong to the IAA-CODULAB collection and have been used in a previous work (Muñoz et al. 2000). Below we describe the bulk properties of these materials, the methods employed to obtain particulate samples suitable for our light scattering experiments, and the physical properties of the particles (optical constants, size distribution, and morphology).

Table 1. Mean composition of CV and CO chondrites and of the Allende meteorite in per cent wt, taken from the meteorite data base METDB (Nittler et al. 2004).

	CO	CV	Allende
Si	15.8	16.0	16.0
Ti	0.08	0.15	0.10
Al	1.58	2.19	1.79
Cr	0.36	0.35	0.37
Fe	24.3	23.1	23.9
Mn	0.18	0.15	0.15
Mg	14.4	14.4	15.0
Ca	1.62	2.5	1.89
K	0.05	0.03	0.03
S	1.94	1.63	1.77
P	0.11	0.13	0.10
Na	0.35	0.35	0.33
Ni	1.31	1.11	1.23
O	37.9	37.9	37.2

4.1 Bulk materials description

4.1.1 Meteorites

CCs meteorites are among the oldest and most primitive materials in the Solar system. Age determination techniques indicate that they formed around 4.5 Gyr ago (Chen & Wasserburg 1981; Mahnes, Göpel & Allégre 1987). Since they are very old, these rocks suffered different primary processes, which record pre-accretionary histories in the solar nebula, and secondary processes like aqueous alteration, thermal metamorphism, and shock metamorphism (Brearley & Jones 1998).

CCs are divided in several classes based on composition: CI, CH, CO, CV, CK, CR. Most of them are fragments of primitive asteroids. They come from the NEO population, which includes about 10 per cent of extinct comets, in addition to former asteroids (DeMeo & Binzel 2008).

The bulk composition of the Carbonaceous Ivuna (CI) group of chondrites is very close to the composition of the solar photosphere. Furthermore, interstellar grains that predate the Solar system formation are found in the matrix of these primitive chondrites (Brearley & Jones 1998). CCs are characterized by chondrule sizes ranging from 1 mm in the CV group down to around 0.15 mm and 0.02 mm in the CO and CH groups, respectively. The CV and CO chondrites have the highest abundances of refractory inclusions, while CR and, above all, CH chondrites have the highest content of metals (Brearley & Jones 1998; Weisberg, McCoy & Krot 2006). In Table 1 we report the mean composition of CO and CV chondrites and of the Allende meteorite (Nittler et al. 2004).

*DaG521 and Allende*The meteorites DaG521 (Dar al Gani 521, found in Lybia in 1997; Grossman 1999) and Allende (fallen near Parral, Chihuahua, Mexico, in 1969) are classified as CV3. CVs chondrites are characterized by large mm-sized chondrules, large refractory inclusions, and abundant matrix (40 per centvol). They are divided into oxidized CV_{OX} and reduced CV_{RED} subgroups based on abundances of metal, magnetite, and Ni content (McSween 1977). The main component of CV matrices is Fe-rich olivine (fayalite Fa ∼ 30–60 and in some cases Fa > 90), but there are substantial differences among the subgroups due to different late stage metasomatism and aqueous alteration (Krot, Scott & Zolensky 1995; Krot et al. 1998). Other mineral constituents are Ca-Fe-pyroxene, andradite, Fe-Ni sulfides, and magnetite. Some chemical

and textural features of the CV chondrites evidence a phase in which the parent body experienced temperatures <300°C (Krot et al. 1998).

DaG521 is the only meteorite of our set with reddish colour, probably due to iron oxide generated by weathering in the Lybian desert.

Allende is classified as CV_{OX}. This group displays Calcium-Aluminum-rich Inclusions (CAIs) and ameboid olivine refractory elements and this suggests they have been formed at high temperature during the early stages of Solar system formation. A recent discovery of a class of asteroids (the so-called Barbarians) seems to have a composition unusually enriched in CAI minerals, like spinel (Cellino et al. 2014). Allende differs from other CV_{OX} meteorites in its lower matrix-chondrule ratio and in having chondrules with more opaque minerals (Brearley & Jones 1998).

*FRO95002 and FRO99040*These two meteorites were found in Antarctica, in the region of the Frontier Mountain in 1995 and 1999, respectively. Both belong to the CO3 class, which presents similar characteristic of CV3 regarding chondrules and matrix abundance, but differ in the chondrule dimensions, which in the CO3 case are μm sized. The CO chondrites are all of petrologic type 3, showing slightly different metamorphic stages, ranging from 3.0 to 3.7 (McSween 1977). CO chondrites usually have low Fe compositions with olivine with Fa < 1 (Brearley & Jones 1998). Also Fe-pyroxenes are rare, only a few pyroxenes with Fs ∼ 10 are reported (Brearley & Jones 1998).

4.1.2 Minerals

The first hint of the presence of silicates in the cometary dust dates back to the observation of the emission feature at 10 μm in comet Bennett and its consequent laboratory modelling (Maas, Ney & Woolf 1970). The measurements of 1P/Halley mineralogical composition revealed Mg-rich olivine (forsterite) and pyroxene (enstatite) as dominant compounds from *in situ* mass spectra of particles provided by *Giotto* and *Vega* Spacecraft (Schulze, Kissel & Jessberger 1997). Crystalline forsterite and enstatite have been detected also on comet Hale–Bopp (Crovisier et al. 1997) and 9P/Tempel from space-based infrared spectra (Lisse et al. 2007) and on 81P/Wild2 from direct measurement of particles collected by Stardust mission (Zolensky et al. 2006). These silicates are predicted by thermodynamic models to condense in a hot gas at 1200–1400 K, while the reaction with Fe occurs only at lower temperature. Thus, the preponderance of Mg-rich silicates in cometary dust can be explained by direct condensation in the inner primordial nebula (Hanner & Bradley 2004). The olivine and pyroxene samples used in this work have, respectively, the composition $Mg_{1.85}Fe_{0.14}SiO_4$ and $Mg_{0.85}Fe_{0.08}Si_{0.99}O_3$, and are therefore close to the Mg-rich endmembers, i.e. forsterite and enstatite. Thus, in the following we will refer to the olivine and pyroxene samples as forsterite and enstatite. The forsterite sample is the one identified as 'Olivine S' in Muñoz et al. (2000).

4.1.3 Organics

Tholins are organic compounds generated by irradiation (solar UV, high energy particles, electrons) of mixtures of common compounds of carbon, oxygen, and nitrogen, e.g. CO_2, CH_4, and HCN (Sagan & Khare 1979). They are thought to be present on the surfaces and/or in the atmospheres of several Solar system bodies. For example, they are likely responsible for the reddish colour of many objects such as Pluto (Gladstone 2016) and Ceres (Combe et al. 2017), and are believed to be responsible for Titan's atmospheric haze (Brassé et al. 2015).

Analysis of 1P/Halley dust mass spectra indicated for the first time the existence of CHON particles in comets (Kissel & Krueger 1987). The complex nature and variety of organics in cometary dust was revealed by analysis of samples returned from 81P/Wild, obtained by *Stardust* (Sandford et al. 2006; Matrajt et al. 2008; Clemett et al. 2010). More recently, the *in situ* analysis of 67P coma dust by COSIMA/*Rosetta* mass spectrometer has confirmed the presence of abundant high-molecular weight organic matter, nearly 50 per cent in mass (Bardyn et al. 2017; Fray et al. 2017). Thus, the abundance of CHON compounds in cometary dust suggests that tholins are likely to form in this environment as well. Tholins have been previously used in laboratory studies as cometary dust simulants, often mixed with other components, typically silicates and ices (Poch et al. 2016a,b; Jost et al. 2017).

The tholins sample used in this work was synthesized using the PLASMA experimental set-up described previously by Brassé et al. (2017). It allows the production and sampling of tholins from N_2–CH_4 electron irradiation in a glove box without contamination by the air of the laboratory. The elemental composition of these tholins has been determined (Brassé 2014). They are carbon rich (C/N = 2.2 to 2.4) with a C/H of 0.7 to 0.8. Several grams of tholins were prepared to perform the CODULAB measurements.

4.2 Sample preparation

In order to obtain particulate samples with different size distributions within the typical size range of cosmic dust particles, the DaG521, FRO95002, and FRO99040 samples were milled and dry sieved at the Department of Geoscience of the University of Padua. After milling, the three samples were first size segregated using a 71 μm sieve. The fraction of sample that passed through the sieve was subsequently sieved using a 53 μm sieve. This procedure generated three subsamples designated as DaG521M, FRO99040M, and FRO95002M with diameters, d, in the range 53 μm < d < 71 μm. The fractions of DaG521M and FRO99040M that passed through the 53 μm sieve were subsequently sieved through a 45 μm sieve producing subsamples DaG521S and FRO99040S (45 μm < d < 53 μm). Not enough material of FRO99040M was left to produce a further sample. A similar sieving procedure was used to produce the olivine samples described by Muñoz et al. (2000).

As far as the organic sample is concerned, after their synthesis, the tholins were kept in gas proof vials under dry N_2 atmosphere, to avoid their chemical evolution. Just before measurements with CODULAB the tholins were first homogenized with a mortar to break the agglomerates and sieved to obtain an homogeneous powder. Then, these tholins were introduced into the cylindrical stainless steel tank of the aerosol generator.

4.3 Sample characterization

4.3.1 Refractive index

The refractive index of a medium is defined as

$$m = c\sqrt{\epsilon\mu} = n + ik \tag{3}$$

where ε is the electric permittivity, μ is the magnetic permeability, and c the speed of light in vacuum. The optical constants n and k

Table 2. Refractive index of each sample and their relative appearance.

Sample	Refractive Index	Appearance
DaG521	$1.65 + i10^{-3}$	reddish
FRO99040	$1.65 + i10^{-3}$	dark grey
FRO95002	$1.65 + i10^{-3}$	dark grey
Allende	$1.65 + i10^{-3}$	dark grey
Forsterite	$1.62 + i10^{-5}$	white
Enstatite	$1.58 + i10^{-5}$	white
Tholins	$1.35 + i2.3 \cdot 10^{-2}$	dark

represent, respectively, the phase velocity of the wave in the medium and the absorption coefficient of the material.

Estimates of the refractive indices of our samples are compiled in Table 2. The refractive indices of forsterite and enstatite (Dorschner et al. 1995) have been obtained from the Jena-St. Petersburg Data base of Optical Constants (http://www.astro.uni-jena.de/Laboratory/Database/jpdoc/index.html). The refractive index of tholins at 532 nm has been reported by Hasenkopf et al. (2010); for a detailed analysis of the tholins optical properties see Brassé et al. (2015).

The refractive indexes of the Allende, DaG521, FRO99040, and FRO95002 meteorite samples are unknown. Therefore, we have assumed estimates based on literature values of the main constituents. The imaginary part of the refractive index of the terrestrial samples is significantly smaller than that of the meteorites and tholins, which indicates a smaller absorbance of these materials, consistent with their light colour. By contrast, the meteorite powders are darker as a result of the higher bulk Fe content and organic components.

It should be kept in mind that the refractive index generally depends on the wavelength of the incident light. While the Mg-rich forsterite and enstatite present a flat wavelength dependence in the visible, the Fe content of the meteorite samples is expected to produce an effect on the refractive index at different visible wavelengths. This fact has been recently taken into account by Devogèle et al. (2018) to interpret the observed wavelength dependence of the inversion angle of polarization of asteroid (234) Barbara as a consequence of the imaginary refractive index, in turn a consequence of the presence of nano-iron phase particles.

4.3.2 Size distribution

The size distributions of our samples have been estimated using a low angle laser light scattering (LALLS) particle sizer (Malvern Mastersizer 2000; Rawle 1993). The LALLS method relies on the measurement of the phase function of samples dispersed in a carrier fluid at 633 nm within a range of low scattering angles (0.02°–30°). The volume distribution of equivalent spherical particles that best reproduces the observed phase function is obtained by inverting a light scattering model based on Mie theory, which requires knowing the complex refractive index of the samples (equation 3). Since the refractive indexes of our meteorite samples are unknown, we have carried out a sensitivity study of the impact on the retrieved size distributions of varying n and k within wide ranges. In these sensitivity tests we have used as reference value the estimated refractive index for the Allende meteorite ($m = 1.65$, $k = i0.001$; Muñoz et al. 2000). First, the imaginary part of the refractive index, k, was fixed to the reference value ($k = 0.001$). The value of real part, n, was then varied between 1.5 and 1.7 in steps of 0.05. Second, the real part was fixed to the reference value ($n = 1.65$), and the imaginary part, k, was varied from 10^{-5} to 10^{-1} in factor of 10 steps.

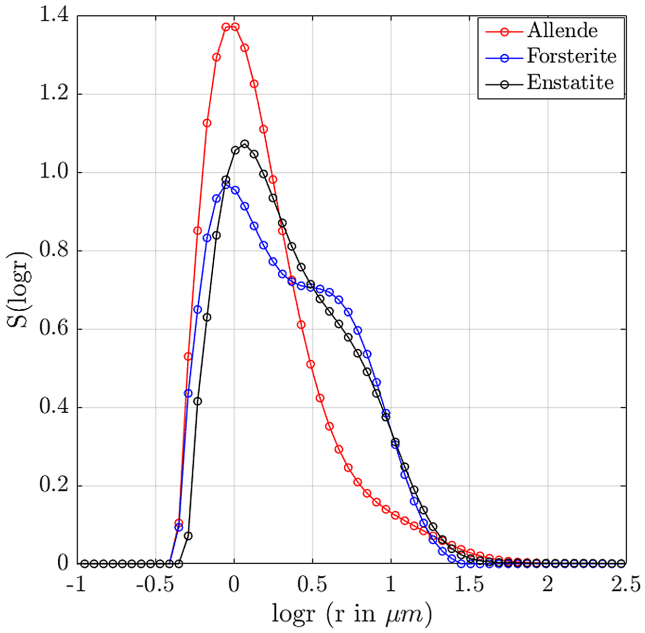

Figure 1. Size distribution of samples of Allende meteorite, Forsterite, and Enstatite.

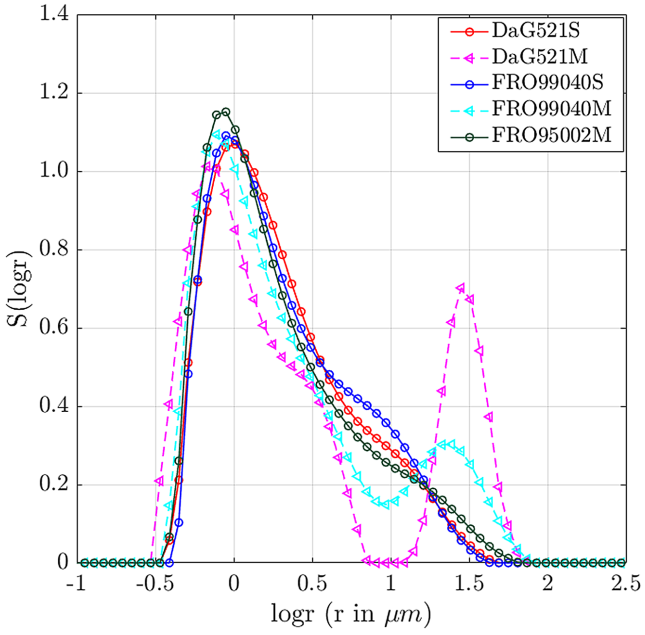

Figure 2. Size distribution of two different samples of DaG521, FRO95002, and FRO99040.

Artefacts are found in the retrieved size distributions in the small size range ($r < 1$ μm) when low values of the real part ($n = 1.5$; $n = 1.55$) or extreme values of the imaginary part ($k = 10^{-5}$; $k = 10^{-2}$; $k = 10^{-1}$) are assumed. Therefore, we consider the reference value $n = 1.65 + i0.001$ as a reasonable estimate of the refractive index of our meteorite samples.

In spite of the sieving procedure described in Section 4.2, the meteorite samples show broad size distributions with volume equivalent radii ranging from 0.3 to ∼ 100 μm. Figs 1 and 2 show the $S(\log r)$ size distributions of the samples. Here, $S(\log r)$ is the

projected surface area for a volume equivalent sphere with radius r. Size distributions are commonly characterized by the effective radius $r_{\rm eff}$ and effective variance $v_{\rm eff}$ as defined by Hansen & Travis (1974). These parameters have a straightforward interpretation for mono-modal distributions, while for multimodal distributions, the $r_{\rm eff}$ and $v_{\rm eff}$ are only first-order indicators of the particles size. For example, the DaG521M and FRO99040M samples show bi-modal size distributions with secondary peaks at ∼30 and ∼20 μm, respectively.

Due to the limited amount of the tholins sample, we could not measure its size distribution. Based on the Field Emission Scanning Electron Microscope (FESEM) images (Figs 3k and 3l) we can estimate a broad size distribution with sizes ranging from submicron up to hundred of microns.

4.3.3 Morphology

Fig. 3 shows Field Emission Scanning Electron Microscope (FESEM) images of our samples. It can be seen that in all cases the particles present a wide variety of irregular shapes. Figs 3(a)–(d) show that the enstatite, forsterite, and Allende meteorite particles present sharp edges and relatively clean flat surfaces compared with the other samples. The DaG521, FRO95002, and FRO99040 particles (Figs 3e–j) present more rounded shapes with rough surfaces covered by a layer of small particles. These morphological differences could be partially caused by the powder preparation method. The dry-sieving procedure could not remove small particles that remained stuck on the surface of the large particles by electrostatic forces. By contrast, the enstatite, forsterite, and Allende meteorite samples underwent wet sieving, which removed a large fraction of the finest particles from the original sample. For this reason the grain surfaces appear generally smoother than for the other samples. Tholins show peculiar structures due to the synthesis process that produced very elongated particles of the order of 10 μm with layered substructure and sub-μm surface roughness (Figs 3k–l).

5 RESULTS AND DISCUSSION

5.1 Measurements

In this section we present the measured phase functions $F_{11}(\alpha)$ (Fig. 4) and degree of linear polarization for unpolarized incident light $P(\alpha) = -F_{12}(\alpha)/F_{11}(\alpha)$ (Fig. 5) for all samples studied in this work. The measurements were performed at a wavelength of 520 nm covering the phase angle range from 3° to 175°. As mentioned, the measured phase functions are normalized to unity at $\alpha = 150°$. The experimental phase function and polarization curves are freely available in the Amsterdam–Granada Light Scattering Data base (http://www.iaa.es/scattering) under request of citation of this paper and Muñoz et al. (2012).

The light scattering behaviour of the samples considered in this work is qualitatively similar to that of other types of irregular mineral dust investigated in the laboratory (see Muñoz et al. 2012 and references therein). The measured phase functions show a strong peak at large phase angles, a plateau with almost no structure at intermediate angles, and a moderate increase at small phase angles. Fig. 4 does not reveal large differences between samples.

The measured P curves display the typical bell shape with a small negative branch starting at an inversion angle, α_0 and reaching a minimum at $\alpha_{\rm min}$ (Fig. 5). The wide positive branch has a maximum $P_{\rm max}$ at $\alpha_{\rm max} = 75°$–$90°$. These polarization curves are also similar to those observed by remote sensing for a variety of Solar system objects such as comets and asteroids. In contrast to the phase functions, the polarization curves of our samples do show significant variability. Table 3 summarizes the main parameters of the degree of linear polarization curve in the region of minimum polarization ($P_{\rm min}$, $\alpha_{\rm min}$), inversion angle (α_0), and maximum polarization ($P_{\rm max}$, $\alpha_{\rm max}$).

Among our samples, tholins show the highest maximum values of linear polarization ($P_{\rm max} = 19$ per cent) and the deepest negative branch ($P_{\rm min} = -6.7$ per cent). Note that the empirical relationship known as *Umov's effect* indicates an inverse relationship between the maximum value of polarization and the geometric albedo (Zubko et al. 2011), and tholins are indeed the darkest material considered in this study. However, for a cloud of irregular particles in single scattering conditions the interrelation between $P_{\rm max}$ and the geometric albedo is dependent on the size distribution of the particle cloud (Zubko et al. 2017, 2018). Thus, the Allende meteorite sample, which has the smallest effective radii, also presents the lowest maximum of the degree of linear polarization in spite of its dark colour. Interestingly, the polarization curve of the Allende sample has a distinct feature compared to the pure silicate samples, showing a shoulder near $\alpha = 150°$ at all wavelengths (see Fig. 6). The measured values of α_0 range from 26° for enstatite to 36° for the Allende sample. We do not find a clear relation between size distribution and position of the inversion angle. By contrast, for the range of sizes of our samples, the location of the inversion angle seems to be dependent on the composition. Terrestrial materials consisting of pure non-absorbing minerals show lower inversion angles than the meteorites and tholins, which present iron and organic material in different proportions.

A fully satisfactory explanation of the negative branch of the linear polarization curve is still missing. Numerous Solar system objects such as cometary comae or asteroids and satellites, which are covered by a thick regolith layer, show this feature. Even quite small asteroids, for which we might assume that the surface regolith layer is thinner, generally exhibit the same general polarimetric behaviour as larger asteroids.

In principle, each powdered material should produce negative values of polarization at low phase angles, when coherent backscattering by small particles is considered. This physical effect results from the interference of wavelets scattered by the particulate medium. At zero phase angle the wavelets are in phase and they combined positively enhancing the intensity. The linear polarization reflects this effect as well, inverting the plane of wave polarization and favouring the parallel component of electromagnetic wave to be scattered, rather than the perpendicular one. The role of coherent backscattering in the development of a negative polarization branch and a backscattering enhancement (BSE) in the phase function has been discussed by Muinonen et al. (2012) using the exact method known as the superposition T-Matrix (Mackowski & Mishchenko 1996).

The origin of the negative branch of clouds of particles in single scattering conditions and corresponding particulate surfaces has also been investigated in several laboratory studies (e.g. Shkuratov et al. 2006, 2007; Escobar-Cerezo et al. 2018). In a recent work, Escobar-Cerezo et al. (2018) compare the scattering behaviour of two samples of the same lunar simulant with different size distributions. The effect of removing particles smaller than ∼1 μm from the pristine sample on the polarization curve is noticeable. The maximum of the linear polarization increases by a factor of 1.5. Apparently the small particle fraction of the pristine sample was

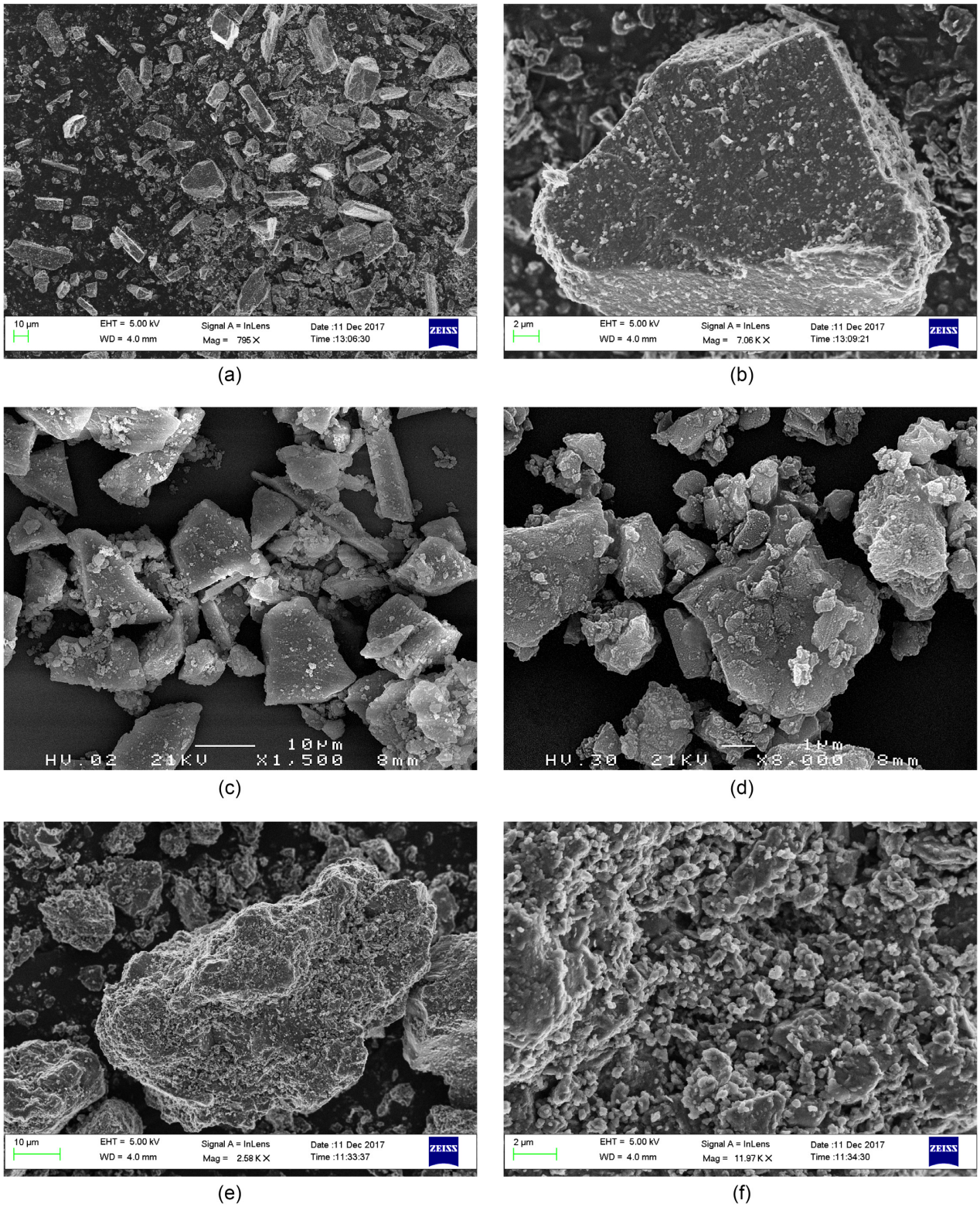

Figure 3. FESEM micro-photographs of enstatite (plates **a** and **b**), forsterite (plate **c**), Allende (plate **d**), DaG521 (plates **e** and **f**), FRO95002 (plates **g** and **h**), FRO99040 (plates **i** and **j**), and tholins (plates **k** and **l**).

limiting the maximum of the degree of linear polarization. Further, the negative polarization branch (absolute values) is decreased from 2.4 per cent to 0.8 per cent after removing particles smaller than 1 µm. This result seems to indicate that submicron scale features might be responsible for the negative branch of the degree of linear polarization.

In summary, it is quite difficult to disentangle all the effects responsible for the polarization curve shape, we can only highlight

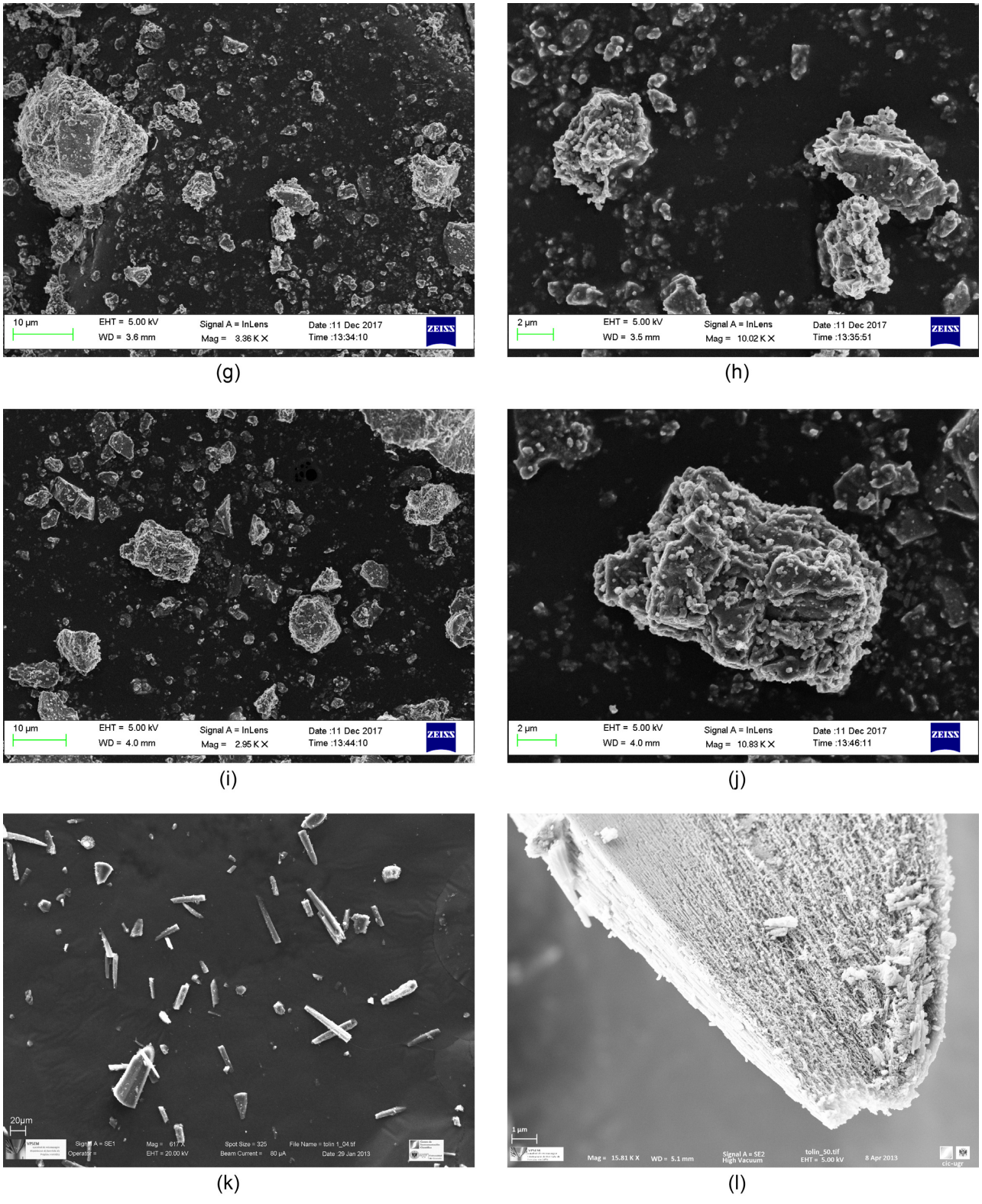

Figure 3 – *Continued*

some empiric relations, but it is essential to further investigate the subject. In sections 5.2 and 5.3 the differences observed in the phase function and degree of linear polarization are discussed in terms of different physical properties (size, colour, shape), in order to investigate their influence on the scattering behaviour of the samples.

5.2 Backscattering enhancement

In order to give an estimation of the trend of the phase function in the backward region for all studied samples, we compute the BSE, defined as the ratio of measured phase function values at

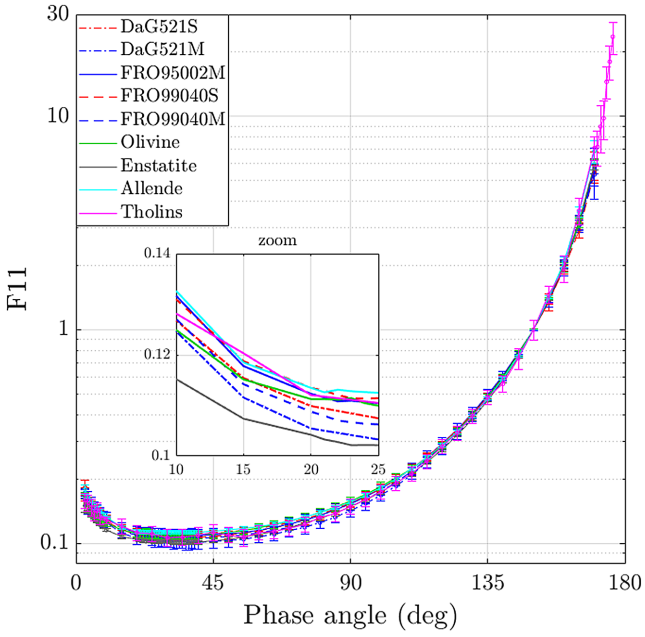

Figure 4. Phase functions of all samples at 520 nm. The inset shows a zoom-in of the backscattering region.

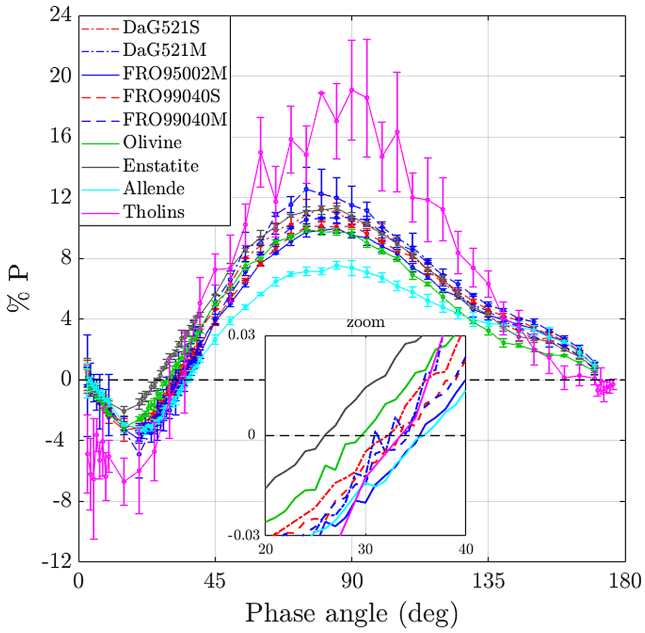

Figure 5. Polarization curve of all samples at 520 nm. The inset shows a zoom-in of the inversion angle region.

$\alpha = 0^\circ$ and $\alpha = 30^\circ$ (Bertini, Thomas & Barbieri 2007). Since our laboratory measurements do not cover the whole phase angle range we extrapolated a synthetic phase function, $F_{11}^{\rm syn}$, from our measurements that range from 3° to 175°. The synthetic phase function is defined in the full angle range from 0° to 180° and is normalized according to

$$\frac{1}{2}\int_0^{\pi} {\rm d}\alpha \sin\alpha F_{11}^{\rm syn}(\alpha) = 1. \quad (4)$$

The extrapolation of the measured phase function in the forward direction is based on the assumption that the forward scattering peak for randomly oriented particles with moderate aspect ratios is mainly dependent on the size and refractive indices of the particles, but not on their shapes (Liu et al. 2003). Between 175° and 180°, we produce Mie calculations for projected surface area equivalent spheres. For the Mie computations we use the measured size distribution of the corresponding sample and the value of the refractive indices presented in Table 2. For the backward direction, we first generate a value for the phase function at 0° by a quadratic function generated by least squares with the measured data points from 3° to 30°. Then all values between 3° and 30° are produced by a cubic splines interpolation considering an additional condition that must be fulfilled in all cases: the first derivative of the phase function at 0° must be zero (Hovenier & Guirado 2014). At this stage, both the forward peak (175°–180°) and the rest of the phase function (0°–175°) are defined, but they are normalized in a different way: the forward peak belongs to a function normalized according to equation (4) and the normalization of the rest of the function is arbitrary. The function defined by the measured (3°–175°) plus the extrapolated (0°–3°) data points is then vertically shifted until the computed $F_{11}^{\rm syn}(175^\circ)$ matches the measured $F_{11}(175^\circ)$. The normalization condition (equation 4) is then checked. If it is not satisfied within a 0.1 per cent accuracy, the value of the measurement at 175° is increased or decreased (within the experimental error bars) until the normalization condition is fulfilled. The BSE for all our samples lays in the range [1.94–2.27] (see Table 4).

5.3 The effect of size and colour on polarization

The degree of linear polarization of the DaG521S and DaG521M, and the FRO99040S and FRO99040M samples are plotted in Figs 7 and 8, respectively. Since each figure refers to the same material, the differences observed are only attributable to the different size distributions of the S and M samples. The salient feature of this comparison is an increase of the maximum polarization with size. In fact, it can be seen in Fig. 2 that the size distributions of the samples with a higher $P_{\rm max}$ (DaG521M and FRO99040M) present a secondary maximum at larger sizes. Thus, the contribution of particles with large size parameters ($x_{\rm eff} = 2\pi r_{\rm eff}/\lambda$) is most likely responsible for the measured increase in $P_{\rm max}$.

The direct relationship between $P_{\rm max}$ and $r_{\rm eff}$ (or $x_{\rm eff}$) apparent in Figs 7 and 8 suggests an inverse relationship between $P_{\rm max}$ and wavelength, since the size parameter is inversely proportional to wavelength.

The polarization curves for the forsterite sample at three different wavelengths (442, 520, and 633 nm) are plotted in Fig. 9. The measurements at 442 and 633 nm have been published previously (Muñoz et al. 2000). It can be seen that $P_{\rm max}$ increases as the size parameter of the particles decreases (λ increases for a fixed $r_{\rm eff}$). In this case the differences in the measured degree of linear polarization are also likely related to the size parameter of the grains, since the refractive index of forsterite presents a flat dependence on wavelength in the studied region.

The apparent contradiction between Figs 7 and 8 on one side and Fig. 9 on the other can be explained by the broad size range of our samples. The scattering properties of dust grains are described by three regimes: Rayleigh, resonance, and geometric optics. When particles are smaller than the wavelength (Rayleigh regime), $P_{\rm max}$ tends to decrease as the size parameter increases. In that case, $P_{\rm max}$ increases with wavelength if the refractive index is constant, i.e. $P_{\rm max} \propto 1/x \propto \lambda$. By contrast, in the geometric optics regime ($x_{\rm eff} \gg \lambda$), $P_{\rm max}$ tends to increase as the size parameter becomes larger,

Table 3. Polarimetric parameters of the samples. $r_{\rm eff}$ and $v_{\rm eff}$ are the effective radius and effective variance. $P_{\rm min}$ is the minimum of polarization and $\alpha_{\rm min}$ the relative phase angle. $P_{\rm max}$ is the maximum of polarization at phase angle $\alpha_{\rm max}$ and α_0 is the inversion angle. h(per cent/deg) is the slope of the polarization curves computed between $\alpha_{\rm max}$ and α_0. Tholins measurements were taken in the red domain, at $\lambda = 632$ nm.

Sample	$r_{\rm eff}$ (μm)	$v_{\rm eff}$	$P_{\rm min}$ (per cent)	$\alpha_{\rm min}$ (deg)	α_0 (deg)	$P_{\rm max}$ (per cent)	$\alpha_{\rm max}$ (deg)	h (per cent/deg)
DaG521S	3.58	1.96	-3.3 ± 0.7	15 ± 5	32 ± 1	11.3 ± 0.91	80 ± 5	0.24
DaG521M	8.69	2.43	-4.9 ± 1.6	20 ± 5	34 ± 1	12.6 ± 1.4	75 ± 5	0.31
FRO95002M	3.92	2.72	-3.9 ± 0.1	20 ± 5	35 ± 1	10.0 ± 0.3	85 ± 5	0.20
FRO99040S	3.68	1.72	-3.3 ± 0.3	20 ± 5	33 ± 1	10.1 ± 0.3	80 ± 5	0.21
FRO99040M	5.90	3.10	-3.5 ± 0.6	20 ± 5	34 ± 1	10.7 ± 0.1	90 ± 5	0.19
Forsterite	3.06	1.04	-3.1 ± 0.3	15 ± 5	30 ± 1	9.9 ± 0.2	75 ± 5	0.22
Enstatite	3.70	3.13	-2.1 ± 0.3	15 ± 5	26 ± 1	11.3 ± 0.2	85 ± 5	0.19
Allende	2.44	3.42	-3.3 ± 0.3	22 ± 1	36 ± 1	7.5 ± 0.2	85 ± 5	0.15
Tholins	-	-	-6.7 ± 1.5	15 ± 5	35 ± 1	19.1 ± 3.3	90 ± 5	0.35

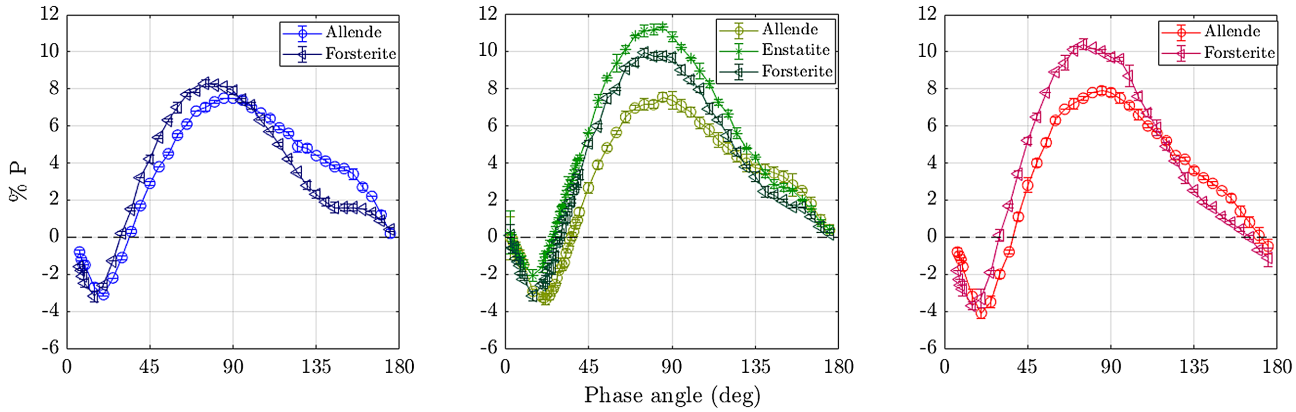

Figure 6. Measured degree of linear polarization curves for Allende meteorite (circles), forsterite (triangles), and enstatite (stars) at three different wavelengths 442 (left-hand panel), 520 (centre panel), and 633 (right-hand panel).

Table 4. Parameters related to the BSE computed for the samples at different wavelengths. BSE $= F_{11}(0^\circ)/F_{11}(30^\circ)$.

Sample	$r_{\rm eff}$ (μm)	$v_{\rm eff}$	$x_{\rm eff}$	$F_{11}^{\rm syn}(0^\circ)$	$F_{11}^{\rm syn}(30^\circ)$	BSE (520 nm)
DaG521S	3.58	1.96	43.3	0.384	0.191	2.01
DaG521M	8.69	2.43	105.0	0.419	0.214	1.96
FRO95002M	3.92	2.72	47.4	0.390	0.201	1.94
FRO99040S	3.68	1.72	44.5	0.612	0.270	2.27
FRO99040M	5.90	3.10	71.3	0.427	0.203	2.10
Forsterite	3.06	1.04	37.0	0.384	0.197	1.95
Enstatite	3.70	3.13	44.7	0.369	0.188	1.96
Allende	2.44	3.42	29.5	0.519	0.266	1.95

i.e. $P_{\rm max} \propto x \propto 1/\lambda$. These trends are well illustrated by computed polarization data for Gaussian random shapes from the Rayleigh to the geometric optics regimes reported by Liu et al. (2015). As shown in Fig. 2, the contribution of grains in the geometric optics domain for samples DaG521M and FRO95002M is relatively large. Therefore, the $P_{\rm max}$ tends to increase as $x_{\rm eff}$ increases (Figs 7 and 8). The majority of the grains in the forsterite sample belong to the Rayleigh and resonance ($x_{\rm eff} \approx \lambda$) domains where the dependence of $P_{\rm max}$ with size is nearly opposite, i.e. it increases as $x_{\rm eff}$ decreases (Fig. 9).

The degree of linear polarization curves for the Allende meteorite sample at three wavelengths (442, 520, and 633 nm) are plotted in Fig. 10. As shown in Fig. 1, the Allende sample mainly consists of particles in the Rayleigh and resonance regimes. In this case there is no clear trend of $P_{\rm max}$ with wavelength. The higher Fe content of the Allende meteorite compared to forsterite indicates a higher imaginary part of the refractive index at shorter wavelengths, implying a higher reflectance at red wavelengths. According to the Umov effect, the larger reflectance, the lower the maximum of the degree of linear polarization. Thus, the increase of $P_{\rm max}$ with wavelength seems to be balanced by a lower albedo at shorter wavelengths. Therefore, the maximum of the degree of linear polarization is dependent not only on the size of the grains but also on their refractive index. A study of tholins generated in plasma with different size distributions by Hadamcik et al. (2009) is in line with our results, showing that in Rayleigh regime $P_{\rm max}$ decreases when the particle size increases, while in optical regime $P_{\rm max}$ increases with the particle size.

It is worth noting that in the case of the forsterite sample (Fig. 9), the inversion angle α_0 does not change with wavelength. However,

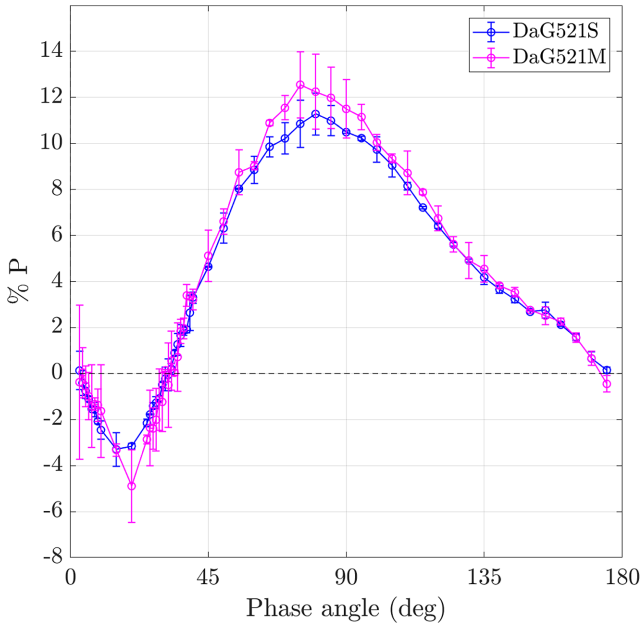

Figure 7. Measured degree of linear polarization curves for the DaG521S (blue symbols) and DaG521M (magenta symbols) samples at 520 nm.

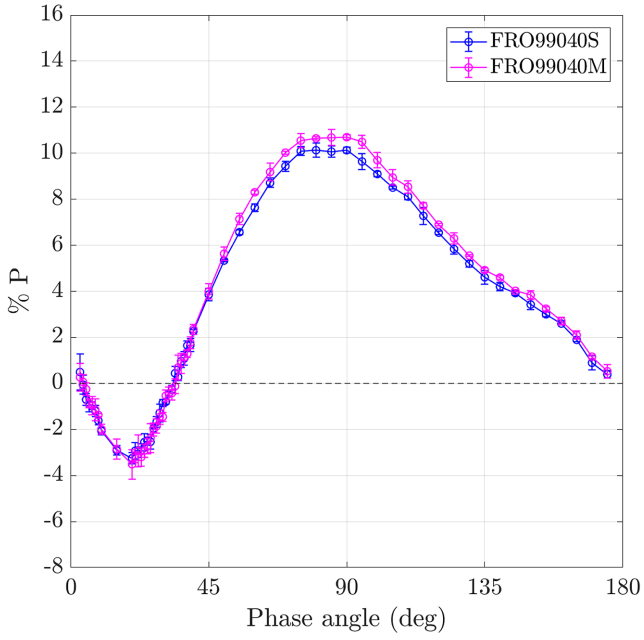

Figure 8. Measured degree of linear polarization curves for the FRO99040S (blue symbols) and FRO99040M (magenta symbols) at 520 nm.

some wavelength dependence of the negative branch minimum can be distinguished at 633 nm. In the case of the Allende sample, both the minimum of the negative branch and the inversion angle vary with wavelength. The apparent dependence of the negative branch parameters on composition (i.e. refractive index) seems to be in agreement with the simulations of Zubko et al. (2009) and Zubko, Videen & Shkuratov (2015), which demonstrate that the negative polarization parameters strongly depend not only on size parameter but also on the material absorption properties.

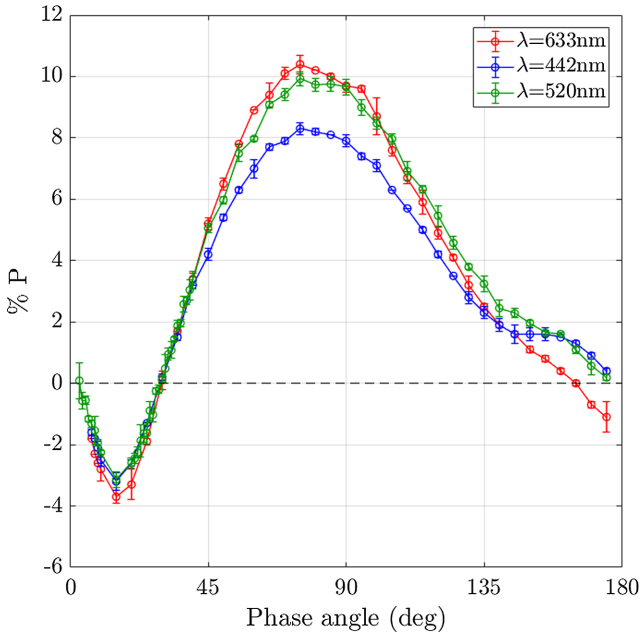

Figure 9. Measured degree of linear polarization curves for the forsterite sample at three different wavelengths.

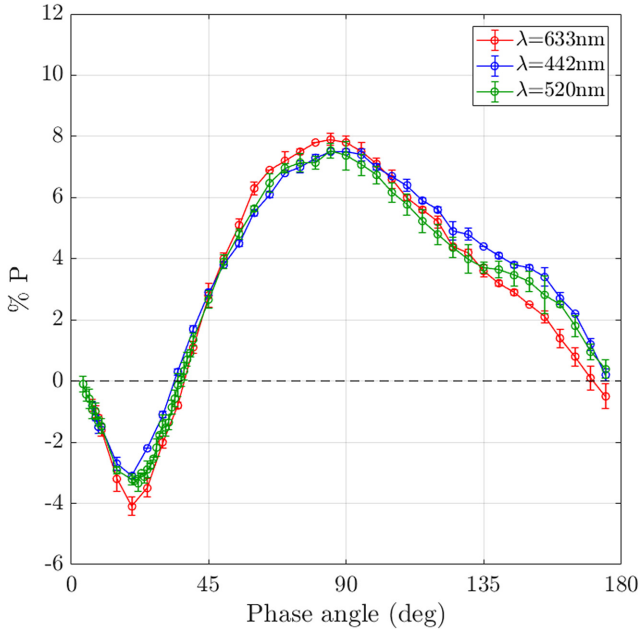

Figure 10. Measured degree of linear polarization curves for the Allende sample at three different wavelengths.

5.4 Comparison with asteroids and comets

Ground-based observations of the intensity of light scattered by cometary dust grains are usually limited to certain observational geometries. Moreover, time variations of the brightness of the coma as observed from Earth do not only depend on the phase angle but also on changes of the dust production rate as the comet moves in its orbit around the Sun (see e.g. Kolokolova et al. 2004). The OSIRIS camera onboard the Rosetta spacecraft revealed the behaviour of comet 67P phase functions from inside the coma (Bertini et al. 2017). They were obtained in a short time period

(about 2.5 h) covering an unprecedented broad phase angle range (from ∼10° to ∼155°). The measured phase functions show a peculiar u-shape with a minimum at a phase angle around 100°. That phase function is not reproduced by any of the μm-sized randomly oriented particles studied in this work or previously presented in the Amsterdam–Granada Light Scattering Data base (Muñoz et al. 2012). However, laboratory measurements of the phase function of mm-sized particles (Muñoz et al. 2017) show a distinct behaviour compared to μm-sized particle clouds, with a minimum placed at much larger phase angles more in line with the 67P phase curve. Further, recent analysis of the OSIRIS phase functions at low phase angles provides a range of BSE values broader [1.7–3.6] (Bertini et al. 2018) than that based on ground-based observations [1.7–2.7] (Ishiguro et al. 2013). As shown in Table 4, the BSE values obtained for our μm-sized cometary dust analogues are within the range obtained from ground-based observations. The highest BSE value obtained from the OSIRIS data (3.6) seem to be produced by a cloud of decimetric chunks orbiting 67P nucleus at distances smaller than 100 km (Bertini et al. 2018). All in all our experimental data suggest that 67P phase function is not dominated by randomly oriented μm-sized particles in line with the conclusions of multiinstrument analysis onboard Rosetta (Guettler, in preparation).

Polarization is a powerful tool to investigate the nature of particles populating cometary comae and asteroidal regoliths. The value of the minimum of the degree of linear polarization together with the slope of polarization curve is generally used to determine the albedo of asteroids. Moreover, polarimetric criteria are used to classify and refine the asteroid taxonomy (Belskaya et al. 2017). A caveat to direct comparisons between observations and laboratory results is that the assumption of single scattering is no longer valid for such bodies, since they are covered by a layer of regolith. Single scattering is considered to be more adequate to explain the behaviour of low-albedo objects, for which multiple scattering is less important. As a result of multiple scattering the minimum polarization value approaches zero, and the inversion angle α_0 decreases. Further, the positive polarization maximum decreases by multiple scattering effects and therefore its slope (Shkuratov et al. 2004, 2006, 2007). We refer to Kolokolova, Hough & Levasseur-Regourd (2015, chapters 5 and 8) for recent reviews on photometric and polarimetric laboratory measurements of particulate surfaces and individual particles. Taking into account the mentioned multiple scattering effects, we can still retrieve information on the physical properties that determines the observed polarimetric features of asteroidal regolith particles by direct comparison with our experimental data. For instance, in the case of (the still few) Near-Earth Asteroids (NEA) observed so far, the maximum of positive polarization can reach, for low-albedo objects like (3200) Phaethon and (101955) Bennu, much higher values of linear polarization (up to 40 per cent), well above the limits reached by the samples analysed in this work. The covered interval of angles did not include α_{max} but the observed data indicate that P_{max} could occur around 130°. Taking into account the decrease of P_{max} due to multiple scattering effects on the regolith layer, we can expect an even larger P_{max} for the single particles forming the regolith. According to previous experimental (Escobar-Cerezo et al. 2018) and computational (Liu et al. 2015) results, a high value of P_{max} shifted towards large phase angles, suggests a surface covered by particles significantly larger than those studied in this work.

Further, spectropolarimetric data of asteroids show that the gradient of linear polarization for increasing wavelength depends on the taxonomic class and upon the phase angle. In the positive polarization branch, the polarization tends to decrease for increasing wavelength for S-class objects (moderate albedo). Similar dependence of P_{max} with λ has been found for single particles that present a significantly higher imaginary part of the refractive index, k, at short (488 nm) than at large (647 nm) wavelengths (Dabrowska et al. 2015). Low-albedo objects do just the opposite as is the case of dust samples with a flat (Fig. 9) or moderate dependence of k with the wavelength (10). Note also that, for any given object of any class, the polarimetric gradient changes sign if the object is observed in the negative or in the positive polarization branch (Bagnulo, Cellino & Sterzik 2015) as is the case of the forsterite and Allende samples studied in this work (Figs 9 and 10).

On the other hand, the angle of inversion of polarization of asteroids is usually around 20°. A few objects exhibit an inversion angle at lower phase angles (15°–17°). Only a few rare objects, the so-called Barbarians, show high values of inversion angles, up to 28° (Cellino et al. 2006; Devogèle et al. 2018). As shown in Section 5.1, for the size range of the samples presented in this work, the position of the inversion angle depends on sample composition. This is also found by Devogèle et al. (2018) in their analysis of Barbarian asteroids. Other observed polarimetric evidence (P_{min} versus inversion angle plot) suggests that these objects should have a very fine surface regolith. This is also in agreement with some estimate of a low thermal inertia for (21) Lutetia, which has also a large inversion angle, not much smaller than that of Barbarians (Cellino et al. 2016). Only S-class NEAs objects have P_{max} values (7 per cent and 10 per cent) compatible with our measurements. As opposite, there are no asteroids reaching negative polarization deeper than −2,−3 per cent.

The condition of single scattering holds for cometary comae. Observational data show the existence of two classes of comets, based on the degree of linear polarization (Levasseur-Regourd et al. 1996; Shestopalov & Golubeva 2017). The high polarization comets, which are considered dust rich, and the low polarization comets, which have a higher gas component (Table 5). The measurements of the samples presented in this work seems to be of the order of the low polarization group. Generally, cometary comae behave qualitatively in a similar manner to our analogue particle clouds: they show a negative polarization branch at small phase angles, and a bell-shaped curve at side and backscattering angles, with a maximum of polarization at a phase angle near 90°. However, the exact parameters defining the cometary polarization phase curve (see Table 5 for comet 67P in particular), are different from our laboratory measurements. The 67P polarization phase curve might be shaped by particles larger than the wavelength, but with wavelength-scale surface features that could produce a polarization roughly similar that of a cloud of isolated scatterers. Moreover, the h slope observed for 67P seems to indicate that it belongs to the family of 'high polarization' comets (Rosenbush et al. 2017). This might be in agreement with the depletion of small particles (<1 μm) observed with Rosetta.

Our laboratory data support the interpretation of the decreasing polarization outward the nucleus of 67P, according to which this results from larger particles near the nucleus and smaller particles moving away from it (Rosenbush et al. 2017). In order to enable a more consistent comparison between astronomical observations and laboratory data, future studies need to consider more appropriate mixtures of components such as silicates, organics, and ices, with improved control on other characteristics such as size, shape, and surface roughness.

Table 5. Polarimetric parameters of two classes of comets from Levasseur-Regourd, Hadamcik & Renard (1996). Values for 67P correspond to post-perihelion period and are taken from Hadamcik et al. (2016). *The h value for 67P is the slope at the inversion angle, since no value for P_{max} are available.

Comet	λ (nm)	P_{min} (per cent)	α_{min} (°)	α_0 (°)	P_{max} (per cent)	α_{max} (°)	h (per cent/deg)
High P_{max}	515	-1.5 ± 0.5	9 ± 2	22.2 ± 0.5	26 ± 2	103 ± 10	0.22 ± 0.02
	670	-1.5 ± 0.5	11 ± 2	22.6 ± 0.5	28 ± 3	95 ± 10	0.25 ± 0.03
Low P_{max}	515	-1.7 ± 0.5	6 ± 3	19.0 ± 0.5	10 ± 3	80 ± 10	0.20 ± 0.02
	670	-1.9 ± 0.5	6 ± 3	20.5 ± 0.5	18 ± 3	95 ± 10	0.22 ± 0.02
67P	red	-1.7 ± 0.1	12 ± 3	22 ± 2	-	-	0.35 ± 0.02*

6 CONCLUSIONS

Our results are summarized as follows:

(i) All measured phase functions present the typical behaviour of μm-sized irregular compact dust particles in random orientation. They show strong peaks at large phase angles, almost no structure at side phase angles and soft increase at small phase angles.

(ii) The measured values of BSE of our samples are within the range obtained from ground-based observations of cometary comae. According to our experimental data small BSE values seem to indicate a coma population of μm-sized grains.

(iii) The dependence of P_{max} with size is opposite for particle sizes belonging to Rayleigh-resonance ($x_{eff} \approx \lambda$) and geometric optic ($x_{eff} \gg \lambda$) regimes. When particles are smaller or of the order of the wavelength (Rayleigh-resonance regimes), P_{max} decreases with size whereas in the geometric optics regime P_{max} tend to increase with size.

(iv) For the range of sizes of our samples, the minimum of the negative polarization branch seems to be dependent on both size and composition of the grains whereas the inversion angle value, α_0, depends on the refractive index.

(v) The measured degree of linear polarization curves are qualitatively similar to those obtained from ground-based observations of cometary comae. This is in line with the finding that the main scatterers in the coma are larger than the wavelength of the incident light, where the surface features of the particles are of the order of the incident wavelength.

ACKNOWLEDGEMENTS

The authors are grateful with the Museo dell'Antartide Felice Ippolito, Siena for providing the meteorite samples required, with the Department of Geoscience of the University of Padua for providing the laboratory facilities necessary to produce the samples. We are indebted to Rocío Márquez from the Scientific Instrumentation centre of the University of Granada for providing the SEM images and with Maurizio Gemelli from the Department of Earth Science of the University of Pisa. This work has been supported by the Plan Nacional de Astronomía y Astrofísica contract AYA2015-67152-R.

REFERENCES

A'Hearn M. F. et al., 2005, Science, 310, 258
A'Hearn M. F. et al., 2011, Science, 332, 1396
Bagnulo S., Cellino A., Sterzik M. F., 2015, MNRAS, 446, L11
Bardyn A. et al., 2017, MNRAS, 469, S712
Belskaya I. et al., 2017, European Planetary Science Congress, 11, EPSC2017
Bertini I. et al., 2017, MNRAS, 469, S404
Bertini I. et al., 2018, MNRAS, 482, 2924
Bertini I., Thomas N., Barbieri C., 2007, A&A, 461, 351
Blum J., Wurm G., 2008, ARA&A, 46, 21
Blum J., Gundlach B., Mühle S., Trigo-Rodriguez J. M., 2014, Icarus, 235, 156
Brassé C., 2014, , PhD thesis, Paris Est Créteil University
Brassé C., Muñoz O., Coll P., Raulin F., 2015, Planet. Space Sci., 109, 159
Brassé C., Buch A., Coll P., Raulin F., 2017, Astrobiol., 17, 8
Brearley A. J., Jones R. H., 1998, in Papike J.J., ed., Planetary materials, Chondritic meteorites. p. 3
Cellino A., Belskaya I. N., Bendjoya P., Di Martino M., Gil-Hutton R., Muinonen K., Tedesco E. F., 2006, Icarus, 180, 565
Cellino A., Bagnulo S., Tanga P., Novaković B., Delbò M., 2014, MNRAS, 439, L75
Cellino A., Bagnulo S., Gil-Hutton R., Tanga P., Canada-Assandri M., Tedesco E. F., 2016, MNRAS, 455, 2091
Chen J. H., Wasserburg G. J., 1981, Earth Planet. Sci. Lett., 52, 1
Clemett S. J., Sandford S. A., Nakamura-Messenger K., Hörz F., McKay D. S., 2010, Meteorit. Planet. Sci., 45, 701
Combe J.-P. et al., 2017, in Lunar and Planetary Science Conference. p. 2849
Crovisier J., Leech K., Bockelee-Morvan D., Brooke T. Y., Hanner M. S., Altieri B., Keller H. U., Lellouch E., 1997, Science, 275, 1904
Dabrowska D. D., Muñoz O., Moreno F., Ramos J. L., Martínez-Frías J., Wurm G., 2015, Icarus, 250, 83
DeMeo F., Binzel R. P., 2008, Icarus, 194, 436
Devogèle M. et al., 2018, Icarus, 304, 31
Dorschner J., Begemann B., Henning T., Jaeger C., Mutschke H., 1995, A&A, 300, 503
Escobar-Cerezo J. et al., 2018, ApJS, 235, 19
Escobar-Cerezo J., Palmer C., Muñoz O., Moreno F., Penttilä A., Muinonen K., 2017, ApJ, 838, 74
Frattin E. et al., 2017, MNRAS, 469, S195
Fray N. et al., 2017, MNRAS, 469, S506
Fulle M. et al., 2016, MNRAS, 462, S132
Fulle M., Blum J., 2017, MNRAS, 469, S39
Gladstone e. a., 2016, Science, 351, aad8866
Grossman J. N., 1999, Meteorit. Planet. Sci., 34, 169
Hadamcik E., Renard J.-B., Alcouffe G., Cernogora G., Levasseur-Regourd A. C., Szopa C., 2009, Planet. Space Sci., 57, 1631
Hadamcik E., Levasseur-Regourd A. C., Hines D. C., Sen A. K., Lasue J., Renard J.-B., 2016, MNRAS, 462, S507
Hanner M. S., Bradley J. P., 2004, Comets II, Composition and mineralogy of cometary dust, University of Arizona Press, Tucson, Arizona, p. 555
Hansen J. E., Travis L. D., 1974, Space Sci. Rev., 16, 527
Hasenkopf C. A., Beaver M. R., Trainer M. G., Langley Dewitt H., Freedman M. A., Toon O. B., McKay C. P., Tolbert M. A., 2010, Icarus, 207, 903
Hörz F. et al., 2006, Science, 314, 1716
Hovenier J. W., Guirado D., 2014, J. Quant. Spectrosc. Radiat. Transfer, 133, 596
Ishiguro M., Yang H., Usui F., Pyo J., Ueno M., Ootsubo T., Minn Kwon S., Mukai T., 2013, ApJ, 767, 75
Johansen A., Youdin A., 2007, ApJ, 662, 627
Jost B., Pommerol A., Poch O., Brouet Y., Fornasier S., Carrasco N., Szopa C., Thomas N., 2017, Planet. Space Sci., 148, 1
Kissel J., Krueger F. R., 1987, Nature, 326, 755
Kolokolova L., Hanner M. S., Levasseur-Regourd A.-C., Gustafson B. Å. S., 2004, Comets II, Physical properties of cometary dust from light

scattering and thermal emission, University of Arizona Press, Tucson, Arizona, p. 577
Kolokolova L., Hough J., Levasseur-Regourd A.-C., 2015, Polarimetry of Stars and Planetary Systems, Cambrige University Press, Cambrige
Krot A. N., Scott E. R. D., Zolensky M. E., 1995, Meteoritics, 30, 748
Krot A. N., Petaev M. I., Scott E. R. D., Choi B.-G., Zolensky M. E., Keil K., 1998, Meteorit. Planet. Sci., 33, 1065
Levasseur-Regourd A. C., Hadamcik E., Renard J. B., 1996, A&A, 313, 327
Lisse C. M., Kraemer K. E., Nuth J. A., Li A., Joswiak D., 2007, Icarus, 187, 69
Liu L., Mishchenko M. I., Hovenier J. W., Volten H., Muñoz O., 2003, J. Quant. Spectrosc. Radiat. Transfer, 79, 911
Liu J., Yang P., Muinonen K., 2015, J. Quant. Spectrosc. Radiat. Transfer, 161, 136
Maas R. W., Ney E. P., Woolf N. J., 1970, ApJ, 160, L101
Mackowski D. W., Mishchenko M. I., 1996, J. Opt. Soc. Am. A, 13, 2266
Mahnes G., Göpel C., Allégre C. J., 1987, Meteoritics, 22, 453
Matrajt G. et al., 2008, Meteorit. Planet. Sci., 43, 315
McSween H. Y., Jr., 1977, Geochim. Cosmochim. Acta, 41, 477
Muinonen K., Mishchenko M. I., Dlugach J. M., Zubko E., Penttilä A., Videen G., 2012, ApJ, 760, 118
Muñoz O. et al., 2010, J. Quant. Spectrosc. Radiat. Transfer, 111, 187
Muñoz O., Volten H., de Haan J. F., Vassen W., Hovenier J. W., 2000, A&A, 360, 777
Muñoz O., Moreno F., Guirado D., Ramos J. L., Volten H., Hovenier J. W., 2011, Icarus, 211, 894
Muñoz O., Moreno F., Guirado D., Dabrowska D. D., Volten H., Hovenier J. W., 2012, J. Quant. Spectrosc. Radiat. Transfer, 113, 565
Muñoz O., Moreno F., Vargas-Martín F., Guirado D., Escobar-Cerezo J., Min M., Hovenier J. W., 2017, ApJ, 846, 85
Nittler L. R., McCoy T. J., Clark P. E., Murphy M. E., Trombka J. I., Jarosewich E., 2004, Antarct. Meteorit. Res., 17, 231
Poch O., Pommerol A., Jost B., Carrasco N., Szopa C., Thomas N., 2016a, Icarus, 266, 288
Poch O., Pommerol A., Jost B., Carrasco N., Szopa C., Thomas N., 2016b, Icarus, 267, 154
Rawle A. F., 1993, The Basic Principles of Particle Size Analysis, Malvern Instruments, UK
Reinhard R., 1986, Nature, 321, 313
Rosenbush V. K., Ivanova O. V., Kiselev N. N., Kolokolova L. O., Afanasiev V. L., 2017, MNRAS, 469, S475
Sagan C., Khare B. N., 1979, Nature, 277, 102
Sagdeev R. Z. et al., 1986, Nature, 321, 262
Sandford S. A. et al., 2006, Science, 314, 1720
Schulze H., Kissel J., Jessberger E. K., 1997, in Pendleton Y. J., ed., ASP Conf. Ser. , Vol. 122, From Stardust to Planetesimals. Astron. Soc. Pac., San Francisco, p. 397
Shestopalov D. I., Golubeva L. F., 2017, Adv. Space Res., 59, 2658
Shkuratov Y., Ovcharenko A., Zubko E., Volten H., Munoz O., Videen G., 2004, J. Quant. Spectrosc. Radiat. Transfer, 88, 267
Shkuratov Y., Bondarenko S., Ovcharenko A., Pieters C., Hiroi T., Volten H., Muñoz O., Videen G., 2006, J. Quant. Spectrosc. Radiat. Transfer, 100, 340
Shkuratov Y., Bondarenko S., Kaydash V., Videen G., Muñoz O., Volten H., 2007, J. Quant. Spectrosc. Radiat. Transfer, 106, 487
Sierks H. et al., 2015, Science, 347, aaa1044
Soderblom L. A. et al., 2002, Science, 296, 1087
van de Hulst H. C., 1957, Light Scattering by Small Particles, John Wiley and Sons , New York
Volten H., Muñoz O., Brucato J. R., Hovenier J. W., Colangeli L., Waters L. B. F. M., van der Zande W. J., 2006, J. Quant. Spectrosc. Radiat. Transfer, 100, 429
Weisberg M. K., McCoy T. J., Krot A. N., 2006, Systematics and Evaluation of Meteorite Classification. Univ. of Arizona, Tucson, p. 19
Zolensky M. E. et al., 2006, Science, 314, 1735
Zubko E., 2015, Opt. Lett., 40, 1204
Zubko E., Kimura H., Shkuratov Y., Muinonen K., Yamamoto T., Okamoto H., Videen G., 2009, J. Quant. Spectrosc. Radiat. Transfer, 110, 1741
Zubko E., Videen G., Shkuratov Y., Muinonen K., Yamamoto T., 2011, Icarus, 212, 403
Zubko E., Videen G., Shkuratov Y., 2015, J. Quant. Spectrosc. Radiat. Transfer, 151, 38
Zubko E., Videen G., Zubko N., Shkuratov Y., 2017, J. Quant. Spectrosc. Radiat. Transfer, 190, 1
Zubko E., Videen G., Zubko N., Shkuratov Y., 2018, MNRAS, 477, 4866

This paper has been typeset from a TEX/LATEX file prepared by the author.